PLATELET ACTIVATION IN ARTIFICIAL HEART VALVES

A Dissertation

by

MOHAMMADALI HEDAYAT

Submitted to the Office of Graduate and Professional Studies of
Texas A&M University
in partial fulfillment of the requirements for the degree of

DOCTOR OF PHILOSOPHY

Chair of Committee,	Iman Borazjani
Committee Members,	J.N. Reddy
	Dorrin Jarrahbashi
	Freddie Witherden
Head of Department,	Andreas A. Polycarpou

May 2020

Major Subject: Mechanical Engineering

ABSTRACT

A numerical framework is developed to perform multi-scale (hinge-to valve-scale) flow simulation and quantify the thrombogenic performance of prosthetic heart valves. This aim is achieved by 1) developing a parallel dynamic overset grid and combining it with the curvilinear immersed boundary (overset-CURVIB) method to reduce the computational cost, and 2) developing a framework for evaluating the thrombogenic performance of heart valves in terms of platelet activation. The dynamic overset grids are used to locally increase the grid resolution near immersed bodies, which are handled using a sharp interface immersed boundary method, undergoing large movements as well as arbitrary relative motions. The new framework extends the previous overset-CURVIB method with fixed overset grids and a sequential grid assembly to moving overset grids with an efficient parallel grid assembly. In addition, a new method for the interpolation of variables at the grid boundaries is developed which can drastically decrease the execution time and increase the parallel efficiency. This overset grid framework is integrated with a framework to quantify the platelet activation which is developed using a Eulerian frame of reference which calculates the activation over the whole computational domain (contrary to Largrangian methods which use a limited number of particles). The new framework is verified and validated against experimental data, and analytical/benchmark solutions. This framework is used to compare the role of the systole phase in the poor performance of bileaflet mechanical heart (BMHV) valve by using the bioprothtetic heart valve as a control. The results show that the activation in the bulk flow during the systole phase might play an essential role in the poor hemodynamic performance of BMHVs. In addition, the contribution of bulk and hinge flow to the activation of platelets in BMHVs is quantified for the first time by performing simulations of the flow through a BMHV and resolving the hinge by overset grids. The total activation by the bulk flow is found to be several folds higher than that by the hinge/leakage flow. This is mainly due to the higher flow rate of the bulk flow which exposes many more platelets to shear stress than the leakage flow. For future work, this framework is going to be applied for thrombogenic optimization of new designs of mechanical heart valves

including trileaflet ones as well as patient-specific hemodynamic analysis of heart valves using fluid-structure interaction in more realistic geometries extracted from the medical images such as echocardiography.

DEDICATION

To my parents and my sisters for their supports, affection and prayers.

ACKNOWLEDGMENTS

I would like to express my sincere gratitude to my advisor, Iman Borazjani for his excellent guidance, patience, and support through this endeavor, without whom this work would have not been possible. I am grateful to the members of my doctoral committee, Professors J. N. Reddy, Dorrin Jarrahbashi and Freddie Witherden whose comments have greatly improved this work.

I owe a great deal of gratitude to my parents for devoting their lives to me, to my sisters for their kind support. Their love and encouragement had a significant influence in my life.

This work was supported by the American Heart Association [AHA: Grant No. 13SDG17220022], National Science Foundation [NSF: CAREER grant CBET 1453982], and the computational resources were provided by Texas A&M High-Performance Research Computing Center (HPRC).

CONTRIBUTORS AND FUNDING SOURCES

Contributors

This work was supported by a thesis committee consisting of Professor Iman Borazjani, J.N. Reddy, and Dorin Jarahbashi of the J. Mike Walker '66 Department of Mechanical Engineering and Professor Freddie Witherden of the Department of Ocean Engineering.

The geometric reconstruction of a left ventricle for Chapter 6 was provided by Tatsat Patel from the State University of New York at Buffalo. All other work conducted for the thesis was completed by the student independently.

Funding Sources

This work was supported by the American Heart Association [AHA: Grant No. 13SDG17220022], National Science Foundation [NSF: CAREER grant CBET 1453982], and the computational resources were provided by Texas $A\&M$ High-Performance Research Computing Center (HPRC).

NOMENCLATURE

CFD	Computational fluid dynamics
FSI	Fluid-structure interaction
MHV	Mechanical heart valve
BMHV	Bileaflet mechanical heart valve
BHV	Bioprothsetic heart valve
LV	Left ventricle
PIV	Particle image velocitometry
ALE	Arbitrary Lagrangian Eulerian
AMR	Adaptive mesh refinement
IBM	Immersed boundary method
OBB	Oriented bounding box
I/O	Input/output
CURVIB	Curvilinear immersed boundary method
MPI	Message passing interface
AABB	Axis aligned bounding box
DNS	Direct numerical simulation
PAS	Platelet activation state
EF	Ejection fraction
SV	Stroke volume
AMI	Acute infarct myocardium
CV	Control volume
CS	Control surface

TABLE OF CONTENTS

Page

ABSTRACT ii

DEDICATION iv

ACKNOWLEDGMENTS v

CONTRIBUTORS AND FUNDING SOURCES vi

NOMENCLATURE vii

TABLE OF CONTENTS viii

LIST OF FIGURES xi

LIST OF TABLES xvi

1. INTRODUCTION AND MOTIVATION 1

    1.1 Artificial heat valves 1
        1.1.1 Mechanical heart valves 2
        1.1.2 Bioprosthetic heat valves 3
        1.1.3 Hemodynamics of available heart valves 5
    1.2 Numerical methods for simulation of artificial heart valves 6
        1.2.1 Numerical methods for problems with moving boundaries 7
            1.2.1.1 Moving grid methods 7
            1.2.1.2 Fixed-grid methods 8
            1.2.1.3 Overset grids 10
        1.2.2 Multi-scale computational analysis 13
        1.2.3 Platelet activation 14

2. NUMERICAL METHOD 17

    2.1 Overview of the overset-CURVIB 17
        2.1.1 Governing equations in a general non-inertial frame of reference in General Curvilinear coordinate 18
    2.2 Grid assembly for moving overset grids 22
        2.2.1 Domain decomposition strategy 23
        2.2.2 Hole-cutting 26
        2.2.3 Identification of query points 27
        2.2.4 Data packing strategy 29

2.2.5 Donor search 31
2.2.6 Interpolation 35
2.3 Moving overset-CURVIB flow solver 37
2.3.1 Flux reconstruction and velocity transformation between inertial and non-inertial frames 39
2.3.2 Handling special cases: Overlap of overset boundaries with immersed boundaries or other overset grids 41
2.3.3 Mass conservation 43
2.4 Quantifying platelet activation in Eulerian framework 43
2.4.1 Platelet activation models 43
2.4.2 Scalar shear stress calculation 46
2.4.3 Platelet activation quantification 47

3. VALIDATION, VERIFICATION AND PARALLEL PERFORMANCE 49

3.1 Flow solver validation 49
3.1.1 Taylor-Green vortex 50
3.1.2 Rotationally oscillating cylinder 53
3.1.3 Forced inline oscillations of a cylinder in a fluid initially at rest 55
3.1.4 Freely falling circular cylinder 57
3.1.4.1 Single cylinder 58
3.1.4.2 Multiple cylinders 60
3.1.5 Multiple mackerels in diamond arrangement 63
3.2 Parallel performance 69
3.3 Platelet activation framework validation and sensitivity studies 71
3.3.1 Shear-induced platelet activation in laminar Taylor-Couette flow 71

4. COMPARISON BETWEEN PLATELET ACTIVATION IN BILEAFLET MECHANICAL AND BIO-PROSTHETIC HEART VALVES 74

4.1 Background 74
4.2 Method and Materials 76
4.3 Results and Discussion 76
4.4 Comparison to previous work 82
4.5 Summary 84

5. COMPARISON OF PLATELET ACTIVATION THROUGH HINGE VS BULK FLOW IN BILEAFLET MECHANICAL HEART VALVES 86

5.1 Background 86
5.2 Methods and Materials 89
5.2.1 Platelet activation 89
5.3 Results and Discussion 91
5.3.1 The interpolation method and comparison with experiments 91
5.3.2 Hinge flow and the gap size 98
5.3.3 Platelet activation in bulk versus hinge flow 99

5.4 Validation and sensitivity studies 107
5.4.1 Validation of the bulk flow and leaflet kinematics 107
5.4.2 Sensitivity of the results to the initial activation distribution 110
5.4.3 Validation/verification of the simulated hinge flow: Comparison with experiments and the role of the coupling method 111
5.5 Limitations 112
5.6 Conclusion 113

6. PATIENT-SPECIFIC VALVE DESIGN AND PLACEMENT: HYBRID ECHO-CFD 114

6.1 Background 114
6.2 Methods and materials 117
6.3 Results and discussion 119
6.3.1 Comparison of LV parameters with their corresponding physiological range 120
6.3.2 Flow simulation for the reconstructed LV assembly 121
6.3.2.1 Effect of mitral valve 123
6.3.2.2 Comparing healthy and acute myocardial infarction reconstructed LV 126
6.4 Validation and sensitivity study 127
6.5 Limitations and future works 129

7. SUMMARY AND OUTLOOK 132

7.1 Future work 135

REFERENCES 138

LIST OF FIGURES

FIGURE Page

1.1 Different types of artificial valves. (a) caged ball; (b) monoleaflet mechanical; (c) bileaflet mechanical; (d) porcine bioprosthetic; (e) Bovine bioprosthetic; (f) Transcatheter bioprosthetic; (g) Sutureless bioprosthetic 4

2.1 schematic position and orientation of non-inertial frame relative inertial frame where x^{int}, $x^{non-int}$ and x^{ctr} are the coordinate vectors in inertial frame, non-inertial frame and origin of non-inertial frame in inertial coordinate. 20

2.2 The flow-chart for parallel grid assembly algorithm presented in the paper and forming interpolation matrix..... 24

2.3 Schematic overset Domain decomposition and domain distribution in different processors for using 9 processors (p). Every block is distributed over all available processors..... 25

2.4 Overset grid layout for the Taylor-Green vortex. The inner domain and blanking region boundaries are shown by thick red and green lines, respectively. 26

2.5 Comparison between an OBB around a swimmer and an AABB which clearly shows OBB provides a much tighter bounding-box around the an object. 28

2.6 Schematic of search and trilinear interpolation for a point p inside a donor cell. d^k for $k = 1, 6$ shows the distance to the k^{th} surface of the donor cell. The point-in-the-box test can be performed based on p^1_{mid}; r^1_1, and r^1_2 which depict the midpoint and vectors for constructing the inward normal on the $k = 1$ surface of the donor cell. (figure from [1]) 32

2.7 Schematic of search strategies used in this work. a) compares the brute force search (filled blue cells) with walking search (red cross) b) shows the scenario where the walking search will stuck and thus a brute force search need to be performed..... 34

2.8 Schematic of assembled parallel interpolation matrix and distributed field vector. Here, rank shows the ID of each processor, rank_index shows index of the processor from which the solution is interpolated, and bi_index shows the block number in each processor. 38

2.9 Integrating grid assembly kernel to CURVIB flow solver for FSI simulations..... 40

2.10 Illustrates the position of overset grids and blanked regions of the background domain for a simulation with bodies in relative motion (here, circular cylinders) and the way the conservation of mass is satisfied. Here, the blanked region in the red grid intersects with one in the blue grid. In this situation, the mass is conserved over Γ_1 which is the boundary of the combined blanked region of red and blue grids. However, in the situation without intersection, e.g., Γ_1 and Γ_2, the mass is conserved on each blanked region separately. 42

2.11 Demonstrates the the strategy chosen for the multiple bodies in relative motion where the interface of overset grid intersects with a solid body. The area around the body is blanked out from the other overset grid, e.g. the area around the res body is blanked out from the blue overset grid, which prevents intersection of interface with solid body. For each interface the mass is conserved separately, e.g. mass conservation is satisfied on Γ_1 and Γ_2 separately. 44

3.1 Taylor-Green vortex problem at $t = 1$ and $Re = 10$: (a) the contour of velocity magnitude for a moving overset with translational speed of $V = PI/4$ b) the contour of velocity magnitude for a rotating overset with rotational speed of $\omega_c = PI/4$. It also compares the streamline contours for both overset grid (black) and background grid (white) 51

3.2 Standard error for Taylor-Green vortex flow as a function of the grid spacing/time-step in log–log scale at $t = 1$ and $Re = 10$. CFL is kept the same for all test cases, i.e.,$\frac{\Delta t}{\Delta t_{max}} = \frac{\Delta x}{\Delta x_{max}}$. The error shows about 2^{nd} order reduction with mesh refinement..... 52

3.3 Time histories of the torque coefficient for the flow around a rotationally oscillating cylinder at $Re = 300$. 54

3.4 Results of numerical simulation for oscillatory cylinder a) contour of velocity for three different phase angles b) Comparison of the inline velocity component (u) profile at position $x_1 = -0.6D$ for three different phase angles between numerical results (overset: - -, single grid: $-$) and the experimental measurements (**o**) of Dutsch et al. [2]..... 56

3.5 (a) Time histories of the velocity of the cylinder in the gravitational direction for the overset ($-$) and the single ($-$) grid simulations (b) contour of velocity magnitude at $tu_c/D = 50$ 59

3.6 Schematic position of overset grids (small black squares), background grid (large rectangle domain), and blank region (small blue squares) relative to each other for simulation of free fall of multiple circular cylinders under gravitational force..... 61

3.7 Comparison of time histories of the velocity for three different cylinder in the gravitational direction between overset and single grids. 61

3.8 Contour of velocity magnitude for overset simulation of multiple circular cylinders at time a) $tu_c/D = 4.4$ b) $tu_c/D = 12$ c) $tu_c/D = 15.6$ d) $tu_c/D = 22$ during the simulation. 62

3.9 Contours of vorticity in the midplane of the four fish swimming in the diamond arrangements. a) initial position of overset grids b) position of overset grids at $t/T = 8.8$ .contour of each overset grid and background grid are consistent. vortical structures are are advected from one domain to the other. Thick black lines represent the boundaries of the overset grids and thick red lines shows the blank region. 66

3.10 The 3D vortical structures visualized by the iso-surfaces of Q-criteria for four fish swimming in diamond arrangement. 67

3.11 Comparison of the self-propelled fish swimming axial and lateral speed for different swimmers in diamond shape. Fish 1 to 4 are denoted in Fig. 3.9..... 68

3.12 Wall-clock time speedup versus the number of processors for the fish schooling using 560 processors. 70

3.13 Schematic setup of rotating Couette flow which used for validation of platelet activation. Reprinted from [3]..... 72

3.14 Comparison of platelet activation using our framework with the experimental results [4]. Reprinted from [3]. 73

4.1 Platelet activation for the MHV and BHV in a straight aorta during the systole phase using the linear level of activation model at time t=(a) 52, (b) 93, (c) 200, and (d) 273 ms within the cardiac cycle. Reprinted from [5]. 77

4.2 Platelet activation for the MHV and BHV in a straight aorta during the systole phase using the damage accumulation model at time t=(a) 52, (b) 93, (c) 200, and (d) 273 ms within a cardiac cycle. Reprinted from [5]. 78

4.3 Platelet activation (ΔPAS) for the MHV and BHV in a straight aorta during the systole phase using Soares model at time t=(a) 52, (b) 93, (c) 200, and (d) 273 ms within a cardiac cycle. Reprinted from [5]..... 79

4.4 The Integration of platelet activation over the whole domain for a MHV and BHV in a straight aorta during the systole phase using different models (the normalized BHV activation is 1 at the end of the systole regardless of the activation model used). Reprinted from [5]. 81

4.5 The scalar viscous shear stress for the MHV and BHV in a straight aorta during the systole phase at time t=(a) 52, (b) 93, (c) 200, and (d) 273 ms within a cardiac cycle. Reprinted from [5]. 83

5.1 (a) large scale domain for over-set numerical simulation (b) flat level is chosen as the plane of reference (c) position of hinge domains and blank regions relative to hinge recess (d) hinge model with butterfly hinge recess. Reprinted from [3]. 90

5.2 Scalar shear stress for hinge domain using one-way interpolation for gap size of $150\ \mu m$ for different plane of view (a) mid-diastole and (b) systole. Reprinted from [3]. 93

5.3 Scalar shear stress for hinge domain using two-way interpolation for gap size of $150\ \mu m$ for different plane of view (a) mid-diastole and (b) systole. Reprinted from [3]. 94

5.4 Velocity contours and vectors in the hinge domain with different interpolation methods at peak systole for the flat level and the plane of $300\ \mu m$ using (a) one-way interpolation and (b) two-way interpolations. Reprinted from [3]. 95

5.5 Velocity contour and vectors for hinge domain at mid-diastole for different plane of view (a) one-way interpolation gap size of $150\ \mu m$ (b) one-way interpolation gap size of $250\ \mu m$ (c) two-way interpolation gap size of $150\ \mu m$ (d) two-way interpolation gap size of $250\ \mu m$. Reprinted from [3]..... 96

5.6 Comparison of total platelet activation for the bulk and the hinge (for difference gap sizes and interpolation models) flows using linear and Soares activation model within a cardiac cycle. The total activation is normalize by total total activation of the bulk flow at the end of cycle for each model. The leaflet angles and the flow rates are also plotted. 1w and 2w denote one-way and two interpolation, respectively. 150 and 250 denote the gap size of the hinge region. Linear and Soares denote the platelet activation model. Reprinted from [3]..... 97

5.7 Platelet activation of hinge domain using Soares model and two-way interpolation for both gap sizes At mid-diastole for different plane of view (a) gap size $150\ \mu m$ and (b) gap size $250\ \mu m$. Reprinted from [3]. 100

5.8 Comparison of out of plan vorticity using two-way coupling simulation with PIV measurements of Dasi et al [6] at four different time instants within a cardiac cycle. Reprinted from [3]..... 101

5.9 Scalar shear stress for the MHV in the large scale domain at time t=(a) 137, (b) 206, (c) 309, and (d) 412 ms within the cardiac cycle. Reprinted from [3]. 103

5.10 Platelet activation for the MHV in the large scale domain using the Soares activation model at time t=(a) 137, (b) 206, (c) 309, and (d) 412 ms within the cardiac cycle. Reprinted from [3]. 104

5.11 Three-dimensional streamtraces at peak systole (a) and mid-diastole (b) for small scale simulation near the hinge recess (c) In-plane velocity on flat level at peak systole. Reprinted from [3]. 105

5.12 Comparison of the calculated leaflet kinematics with experimental observations [6]. Reprinted from [3]. 108

5.13 Pressure difference between the aortic and ventricle (for planes $\pm 25.4\ mm$ upstream and downstream of the valve) side during a cardiac cycle in the numerical simulations compared to the experiments by [7] for $23\ mm$ St. Jude BMHV. Reprinted from [3]. 109

5.14 Truncated normal probability distribution used for $PAS0$ in Soares model. Reprinted from [3]. 110

6.1 The final reconstructed LV based on 2D echo images attached to the approximated aorta and atrium surfaces for a) baseline and b) AMI case. 119

6.2 Comparison of a) volume (V), and b) flux (dV/dt) for baseline and AMI left ventricle during a cardiac cycle. 120

6.3 The schematic control volume (CV) and control surface (CS) used for calculating energy loss in the LV on the mid-plane passing through the aorta. 122

6.4 3D vortical structures visualized at different time instances during the diastolic filling using the iso-surfaces of q-criteria for a baseline LV with reconstructed valves for different time instants during diastole (t/T=instance time / cardiac cycle length). . 124

6.5 3D vortical structures visualized at different time instances during the diastolic filling using the iso-surfaces of q-criteria for a baseline LV without valves, for different time instants during diastole (t/T=instance time / cardiac cycle length) 125

6.6 Comparison of the flow velocity in the aortic orifice at peak systole between (a) baseline (b) AMI left ventricle. 127

6.7 3D vortical structures visualised at different time instances during the diastolic filling using the iso-surfaces of q-criteria for a acute myocardial infarction afflicted LV (t/T=instance time / cardiac cycle length) 128

6.8 Comparison between the Doppler velocity measurements and the velocity from the numerical simulation during diastole on a section below the mitral valve. 130

6.9 Comparison of the volume of 3D reconstructed baseline LV using different number of long-axis cross-sections. 130

LIST OF TABLES

TABLE Page

1.1 Hemodynamic property of different type of MHVs 5

2.1 Constants of Soares et al. model from ([4]) 46

3.1 Wall-clock time of different parts of the CURVIB-overset solver for different number of processors 69

5.1 Comparison of velocity and viscous shear stress at mid diastole using different interpolation methods for current study to the previous experiments for 23mm St. Jude Medical mechanical heart valve. Reprinted from [3]. 97

5.2 Comparison of velocity and viscous shear stress at the lateral, adjacent, and ventricular jets at the peak systolic and mid-diastolic phases for current study to the previous experiments on flat level. Reprinted from [3]. 112

6.1 Comparison of the computed cardiac parameters of the reconstructed LV to their physiological range of Porcine LV (EF: ejection fraction, E/A ratio: ratio of maximum fluxes during the E-wave and A-wave) 121

6.2 Comparison of LV $\dot{loss}$ for different test cases 123

1. INTRODUCTION AND MOTIVATION*

Heart valves play an important role in blood circulation in humans. Because higher blood pressure is exerting on the valves in the left ventricle (LV) the valvular diseases are more common for the valves in the LV, i.e., mitral and aortic valves. The function of valves is to ensure that the blood flows in the forward direction during the systole and minimizing the backflow from the aorta to the LV during diastole. The opening and closing of valves repeat more than $102,000$ times each day in which the valves undergo mechanical as well as flow-induced stresses. These stresses play an important role in the valve's leaflets failure in the long term. In addition, infection, rheumatic fever, calcification, etc. can also contribute to heart valve diseases (e.g., stenosis and regurgitation). These diseases can interfere with the functionality of the heart and result in death in some cases. The available treatments for heart valve diseases are either to repair or replace the native heart valve with an artificial one through surgery. It is estimated that about 2.5% of the U.S. population suffer from heart valve defects ([8]) which leads to approximately $67,500$ valve replacement surgeries each year ([9]).

1.1 Artificial heat valves

The ideal prosthetic valve should have the same characteristics as the native valve in terms of hemodynamics, durability, and good implantability. Currently, two major types of valves are available: mechanical heart valves (MHV), which account for approximately 30% of implantation [10], and bioprosthetic heart valves (BHV). Despite the improvement in the design of prosthetic valves and surgical procedures during the past decades, these valves are far from ideal, e.g., MHVs are highly thrombogenic and require life-long anticoagulant therapy. BHVs do not require life-long anticoagulant therapy because of better hemodynamics performance but deteriorate after 10 to 15 years. Different designs for mechanical and bioprosthetic heart valves have been introduced in the

*Part of this chapter is reprinted with permission from "Platelet activation of mechanical versus bioprosthetic heart valves during systole" by M. Hedayat et al., 2017, Journal of biomechanics, 56, 111-116, Copyright 2017 by Elsevier Ltd.

market during the past decades. However, each of these models has its limitations.

1.1.1 Mechanical heart valves

Four major different types of mechanical heart valves are available. Figure 1.1 shows the design of each type of MHVs.

- Caged Ball valves

  The caged Ball valve is the first artificial heart valve introduced in the market. It is consists of a ball in a cage formed by 3 metal arches and a circular sewing ring (Fig.1.1-a). The ball is pushed against the cage during the systole and allows the blood to flow through the aorta. While during the diastole the pressure drop inside the LV moves the ball back toward the sewing ring. This valve was discontinued by Edwards at 2007, however, thousands of patients still have this valve.

- Monoleaflet valves

  Monoleaflet valves are composed of a single graphite disc coated with pyrolite carbon (Fig.1.1-b). The disc tilts between two struts of the housing with the angle from 60° to 80° relative to the valve annulus. Some versions of this valve were prone to fracture of one of the retaining struts which resulted in releasing of the disc. The Monoleaflet valves are still being implanted but the manufacturing has been stopped by some of the manufacturers such as Bjork-Shiley.

- Bileaflet valves

  Bileaflet valves are made of two semicircular leaflets attached to the valve's ring using two hinges (Fig.1.1-c). The leaflets open with the angle from 75° to 90° relative to the valve annulus which create one central and two peripheral orifices. The St. Jude medical bileaflet mechanical heart valve (BMHV) was introduced in 1977. More than $600,000$ of this valve have been produced and implanted. BMHVs are the most common type of MHVs which is currently being used in clinical surgeries around the world [11].

- Trileaflet Valve

  Trileaflet valves have three leaflets instead of two leaflets in BMHVs. These valves are more similar to the native valves in terms of hemodynamics. Thus, they combine the hemodynamic superiority of the trileaflet native or bioprosthetic aortic valves with the durability of mechanical ones. The computational and experimental studies show that these valves have better hemodynamics compared to the conventional BMHVs [12].

1.1.2 Bioprosthetic heat valves

Bioprosthetic heart valves (BHVs) are constructed from porcine heart valves or bovine pericardium preserved with glutaraldehyde. These valves typically provide better hemodynamic performance compared to the mechanical heart valves, however, the structural valve deterioration may occur after 10-15 years. Thus, most of the annual valve replacements using these valves are carried out in elderly patients in developed countries [13]. The most common types of BHVs are introduced below.

- Xenograft or Heterograft

  These valves are made of animal tissues, usually porcine aortic valve followed by calf pericardium (Fig.1.1-d). The valve tissue is sewn on to a fabric-covered metal wire stent [14]. These valves last for 10–15 years.

- Bovine bioprosthetic valves

  These valves are similar in design to porcine valves in the leaflets but they are made from bovine pericardium mounted on a stented frame (Fig.1.1-e). The experiments show that these valves provide significantly better hemodynamics with lower valve gradients and larger aortic valve areas than porcine valves [15]. Due to these experimental results most of the newer design of the bioprosthetic heart valves are typically contain bovine tissue leaflets.

- Transcatheter valves

  These valves (Fig.1.1-f) are used for a minimally invasive surgery that repairs the valve

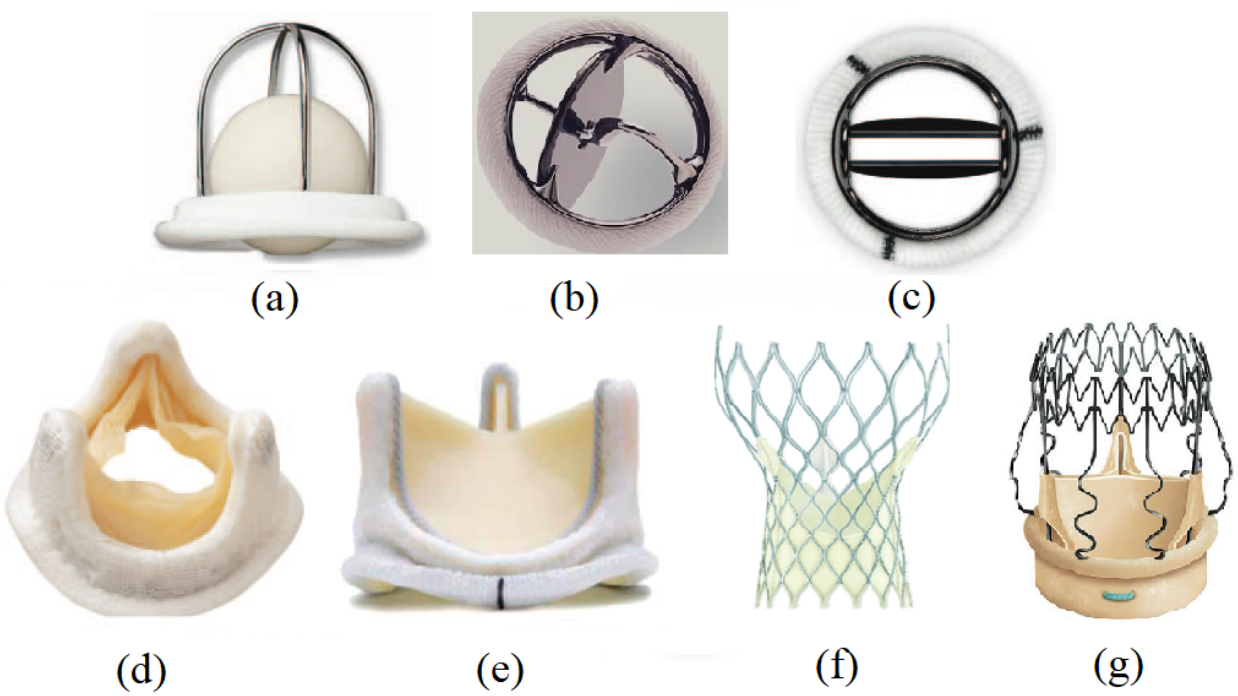

Figure 1.1: Different types of artificial valves. (a) caged ball; (b) monoleaflet mechanical; (c) bileaflet mechanical; (d) porcine bioprosthetic; (e) Bovine bioprosthetic; (f) Transcatheter bioprosthetic; (g) Sutureless bioprosthetic

without removing the old one. Compared to the other valves for which the native aortic valve needs to be removed, using this procedure the transcatheter valves are placed into the aortic valve's place without removing it. These valves are typically used for the elderly patients, however, the low invasiveness and faster recovery for these procedure makes these valves favorable for young patients too [15].

- Sutureless valves

  The same as transcatheter valves, Sutureless valves (Fig.1.1-g) have been designed to provide a minimally invasive procedure by simplifying the surgical implantation and reducing operative time. In addition, the cost of the procedure is reduced considerably compared to the conventional prosthetic valves.

Table 1.1: Hemodynamic property of different type of MHVs

MHV type	property
caged ball	generates high pressure plus high level of shear stress drop [16]
	prone to thrombus growth about the cage struts [17]
monoleaflet	causes energy loss and generates turbulence flow [18]
	in some cases struts disruption due to fatigue and fracture [18]

1.1.3 Hemodynamics of available heart valves

During the past couple of decades, a lot of effort has been made to improve the design of prosthetic heart valves in terms of durability, and hemodynamic performance (which are the major concerns for designing a new prosthetic heart valve). Specifically, several designs of MHVs are available among which BMHVs are the most popular ones [11]. The problems and hemodynamic deficiency associated with other types of MHVs (e.g., caged ball valves and Monoleaflet valves) are mentioned in the table 1.1.

BMHVs have the best hemodynamic performance among the MHVs [11], however, even these valves are associated with a high risk of platelet activation and clot formation in the valvular region [19]. Several studies have shown that the hemodynamic factor plays an important role in the thrombogenicity of prosthetic heart valves which is believed to be initiated by platelet activation [20]. The platelet activation in BMHVs can be due to the elevated shear stress, flow separation, vortex shedding from the leaflets, and recirculation zones due to the non-physiological flow pattern in the wake of the leaflets in the bulk flow [21]. A recirculation region can be generated due to the sharp edges of the MHVs which usually can be observed in the sinus area [22]. This non-physiological pattern can make the platelets undergo high shear stress and long resistance time which can result in platelet activation and aggregation [5]. In addition, the leaflets in MHVs are attached to the housing by a hinge. This hinge has a small gap size of around $100\mu m$ [7]. This gap will be subject to leakage during the diastole phase of the cardiac cycle [7]. This leakage jet generates a high velocity with high shear stress and thereby increases the risk of platelet activation

and consequently blood clot formation [3]. The role of each of these sources of platelet activation is yet to be investigated.

Other than the above sources of platelet activation, cavitation can also play an important role in the platelet activation and blood clotting [23, 24]. The fast closing of the leaflets and the rebound happens due to that can extremely drop the pressure near the leaflets for a few milliseconds [25]. This low pressure can be below the vapor pressure which results in cavitation and generation of bubbles in the blood [12]. Investigating all these parameters for a new design of heart valves requires a robust, accurate, and highly efficient numerical method. The details, as well as advantages and disadvantages of available numerical methods for simulation of the prosthetic heart valves, are explained in section 1.2.

1.2 Numerical methods for simulation of artificial heart valves

Several in-vivo and in-vitro studies have been conducted to investigate the flow patterns and hemodynamic performance of BMHVs using state-of-the-art image velocitometry (PIV) [26, 25, 27, 28]. However, the experimental measurements can only provide 2D cross-section of the flow while the flow through the BMHVs is very complicated involving 3D vortical structures. In addition, 3D velocity measurements are very challenging and typically suffer from a lack of spatio/temporal resolution. On the other hand, computational fluid dynamic provides (CFD) emerged as a powerful tool for simulation of flow in different applications [29, 30, 31, 32, 33, 34, 35, 36], especially, to quantify the hemodynamic of BMHVs with the detail and the resolution needed for evaluating the performance of BMHVs in terms of leaflet motions and thrombogenicity [37]. However, performing a simulation under the physiological condition and complex geometries with high spatio/temporal resolution where the flow is dominated by fluid-structure interaction (FSI), the pulsatile flow effects, and undergo a transition to turbulence can be very challenging even for the most advanced computational techniques available today.

The early simulations of BMHVs were performed using 2D grids [38, 39]. These simulations showed the complex flow pattern in the MHVs during the systole. However, due to the 3D nature of the flow in these valves, 2D simulations can only provide a limited amount of information. The first

3D simulations of MHVs were performed under the fixed inflow with fixed leaflet positions [40, 41, 42]. These simulations showed that the vortex shedding from the leaflets can break down the symmetric flow to small scale vortical structures. Later, several 2D studies were conducted to perform 2D fluid-structure interaction simulation through MHVs [43, 44, 45]. Borazjani et al. [46] and later Tullio et al. [47] performed the three-dimensional of BMHVs. These simulations showed the break down of the organized flow into chaotic small scale structures can happen before the peak systole. Since then several numerical simulations have been performed under different conditions (different geometries, boundary conditions etc.) [48, 49, 50, 51]. The simulation of flow through MHVs can be divided into two main categories based on the region of interest, i.e., bulk flow [52, 53] or hinge region [3, 54, 55, 56]. Due to the difference in the scale of bulk flow and hinge region, the computational method required for the flow simulation of each category is different. The available method for simulating the flow through the MHVs are presented below.

1.2.1 Numerical methods for problems with moving boundaries

The governing equations for the blood flow through mechanical heart valves are the 3D, unsteady incompressible continuity and Navier–Stokes equations where the blood has been assumed to be Newtonian. The valve leaflets are pivoting around their hinge and can open and close in response to the cardiac flow pulse. Thus, the Navier-stokes equations are solved in a domain enclosed by a moving boundary that contains moving immersed boundaries undergoing arbitrarily large deformations. Simulations of unsteady flows with moving/deforming bodies remain challenging due to the constraints and difficulties in mesh generation and boundary condition implementation. For handling moving boundaries inside a fluid domain generally two categories are available 1) moving grids 2) fixed grids which are explained in detail below.

1.2.1.1 Moving grid methods

Moving grid methods are methods in which the computational grid is fitted to and moves/deforms with the moving boundary. The movement of the grid is taken into account by using the arbitrary Lagrangian-Eulerian (ALE) formulation of the governing equations [57]. Although con-

forming grids [58, 59, 60, 61, 62] have been used for simulating flows around moving bodies, for large displacements such as for simulation of flow through mechanical heart valves in some studies [45, 63] ALE methods can result in poor grid quality that decreases the accuracy of calculations. For example, Cheng et al. [63] interpolated the mesh between two previous generated meshes to obtain the intermediate mesh and apply an elliptic solver to smooth out the mesh for each angle of leaflet during the simulation. Thus obtaining smooth computational meshes at every time step of the simulation is not very trivial using the ALE technique. Therefore, using the ALE method is not the best choice for the simulation of mechanical heart valves. For large deformations, consequently, remeshing methods (e.g., global remeshing [64, 65] or refinement methods [66, 67, 68, 69]) are required to rediscretize the whole computational domain or part of it in such a way that the grid is conformal to the structure and the quality of the fluid mesh is preserved as much as possible. However, re-meshing suffers from the loss of accuracy during time evolution due to solution interpolation from the old domain to the new one [70]. In addition, this method can increase the computational cost of simulations significantly especially for complicated geometries. Furthermore, the efficient parallelization of a solver in re-meshing techniques is not straightforward. On the other hand, non-boundary conforming methods, e.g., immersed boundary method (IBM) [46, 71, 72, 73, 74], or fictitious domain method [75, 76], among others, can handle large body deformation but they may decrease the solution's accuracy near the fluid-solid interface due to interpolation errors. In addition, non-boundary conforming methods require high grid resolution in the regions where the boundary movement occurs which can increase the number of grids points relative to ALE methods.

1.2.1.2 Fixed-grid methods

Fixed-grid methods in which the grid is fixed during the simulations can also be used for handling the moving bodies in the domain. The example of fixed grid methods are cut-cell methods [77], fictitious domain [78], and immersed boundary methods [79, 80]. In cut-cell methods, [77] the background is cut by the solid body and the cells at the interface are modified based on the intersections with the underlying Cartesian grid and the boundary conditions are imposed

along the intersecting surface. Several numerical challenges are associated with cut-cell schemes. The fictitious domain is a diffused boundary approach where fluid and solid nodes are treated the same and the boundary conditions are locally forced on the solid interface [81]. Thus the mesh is adaptation is not required contrary to the cut-cell methods. Immersed boundary methods can be categorized into diffuse methods [82] and sharp interface methods [80]. The diffuse methods provide a diffused solid/fluid interface (the same as the fictitious methods) while sharp interface methods explicitly account for the interface [81].

Among the above methods, immersed boundary methods have emerged as a powerful tool to efficiently study complicated real-life flow problems which involve arbitrarily complex bodies/flow domains [83, 84, 85]. These methods are inherently capable of handling problems involving large structural displacement such as mechanical heart valves. In these methods, the computational domain is discretized with a single, fixed, non-boundary conforming mesh system which can be curvilinear or Cartesian. Immersed boundary methods have been successfully used for simulations of cardiovascular flows [86, 47, 87, 37, 88, 89], aquatic swimming [90, 91], vortex generation/control [92, 93, 94], etc. Peskin is a pioneer of using immersed boundary method for simulation of heart valves [86]. Later several researchers used different approaches of immersed boundary method for simulation of prosthetic heart valves [3, 95, 96, 97, 98]. Nevertheless, despite many attractive features of the immersed boundary methods, they suffer from a major limitation which raises from the fact that the background grid stays the same and there is no ability for clustering the grid nodes in the boundary layer of moving bodies during a simulation. This limitation makes the application of the immersed boundary method very challenging for flows in which an immersed body undergoes an arbitrary large displacement or rotation, such as aquatic swimmers [99], wind turbines [100], or flapping wings [101]. In such simulations, the entire background grid should be discretized with a fine grid to resolve the boundary layer near the immersed bodies which increases the computational cost drastically. Although solving Navier-stokes equations in a non-inertial frame of reference can overcome this problem for a single body, the problem still remains for multiple bodies in arbitrary relative motions.

To address the above issue for moving bodies, a few strategies have been proposed which provide high grid resolution near an immersed body while the grid is coarsened away from the body. Among those are the adaptive mesh refinement (AMR) and overset grids. THE hierarchical AMR technique for Cartesian grids was pioneered by [102]. Since then this technique has been applied and developed by many researchers [103, 104, 105, 106]. Local mesh refinement methods have been used for simulation of heart valves [107, 108, 109]. However, the application of these techniques for simulation of MHVs remains limited in the literature. Although AMR method is accurate and efficient for steady problems [110, 111, 112] several drawbacks are associated with this method for unsteady flows [113, 70, 114, 106]. The most important problem is the latency between the mesh and flow solution. A few remedies have been proposed in the past few years to overcome this problem. Some work adjusts the mesh every n time step and thus the mesh is lagging behind the unsteady solution. However, there is no guarantee that features of interest remain in the refined area in this method [115]. Other strategies such as local adaptive re-meshing [116, 117] adjust the mesh more frequently. However, errors due to solution interpolation from the old mesh to the new one can generate unquantified errors [70]. In addition, developing a robust algorithm and data structure for the AMR method is usually not straightforward [106]. Finally, the parallelization of AMR solver with high efficiency is very challenging because the load (number of grid points) on each computing core is dynamically changing.

1.2.1.3 Overset grids

Overset or Chimera grids provide an elegant solution for the issue of large displacement in simulations by discretizing a complex flow domain into a set of simpler, overlapping sub-domains which can move relative to each other. The problem of overset grids was first proposed during the 1970s for the solution of the elliptical and hyperbolic partial differential equations for the inviscid shallow-water equations using two-dimensional domains and a non-moving overset grid [118, 119, 120]. Steger and Benek [121] and later Meakin and Suhs [122] adopted the idea to tackle more complicated problems of simulating compressible flows around multiple complex geometries. Since then several attempts have been conducted to develop an overset grid framework

to handle an arbitrary number of overlapping grids for both compressible and incompressible flows using staggered [123, 124, 125, 126], non-staggered grids [127, 128], and hybrid staggered/non-staggered grids [1]. This method has been used for simulation of heart valves in a few studies [129, 130, 131, 1, 132] to either provide the ability to handle complex geometries related to the cardiovascular system or provide high grid resolution near the valve leaflets. However, these simulations remained limited to large scale simulation of MHVs. The only simulation which uses overset grids for multi-scale simulation of MHVs is performed by Hedayat et al. [3] which performed an FSI simulation to capture the flow features of bulk flow and flow through the hinge region simultaneously in their simulations. The restriction of using overset grids for FSI simulation of heart valves is typically due to the computation cost associated with using this approach especially for the grid assembly part needed in this method. To reduce the computational cost required for performing overset grids simulation developing an efficient grid assembly kernel is essential. The operation involved in grid assembly function and the challenges associated with developing it especially in parallel are mentioned as follows.

In overset grid solvers, the governing equations are solved independently in each sub-domain and the connection between different sub-domains is achieved by interpolating the flow variables at the interface of overlapped domains. The connection between different overlapping domains is established via a grid assembly process. The main tasks in this process are 1) Hole-cutting; 2) donor search, and 3) variable interpolation. While performing these tasks using a single processor may be trivial, the problem can be very challenging in parallel considering that each grid is partitioned and distributed among several processors. Several grid-assembly packages have been developed in recent years [133, 134, 135]. All these codes have their advantages and disadvantages. Some of these packages are dedicated assembly codes which provide a general overset grid assembly capability and need a mechanism for integrating with an existing flow-solver [136, 137, 138, 139] while others are developed for a specific flow solver and directly added to that solver [140, 141, 142, 143, 144, 1]. Most of dedicated grid assembly packages use out-of-core algorithms to be linked to an existing flow-solver, e.g. through an Input/Output (I/O)

file [145], which suffer from a high overhead especially for moving overset grids.

In addition, some codes are not implemented in parallel [1]. Because the overset grid assembly should be performed at each time-step as the grids are moving during a simulation, parallel implementation of grid assembly is essential for parallel solvers. However, the scalability of a parallel grid assembly code can be limited due to the inherent algorithmic complexity and difficulty of efficiently distributing the computations between available processors. Several strategies are available for handling the grid-assembly task in parallel. Some codes maintain the entire meshes in all processors [146] while others use a partitioning scheme for overset grid assembly which is different from the partitioning used for the flow solver [147, 148]. However, this requires a merge-and-repartition for the entire grid data at each time step of the simulation which can drastically increase the execution time due to memory latency and the algorithm overhead especially in the unsteady flow simulations where these tasks need to be performed at each time step. To overcome the above weaknesses, an algorithm with the capability to handle an already distributed composite grid is required.

Some attempts have been conducted to address the above problems in recent years [133, 149, 150]. Zagaris et al. [133] developed an in-core parallel grid assembly to tackle the distributed assembly problem. However, the scalability of their method was not satisfying. Roget and Sitaraman [149] implemented a dynamic load balancing algorithm for PUNDIT [139]. Although they achieved very good scalability for a large number of processors, this method is originally developed for unstructured grids and is not suitable for structure grids [151]. Martin et al. [150] developed a grid decomposition method for the overset grid assembly problem which leads to a scalable computation for very large simulations of moving bodies as well as a reduction in memory requirement while the method has some limitations in terms of overlap minimization and optimal donor selection. More recently,Horne and Mahesh [152] developed a massively-parallel overset grid assembly for a PR-DNS of particle-laden turbulent channel flows to simulating large numbers of moving bodies with exceptional parallel scalability. However, this method is not readily applicable to general curvilinear problems and multi-connected geometries such as the cardiovascular

system. In addition, the above packages are not easily accessible to a third party and the task of efficiently integrating the existing grid assembly codes to a specific flow solver is problematic.

Here, we developed a new computational framework to extend our previous overset grid code [1] to perform the grid assembly tasks for moving overset grids fully in parallel. The grid assembly is integrated with our sharp-interface CURVIB solver in a general non-inertial frame of reference with a conservative formulation [46, 1] which provides us the ability to tackle high-resolution, fluid-structure interaction (FSI) simulations of complex real-life problems. To achieve this goal a number of major algorithmic developments have been presented in this paper compared to the previous work [1] which include: 1) developing a new donor search algorithm which enables us to perform the search fully in parallel compared to our previous work which could only run on a single processor; 2) developing a new walking strategy to identify the donor compared to the previous work which utilized a brute force approach; 3) developing a new parallel interpolation method which can drastically reduce the execution time compared to the previous work; 4) directly integrating the grid assembly kernel to the flow solver to maximize the overlap between computations and data communication compared to the previous work which used an out-of-core method through an I/O file; 5) adding the ability to handle moving overset grids to our CURVIB solver which uses a non-inertial frame of reference for moving girds and an inertial frame of reference for non-moving ones versus our previous work in which all grids were solved either in inertial or non-inertial frame of reference. Our framework has been validated against several experimental and numerical test cases and its versatility is demonstrated by applying it to simulate a challenging FSI simulation of fish swimming in a school.

1.2.2 Multi-scale computational analysis

An overview of the literature on numerical simulation of artificial heart valves up to now shows that major advancements have been made on the FSI simulation of heart valves including realistic geometries, material properties, and physiological boundary conditions. Most of these studies are validated against experimental measurements which shows the power of numerical simulation for simulation of heart valves. However, multi-scale simulation of heart valves remains a challenge due

to wide disparity in the length scale. As an example in the diameter of the mechanical heart valves typically varies from 21 to 25 mm where the leaflet can undergo large displacement of the same dimension. On the other hand, the hinge gap sizes in BMHVs as an example mechanical heart valve has a dimension of around $100\mu m$. In addition, the red blood cells and platelets in human blood which are the components of interest in investigating the hemodynamic performance of MHVs have a dimension in the order of micrometers. In addition, the change in platelet activation and thrombus ac occur in order of microseconds. Therefore, to accurately simulate the flow through the prosthetic heart valves a multi-scale (both temporal and spatial) approach is needed.

Therefore, performing a multiscale flow simulation through the heart valves can be very challenging. While using overset grids can help to the multi-scale simulation of the BMHVs by providing a higher grid resolution near the hinge region, considering the dimension and a huge number of the platelets available in the blood treating platelets as particles with mass is not possible due to the high computational cost and limitation in computational resources. Thus, platelets are either considered as massless particles through Lagrangian or continuum field through the Eulerian approach. Based on this fact, the platelet activation which can happen due to the strain and stresses on the surface of the platelets should be modeled using the empirical methods which are explained in detail in section 1.2.3.

1.2.3 Platelet activation

Thrombosis is a major concern in the recipient of mechanical heart valves [153]. Several factors can trigger thrombosis formation in patients including red blood cell damage (hemolysis) or platelet activation. red blood cells have flexible membranes which can resistance under a high level of shear stress [154]. On the other hand, platelets are usually found near the wall where the shear stress is higher. It is shown that a shear stress of $1500-2500$ $dyne/sec$ with an exposure time of 102 sec is required for hemolysis ([155, 156, 157]) while the platelets can be activated with a shear stress of as low as $100-300$ $dyne/sec$ ([158]). Since the threshold of $1500-2500$ $dyne/sec$ is considerably higher than the shear stress reported in the mechanical heart valves [3] it is mainly believed that platelet activation is the underlying mechanism for thrombus formation not hemolysis

through the red blood cell damage.

Several mechanical and chemical agonists can play a role in platelet activation. Among those flow-induced shear stress is playing a major role in the activation of the platelets in MHVs. Several studies investigated the platelet activation in terms of shear stress and exposure time ([158, 159]). Hellums et al. [159] suggested the shear-induced platelet activation happens due to a combination of shear stress and the exposure time. Since then several mathematical models for platelet activation are proposed. Blackshear et al [160] made the first attempt to propose a formula to relate blood damage/hemolysis with shear stress and exposure time. They proposed the power-law model based on their experiments for constant shear stress

$$P(t) = C\tau^{\alpha}t^{\beta} \tag{1.1}$$

where $P(t)$ is the level of damage, τ is the level of shear stress, t is the exposure time, C, α, and β are the model coefficients. Wurzinger et al. [161] performed an experiment in which they measured the hemolysis of red blood cells as well as platelet lysis for constant exposure of blood to constant levels of shear stress. Giersiepen et al. [162] later suggested a power-law model with $\alpha = 3.075$ and $\beta = 0.77$ based on these experiments which showed good agreement with the experimental results. Since then several mathematical models have been suggested for hemolysis and platelet activation. Each of these models is good for a specific application and a special range of shear level and exposure time. Hellums [163] suggested linear level of activation (power-law model with $\alpha = 1$ and $\beta = 1$) for platelet activation for platelets undergoing constant shear in which the activation was assumed to be activated if the value of $P(t) = \tau\ t$ is higher than a threshold otherwise not activated. Later, Grigioni et al. [164] developed a modified version of the power-law model to account for piecewise constant shear stress during the exposure time. In order to account for the dynamic nature of the flow in which the platelets can undergo dynamic shear stress Alemu and Bluestein [165] suggested a platelet damage model based on the theory of damage proposed by yeleswarapu et al. [166]. Where the model accounts for damage history, shear stress loading history, and loading rate. However, the models based on the power-law model are not suitable

for highly dynamic flow condition which is typically is observed in the MHVs. To overcome this limitation Soares et al. [4] proposed a novel model for highly dynamic flow conditions arising from pathological flow patterns. This formulation quantifies the rate of activation of platelets as a function of their current activation state which accounts for dynamic shear stress, platelet sensitization, shear rate.

These activation models can be treated based on Lagrangian and Eulerian approaches. using the Eulerian approach the activation is quantified over the whole computational domain. However, in the Lagrangian one, the activation is integrated over the pathlines of many particles. Considering the normal range of platelets in artery vessels, which is $150,000$ to $400,000$ per cubic millimeter ([167]), millions of particles need to be calculated in Lagrangian approach to get statistically significant results. Handling millions of particles is computationally quite expensive. Thus using a Eulerian approach is more realistic for quantifying the platelet activation in measurements which will be discussed in detail in section 2.4.

2. NUMERICAL METHOD *

This chapter is organized as follows: In section 2.1 we present the governing equations used to solve the flow in a non-inertial frame of reference is presented in general curvilinear coordinates. In section 2.2 we describe the grid assembly problem and the method that s needed the for grid assembly method. Section 2.2.1 shows the domain decomposition strategy that is used in for the grid Assembly kernel developed in this work. Section 2.2.2 provides the technique that is used for the hole-cutting which is needed for handling the overlapping grids. Later, in section 2.2.3 the method for identifying the potential nodes, for which interpolation is needed, is explained. To reduce the overhead associated with the parallel algorithm of grid assembly in a distributed environment a data packing strategy is used which is explained in section 2.2.4. Section 2.2.5 describes the techniques which are used for donor cell identification. The efficient algorithm that is developed in this work for the velocity interpolation is presented in section 2.2.6. Later, the integration of this grid assembly kernel with the CURVIB flow solver for performing FSI simulations as well as the methods used for the treatment of special cases in which several immersed bodies or overset grids can intersect (which can happen when dealing with overset grids in arbitrary movements) is explained in section 2.3. Finally, the framework which is developed for quantifying the platelet activation for flow through heart valves using a Eulerian frame of reference is presented in section 2.4.

2.1 Overview of the overset-CURVIB

We developed a new parallel dynamic overset-CURVIB framework by extending the previous overset-CURVIB method [1] for fixed overset grids and a sequential grid assembly to moving overset grids with an efficient parallel grid assembly[168]. Our new framework utilizes a non-inertial frame of reference to solve the moving/rotating overset grids to avoid recalculating the curvilinear metrics of transformation while the background/stationary grids are solved in the inertial frame. In

*Part of this chapter is reprinted with permission from "Comparison of platelet activation through hinge vs bulk flow in bileaflet mechanical heart valves" by M. Hedayat and I. Borazjani, 2019, Journal of biomechanics, 83, 280-290, Copyright 2019 by Elsevier Ltd.

addition, a sharp-interface curvilinear immersed boundary method, as well as an strong-coupling FSI method, are used to handle solid immersed bodies in the domain in the context of our CURVIB flow solver. The framework enables us to perform high-resolution fluid-structure interaction simulations of real-life complex flows, which could not be handled with our previous strategy. Using dynamic overset grids allows us to increase the grid resolution locally around moving immersed bodies without drastically increasing the total number of grid points in simulations.

Major developments of this work compared to the previous method [1] are: 1) developing a new grid assembly algorithm for partitioned grids (parallel distributed environment); 2) using a new walking strategy for donor search; 3) developing a new algorithm for variable interpolation by forming an interpolation matrix; 4) directly integrating the grid assembly kernel into the flow solver instead of using an out-of-core strategy; 5) extending our previous framework to handle moving overset grids in a non-inertial frame of reference while stationary ones in an inertial frame.

The major challenge in developing a parallel dynamic overset framework is the need for an efficient parallel communication strategy to transfer information between subdomains for a domain decomposition in which all grids are distributed to all processors (optimal domain decomposition for our flow solver). Several steps have been made to increase the scalability and decrease the computational/communication cost of our framework including 1) using OBBs to decrease the search space; 2) using the control cells to accelerate the donor search; 3) data packing to combine multiple messages into a single message which results in decreasing the total number of communications and consequently decreases the overhead associated with it; 4) using non-blocking data transfer to reduce the overhead and maximize the communication/computation overlap, and 5) developing a vectorized implementation for data interpolation in parallel which can drastically decrease the interpolation time.

2.1.1 Governing equations in a general non-inertial frame of reference in General Curvilinear coordinate

The three-dimensional unsteady incompressible continuity and Navier-Stokes equations are the governing equation in the fluid domain and are solved using the curvilinear/immersed bound-

ary (CURVIB) solver. The CURVIB and fixed overset methods are extensively described and validated in our previous works [1, 169, 46, 95, 170]. Thus, just a brief overview is presented here. A fully-curvilinear formulation based on the hybrid staggered/non-staggered approach [169] is used which eliminates the need for evaluation of the Christoffel symbols. A sharp-interface immersed boundary method is used to handle the 3D, arbitrary complex moving bodies inside the curvilinear background domain which utilizes an efficient ray-tracing algorithm for immersed/fluid node classification [46]. The boundary conditions are reconstructed on the fluid nodes in the immediate vicinity of the immersed bodies along the normal to the body surface [80]. The solver has been shown to be second-order accurate [1, 171].

In this study, a conservative form of Navier-stokes equations in a non-inertial frame of reference for a curvilinear coordinate is employed which was previously developed by [1] based on the work by [172] and [173]. Fig. 2.1 illustrates the position and orientation of inertial and non-inertial coordinates relative to each other. Using a general arbitrarily moving non-inertial frame of reference allows us to enhance the versatility and efficiency of our numerical framework for problems involving rigid body motions of an immersed body. Furthermore, using a non-inertial frame of reference for dynamic overset grids enables us to avoid recomputing the metrics of curvilinear transformation at each iteration of the momentum solver where the grid position and orientation change with respect to the inertial frame of reference which can reduce the computational cost drastically. In addition, when a non-deforming immersed body is present in the fluid domain, using a non-inertial frame can prevent the use of a ray-tracing algorithm for the background grid node classification at each time step which also reduces the computational costs especially if a large number of immersed bodies are present in the fluid domain.

The momentum equations in a non-inertial frame of reference is formulated as follows in tensor notation [1]:

$$J\frac{\partial}{\partial \xi^r}(U^r) = 0 \tag{2.1}$$

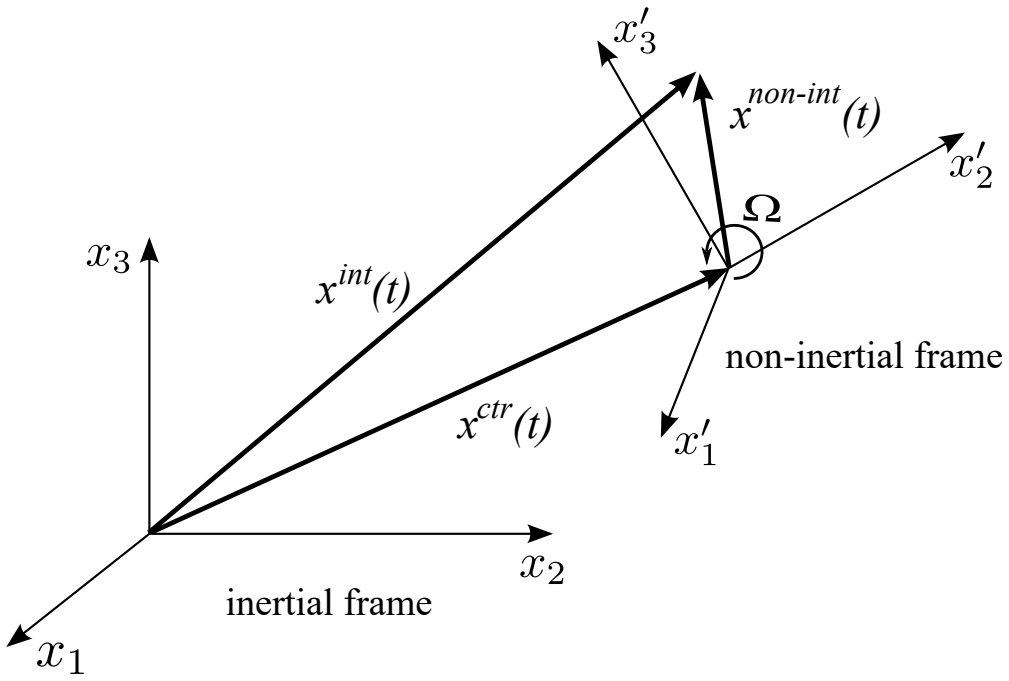

Figure 2.1: schematic position and orientation of non-inertial frame relative inertial frame where x^{int}, $x^{non-int}$ and x^{ctr} are the coordinate vectors in inertial frame, non-inertial frame and origin of non-inertial frame in inertial coordinate.

$$\frac{\partial U^r}{\partial t} = \frac{\xi_q^r}{J}\Big(\frac{\partial u_q}{\partial t}\Big) = \frac{\xi_q^r}{J}\Big(- C_1(u_q) - C_2(w_q) - G_q(p) + \frac{1}{Re}D(u_q)\Big) \tag{2.2}$$

where $\xi^r = \xi^r(x_1, x_2, x_3)$, $r = 1, 2, 3$ are the curvilinear transformation of the Cartesian coordinates (x_1, x_2, x_3) based on the hybrid staggered/non-staggered approach [169]. $C_1,\ C_2,\ G$, and D are the convective, gradient, and viscous operators in curvilinear coordinates

$$C_1(*) = J\frac{\partial}{\partial \xi^r}\Big[\Big(U^r - V^r\Big) * \Big] \tag{2.3}$$

$$C_2(*) = J\frac{\partial}{\partial \xi^r}\Big[U^r * \Big] \tag{2.4}$$

$$G_q(*) = J\frac{\partial}{\partial \xi^r}\Big(\frac{\xi_q^r}{J} * \Big) \tag{2.5}$$

$$D(*) = J\frac{\partial}{\partial \xi^r}\Big(\frac{g^{rm}}{J}\frac{\partial}{\partial \xi^m} * \Big) \tag{2.6}$$

J is the determinant of the Jacobian of the transformation, $J = |\partial(\xi_1, \xi_2, \xi_3)/\partial(x_1, x_2, x_3)|$, $\xi_q^r = \frac{\partial \xi^r}{\partial x^q}$, g^{rm} is the contravariant metric tensor, $g^{rm} = \xi_q^r \xi_q^m$, U^q and V^q are the contravariant velocity components, which are correlated with the Cartesian velocity components as follows:

$$U^r = u_q \frac{\xi_q^r}{J}, \; and \, V^r = v_q \frac{\xi_q^r}{J} \tag{2.7}$$

and

$$u_q = Q_{qr} u_r^{int} \tag{2.8}$$

$$v_q = w_q + u_q^{ctr} \tag{2.9}$$

$$w_q = \epsilon_{qlm} \Omega_l X_m^{int} \tag{2.10}$$

$u_q^{ctr} = u_q^{ctr}(t)$ and $\Omega_q = \Omega_q(t)$ are the translational and rotational velocity of the non-inertial frame, respectively, relative to the inertial frame. $Q_{qr}, (q, r = 1, 2, 3)$ is the orthogonal rotation tensor that rotates the non-inertial frame to the inertial frame orientation. X_q^{int} is a component of the position vectors in the inertial reference frame (for more detail readers can refer to [1]).

The above governing equations are advanced in time using a fractional step method on curvilinear grids [169, 1]. The momentum equations (Eqs. 2.1 and 2.2) are discretized in time in a fully implicit manner using a second-order backward difference scheme (Italic variables are scalar while the Boldface variables are vectors):

$$\frac{3\boldsymbol{U}^{(*)} - 4\boldsymbol{U}^{(n)} + \boldsymbol{U}^{(n-1)}}{2\Delta t} = RHS(\boldsymbol{U}^{(*)}, \boldsymbol{u}^{(*)}, p^{(n)}) \tag{2.11}$$

where $\boldsymbol{U}$, $\boldsymbol{u}$, and p are the contravariant velocity, Cartesian velocity, and pressure, respectively. n denotes the time level and RHS is the right-hand side of Eq. 2.2. Eq. 2.11 is solved implicitly using a Newton-Krylov method to obtain the intermediate fluxes $U^{(*)}$. These steps are followed by solving Poisson equation for the pressure correction which is solved using flexible GMRES with multigrid as a preconditioner to obtain divergence-free solution [169]. The solver is fully

parallelized using MPI and PETSc libraries [174].

2.2 Grid assembly for moving overset grids

The problem of overset grids refers to the use of multiple disconnected grids that are arbitrarily overlapped to discretize a complex flow domain. The whole domain is partitioned and distributed to every available processor in a way that each processor has a portion of the mesh form all blocks. Figure 2.3 shows the schematic of an arbitrary overset grid with three blocks (sub-grids) $bi = 1$ to $bi = 3$ and the distribution of each grid on different processors in our framework at a given time instant. To solve the governing equations on each overset grid, boundary conditions on the nodes at the interface of each block (e.g., Γ_0,..., Γ_3) need to be interpolated from another grid. If a block is enclosed by another one (e.g., in Fig. 2.3 $bi = 1$ is completely inside $bi = 2$), some nodes from the outer block (here, $bi = 2$) in the overlapping region are blanked out to transfer the information from the inner block to the outer block (Γ_4) by interpolating the solution from the inner domain to several grid points inside the interface of the blanked region. The interpolation on a layer of nodes inside the blanked region, called the buffer layer, is needed to maintain a similar discretization stencil on the fluid node in the immediate vicinity of the blanked region as can be observed from Fig. 2.4. The nodes at the interface and/or the blanked region on which the interpolation occurs are known as the query points.

To construct the boundary conditions on the query points, the flow variables are interpolated from the solution of source points known as donors (from another grid), which may lie in any partition (each grid can be decomposed in different partitions; in this work, a one-to-one correspondence is present between processors and partitions, e.g. see Fig. 2.3) of that grid. For example, the interface for block $bi = 0$, i.e., Γ_0 needs to be interpolated from $bi = 1$ and $bi = 2$ grids while the interfaces of $bi = 1$, i.e. Γ_1, needs to be interpolated from $bi = 2$ and $bi = 0$ grids. Finally, the interface for block $bi = 2$, i.e. Γ_2 needs to be interpolated from block $bi = 0$. While performing these operations using a single processor seems trivial, the challenge arises when these tasks are performed in a distributed parallel environments in which data exchange between different domains and different processors/partitions is necessary at each time step.

To achieve reasonable parallel performance, a new parallel algorithm is developed and implemented which is outlined in Fig. 2.2 and will be explained in detail in this section. As can be seen in Fig. 2.2, the main steps of our grid assembly method are: 1) domain decomposition which is partitioning and distributing the computational domains to different processors (section 2.2.1); 2) hole-cutting (yellow box) which is identifying the grid points that are inside of an immersed body or another grid that need to be blanked out (section 2.2.2); 3) query point identification (orange box) which is performed to identify the points on which the solution needs to be interpolated from another grids/partition (section 2.2.3) as well as identifying the communication map between processors/partitions and eventually transferring data between different processors (section 2.2.4); 4) donor search and donor selection (green box and section 2.2.5); and 5) forming the interpolation matrix (blue box) which is a parallel matrix assembled using the interpolation coefficients obtained during the donor search to interpolate the variables (velocities) form the donor points to the query points (section 2.2.6). The detail of each part is provided in sections below.

2.2.1 Domain decomposition strategy

Several factors play a role in the parallel performance of an overset grid solver in terms of both memory and run-time including 1) the scalability of flow solver, 2) the scalability of the grid assembly method, and 3) the communication between flow and grid assembly solvers. These tasks need to be performed at every time step for a simulation involving moving overset grids in a parallel environment. In this work, message passing interface (MPI) is used for interprocessor communication required for the overset grid assembly. To reach acceptable scalability in the flow solver, the workload and, consequently, grid points should be evenly partitioned and distributed among all available processors such that every processor will be involved in solving the flow during the time that the flow solver is running using either implicit and explicit overset coupling. To achieve this goal, the mesh in every block is distributed to all available processors (e.g. mesh= $[block_1^{rank=\{0...m\}}$ ... $block_n^{rank=\{0...m\}}]$ where $m+1$ = number of processors, and n= number of blocks) as illustrated in Fig. 2.3.

To understand the effect of this decomposition on the grid-assembly method, it worth knowing

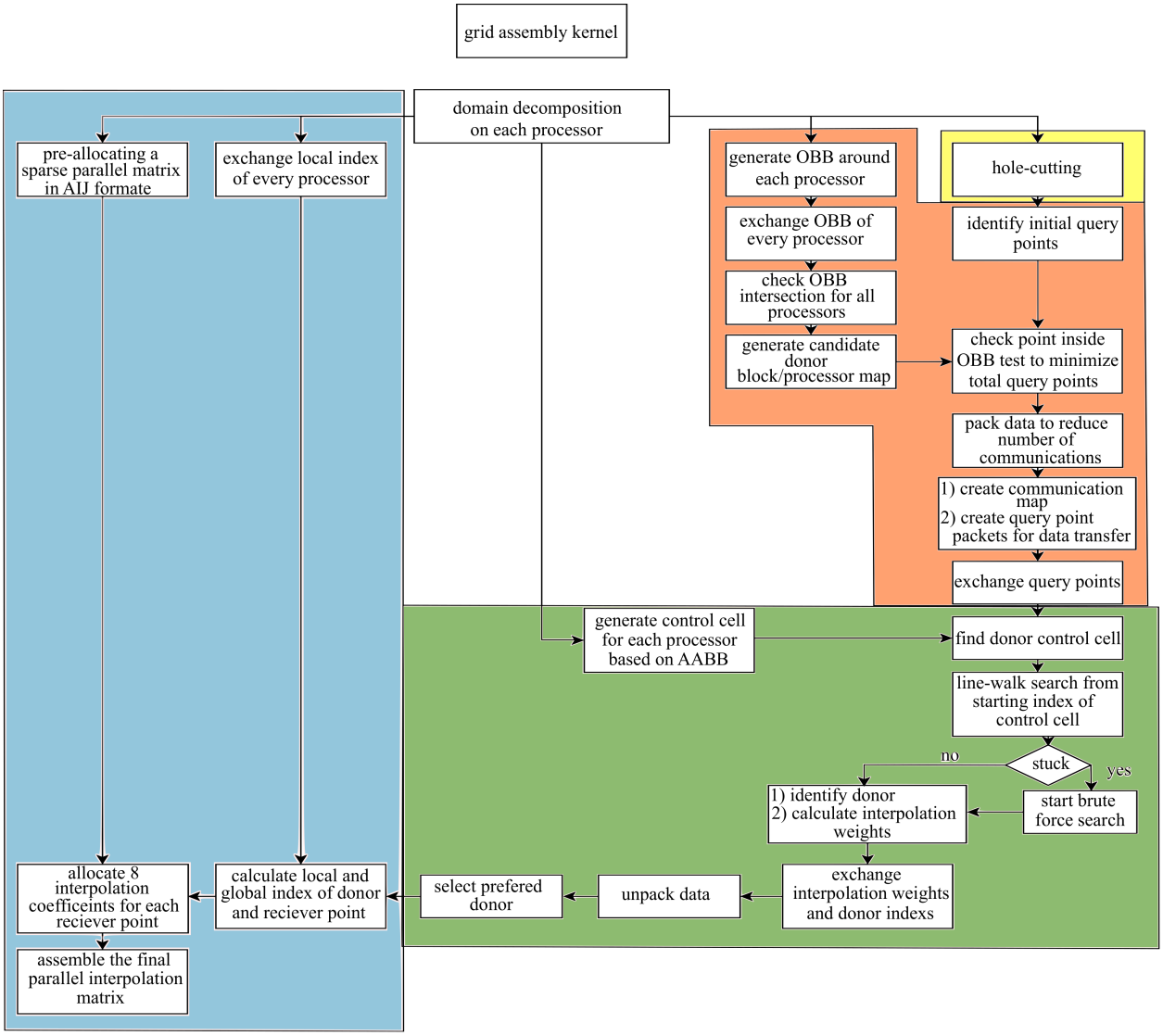

Figure 2.2: The flow-chart for parallel grid assembly algorithm presented in the paper and forming interpolation matrix

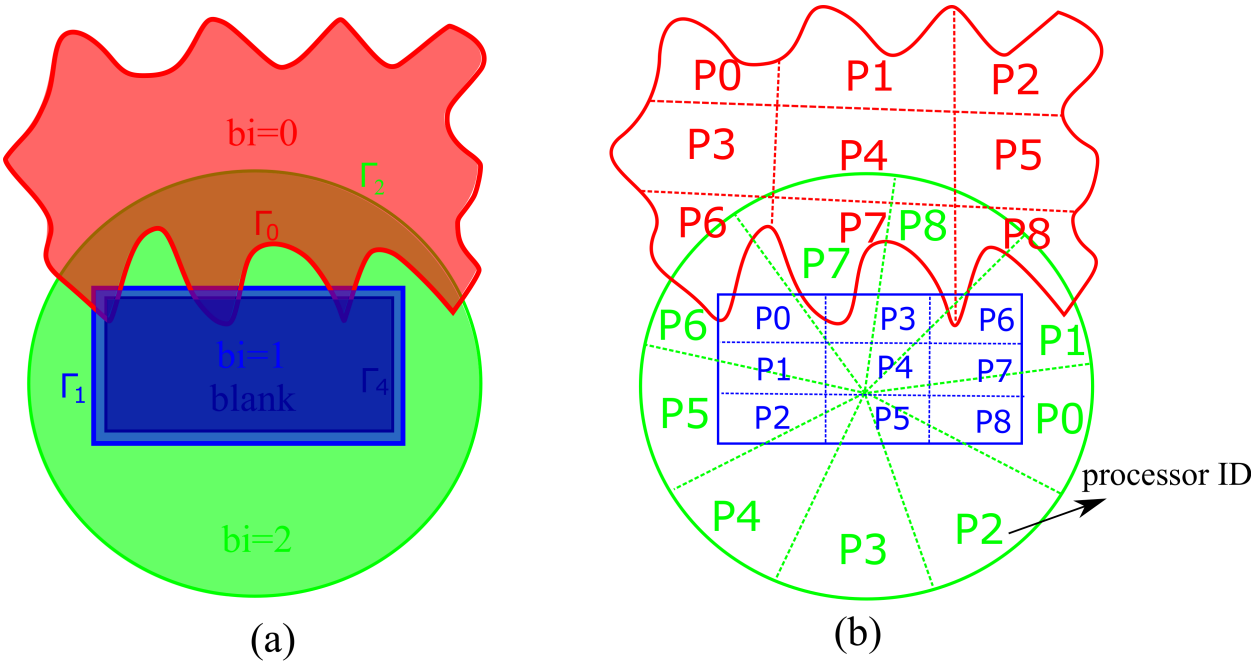

Figure 2.3: Schematic overset Domain decomposition and domain distribution in different processors for using 9 processors (p). Every block is distributed over all available processors.

that the most time-consuming parts of the grid assembly are hole-cutting and the overhead associated with grid assembly (due to communication/data transfer). This decomposition can increase the performance of the hole-cutting process which works based on the parallel ray-tracing algorithm presented in [46] as every processor can separately do the hole-cutting within its partition of each domain. However, it is easy to see that this type of decomposition can drastically increase the number of communications needed between different processors from different blocks in the process of domain assembly (in the worst-case scenario the number communications can reach to $C(n,2) \times P(m,2)$, where C and P are the combination and permutations in Algebra). Two remedies are considered in our framework to treat this problem which can result in decreasing the total number of communication, and, consequently, reducing the total overhead associated with parallelism as well as increasing the overlap between communication and donor search computations. These steps are 1) data packing, and 2) non-blocking data transfer which is explained later in the section 2.2.4.

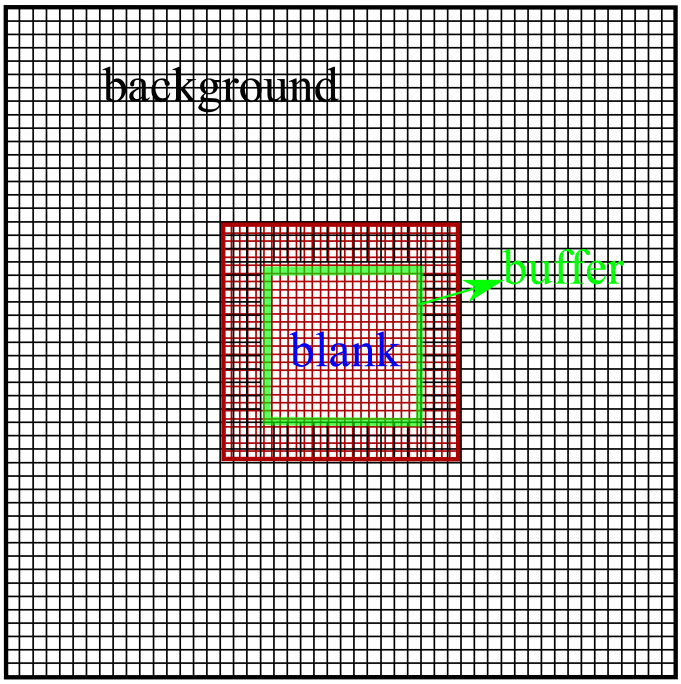

Figure 2.4: Overset grid layout for the Taylor-Green vortex. The inner domain and blanking region boundaries are shown by thick red and green lines, respectively.

2.2.2 Hole-cutting

The first step of the overset grid assembly framework is to identify the blanked (hole) points in the fluid domain. Hole points (blanked regions) are the points that will be eliminated from the domain, i.e., the flow will not be solved on these points but interpolated from the inner domain, to transfer information from the inner (typically higher-resolution) domain to the outer one (Fig. 2.4).

Currently, two types of hole-cutting algorithm are available: 1) explicit hole-cutting method [175, 176, 1] in which the user specifies the hole points through the inputs to the algorithm, e.g., user-defined surfaces which are needed for utilizing the ray-tracing algorithm, or 2) implicit hole-cutting methods [177, 178, 179, 180] in which no user-defined input other than the flow solver's boundary conditions are needed. The implicit hole cutting methods work based on an iterative approach for comparing volume grid information and flow boundary conditions to find the best resolution

grid. Although implicit hole-cutting methods remove the user-defined inputs to the code, it has approximately an order of magnitude higher computations compared to the explicit one. Therefore, explicit hole-cutting can be more suitable for dynamic overset grids where hole-cutting should be performed at every time step of the flow solver as well as for all strong-coupling iterations within fluid-structure interaction problems [46]. Hence, in this work, an efficient ray-tracing algorithm similar to the one used for identifying grid nodes located within an immersed boundary in the CURVIB method [1, 46] is used to perform the hole-cutting in the overlapping regions based on the user-defined surface provided to the code as an input.

2.2.3 Identification of query points

The next step after hole-cutting is to identify the query points on which the variables are needed to be interpolated from another domain. The functions involved in identifying the query points are briefly explained below:

1. Generate the list of potential query-points: a list of potential query points is formed on every processor, which include the boundary of blank region (buffer layer in Fig. 2.4) as well as the boundaries of each moving overset grid (points on $i = 0, I_{max}$, $j = 0, J_{max}$, and $k = 0, K_{max}$ where i, j, k are the grid numbering in curvilinear ξ^1, ξ^2, and ξ^3 directions, respectively).

2. Generate an oriented bounding-box around each processor: To facilitate faster donor search and decreasing the communication time among different processors when dealing with a distributed parallel environment, minimizing the number of query points is essential. Therefore, an oriented bounding box (OBB) which approximately provides the optimal minimum bounding box is generated around the portion of the distributed grid in each processor as follows:

$$\text{OBB} = \left\{ ctr + \sum_{n=1}^{3} A_n x_n \;\middle|\; |x_n| < |a_n|, n = \text{[1,2,3] for } \mathbb{R}^3 \text{ space} \right\} \tag{2.12}$$

and where ctr is the center of the grid points, A_i are right-handed orthonormal axes which are

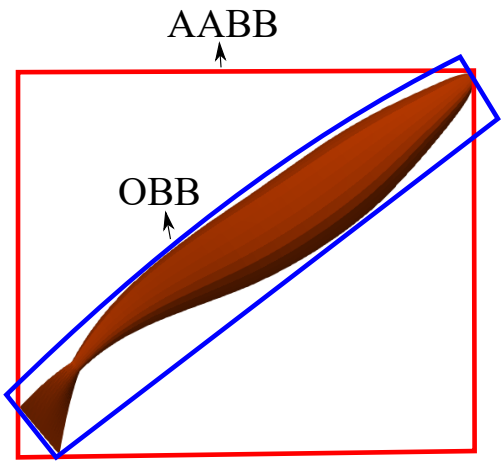

Figure 2.5: Comparison between an OBB around a swimmer and an AABB which clearly shows OBB provides a much tighter bounding-box around the an object.

calculated as eigenvectors of the covariance matrix of the ghost points (x[min, max], y[min, max], z[min, max]) in each processor, and a_n is the dimension of OBB in A_i direction. Figure 2.5 compares the axis-aligned bounding box (AABB), which will be discussed in section 2.2.5, and OBB around a sample swimmer. As can be seen in Fig. 2.5, an OBB can provide a tighter bounding box compared to AABB which minimizes the search space for identifying the query points.

3. Broadcast the information of OBB of each processor: Since each domain is distributed to all available processors, every block has its own OBB on each processor (total number of OBBs = number of blocks $\times$ number of processors). The information of the bounding-boxes is then shared between all the processors. Thus, each processor has access to the information of the bounding-box of every other processor in different blocks.

4. Check OBB intersections for all processors: After having all the bounding-box information, a test will be performed to identify the possible intersection of each processor with any other processor. A geometric separation test, explained in [181], is performed to identify

the potential intersection of bounding-boxes. Due to our domain decomposition strategy, a total number of $C(n, 2) \times P(m, 2)$, where m and n are number of processors and blocks, respectively, tests should be performed to find the intersection of different processors.

5. Generate the final list of query points from one processor to the other: After the OBB intersection tests for all the processors, if two processors have intersection with each other the query points should be sent from one processor to the other and vice versa. However, not all the potential query points formed in step 1 need to be sent to the other processor since none of the potential query points identified in step 1 may lie inside the other processor's OBB (even if OBB of two processors can intersects). Thus, to further minimize the number of query points, a point inside OBB test [181] is performed (to check if the potential query point from one processor lies inside the OBB of another processor) to form the final query points list in one processor that needs to be transferred to and be interpolated from another processor. This step helps to reduce the interprocessor communications in the grid assembly method.

6. Data exchange: Following the above steps, the final communication map between all the processors is generated (if the number of query points in the final list from the previous step is not zero then a communication should be performed otherwise no communication is needed). To transfer data, transfer packets which consist of a list of coordinates of all potential receiver points that need to be interpolated are generated. Then, these packets are exchanged between all the processors based on the final communication map.

After a successful data transfer, every processor will have a list of points for which it needs to perform a donor search. Algorithm 1 summarizes the query point identification and transfer in our framework.

2.2.4 Data packing strategy

The schematic of the data packing strategy implemented in this work is outlined in Algorithm 2. The data is packed in a way that if the OBB of each two random processors intersects (section

Algorithm 1 Algorithm for identifying the query points

```
NP=Number of processors, NB=number of blocks, rank= processor's ID, NQ= number of query
points
for bi = 0 to bi = NB do
    for P = 0 to P = NP do
        for sb = 0 to sb = NB do
            if (sb!=bi & rank!=P & (OBB(rank) intersects with OBB(P))) then
                potential query points: identify the boundary points in rank
                run point (from rank) inside OBB (of processor P) test
                if (point (from rank) inside OBB (of processor P)) then
                    add point to query points
                end if
                NQ= calculate number of query points
                generate transfer packet (send-packet_rank[P][QP])
                copy query points to send-packet_rank[P][QP]
                transfer send-packet_rank[P][QP]
            end if
        end for
    end for
end for
```

2.2.3), the data (here, Cartesian coordinates of the receptors) is appended to the transfer buffer regardless of their block number. For the case presented in Fig. 2.3, for example, to interpolate on the boundary interface of processor $P = 0$ from block $bi = 1$ the data should be sent to processor $P = 6$ (to be interpolated from $bi = 0$ and $bi = 2$). Without packing the data, this process should be performed separately, i.e., the information will be sent from Processor $P = 0$ to Processor $P = 6$ to do the donor search (section 2.2.5) for block $bi = 0$ and then sent again to do the same process for block $bi = 2$. However, the communication from processor $P = 0$ to $P = 6$ will be performed one time by packing the data for both blocks (bi=0, 2). Such data packing helps to reduce the maximum number of the communications to $n \times P(m, 2)$ instead of $C(n, 2) \times P(m, 2)$ for the worst-case scenario which can reduce the overhead related to parallelism (e.g. communications in MPI transfer). In addition, by using a non-blocking communication in data transfer between processors, it allows the algorithm to overlap some of the computations regarding the donor search with communication. In addition, to increase the performance of our framework, the grid assembly

is directly linked to the flow solver rather than using any I/O file to exchange the information (will be explained in section 2.2.6) which are needed for velocity interpolation on the query points from grid assembly to the flow solver.

Algorithm 2 Algorithm for packing data for intercommunication data transfer

```
NP=Number of processors, QP=Number of query points, NB=number of blocks
exchange processors' oriented bounding box
create communication map
for bi = 0 to bi = NB do
    for P = 0 to P = NP do
        for sb = 0 to sb = NB do
            if (sb!=bi & rank!=P & (OBB(rank) intersects with OBB(P))) then
                append data to send-packet_rank[P][QP]
            end if
        end for
    end for
    send/receive send-packet_rank[P][QP]
end for
```

2.2.5 Donor search

After receiving the list of query points from all other processors, each processor starts to search for a potential donor. To facilitate the search, localizing the donor is the first step. Hence, an axis-aligned bonding box (AABB) is generated around the grid partition in each processor to perform a control cell strategy for localization [46, 1] in which an auxiliary grid aligned with Cartesian coordinate is generated around each processor and then divided into several Cartesian boxes, i.e., control cells. The choice of AABB instead of OBB (Fig. 2.5) is made due to easy implementation and avoiding extra computation required for using OBB. After the localization of the donor by finding the proper control cell, the search for the donor cell will start. The donor cell is identified using the point-in-the-box test [1] where the points are the cell corners of each recipient grid while the boxes are the grid cells from the cell centers of the donor grid (Fig. 2.6). A point is inside the

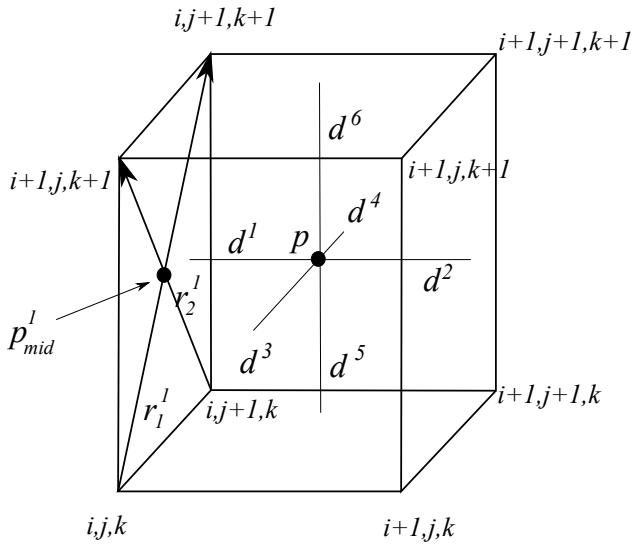

Figure 2.6: Schematic of search and trilinear interpolation for a point p inside a donor cell. d^k for $k = 1, 6$ shows the distance to the k^{th} surface of the donor cell. The point-in-the-box test can be performed based on p^1_{mid}; r^1_1, and r^1_2 which depict the midpoint and vectors for constructing the inward normal on the $k = 1$ surface of the donor cell. (figure from [1])

box if the following inequality is satisfied:

$$d^\kappa = (p - p^\kappa_{mid}).\hat{n} > 0 \tag{2.13}$$

where p^κ_{mid} is the surface center of the κth each face of the box and $\hat{n}$ represents the inward unit normal vector to the face which can be computed as $\hat{n} = \frac{r^\kappa_1 \times r^\kappa_2}{r^\kappa_1 . r^\kappa_2}$ in which r^κ_1 and r^κ_2 are vectors formed by opposite surface corners of this face as can be seen in Fig. 2.6.

In order to increase the speed of the donor search by avoiding a brute force search in each control cell to find a proper donor, a walking search strategy is used. Walking search performs the point-in-the-box test to check if the point is inside the cell and it also utilizes the sign of d^κ in the above formula to choose the walking direction, e.g. if $d^\kappa < 0$ it will check the cell in the direction of opposite to the inward normal of n^κ and vice versa as outlined below in algorithm 3.

Although the walking search works fine if the receptor point lies inside the boundaries of the donor grid (Fig. 2.7-a), it will be stuck if the point is outside the boundaries of the donor grid (Fig. 2.7-b, point 1) or if the boundaries of the donor grid have a very high curvature inside

Algorithm 3 Algorithm for donor search

find=0
Stuck=0
Locate the control cell (i_x, i_y, i_z) where point p is located:
$i = I(i_x, i_y, i_z)$, $j = J(i_x, i_y, i_z)$, $k = K(i_x, i_y, i_z)$
while (find< 1) **do**
  for ($\kappa = 0$ to $\kappa = 6$) **do**
    if ($d^1 < 0$ & $d^2 > 0$) **then**
      $i = i - 1$
    else if ($d^1 > 0$ & $d^2 < 0$) **then**
      $i = i + 1$
    end if
    do the same for other directions
  end for
  if $i = i^{old}$ &$j = j^{old}$ &$k = k^{old}$ **then**
    Stuck++
  end if
  if (Stuck> 0) **then**
    goto nxtp
  end if
end while
nxtp: search the control cell using brute force search

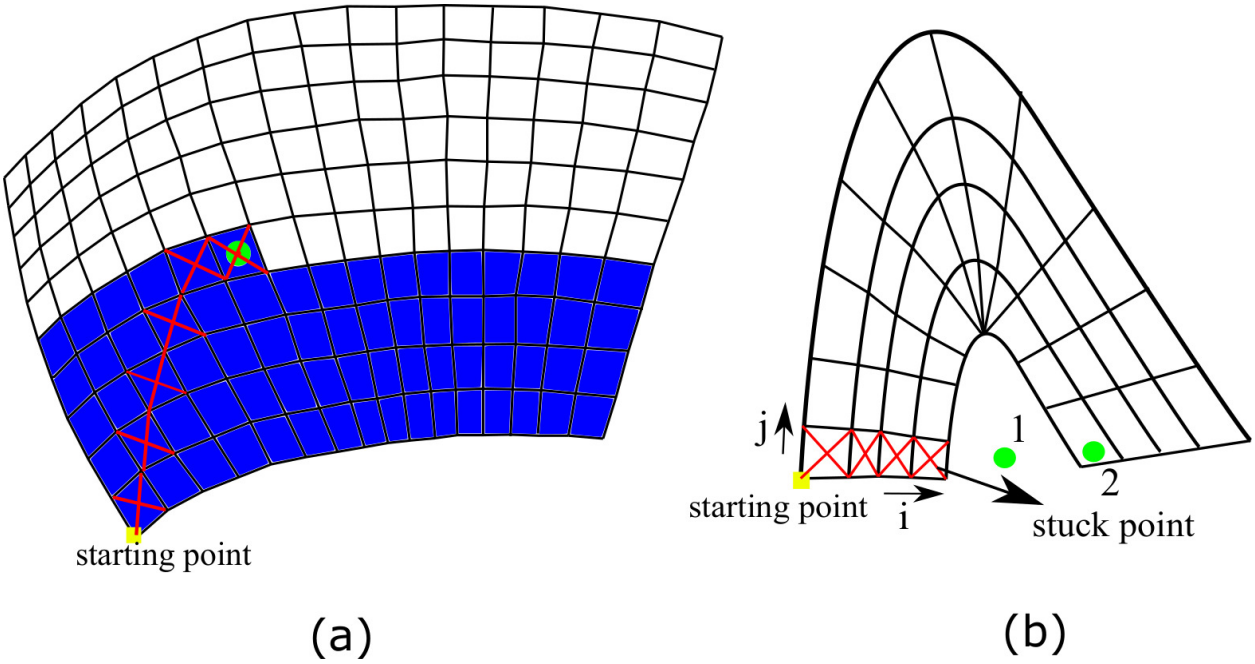

Figure 2.7: Schematic of search strategies used in this work. a) compares the brute force search (filled blue cells) with walking search (red cross) b) shows the scenario where the walking search will stuck and thus a brute force search need to be performed.

a control cell (Fig. 2.7-b, point 2). The last scenario (Fig. 2.7-b, point 2) can be prevented by changing the size of the control cell. To overcome this problem in practice, if the location provided by the walking strategy is the same as the previous location, i.e, it is stuck in a cell, the algorithm will break and a brute force search will be performed instead. Using this walking strategy, the cost of donor search reduces from $\mathcal{O}(3)$ in brute force search to $\mathcal{O}(1)$ in the walking strategy. After finding all the donor cells in the donor processor, the communication map between processors generated in section 2.2.3 is reversed and the data buffers (interpolation coefficients and index (i,j,k) of the donor) are exchanged back between donor and receiver processors through inter-processor communication.

2.2.6 Interpolation

Followed by the donor identification, the interpolation coefficients are computed for a trilinear interpolation of flow fields from one domain to the other as follows:

$$\begin{aligned} q_p = {} & a_1 a_2 a_3 q_{i,j,k} + (a_1 - 1) a_2 a_3 q_{i+1,j,k} + a_1 (a_2 - 1) a_3 q_{i,j+1,k} + \\ & (a_1 - 1)(a_2 - 1) a_3 q_{i+1,j+1,k} + a_1 a_2 (a_3 - 1) q_{i,j,k+1} + (a_1 - 1) a_2 (a_3 - 1) q_{i+1,j,k+1} \\ & + a_1 (a_2 - 1)(a_3 - 1) q_{i,j+1,k+1} + (a_1 - 1)(a_2 - 1)(a_3 - 1) q_{i+1,j+1,k+1} \end{aligned} \tag{2.14}$$

Where q_p is the interpolated flow variable at a query point and a_i are the trilinear interpolation coefficients that are obtained from the distances to the sides (Fig. 2.6) as follows:

$$a^1 = \frac{d^1}{d^1 + d^2} \tag{2.15}$$

$$a^2 = \frac{d^3}{d^3 + d^4} \tag{2.16}$$

$$a^3 = \frac{d^5}{d^5 + d^6} \tag{2.17}$$

After computing the interpolation coefficients two options are available: 1) directly calculating the interpolated velocities at the donor processor and just return the calculated values (3 components of velocity); 2) return the interpolation coefficients ($[a^1,\ a^2,\ a^3]$) as well as the index (i, j, k) of the donor and form an interpolation matrix. Using the fist option only 3 real numbers (24 byte for each point) need to be returned while in case of forming an interpolation matrix, 3 real numbers ($[a^1,\ a^2,\ a^3]$) as well as 3 integers ($i,\ j,\ k$ of the donor) should be transferred which will be a total of 36 bytes of data. Although for forming an interpolation matrix more data needs to be transferred, the matrix formation needs to be performed only once before the iterations of the Newton-Krylov method for momentum equation (Eq. 2.11) begins. In addition, by using an interpolation matrix and using available toolkits, e.g., PETSc [174], which utilizes highly optimized libraries and parallel algorithms for matrix multiplication, the interpolated values are obtained by performing a matrix-vector multiplication and thus will be very robust. Furthermore, the inter-

polation method will be general and can also be easily used for any flow variable, e.g. scalar concentration, etc. Therefore, the interpolation matrix is used in this work, which has also been more efficient based on our numerical tests. Compared to our previous method [1] in which the domain connectivity information was calculated using a single processor and then the information was broadcast to all other processors (which obviously is not efficient and thus not suitable for large scale problems), our current interpolation method is quite faster and more efficient for a large number of grid points.

In this work, PETSc toolkit [174] is used for parallel matrix assembly and matrix-vector multiplication. The final interpolation matrix is stored in a compressed sparse row format to minimize memory storage. However, forming a parallel interpolation matrix efficiently is not a very straightforward task. The first step to allocate the interpolation matrix is to define a local and a global index for the points in all domains and processors. Fig. 2.8 shows the architecture of the allocated matrix and the parallel vector of flow variables. As it can be seen in the parallel distributed vector of the flow variables (Fig. 2.8), each processor packs the variables in that processor for different blocks one after the other based on their block number (bi), e.g. processor zero ($P = 0$) packs all the velocity vectors $u_{p=0} = \{u_{bi=0}, ..., u_{bi=n}\}$. Based on this strategy the local index ($L\_index_P^{bi}$) in each processor P for block bi can be defined as follows:

$$L\_index_P^{bi}(i,j,k) = \Big(I_x^0 + I_x \times I_y^0 + I_x^0 \times I_y^0 \times I_z^0\Big)_P^0 + \ ... + \Big(i + I_x^{bi} \times j + I_x^{bi} \times I_y^{bi} \times k\Big)_P^{bi} \quad (2.18)$$

where (i, j, k) are the index of the point and $[I_x, I_y, I_z]$ are dimensions of distributed grid in processor P in x, y, z directions, respectively. Since the donor cell can be in any processor and any block, to be able to define a global index ($G\_index_P^{bi}(i, j, k)$), it is necessary for all the processors to know the domain decomposition pattern for every domain. Since we are using a structured grid, the starting and end grid numbers for all curvilinear coordinates in every processor will be enough

to define the global index as follows:

$$G\_index_P^{bi}(i,j,k) = \sum_{proc=0}^{P-1} \sum_{block=0}^{n} L\_index_{Proc}^{block} + L\_index_P^{bi}(i,j,k) \tag{2.19}$$

where P and n are the processor's number and the number of blocks, respectively. After the indexing is done, each processor will form a portion of the interpolation matrix related to its grid point and then the whole matrix will be assembled. The Algorithm 4 outlines the process for the parallel interpolation matrix assembly.

Algorithm 4 Algorithm for interpolation matrix assembly

```
get donor-index and interpolation coefficients
NQ=Number of query points
for i = 0 to i = NQ do
    if (donor is available) then
        identify ID of the donor processor
        column-index= global index for the corners of the donor cell
        row-index= global index for the receptor point in processor rank
    end if
end for
Creates a sparse parallel interpolation matrix in AIJ format
```

2.3 Moving overset-CURVIB flow solver

The above grid assembly is directly integrated into our CURVIB flow solver. Fig. 2.9 illustrates the flow-chart for the flow solver and how the grid assembly and the interpolation kernels are integrated into our CURVIB flow solver. At the beginning of each simulation, the location of immersed bodies and the flow is initialized. Then for dynamic overset grids, the overset grid over each immersed body is moved based on the motion of that immersed body, i.e., the overset grids are moved with the center of mass of that immersed bodies. This movement can be either prescribed or calculated based on hydrodynamic forces applied to each immersed body for FSI simulations. After each grid movement, the grid assembly task (section 2.2) is performed because

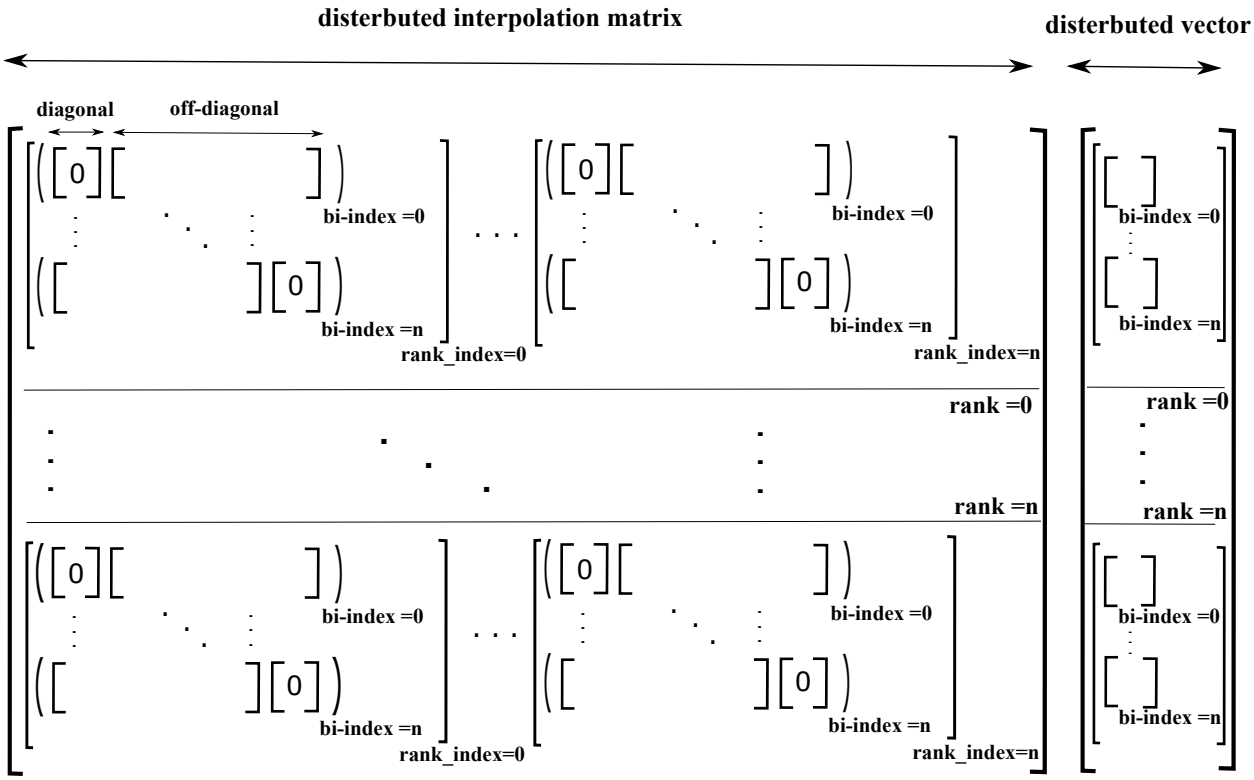

Figure 2.8: Schematic of assembled parallel interpolation matrix and distributed field vector. Here, rank shows the ID of each processor, rank_index shows index of the processor from which the solution is interpolated, and bi_index shows the block number in each processor.

of the relative position of the grids and, consequently, the donors and interpolation coefficients have changed. After performing the grid assembly and obtaining the query points, donors, and interpolation coefficients, the velocities are interpolated and the fluxes are reconstructed on the query points as will be explained in section 2.3.1. Since a non-inertial frame of reference is used for solving the flow in this work, the velocities cannot be interpolated directly from one domain to the other, thus, a transformation from the reference of one domain to the other is needed (see section 2.3.1). Having the fluxes at the interfaces and the buffer layer, the flow is solved using the CURVIB method (section 2.1.1). Since an implicit method using a Newton-Krylov solver is used for solving the momentum equation in this work, the interpolation needs to be performed in each iteration of the Newton-Krylov solver. After solving the momentum equation, the mass conservation should explicitly be satisfied on the query points (see section 2.3.3), and then the Poisson equation for the correction step is solved to enforce continuity. Furthermore, for strong-coupling FSI simulations, all the above steps should be performed in every sub-iteration of the strong-coupling iterations until the desired convergence for criteria in the structure solver is satisfied [46].

2.3.1 Flux reconstruction and velocity transformation between inertial and non-inertial frames

Following the interpolation process, the interpolated velocities will be available in each processor. Because a non-inertial frame of reference is used for solving the momentum equations in each block of the domain, however, the interpolated velocities will be in a non-inertial frame and cannot be used directly in another domain since based on Eq. 2.20 the non-inertial velocity is related to inertial velocity by an orthogonal rotation tensor. Using the communication map generated in section 2.2.3, the donor and receiver blocks are known and the velocities from one domain to the other can be converted using the following formula:

$$\left\{u_p^{non-int}\right\}_{(bi=m)} = \left(Q_{pr}^{bi=m}\right)\left(Q_{qr}^{bi=n}\right)^{-1}\left\{u_q^{non-int}\right\}_{(bi=n)} \tag{2.20}$$

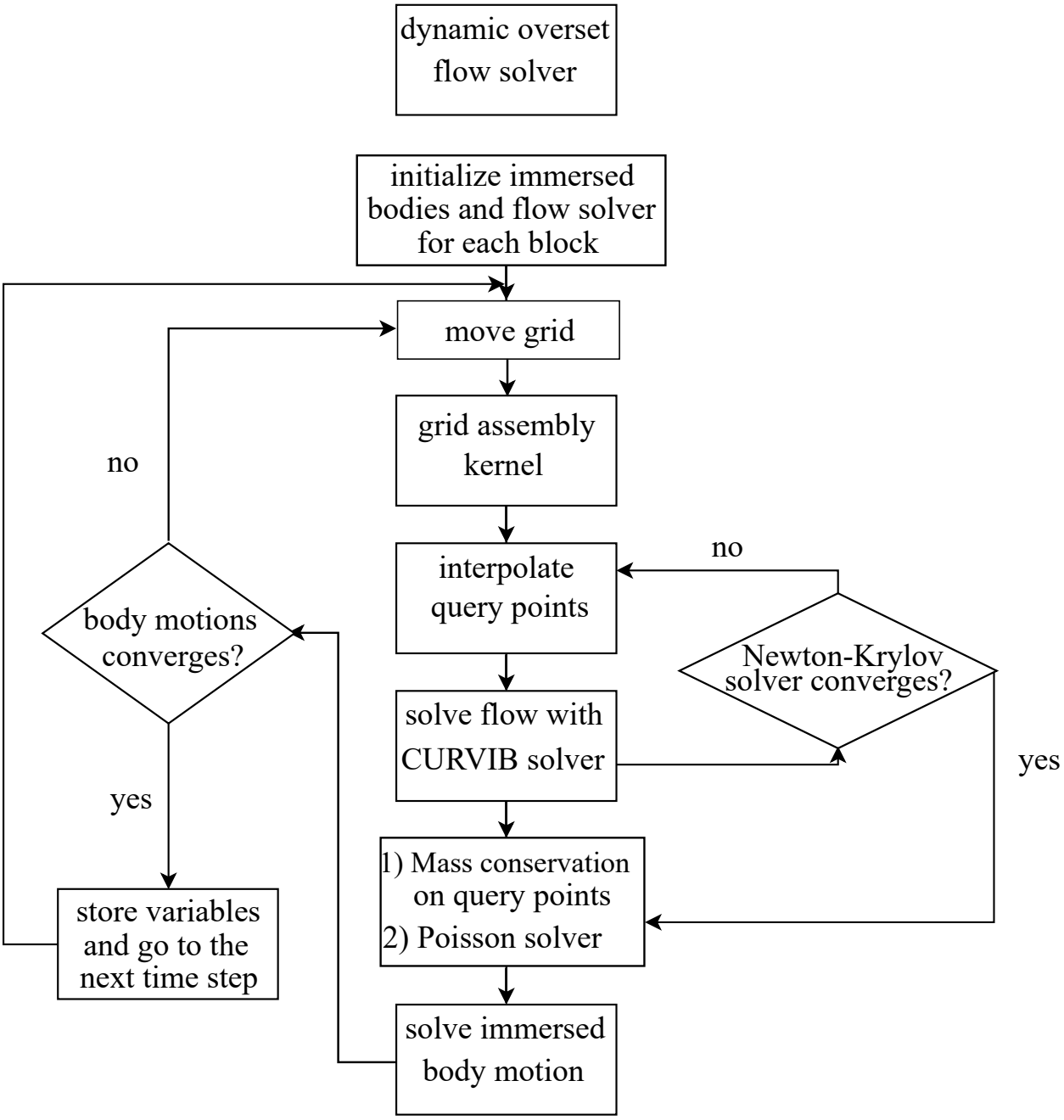

Figure 2.9: Integrating grid assembly kernel to CURVIB flow solver for FSI simulations

where $\left\{u_p^{non-int}\right\}_{(bi)}$ is the non-inertial velocity in block bi and Q_{pr}^m is an orthogonal rotation matrix (note, $\left(Q_{qr}^n\right)^{-1} = Q_{rq}^n$) which relates coordinates of block $bi = m$ to inertial coordinates. Finally, the flux U^r for each recipient cell surface is obtained by Eq. 2.7 using the scheme discussed in [1].

2.3.2 Handling special cases: Overlap of overset boundaries with immersed boundaries or other overset grids

To be able to apply the above algorithm (Fig. 2.9) when multiple overset grids or immersed boundaries overlap after grid motion, some special cases should be considered. These considerations are as follows:

1. Donor selection: In the case of multiple overlap grids in the simulation, there may be multiple donors available for a query point. There are several ways to select the donor in these situations. In this study, the query points for each blanked region of the background grid will be interpolated from a specified moving overset which will be provided to the code as an input, whereas the interface of a moving grid inside the background grids is either interpolated from other moving grids or the background grid. To interpolate the interface of a moving grid, the priority is given to the background grid, but it will be interpolated from other available overset grids if a suitable donor does not exist in the background grid, e.g., the donor in the background grid is a blanked node.

2. Interpolation near solid wall boundaries: Another case happens when the interface of one grid crosses/intersects a solid body or a wall boundary condition. Fig. 2.10 illustrates this situation where the interface of the red and blue grids are crossing/intersecting immersed bodies. Therefore, some of the nodes of the donor cell (Fig. 2.6) might be inside the immersed body, i.e., a velocity inside the immersed boundary is needed for interpolating onto the interface of the moving grid. Since the flow is inside the solid body is not available, two options are possible: 1) assigning an approximate velocity to solid nodes inside the immersed body based on the velocity of the body; or 2) blanking the region around the im-

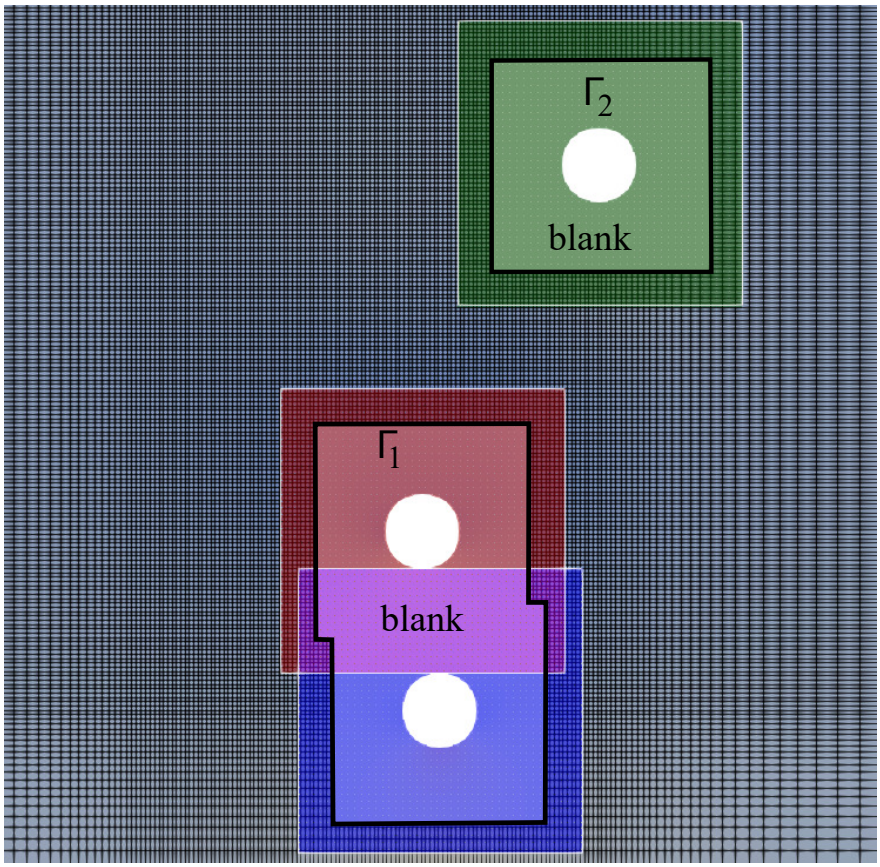

Figure 2.10: Illustrates the position of overset grids and blanked regions of the background domain for a simulation with bodies in relative motion (here, circular cylinders) and the way the conservation of mass is satisfied. Here, the blanked region in the red grid intersects with one in the blue grid. In this situation, the mass is conserved over Γ_1 which is the boundary of the combined blanked region of red and blue grids. However, in the situation without intersection, e.g., Γ_1 and Γ_2, the mass is conserved on each blanked region separately.

mersed body in the other domain (Fig. 2.11). Assigning an approximate velocity to solid nodes will reduce the accuracy of simulations especially in FSI simulations. Hence, the area near the immersed boundary is blanked out and the boundaries of this region are interpolated from the other moving grid (Fig. 2.11). Fig. 2.10 shows the position of the blanked region of the background grid while Fig. 2.11 shows the position of the blanked region of the moving overset grid.

2.3.3 Mass conservation

For incompressible flows, the flux over any closed, non-deforming surface Γ within the fluid should be zero:

$$\int_{\Gamma} \boldsymbol{u}.\hat{\boldsymbol{n}} d\Gamma = 0 \tag{2.21}$$

where $\hat{\boldsymbol{n}}$ is the outward normal to the boundary. Therefore, the flux over blanked regions (Fig. 2.10) or the interface of overset grids needs to be zero (Fig. 2.11). However, the flux on the interfaces is reconstructed using the most recent solution of the donor domain based on the intermediate velocities ($\boldsymbol{u}^*$) in the projection method (Eqn. 2.11). Since the $\boldsymbol{u}^*$ does not satisfy the continuity equation and a trilinear interpolation is not a conservative scheme, the global conservation of mass is not satisfied at the overset grid interfaces (for more details refer to [1]). The mass conservation is enforced by adding a correction to the flux, which is calculated by setting the summation of fluxes at the interfaces of each domain and over the blanked region to zero similar to the non-moving overset grids [1]. For multiple body collisions (Fig. 2.10), the summation of fluxes at all the blanks together are forced to be zero, e.g., the flux over Γ_1 and Γ_2 are forced to be zero in the background grid (Fig. 2.10) while the flux over Γ_3 and Γ_4 which are the boundaries of overset grids are forced to be zero separately (Fig. 2.11).

2.4 Quantifying platelet activation in Eulerian framework

In this section, the numerical method used for quantifying platelet activation including the activation models formulations, scalar viscous shear stress calculation, Eulerian implementation, and the integration of activation in the fluid domains is explained.

2.4.1 Platelet activation models

Several mathematical models for platelet activation have been proposed in the literature ([158, 159, 182, 183, 184, 4]). To show that the results are not dependent on a specific model, two different activation models are used: 1) linear level of activation and 2) Soares model. Linear level of activation is developed for quantifying the activation under constant shear stress. However,

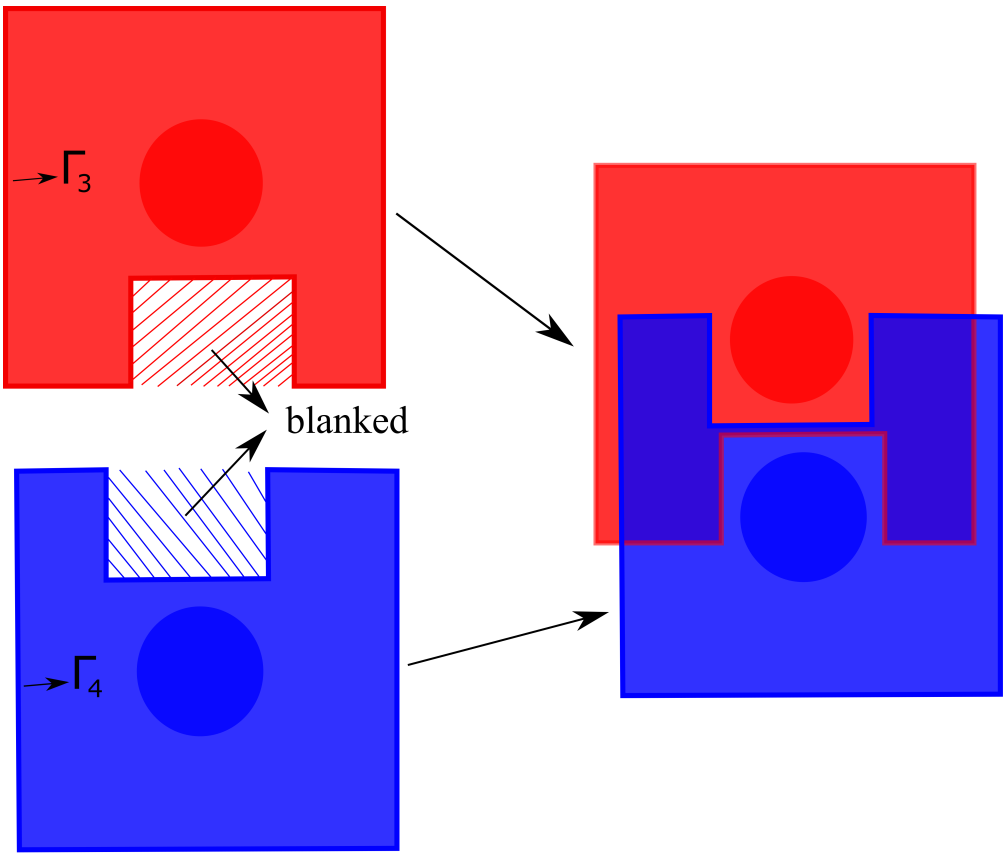

Figure 2.11: Demonstrates the the strategy chosen for the multiple bodies in relative motion where the interface of overset grid intersects with a solid body. The area around the body is blanked out from the other overset grid, e.g. the area around the res body is blanked out from the blue overset grid, which prevents intersection of interface with solid body. For each interface the mass is conserved separately, e.g. mass conservation is satisfied on Γ_1 and Γ_2 separately.

due to the simplicity, it has been widely used to investigate thromboembolic performance of heart valves ([5, 56, 185]). In this model, the activation is modeled as the summation of shear stress times the exposure time over the platelet path ([186]).

$$P(t) = t \times \tau \tag{2.22}$$

where $P(t)$ is activation, t is the exposure time and τ is the scalar shear stress. According to the Hellums criterion, using the linear model, platelets are considered as activated when the $P(t)$ value exceeds $35\ dyne.s/cm^2$.

The second model is the Damage accumulation model that quantifies the platelet activation ([165]) based on the theory of damage previously developed for red blood cell by [166], which is defined as follows

$$P(t) = (\frac{\tau(t)}{\tau_0})^{\ r} \left(\frac{1}{(1 - P(t))^k} \right) \tag{2.23}$$

where $P(t)$ is cumulative damage due to shear stress at time t which can vary from 0 for non-activated platelets to 1 for fully activated ones. Where r and k are constants with value of -1 and 5, respectively. This model can deal with cumulative effect of stress history as well as considering the effect of past damage.

Soares model has been developed based on the Platelet Activation State (PAS) by [4]. This model is defined as follows

$$\frac{d\,P(t)}{dt} = \ K_0 \left[P(t),\, \tau^t(s) \right] \ (1 - P(t)) \tag{2.24}$$

where

$$K_0 \left[P(t),\, \tau^t(s) \right] \ = S(P(t), H_\tau) + F\left(P(t), \tau\right) + G(P(t), \dot{\tau}) \tag{2.25}$$

and

$$H_\tau = \int_0^t \tau(s) ds \tag{2.26}$$

S_r	C	α	β	C_r	γ	δ
1.5701×10^{-7}	1.4854×10^{-7}	1.4854	1.4401	1.3889×10^{-4}	0.572	0.5125

Table 2.1: Constants of Soares et al. model from ([4])

H_τ is the history of scalar shear stress accumulation up to time t which is similar to linear level of activation. In addition, $S(P(t), H_\tau)$ is a term which accounts for platelet sensitization and, is a function of shear stress accumulation and level of activation

$$S(P(t), H_\tau) = S_r P(t) H_\tau \tag{2.27}$$

$F\left(P(t), \tau\right)$ and $G(P(t), \dot{\tau})$ are the nonlinear terms of platelet activation which account for shear and rate of shear , respectively as follows

$$F(P(t), \tau) = C^{\frac{1}{\beta}} \beta P(t)^{\frac{\beta-1}{\beta}} \tau^{\frac{\alpha}{\beta}} \tag{2.28}$$

$$G(P(t), \dot{\tau}) = {C_r}^{\frac{1}{\delta}} P(t)^{\frac{\delta-1}{\delta}} |\dot{\tau}|^{\frac{\gamma}{\delta}} \tag{2.29}$$

the value of constants for this model are shown in Table 2.1.

Here $P(t)$ is platelet activation state at time t which can vary from 0 to 1. $P(t) = 0$ measures non-activated platelets while the upper bound, $(P(t) = 1)$ is assigned to fully activated platelets. This model accounts for the platelet sensitization as well as the shear stress rate.

2.4.2 Scalar shear stress calculation

Based on the work by [187], viscous shear stress is the mechanical force experienced by platelets in a turbulent flow field and Reynolds shear stress is a statistical quantity, not an actual physical force. In addition, we used Direct Numerical Simulations (DNS) in this work which can resolve the unsteady time history of the viscous shear. Therefore, just the effect of viscous shear stress is considered in this work which for Newtonian fluid can be written in tensor notation

as follows

$$\sigma_{ij} = \mu \, (\frac{\partial u_j}{\partial x_i} + \frac{\partial u_i}{\partial x_j}), \quad (i, j = 1 \; to \; 3) \tag{2.30}$$

where σ_{ij} is viscous shear stress, μ is the molecular viscosity, and u_i is the i^{th} component of the cartesian velocities.

The shear stress tensor is reduced to a scalar quantity τ, according to the formulation performed by [188]

$$\tau(t) = [\frac{1}{6} \sum_{i,j=1}^{3} (\sigma_{ii} - \sigma_{jj})(\sigma_{ii} - \sigma_{jj}) + \sigma_{ij}\sigma_{ij}]^{1/2} \tag{2.31}$$

2.4.3 Platelet activation quantification

The activation models can be treated based on Lagrangian and Eulerian approaches. In the Eulerian approach, the activation is quantified over the whole computational domain. However, in the Lagrangian one, the activation is integrated over the pathlines of many particles. Considering the normal range of platelets in artery vessels, which is 150,000 to 400,000 per cubic millimeter ([167]), millions of particles need to be calculated in the Lagrangian approach to get statistically significant results. Handling millions of particles is computationally quite expensive. Therefore, a Eulerian approach is used in this work. Using the definition of the total derivative ([189]), the activation can be quantified in Eulerian frame as follow

$$\frac{\partial p}{\partial t} + \nabla.(p\vec{u}) = \dot{P} \tag{2.32}$$

where $\vec{u}$ is the velocity of the flow field, $p = p(\vec{x}, t)$ is the activation level in the Eulerian form, and $\dot{P}$ ($P(t) = P(t, \tau(t))$) is the activation rate based on the above activation models in the Lagrangian form, i.e., $p(\vec{x}, t) = P(t)$ for a particle at location $\vec{x}$. The strang operator splitting ([190]) along with a second-order MUSCL scheme ([191]) for spatial discretization and a second-order TVD Runge Kutta scheme ([192]) for time discretization is used to solve the above equation.

In order to compare the total activation of platelets generated in bulk flow and hinge domains (Fig. 5 in the paper), the integral form of Eqn. 2.32 , i.e., the Reynolds transport theorem for

the conservation of scalar (activation) ([189]), is considered over the domain

$$\frac{d}{dt}\,(\text{total activation})_{sys} = \frac{\partial}{\partial t}\int_{CV} p(\vec{x},t)\;dV \;+\; \int_{CS} p(\vec{x},t)\;\vec{u}\;.\;\vec{n}\;dA \tag{2.33}$$

where CV is the control volume, sys is the system, CS is the control surface and $\vec{n}$ is the unit outward normal to the control surface. By integrating over time, the total activation from $t = 0$ to $t = T$ can be calculated as

$$\text{total activation}\,\Big|_0^T = \left(\int_V p(\vec{x},t)\;dV\right)\Big|_0^T \;+\; \int_0^T \left(\int_A p(\vec{x},t)\;\vec{u}\;.\;\vec{n}\;dA\right)\;dt \tag{2.34}$$

The normalization is performed to compare the total activation in the bulk flow and hinge region with different gap sizes and interpolation methods. In order to normalize the activation in all domains the total activation in the bulk flow at the end of the cardiac cycle is calculated using the above formula (Eqn. 2.32) and this value is used as a reference for normalizing the total activation in the hinge region for all cases:

$$\text{Normalized Activation}(\%) = \frac{\text{total activation in the domain}}{\text{total activation in bulk flow at the end of the cycle}} \times 100 \tag{2.35}$$

3. VALIDATION, VERIFICATION AND PARALLEL PERFORMANCE*

This chapter is organized as follows: In section 3.1 several test cases have been performed for the validation of the overset-CURVIB framework. This framework is validated against the analytical solution of Taylor-Green vortex in section 3.1.1 in which the simulations show second-order accuracy both in time and space. Then, the results of the overset grid are validated against the results of a single grid for a rotationally oscillating cylinder in an infinite flow at rest in section 3.1.2. The results of the overset grid compare to the single grid and experimental results for a forced inline oscillation of a cylinder in a fluid initially at rest in section 3.1.3. Later, to validate the framework for FSI simulations the results of the overset grid and single grid are compared to each other for the free fall of Single cylinder 3.1.4.1 and Multiple cylinders 3.1.4.2 under gravity. To show the capability of the framework to handle complex simulations multiple mackerels in the diamond arrangement are simulated in section 3.1.5. The parallel performance of our framework is investigated for multiple mackerels simulation in section 3.2. Finally, the platelet activation framework is validated against experimental results in section 3.3

3.1 Flow solver validation

In this chapter, the new overset-CURVIB framework is verified and validated against experimental data, the analytical solution of Taylor-Green vortex, and other benchmark solutions and the capability of the new framework is shown by performing multiple circular cylinders in a free fall under gravity in a fluid domain as well as a school of swimmers in a diamond shape. Using overset grids reduced the total number of grid points from 500 to 30 million while preserving the same resolution in the self-propelled fish school. This new framework enables us to tackle challenging real-world problems that cannot be handled without moving overset grids. later, the parallel scalability of our solver is tested for different parts of our framework for the school of swimmers

*Part of this chapter is reprinted with permission from "Comparison of platelet activation through hinge vs bulk flow in bileaflet mechanical heart valves" by M. Hedayat and I. Borazjani, 2019, Journal of biomechanics, 83, 280-290, Copyright 2019 by Elsevier Ltd.

test case (section 3.2). While good scalability is achieved for our flow solver for up to 560 processors, the scalability of grid assembly kernel drops off for more than 140 processors due to the load-imbalance related to the partitioning strategy used in this work (as discussed in section 3.2). A better initial partitioning strategy that takes the communications costs of the overset grids into account in the future can help to enhance the scalability of the grid assembly kernel. Nevertheless, the time required for the grid assembly is less than 7% of the total simulation time even at the highest number of CPUs tested (560 cores). Finally, the platelet activation framework is validated against the experimental results for shear-induced platelet activation in the laminar Taylor-Couette flow in section 3.3.

3.1.1 Taylor-Green vortex

The Taylor-Green vortex problem is adopted to investigate the performance and accuracy of the dynamic overset-CURVIB framework. Two-dimensional Taylor-Green vortex is an unsteady flow of a decaying vortex with periodic boundary conditions in two directions (here, x and y) and symmetric in the other direction (here, z). The existence of an exact analytical solution that satisfies the $2D$ incompressible Navier-Stokes equations makes Taylor-Green vortex a suitable benchmark to examine the precision of the computational results. The initial condition is the analytical solution at $t = 0$ in all the domains for all the simulations. The background domain with the size of $2\pi \times 2\pi$ in periodic directions (x and y) is discretized uniformly with 201×201 nodes. A square overset grid with the dimension of 2.2 centered at the center of coordinates at the initial condition is discretized uniformly with 121×121 nodes. In addition, a square blank region with a size of 1.5 on each side is used to blank out the nodes inside the background region. To test the accuracy of our framework for a moving overset grid, two test cases, one for an overset grid with translational movement and the other one with rotational moving are tested. For the translationally moving overset grid, the overset grid is moving with time using a constant translational velocity of $V = \pi/4$ in x direction. In the rotating case, the overset grid is rotating with a constant rotational velocity of $\omega_c = \pi/4$ around z axis. Figure 3.1 show the contour of velocity and the streamline at a cross-section of the computational domain at t=1 ($\Delta t = 2.5 \times 10^{-4}$) in the simulation with

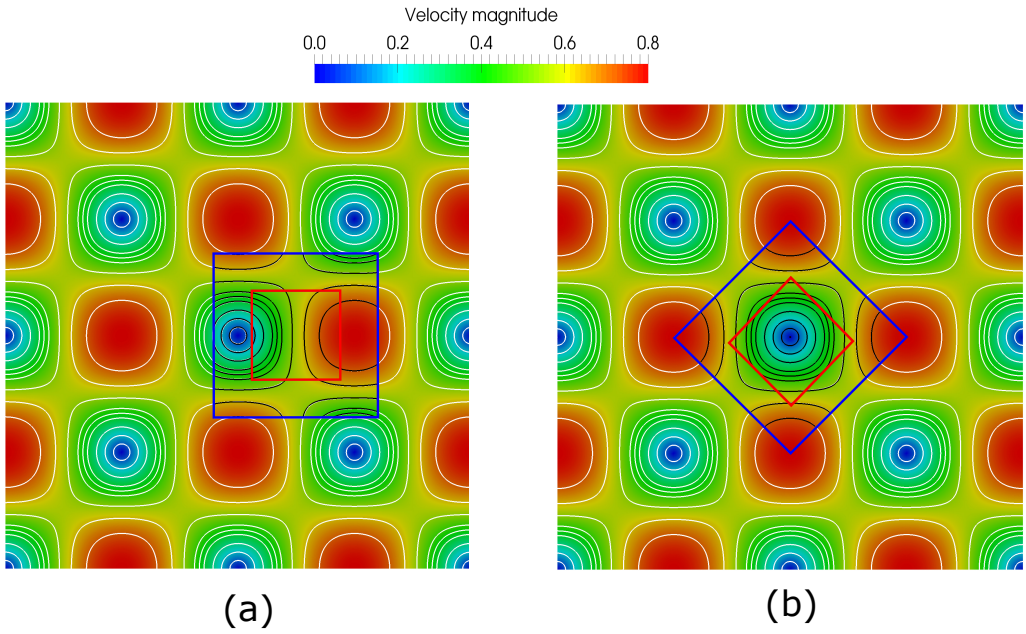

Figure 3.1: Taylor-Green vortex problem at $t = 1$ and $Re = 10$: (a) the contour of velocity magnitude for a moving overset with translational speed of $V = PI/4$ b) the contour of velocity magnitude for a rotating overset with rotational speed of $\omega_c = PI/4$. It also compares the streamline contours for both overset grid (black) and background grid (white)

Reynolds number (Re) equal to 10. As can be observed in Fig. 3.1 the contour of streamlines in the overset domain and the background domain almost exactly match with each other for both rotational and translational moving overset.

The accuracy of the solver in time and space is calculated by computing the error of the numerical results compared to the analytical solution for five simulations with grid size of (size of larger domain $\times$ size of smaller domain) of 51×31, 81×49, 81×49, 101×61, 161×98, 201×121 and time-steps of $\Delta t = 1 \times 10^{-2}$, 6.29×10^{-3}, 5×10^{-3}, 3.16×10^{-3}, 2.5×10^{-3} for the largest to smallest grids, respectively. The standard error is used to calculate the error in the computational domain as follows:

$$\text{Standard Error} = \sum_{b=1}^{b=2} \frac{1}{N_x^b N_y^b} \sqrt{\sum_{i=1}^{i=N_x^b} \sum_{i=1}^{i=N_y^b} (u_{(i,j)}^b - u_{(i,j)}^{exact})^2 + (v_{(i,j)}^b - v_{(i,j)}^{exact})^2} \tag{3.1}$$

where N_x^b and N_y^b are the number of grid points in i and j direction, respectively, $u_{(i,j)}^b$ and $v_{(i,j)}^b$ are

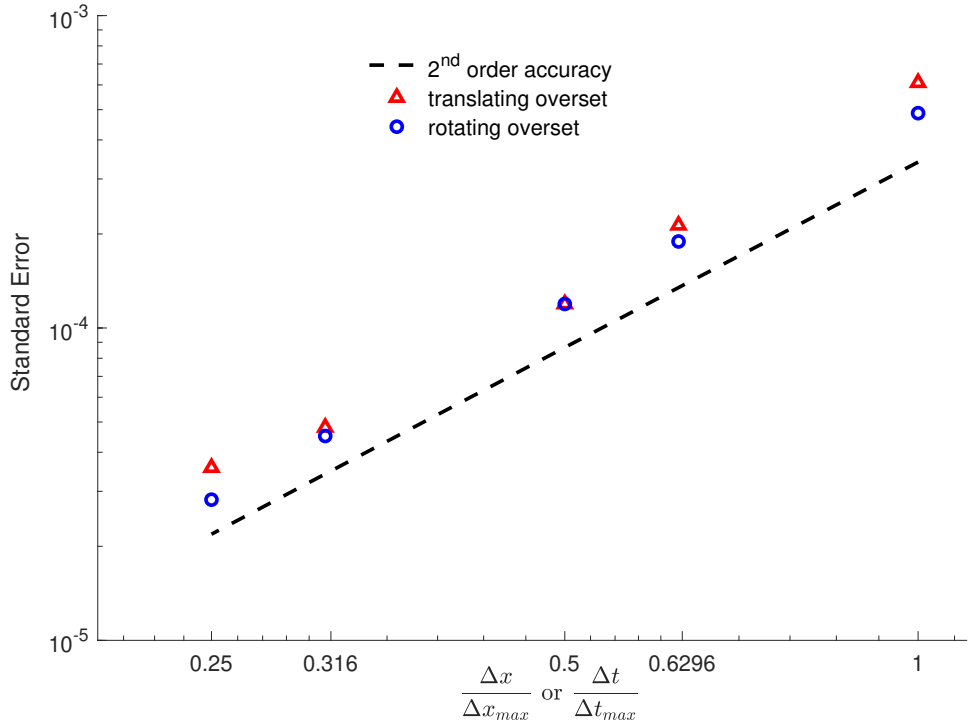

Figure 3.2: Standard error for Taylor-Green vortex flow as a function of the grid spacing/time-step in log–log scale at $t = 1$ and $Re = 10$. CFL is kept the same for all test cases, i.e., $\frac{\Delta t}{\Delta t_{max}} = \frac{\Delta x}{\Delta x_{max}}$. The error shows about 2^{nd} order reduction with mesh refinement.

the numerical solutions of velocities on the (i, j) grid point of each sub-grid (b) of the overset grid, and $u^{exact}_{(i,j)}$ and $v^{exact}_{(i,j)}$ are the analytical solutions. Figure 3.2 plots the error against grid spacing and time step for both rotational and transitional overset in Taylor-Green vortex problem at $t = 1$ and $Re = 10$ in log-log scale and demonstrates that the error reduces with about second order accuracy with grid/time refinement.

3.1.2 Rotationally oscillating cylinder

To test the ability of overset-CURVIB for rotational immersed bodies, we simulate a rotationally oscillating cylinder in an initially stagnant fluid. The simulations are performed in the inertial frame of reference for the background grid and the non-inertial frame of reference attached to the cylinder for the overset grid. The cylinder is rotating with a rotational motion prescribed by a harmonic oscillation as follows:

$$\omega_c(t) = A_m sin(2\pi f t) \tag{3.2}$$

where $\omega_c(t)$, A_m, and f are the angular velocity of the cylinder, amplitude, and frequency of the oscillation, respectively. Consequently, the Reynolds number can be defined as $Re = U_m D/\nu$, where $U_m = A_m D/2$, D is the diameter of the cylinder, and ν is the kinematic viscosity. In this study, all the parameters including the flow parameters, domain size, boundary conditions are chosen similar to [193]. The size of the background domain is $50D < x_r < 50D$ and $50D < y_r < 50D$. The Reynolds number is defined as $Re = U_m D/\nu$, where $U_m = A_m D/2$, D is the diameter of the cylinder, and ν is the kinematic viscosity. The simulations are performed for $Re = 300$ and $f = 0.1$. An overset grid with the dimension of $2D \times 2D$ discretized by 201 grid points in both x and y directions is used around the cylinder. In addition, a square region at the center of the overset grid with a size of $1.6D \times 1.6D$ is blanked on the background grid. The background grid is fixed, however, the overset grid is fixed to the center of the cylinder and rotates with its motion. Dirichlet boundary condition is used for all outer boundaries of the background domain similar to [193] where the velocities are equal to zero on the boundaries, and the boundary condition for the overset grid are interpolated from the background grid using the Eq. 2.8 as

$$u^{overset} = Q u^{background}_{interpolate} \tag{3.3}$$

Figure 3.3 shows the torque coefficient defined as $C_T = T/(0.5\rho_m U^2 D^2/2)$ during the time, where T is the torque and ρ_m is the density of the fluid. In order to compare the numerical results, a simulation using a single grid with the same dimension as the background in overset simulation

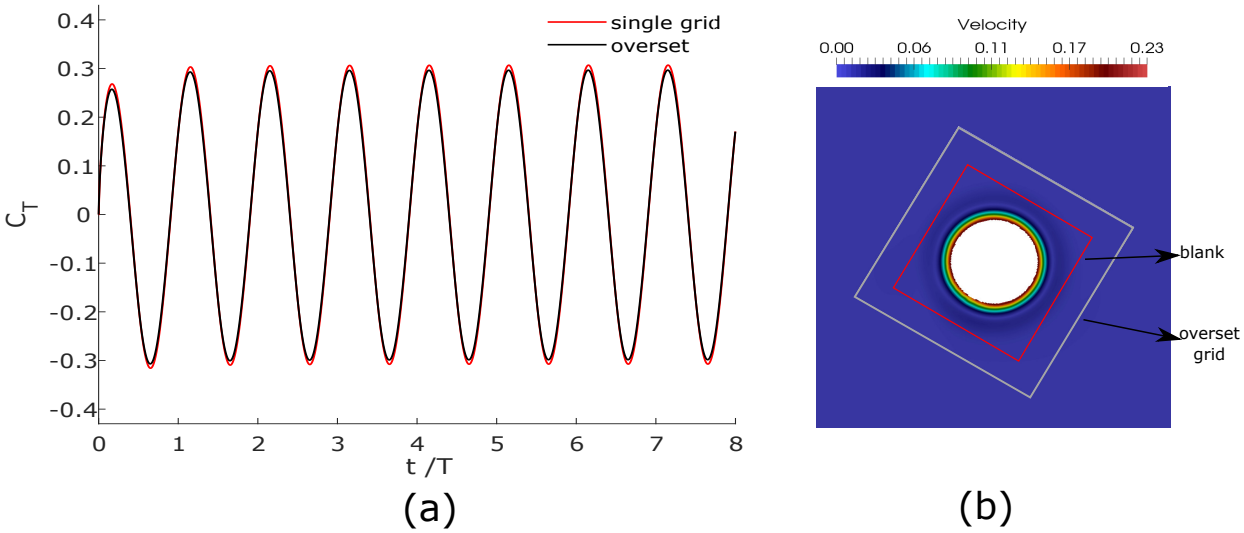

Figure 3.3: Time histories of the torque coefficient for the flow around a rotationally oscillating cylinder at $Re = 300$.

is performed in a non-inertial frame of reference. The single grid is discretized using 401 grid point in both x and y directions which provides a grid resolution of $0.01D$ near the cylinder. Fig. 3.3 compares the results of the overset grid with a single grid for eight cycles. The result of the torque coefficient using the overset grid and single are in good agreement with each other and also they are in good agreement with the results of [1] and slightly lower than the result of [193].

3.1.3 Forced inline oscillations of a cylinder in a fluid initially at rest

The developed framework is validated for the case of a circular cylinder starting to oscillate in the horizontal direction in a fluid initially at rest. The translational motion of the cylinder is given by a harmonic oscillation:

$$x_c(t) = -A_m sin(2\pi f t), \tag{3.4}$$

where x_c is the location of the center of the cylinder, f is the oscillation frequency, and A_m is the oscillation amplitude which result in two non-dimensional flow parameters, i.e., Reynolds number and Kuelegan-Carpenter number as follows:

$$Re = \frac{U_m\, D}{\nu}, \;\; KC = \frac{U_m}{f\; D} \tag{3.5}$$

where U_m is the maximum oscillation velocity, D is the diameter of the cylinder, and ν is the kinematic viscosity of the fluid. The simulation is performed for $KC = 5$ and $Re = 100$, for which the experimental results have been reported by [2]. The size of the background grid is $100D \times 100D$ which is discretized using 301×301 nodes, and 100×100 nodes are distributed uniformly in a $3D \times 3D$ box which contains the cylinder during the oscillations. 201×201 grid nodes are uniformly distributed in the smaller domain with the size of $2.4D \times 2.4D$ aligned and moving with the center of the cylinder ($x_c(t)$). In addition, a blank region with a size of $2.1D \times 2.1D$ is used to blank out the nodes in the background grid. The non-dimensional time-step of $\Delta t = 0.0167$ is used for this simulation in both domains. The far-field boundary condition is applied to the boundaries of the background grid while the boundaries of the small grid are interpolated from the background domain. In addition, to compare the overset results with the results obtained using a single grid, a grid with the same dimension as the background grid explained above ($100D \times 100D$) is discretized using 401×401 grid nodes which provides a grid resolution of $0.01D$ near the cylinder is used. The simulation for the single grid is performed in a non-inertial frame of reference. Fig. 3.4-a shows the position of the overset grid as well as the velocity contours for three the different angles in the overset and background grids. The comparison between the inline velocity profiles

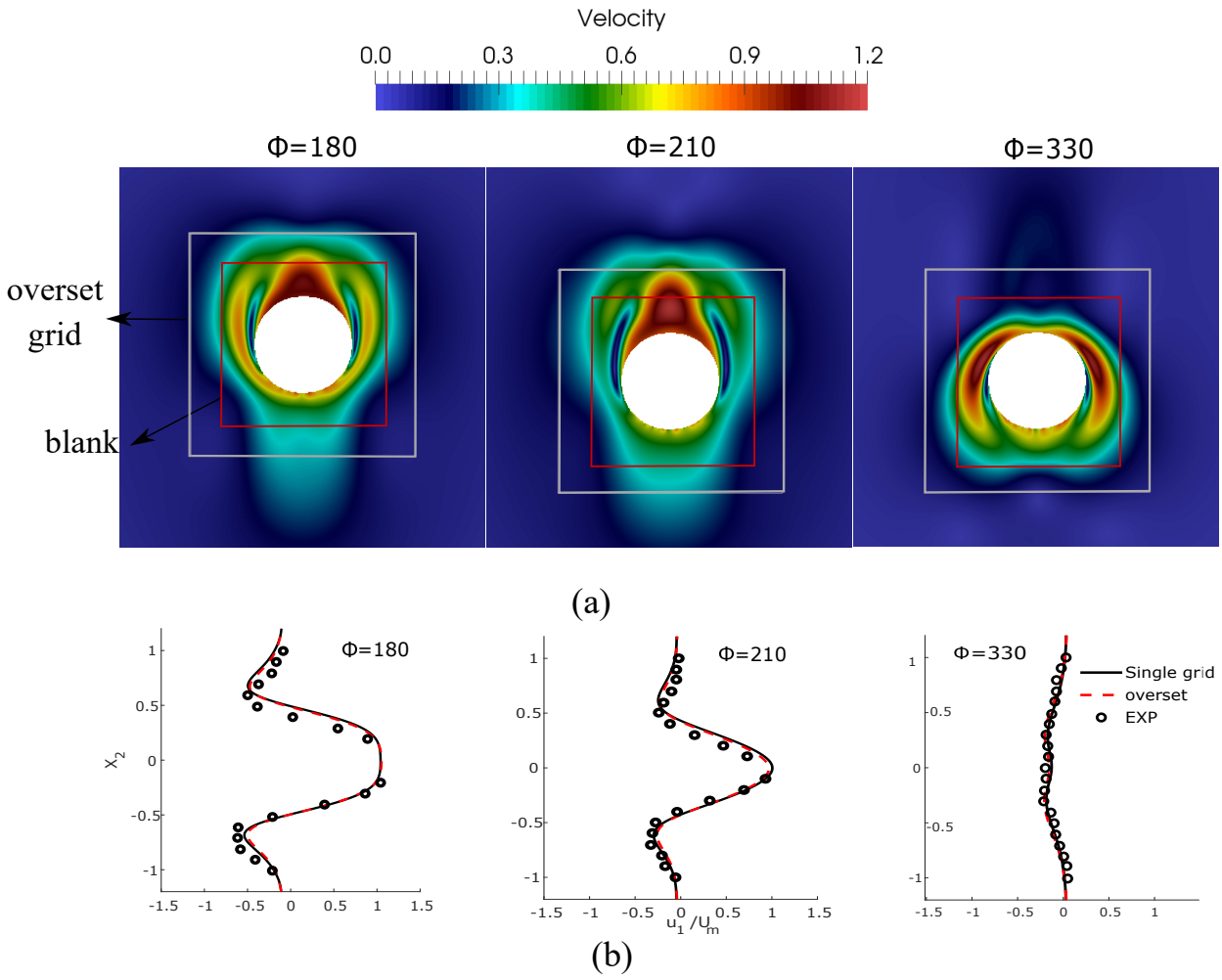

Figure 3.4: Results of numerical simulation for oscillatory cylinder a) contour of velocity for three different phase angles b) Comparison of the inline velocity component (u) profile at position $x_1 = -0.6D$ for three different phase angles between numerical results (overset: - -, single grid: $-$) and the experimental measurements (**o**) of Dutsch et al. [2].

at $x_1 = 0.6D$ for three different phase angles ($\phi = 2\pi ft$) calculated by our framework and experimental measurements by [2] is presented in Fig. 3.4-b. Our numerical results show good agreement with the experimental data.

3.1.4 Freely falling circular cylinder

In this test case, we consider freely falling of circular cylinder under gravity using fluid-structure interaction in which the cylinder falls due to the gravitational and fluid forces. Assuming that the wake behind the cylinder is two dimensional and the cylinder is moving in an infinite fluid the numerical simulations are performed using a two-dimensional grid with symmetric boundary condition in two-dimensional direction (z) and far-field boundary conditions for all the boundary points in x and y direction. The acceleration of the body due to the gravitational and Buoyancy forces is $(\rho_s/\rho_f - 1)g$, where g is the gravitational acceleration, and ρ_s and ρ_f are the density of the cylinder and fluid, respectively. The Reynolds number is considered to be the same as the Galileo number defined as

$$Re = \frac{(|\rho_s/\rho_f - 1|g)^{1/2} D^{3/2}}{\nu} \tag{3.6}$$

where $(|(\rho_s/\rho_f - 1)gD|)^{1/2}$ is the characteristic velocity, ν is the dynamic viscosity of water and D is the diameter of the cylinder. Neglecting the body rotation, the equation of motion for the cylinder in the inertial frame of reference can be obtained using the two-dimensional Newton's equations of motion for a rigid body as

$$M\frac{du}{dt} = F_f - (\rho_s - \rho_f)Vg \tag{3.7}$$

where $M = \rho_s \pi D^2/4$ is the mass of cylinder, V is the cylinder's volume, and F_f is the force exerted on the body by fluid in the non-inertial reference frame. The above equation can be written in non-dimensional form as

$$\frac{\pi}{4}\frac{\rho_s}{\rho_f}\frac{du^*}{dt^*} = F_f^* - \frac{\pi}{4} \tag{3.8}$$

where u^*, t^*, and F_f^* are the non-dimensional velocity, time, and fluid force, respectively. Considering density ratio of solid to fluid $\rho_s/\rho_f = 2.5$, $\nu = 8 \times 10^{-4} N.s/m^2$, and $D = 0.05m$ leads to $Re = 53.61$ in this simulations. Both the fluid and the cylinder are initially at rest and the cylinder starts the free-fall abruptly after start of the simulations. Two test cases, one with a single

cylinder (section 3.1.4.1) and the other with multiple cylinder (section 3.1.4.2), are performed for verifying our framework.

3.1.4.1 Single cylinder

A circular cylinder is placed in the domain similar to the schematic setup presented in Fig. 3.6, for particle number 1 (the bodies and overset grids for particle 2 and particle 3 are not included in this simulation). The background grid with the size of $60D$ in x and $100D$ in y-direction is discretized using 301 and 801 grid points, respectively. The grid points for the background grid are distributed such that the spatial resolution is $0.06D$ around the overset grid during the whole simulation. For the overset domain with the dimension of $4D \times 4D$, 201 grid points are uniformly distributed in both x and y directions which provide the grid resolution of $0.02D$. In addition, a blank region with a size of $3.4D \times 3.4D$ is used to blank out the nodes in the background grid. The flow in the overset grid is solved using a non-inertial frame of reference attached to the center of the cylinder which moves with the cylinder as it falls, whereas the equations for the background grid are solved in the inertial frame of reference. The simulation using the overset grid framework is compared with the numerical results of a single grid with the same dimension as the background grid in the overset simulation, which was performed in a non-inertial frame of reference. For the single grid, 801 and 1931 grid points were distributed in x and y directions, respectively, which provides the spatial resolution of $0.02D$ around the cylinder. Fig. 3.5 compares the time histories of the velocity of the cylinder in the gravitational direction for the overset grid and the single grid simulations. In both cases, the cylinder accelerates monotonically and almost reaches its terminal velocity around $tu_c/D = 50$. As can be observed in Fig. 3.5 the results for the overset grid and the single grid are in good agreement with each other and the difference in the translational velocity of the cylinder using a single grid and the overset grid at time $tu_c/D = 50$ is around 0.2%.

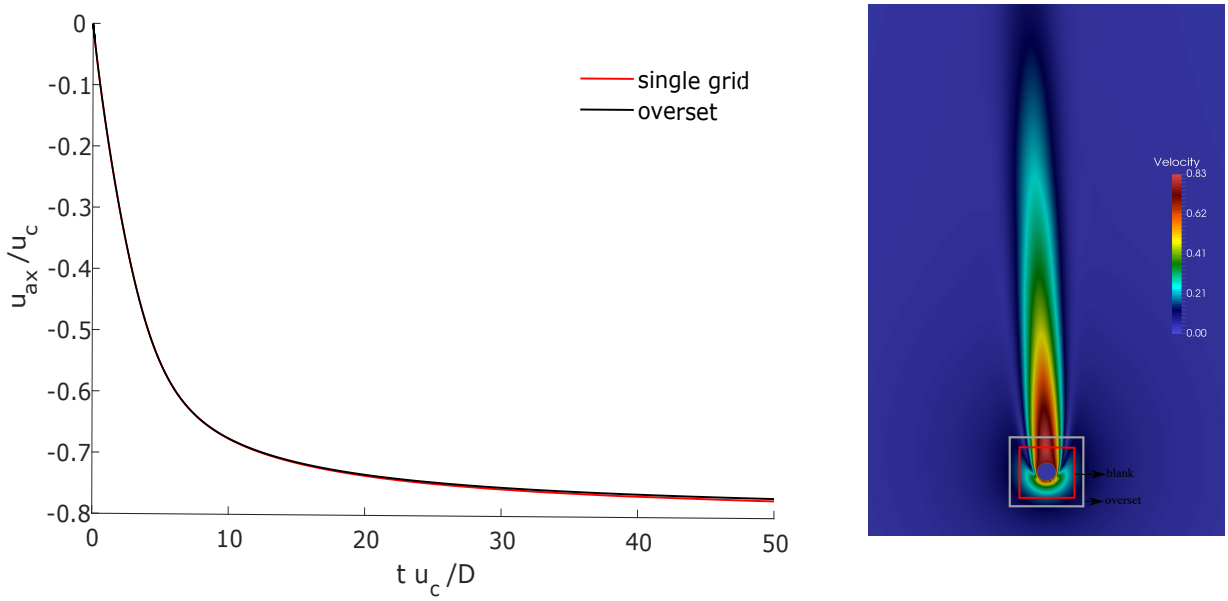

Figure 3.5: (a) Time histories of the velocity of the cylinder in the gravitational direction for the overset (−) and the single (−) grid simulations (b) contour of velocity magnitude at $tu_c/D = 50$

3.1.4.2 Multiple cylinders

To test our framework for multiple overset grids, the simulation for free fall of multiple cylinders in an infinite flow is performed. Fig. 3.6 shows the schematic setup used in this simulation. Three cylinders centered at $(0, 0)$, $(3D, 5D)$, and $(-2D, 5D)$ are placed in the flow domain. An overset grid is generated around each cylinder with the dimension of $4D \times 4D$ and the center are aligned with the center of each cylinder as showed in Fig. 3.6. The grid dimension and the number of grid points are the same as the overset simulation of single cylinder (overset grids are discretized uniformly using 201 grid points in each direction, and the background grid is discretized using 301 and 801 grid points distributed the same as the previous section). In order to verify the result of the overset grid the same simulation is performed using a single grid in an inertial frame of reference (since a non-inertial frame of reference cannot be used for this simulation due to existence of multiple particles with different velocities). The computational domain is discretized the same as the single grid used in the previous section (801 and 1931 grid points are distributed in the $60D \times 100D$ domain which guarantees the spatial resolution of $0.02D$ through the trajectory of the cylinder at all times). The simulations are performed using a strong-coupling fluid-structure interaction for both overset and single grid cases [46]. Figure 3.7 compares the time history of the translational velocity of cylinders in the gravitational direction for a single grid versus overset grids. The results of the overset grids and single grid are in good agreement with each other considering that different methods and grid are used for each simulation. The maximum difference in translational velocity of cylinders using a single grid compared to the overset grid is observed for cylinder number 3 which is around 4%. Fig. 3.8 shows the position of the overset grids relative to each other as well as the background grid at several time instants. In addition, the special scenarios discussed in section 2.3.2 regarding the overlap of overset boundaries with immersed boundaries or other overset grids can be observed in this figure.

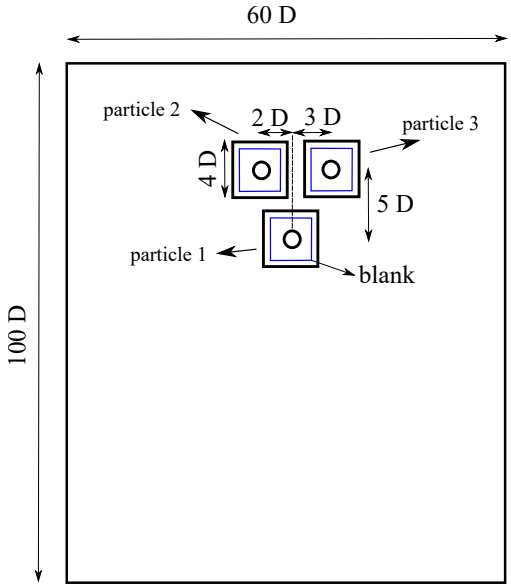

Figure 3.6: Schematic position of overset grids (small black squares), background grid (large rectangle domain), and blank region (small blue squares) relative to each other for simulation of free fall of multiple circular cylinders under gravitational force.

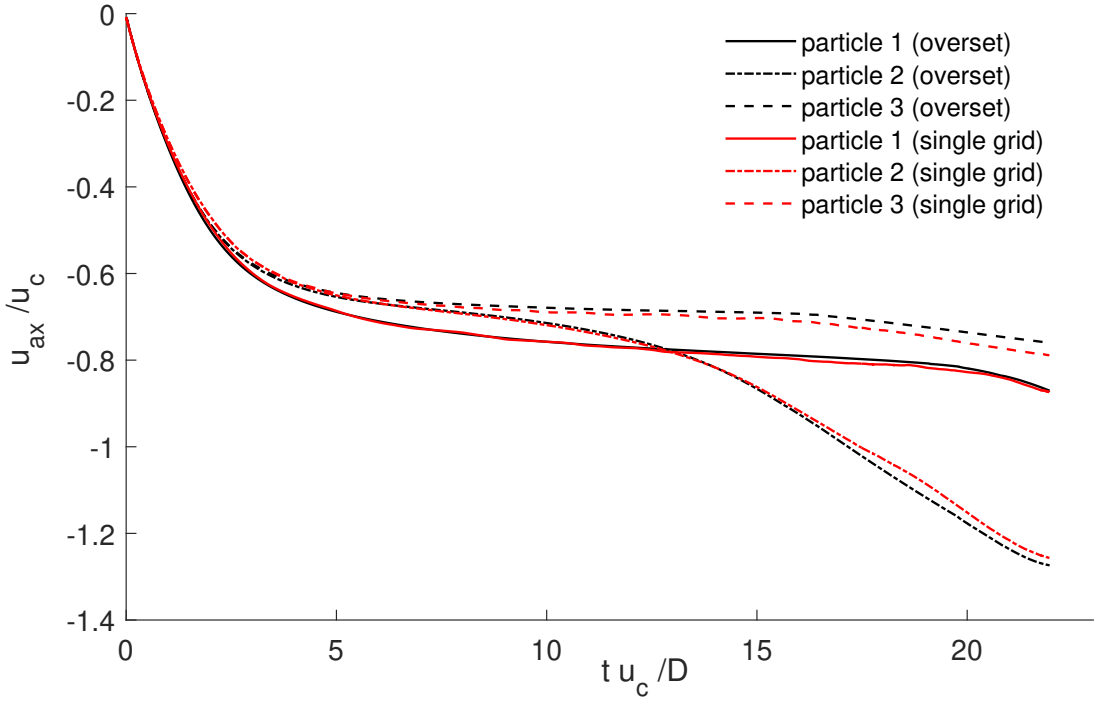

Figure 3.7: Comparison of time histories of the velocity for three different cylinder in the gravitational direction between overset and single grids.

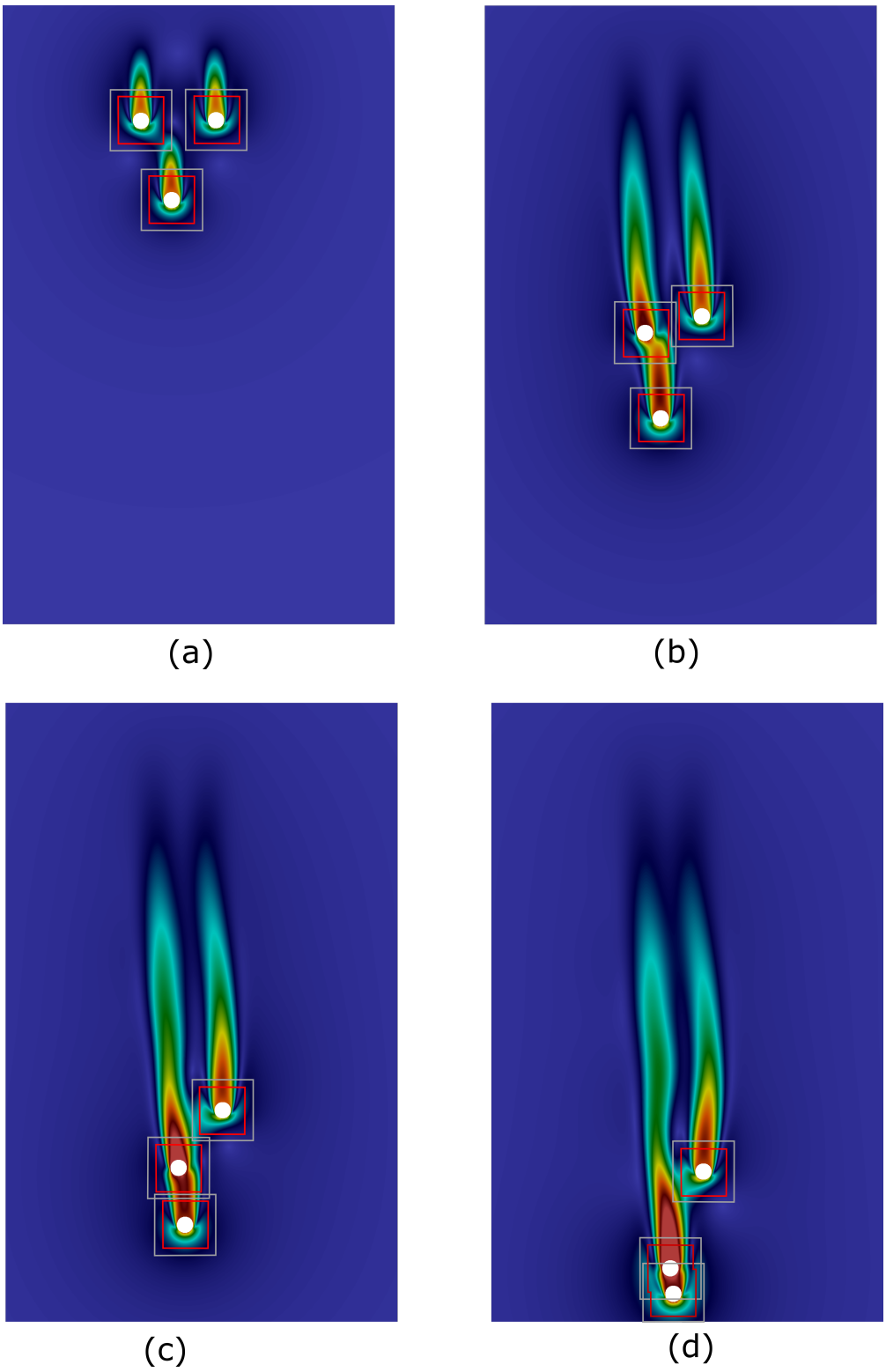

Figure 3.8: Contour of velocity magnitude for overset simulation of multiple circular cylinders at time a) $tu_c/D = 4.4$ b) $tu_c/D = 12$ c) $tu_c/D = 15.6$ d) $tu_c/D = 22$ during the simulation.

3.1.5 Multiple mackerels in diamond arrangement

To show the capability of our numerical framework in handling complex biological flows, a simulation with multiple self-propelled mackerels swimming in the diamond arrangement is performed. The swimmers can move in the background domain, thus, a high-resolution grid would be required in the path of the swimmers. While using a single grid can drastically increase the computations due to a huge number of grid points required, the overset method can provide a high-resolution grid locally around the swimmers without considerably increasing the total number of grid points.

The geometry of the mackerels used in this study is exactly the same as the previous simulations by [194] and [1]. The kinematic motion of the mackerels is approximated by a backward traveling wave with the largest wave amplitude at the fish tail. The lateral undulations of the swimmers' body in non-dimensional form (all lengths are non-dimensionalized with the fish length L) can be described as

$$h(z,t) = a(z)sin(2\pi z/\lambda - 2\pi ft) \tag{3.9}$$

where z is the axial direction measured along the fish axis from the tip of the fish head; $h(z,t)$ is the lateral excursion of the body at time t; $a(z)$ is the amplitude envelope of lateral motion as a function of z; λ is the wavelength, and f is the frequency of the backward traveling wave. The amplitude envelop for a typical mackerel can be approximated by a quadratic curve [195]

$$a(z) = a_0 + a_1 z + a_2 z^2 \tag{3.10}$$

where a_0, a_1, and a_2 are chosen to be 0.02, 0.08, and 0.16, respectively, to match the experimental curve of [196] obtained for a typical mackerel. The maximum displacement of mackerel occurs at its tail $h_{max} = 0.1L$. The non-dimensional wavelength is chosen to be $\lambda/L = 0.95$ based on the experimental data by [196]. The simulations are discretized using 240 time steps per a tail beat period, which corresponds to a non-dimensional time step of $\Delta t = 1.39 \times 10^{-3}$. The Strouhal number $(St) = fL/U$ and Reynolds number are chosen to be 0.6, and 4000, respectively, which

has been shown to result in the final non-dimensional average velocity (Ut/L) close to 1 during a a self-propelled steady-state simulation of a mackerel [195].

The side swimmers are placed $0.45L$ and $1.45L$ laterally and posteriorly, respectively, relative to the front swimmer (where L is the fish length) and the last swimmer is placed $2.9L$ behind the front swimmer. The background grid is a cuboid with dimensions of $4.2L \times L \times 14L$ (in, x,y and z directions, respectively), and the overset grids are also cuboids with dimensions of $0.8L \times 0.5L \times 1.5L$. Each fish is placed at the center of its corresponding overset grid. A region with dimensions of $0.6L \times 0.3L \times 1.3L$ inside each overset grid is blanked from the background grid, whose solution is interpolated from the inner overset grids. The background grid is discretized by 9.7 million grid nodes using a uniform mesh with constant spacing $\Delta x = 0.0187L$. Each overset grid is discretized with a uniform mesh with spacing $\Delta x = 0.005L$ in all directions with $161 \times 101 \times 301$ nodes results in 4.9 million grid nodes. Therefore, the total number of grid points in this simulation is about 29 million while a single grid with a similar resolution would require at least 470 million grid points which is impractical for strong-coupling FSI simulations.

The Naiver-stokes equations are solved in a non-inertial frame of reference for moving overset grids where the reference frame is attached to the center of mass of the fish, however, the background grid is solved in an inertial frame of reference. Slip wall boundary condition is applied to the boundaries of the background grid and the boundaries of overset grids are interpolated from the background grid. The body motion of fish relative to the center of mass is prescribed as mentioned in Eq. 3.9 and there is no phase difference between the backward traveling waves of different swimmers. The velocity of the frame for each grid (center of mass for each fish) was calculated based on the fluid forces on the body of the fish with two degrees of freedom, in x and z directions, using a strongly-coupled fluid-structure interaction strategy [46].

Figure 3.9 shows the out of plan vorticity contours on the midplane of the fish as well as the position of overset grids compared to each other and background grid. As can be seen in this figure the solution is consistent over the overset grids and the background grid and the vortical structures are advected and from one domain to the other. It can be observed that the wake of

each mackerel bifurcates into two rows of vortices (double row structure), which is expected for the Strouhal number of 0.6 based on the work by [195], and interact with downstream immersed bodies and their wakes. Fig. 3.9 and Fig. 3.8 show that our parallel framework (regardless of parallel grid distribution) is capable of handling different scenarios regarding the relative position of overset grids and blank regions compared to each other including multiple grid overlapping, overset interface intersection with interface/blank as well as immersed bodies.

Figure 3.10 shows the 3D flow field visualization using the iso-surface of Q-criteria generated by the swimmers. The wake of each swimmer bifurcates into two rows of vertices and interact with the wake of downstream fish. The swimmers can move relative to each other with two degrees of freedom in the lateral and axial directions and thus they can have different velocities in these directions. Fig. 3.11 compares the axial and lateral velocity for all the swimmers during the time. As can be observed the leading swimmer has the highest axial velocity among all while the last swimmer has the lowest one. However, swimmers on the side (swimmers 2 and 3) have a higher lateral velocity compared to the swimmer 1 and 4 which have almost the same lateral velocities.

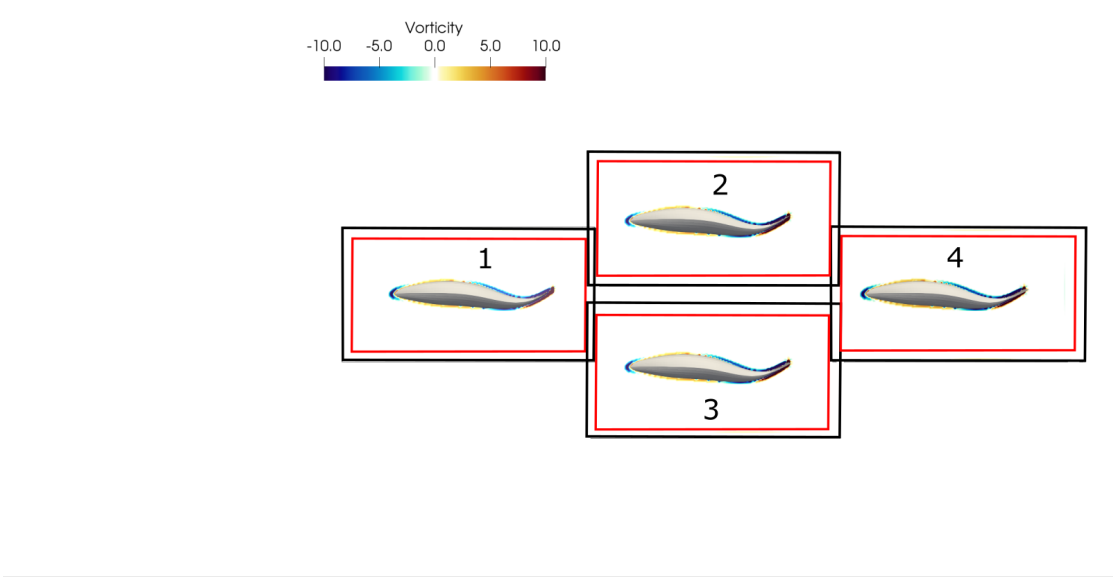

(a)

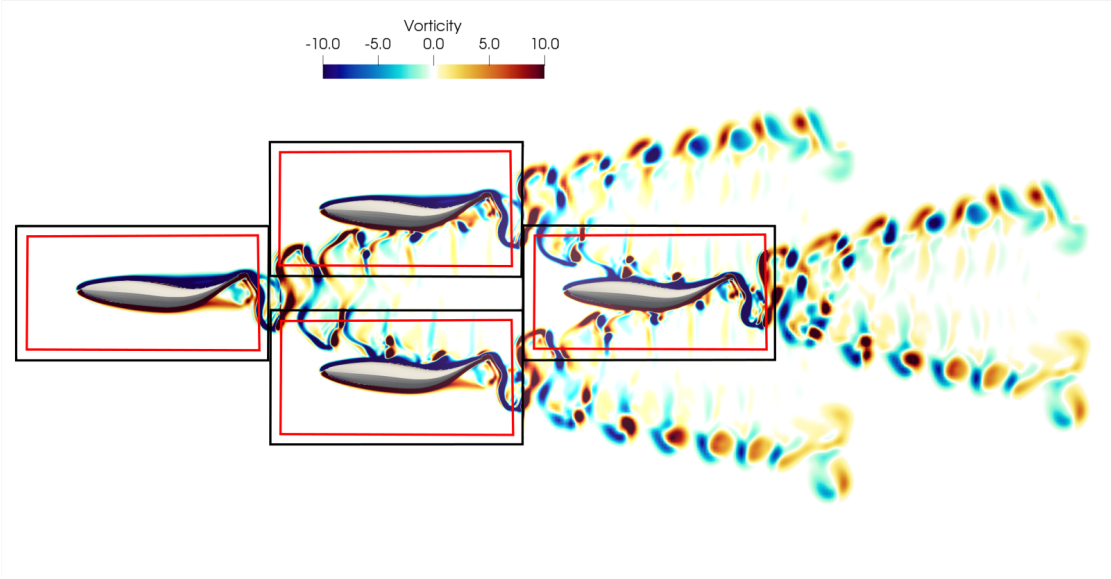

(b)

Figure 3.9: Contours of vorticity in the midplane of the four fish swimming in the diamond arrangements. a) initial position of overset grids b) position of overset grids at $t/T = 8.8$ .contour of each overset grid and background grid are consistent. vortical structures are are advected from one domain to the other. Thick black lines represent the boundaries of the overset grids and thick red lines shows the blank region.

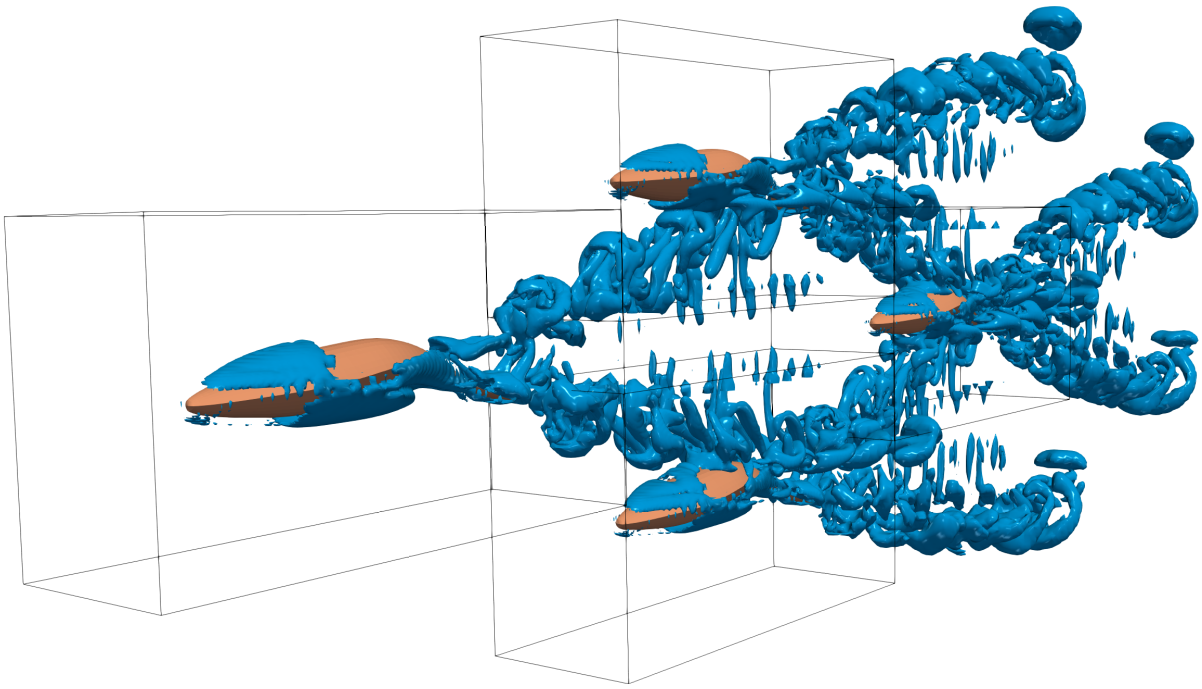

Figure 3.10: The 3D vortical structures visualized by the iso-surfaces of Q-criteria for four fish swimming in diamond arrangement.

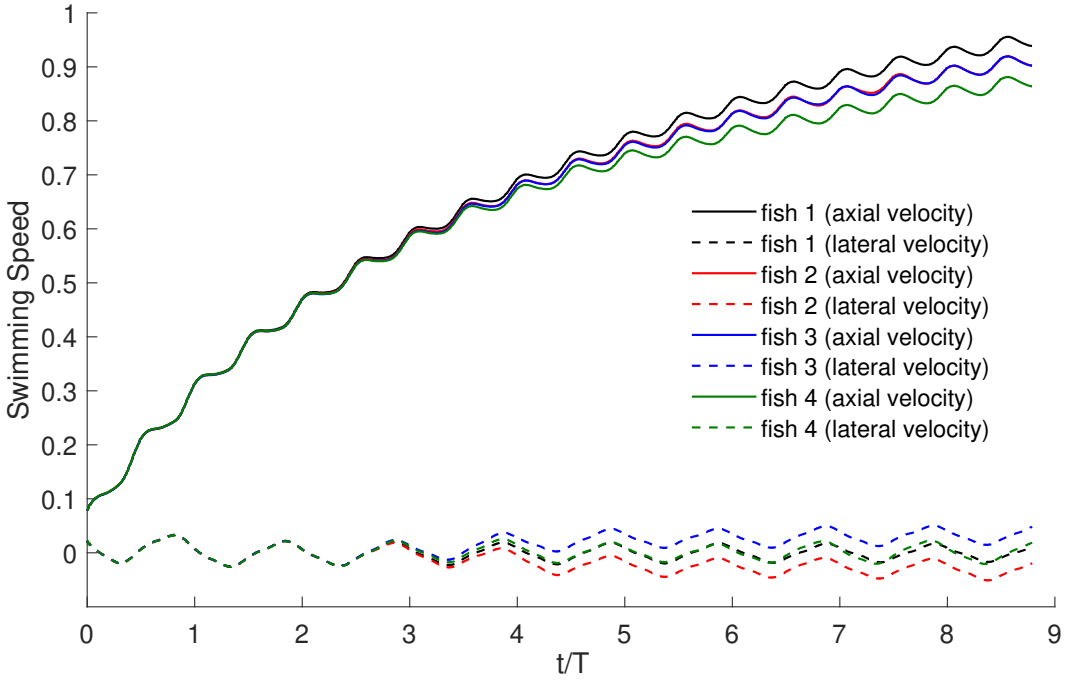

Figure 3.11: Comparison of the self-propelled fish swimming axial and lateral speed for different swimmers in diamond shape. Fish 1 to 4 are denoted in Fig. 3.9

Wall-clock time (sec)			
No. of cores	flow solver	grid assembly	interpolation
1	4053	53.2	8.9×10^{-1}
8	440.3	5.1	1.1×10^{-1}
84	41.5	0.54	2.7×10^{-2}
112	32.3	0.45	2.1×10^{-2}
140	28.1	0.40	1.8×10^{-2}
280	14.4	0.43	9.8×10^{-3}
420	11.2	0.58	7.6×10^{-3}
560	8.2	0.58	5.1×10^{-3}

Table 3.1: Wall-clock time of different parts of the CURVIB-overset solver for different number of processors

3.2 Parallel performance

In this section, the swimming simulation is used to investigate the speedup for different parts of our solver. The total number of grid points in this simulation is about 30 million grid points and approximately 1.2 million query points. The simulations are run using 560 core on Terra cluster at Texas A&M University, which contains 320 computing nodes, each node contains 2 Intel Xeon E5-2680 v4 2.40GHz 14-core each, and uses Intel Omni-Path as the cluster-interconnect. The code was compiled using MPICC compiler with $-O3$ optimization level. Table 3.1 represent the wall-clock time for the CURVIB flow solver, grid assembly task, and interpolation for 1 up to 560 cores. As can be seen from this table, the computational time required for the grid assembly is relatively very small compared to the computational time needed for the flow solver. The grid assembly time decreases for up to 140 cores while after that the time does not show a significant change. However, even using 560 the time required for the grid assembly is about 7% of the flow solver. In addition, comparing the interpolation time and the flow solver time shows the efficiency of our interpolation method, where using all number of cores, it is less than 0.1% of the flow solver time.

Figure 3.12 shows the strong scalability for wall-clock time for a different part of our overset-CURVIB solver. As can be observed our flow solver shows good speedup for the maximum number

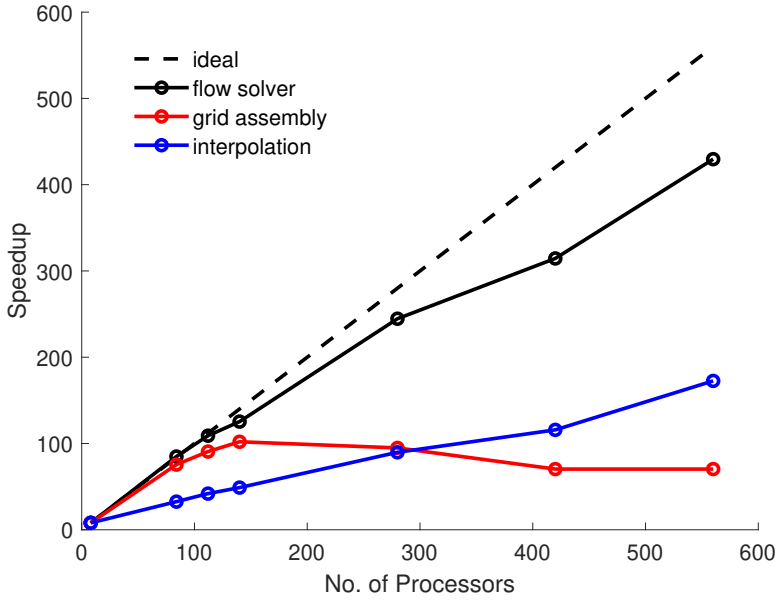

Figure 3.12: Wall-clock time speedup versus the number of processors for the fish schooling using 560 processors.

of processors used in this work (560 processors). The grid assembly kernel has a speedup close to ideal for up to 140 processors while after that the scalability drops. The reason for speedup drop-off using more than 140 processors is the load-imbalance for grid assembly method using our available grid partitioning strategy in which all the grids are distributed to all the available processors. As previously mentioned, this partitioning strategy results in the best speedup for the flow solver while it can increase the communication cost and overhead for the grid assembly. However, by comparing the time required for flow solver to the time of the grid assembly kernel (Table 3.1), optimizing the grid partitioning for flow solver is more reasonable. Using another partitioning strategy for load balancing, depending on the problem, in the future to balance the number of query points in each processor can help to improve the speedup for more processors. However, load balancing is out of the scope of this work. Finally, the speedup for interpolation is also presented in Fig. 3.12. The interpolation's speedup is not close to ideal, however, considering the small computational time required to interpolation this speedup is not unexpected.

3.3 Platelet activation framework validation and sensitivity studies

In this section, We validate our numerical simulations with the exact or closest available experiments for the hinge region, bulk flow, and platelet activation in the literature.

3.3.1 Shear-induced platelet activation in laminar Taylor-Couette flow

A rotating Couette flow with rotating inner cylinder which is similar to the Couette device used in measuring the platelet activation or blood damage is simulated using our framework by considering the inner cylinder as an immersed object and outer cylinder as the wall boundary condition. The schematic setup for this simulation is presented in Fig. 3.13. This setup can expose the platelets to uniform shear stress. The rotating Couette flow assumes to be laminar which is valid for Taylor numbers T less than the critical Taylor number, T_{cr}

$$T_{cr} = \frac{\Omega r_m (b-a)}{\nu} \tag{3.11}$$

where $r_m = (a+b)/2$, Ω is the rotational velocity of the inner cylinder, a is inner radius, b is the outer radius, and ν is the dynamic viscosity. The critical Taylor number with a narrow gap annulus and a stationary outer cylinder is 41.19. Here, a and b are assumed to be $2\ \mu m$ and $1.975\ \mu m$, respectively. Rotational velocity (Ω) can vary to generate different shear stresses and the dynamic viscosity of the fluid is assumed to be $0.01\ cP$. The exact solution for Navier-Stokes equations reduce to following equations

$$u_\theta = C_1 r + \frac{C_2}{r} \tag{3.12}$$

$$C_1 = \frac{-\Omega b^2}{b^2 - a^2} + \frac{\Omega (a^2 b^2)}{b^2 - a^2} \tag{3.13}$$

$$\tau = \mu \frac{r \partial (u_\theta / r)}{\partial r} = 2\mu \frac{\Omega a^2 b^2}{b^2 - a^2} \frac{1}{r} \tag{3.14}$$

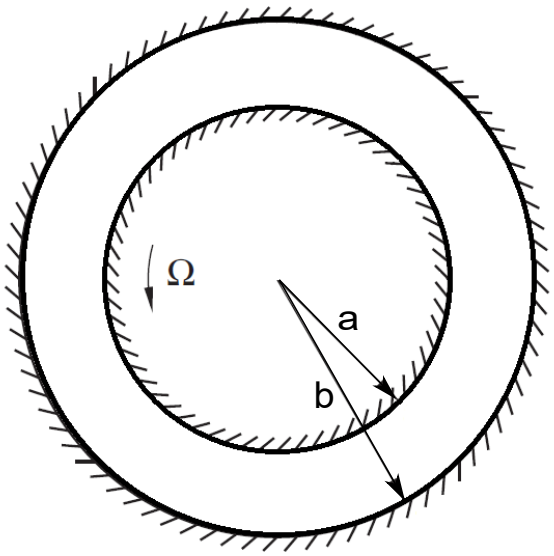

Figure 3.13: Schematic setup of rotating Couette flow which used for validation of platelet activation. Reprinted from [3].

The simulations are performed for three different shear stresses: $30\ dyne/cm^2$, $50\ dyne/cm^2$, $70\ dyne/cm^2$ which resulted from angular speed of $3.75\ rad/s$, $6.25\ rad/s$ and $8.75\ rad/s$, respectively. The predicted platelet activation by our numerical framework using the Soares model is compared to the experimental results reported by [4] in Fig. 3.14. This figure shows the evaluation of platelet activation in response to different viscous shear stresses as a result of different angular velocities in Taylor-Couette flow. In these simulations, the inner cylinder is rotating for up to $2\ mins$ which exposes the platelets to almost constant shear stress and after that, the inner cylinder stops suddenly which results in small shear stress around zero. As can be seen the results of our numerical framework matches well with the experimental observation for different shear stresses. Figure. 3.14 also shows that the Soares model accounts for the effect of platelet sensitization since even after $2\ min$ where the shear stress is zero, the PAS still increases.

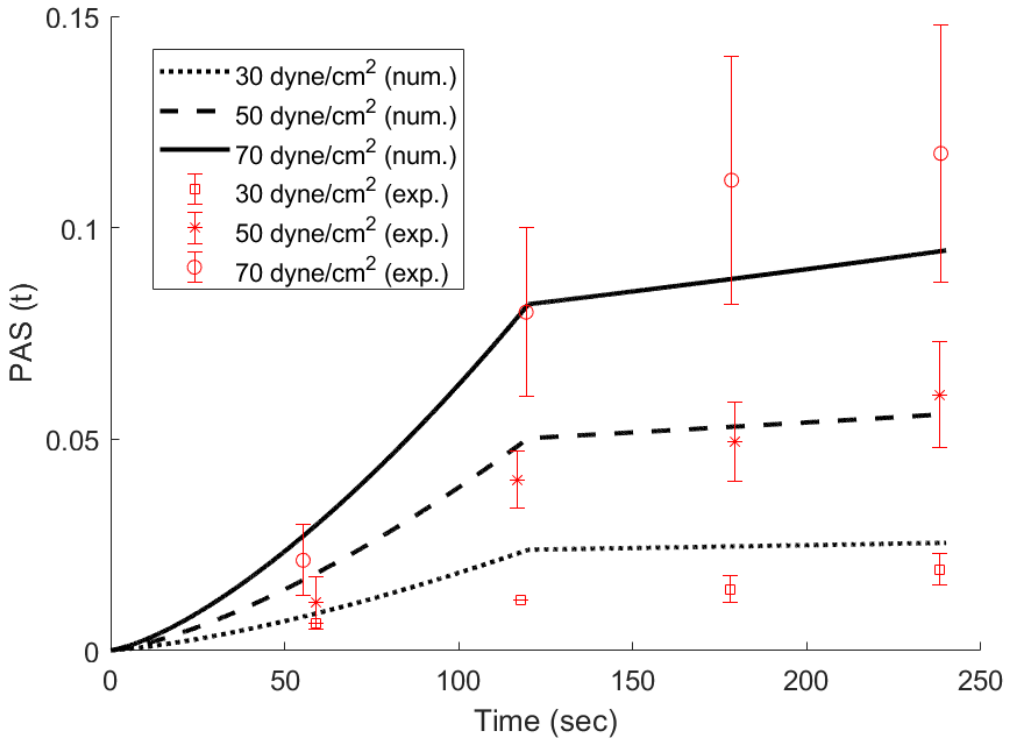

Figure 3.14: Comparison of platelet activation using our framework with the experimental results [4]. Reprinted from [3].

4. COMPARISON BETWEEN PLATELET ACTIVATION IN BILEAFLET MECHANICAL AND BIO-PROSTHETIC HEART VALVES*

The thrombus formation is initiated by the platelet activation which is thought to be mainly generated in MHVs by the flow through the hinge and the leakage flow during the diastole [25, 197]. In this chapter, we investigate the importance of the systole phase on the poor performance of BMHVs by comparing the thrombogenic performance of a MHV and a BHV (as control) in terms of shear-induced platelet activation under the same conditions. This chapter is organized as follows: Section 4.1 provides a background on the source of platelet activation in BMHVs and available methods for quantifying the platelet activation in terms of shear stress and exposure time and why a control case is needed. In Section 5.2 a brief overview of the method is provided. In Section 4.3 the platelet activation of MHV and BHV (as a control case) during systole are compared using three different models. Finally, the findings are summarized in Section 5.6.

4.1 Background

The prosthetic heart valves are far from ideal, e.g., MHVs are highly thrombogenic and require life-long anticoagulant therapy. BHVs do not require life-long anticoagulant therapy because of better hemodynamics performance but deteriorate after 10 to 15 years. There are many mechanical and chemical agonists involved in thrombus formation, but it is believed that it is initiated by the platelet activation ([198, 199]). The platelet activation in MHVs is thought to be mainly created by the non-physiologic leakage flow through the hinge and the small gap between the leaflets during diastole ([200, 201, 202, 7, 44]) because the thrombus formation typically starts from these regions [203]. However, thrombus formation does not directly translate to platelet activation. Currently, two major hypotheses are available regarding the source of platelet activation in BMHVs. First, platelets can be activated by non-physiologic shear stresses in the bulk flow and second, the high velocity and shear stress in the hinge region during the diastole phase causes the platelet acti-

*Reprinted with permission from "Platelet activation of mechanical versus bioprosthetic heart valves during systole" by M. Hedayat et al., 2017, Journal of biomechanics, 56, 111-116, Copyright 2017 by Elsevier Ltd.

vation. Therefore, understanding the underlying reason of platelet activation in BMHVs is essential to optimize the thrombogenic performance of BMHVs. The aim of this section is to investigate the importance of bulk flow during the systole phase in the platelet activation in BMHVs using the empirical models available for quantifying the platelet activation.

Several studies investigated the platelet activation in terms of shear stress and exposure time ([158, 159]). Hellum et al. [163] conducted experiments under constant shear stress and obtained a threshold based on locus of points on the shear stress and exposure time plane [182]. Later, several models were proposed based on the power-law formulation for platelet stimulation and platelet lysis ([204, 205]). Bluestein et al. [186] proposed linear level of activation formulations as an approximation for platelet activation. Alemu and Bluestein [165] developed a platelet activation model based on the previous work of Yeleswarapu et al. [166] for red blood cell damage. More recently, Nobili et al. [183], Sheriff et al. [184] and Soares et al. [4] proposed different models based on the Platelet Activation State (PAS) using modified prothrombinase method introduced by Jesty and Bluestein [206]. The PAS is the non-dimensional level of platelet activation within the interval of $[0, 1]$ in which 0 and 1 corresponds to non-activated and fully activated platelets.

Because each model of the blood damage is tuned for a specific experiment, as explained by Grigioni et al. [207] and Sheriff et al. [184], the model coefficients are not universal and change from experiment to experiment. Consequently, the absolute values for platelet activation, calculated in a simulation based on a model, depending on the model. Previous works on platelet activation of the MHVs ([202, 185, 20, 208, 209, 210]), therefore, are subjective and their results depend on the model used. To overcome this subjectivity and dependence on the model, the activation in the BHV is taken as a control in this work, i.e., the platelet activation in MHV based on a specific model is compared against the activation in the BHV based on the same model, due to the good hemodynamic performance of BHV [211]. Therefore, we compare the activation of a MHV against BHV under exactly the same initial hemodynamic and boundary conditions, i.e., against a control case for the first time. In addition, we use three different activation models to test if different models provide consistent/similar conclusions.

4.2 Method and Materials

Here, the hemodynamic performances of a MHV and a BHV are investigated in terms of shear-induced platelet activation in a Eulerian framework which is explained in section 2. The simulations are performed based on the previous flow simulations through MHVs and BHVs using strong coupling fluid-structure interaction under the same physiological condition during the systole phase of a cardiac cycle ([95, 46]). The valves have been placed in an idealized axisymmetric aorta geometry with a sudden expansion of the aortic sinus region ([46, 6]). The results of platelet activation through the MHV and BHV are compared against each other for each platelet activation model as discussed in the 4.3.

Three different platelet activation models are tested to investigate the dependence of the results on the activation models: (1) the linear level of activation which was originally developed to quantify the platelet activation under constant shear stress; (2) the damage accumulation model [165], which accounts for the transient nature of the flow and senescence but needs collaboration for each test case; and (3) the Soares model [4], which considers the effect of loading rate and sensitization for platelets under highly dynamic shear stress. The details of these models are explained in section 2.

4.3 Results and Discussion

The results of platelet activation using a linear level of activation in the MHV and BHV are presented in Fig. 4.1 for various time instants within the systole phase. Fig. 4.2 and 4.3 show the results for the platelet activation using damage accumulation [165] and Soares [4] models, respectively. The background level of 1% is used for the Soares model since it requires a non-zero initial activation level. However, for the rest of the simulations, this value is assumed to be zero. Although there are some differences in the prediction of platelet activation using different models, all the models show that the platelet activation for the MHV is considerably higher than the BHV after peak systole near the leaflets and in the sinus area (Figs. 4.1-4.3 (c) and (d)).

The integration of platelet activation in the whole domain (Eq. 2.34) with different activation

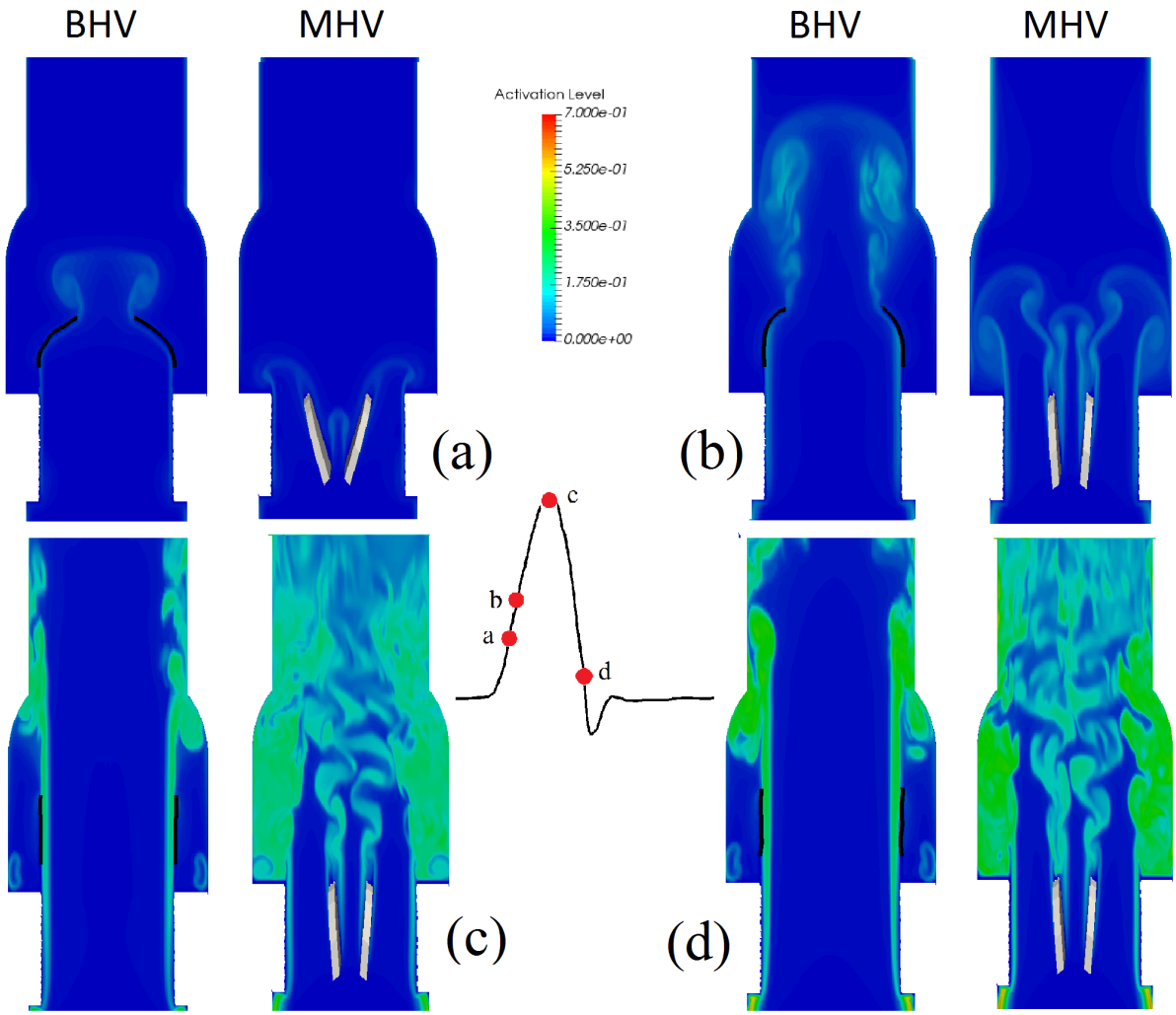

Figure 4.1: Platelet activation for the MHV and BHV in a straight aorta during the systole phase using the linear level of activation model at time t=(a) 52, (b) 93, (c) 200, and (d) 273 ms within the cardiac cycle. Reprinted from [5].

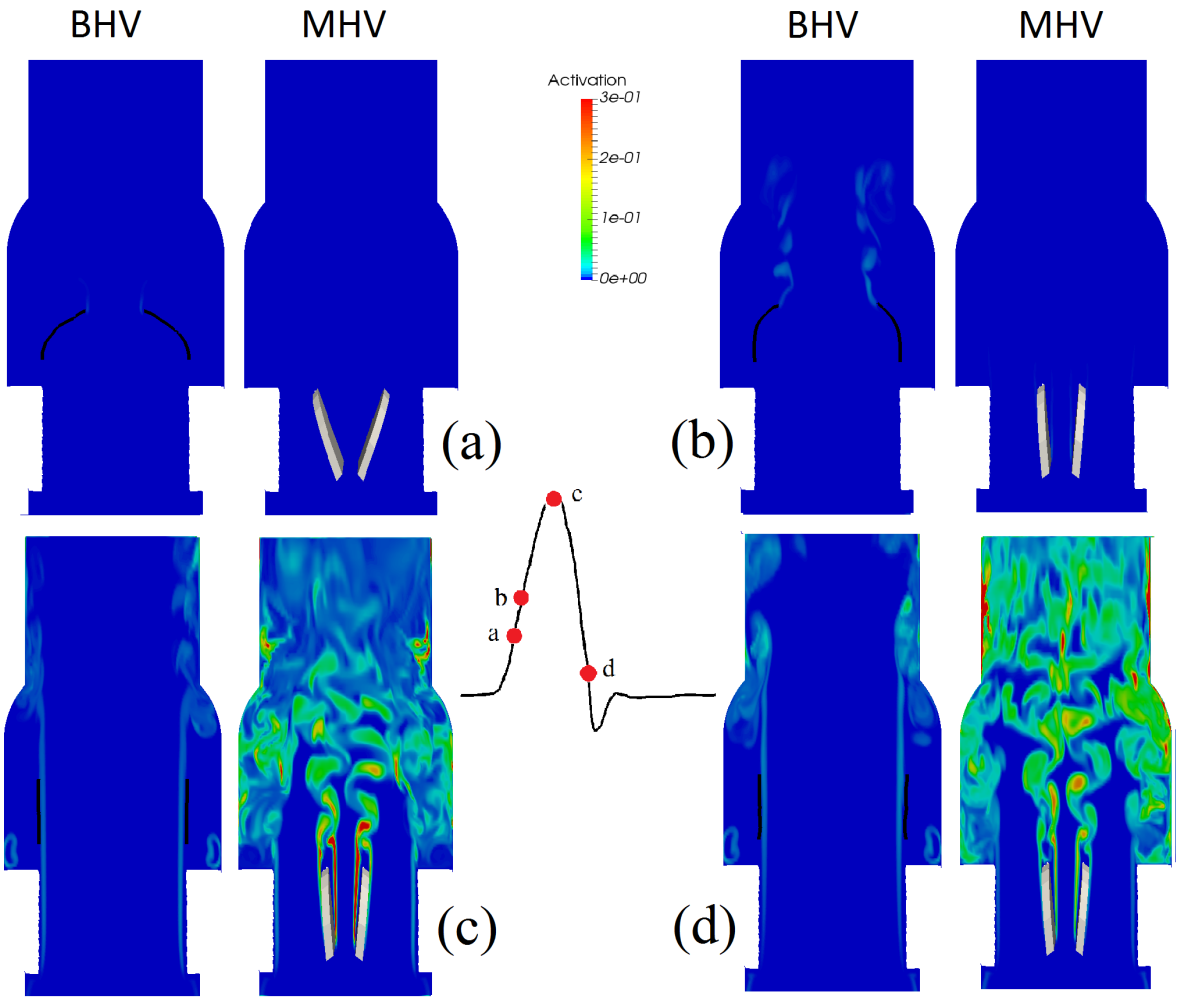

Figure 4.2: Platelet activation for the MHV and BHV in a straight aorta during the systole phase using the damage accumulation model at time t=(a) 52, (b) 93, (c) 200, and (d) 273 ms within a cardiac cycle. Reprinted from [5].

models for both the BHV and MHV is shown in Fig. 4.4. The platelet activations of the MHV and BHV for each model are normalized by the total platelet activation in the BHV at the end of systole (the normalized BHV activation is 1 at the end of the systole regardless of the activation model used). As it can be observed in this figure, the total platelet activation by the linear level of activation in the MHV at the end of the systole is 1.41 times more than the BHV. This ratio is 5.12 and 2.81 for the damage accumulation and Soares models, respectively.

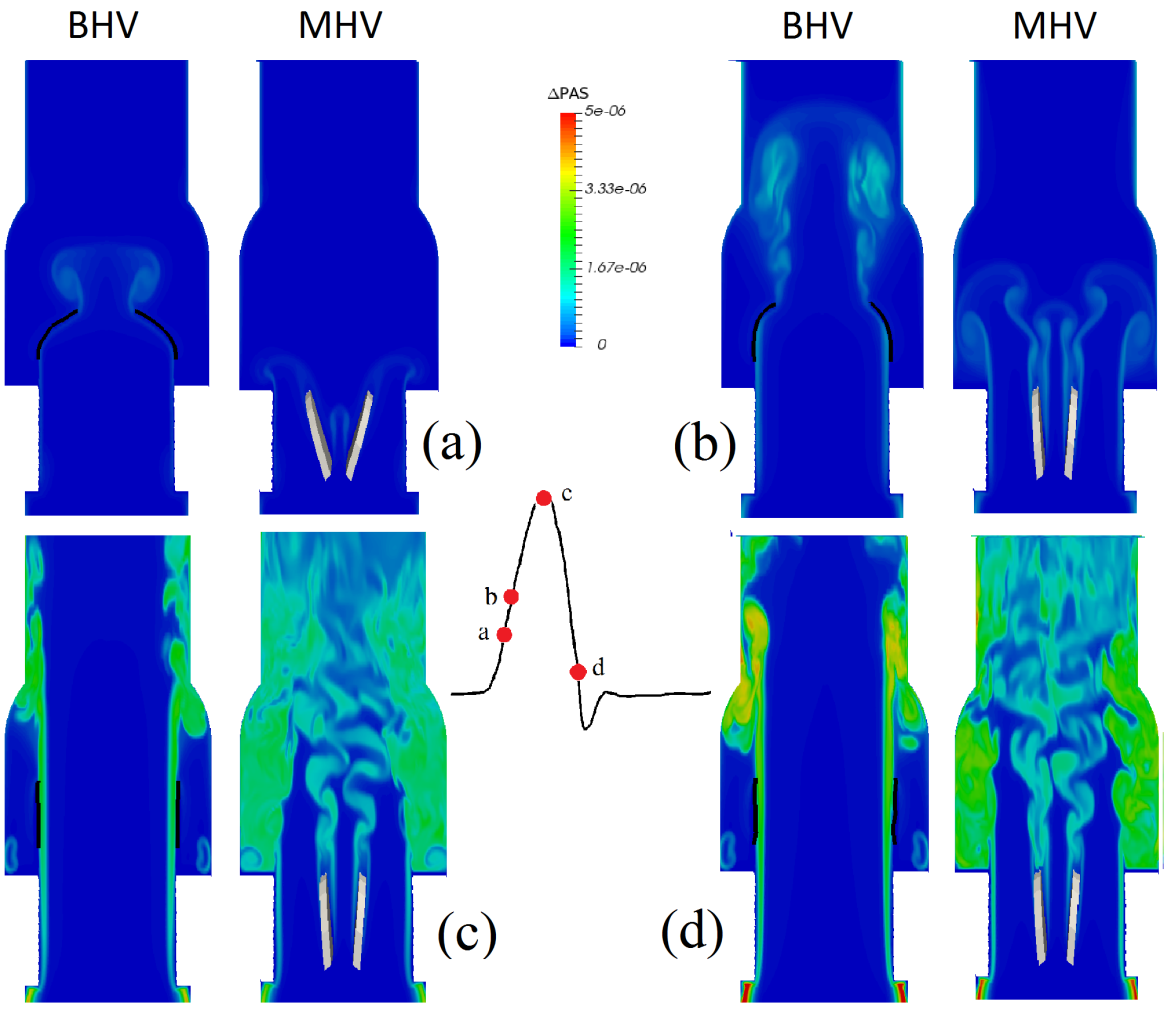

Figure 4.3: Platelet activation (ΔPAS) for the MHV and BHV in a straight aorta during the systole phase using Soares model at time t=(a) 52, (b) 93, (c) 200, and (d) 273 ms within a cardiac cycle. Reprinted from [5].

The difference in the above ratios is due to the difference in the activation models, which are developed using different assays under different experimental conditions. The linear level of activation model shows the smallest ratio among all activation models. As it has been previously discussed ([4, 184, 164]), this model may not be adequate for predicting the activation under highly dynamic stress condition since it does not address the transient nature of the flow, which can have a significant effect on platelet activation ([184, 212]). The damage accumulation model [165] accounts for the damage history and the transient nature of the flow and shows the highest activation rate among all models. It might be due to the fact that although this model shows good agreement with experiments for red blood cell damage under constant shear stress [166], in order to use it for platelet activation it needs empirical calibration of several coefficients [165]. Based on the results, while the linear level of activation underestimates and damage accumulation overestimates the platelet activation in the MHV in comparison to the BHV (due to their limitations), the Soares model seems to be the most adequate model to compare the thrombogenic performance of these prosthetics heart valves.

The above differences, notwithstanding, Fig. 4.4 shows that the activation in MHV is several folds higher than the BHV for all tested models. Platelet activation mainly depends on stress history, the shear stress (including loading rate for models considering the effect of dynamic shear) and the time of exposure to shear stress. To explain why platelet activation in MHV is several folds higher than BHV, here we focus on platelet activation due to the shear stress and the time of exposure. We start by the scalar shear stress generated in the MHV and BHV which is shown in Fig. 4.5 for different time instants. As it can be observed in Fig. 4.5, the flow field in the MHV is considerably different from the BHV. In the MHV the platelets are activated mainly due to shear layers of three jet structures (two side jets between the leaflets and the valve's housing and a central jet between the leaflets). Nevertheless, since there are no side jets in BHV, the platelets are activated by the central jet. As previously discussed in ([95, 6]), during the beginning of the systole phase, the vortical structures are well organized in the MHV. In contrast, the shear layer in the BHV becomes unstable sooner than MHV due to slower opening [46]. This results in the

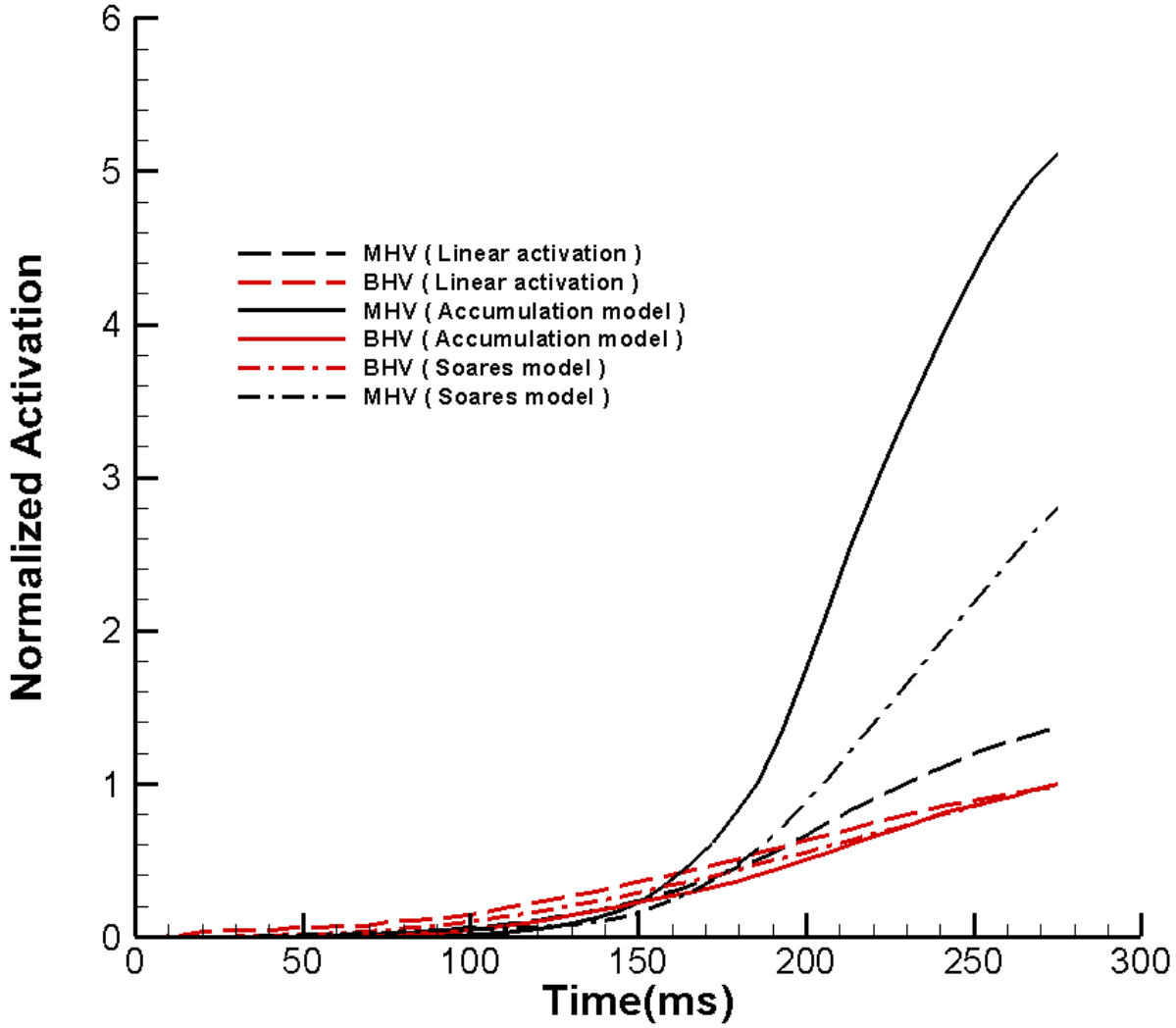

Figure 4.4: The Integration of platelet activation over the whole domain for a MHV and BHV in a straight aorta during the systole phase using different models (the normalized BHV activation is 1 at the end of the systole regardless of the activation model used). Reprinted from [5].

breakdown of the threefold symmetry in the BHV at the beginning of the systole, while the flow is still organized in MHV [95]. This flow pattern can create regions of high shear stress near the BHV at early systole. Therefore, platelet activation in the BHV is slightly higher by 10% in comparison to the MHV at the beginning of the systole. This trend is reversed just before the peak systole ($t \approx 0.175s$ in Fig. 4.4). This is because the vortical structures in the MHV break down into small-scale disorganized vortices just before peak systole (as seen in the previous simulations [46] and experiments [6], whereas no vortex breakdown is happening in the BHV. Such flow pattern generates high shear stress regions that activate platelets near the valve and sinus area for the MHV, whereas almost no shear stress, and consequently very small activation is produced in these areas for the BHV.

In addition to the differences between shear stress applied on platelets, the exposure time of platelets to the elevated shear stress in the BHV and MHV are different. Platelets can be entrapped in the wake and recirculation regions produced near the leaflets and the sinus area in the MHV (Figs. 4.1-4.3 (c) and (d)). These platelets undergo elevated shear stress along with high exposure time which increases the risk of free emboli formation and eventually the clot formation in the MHVs [213]. In contrast, since there is no side jets and the shear layer of the central jet is far from the sinus area, almost no shear stress and circulation zones are generated near the leaflets and housing in the BHV. Hence, the platelets are exposed to elevated shear stresses only during early systole because the platelets are washed away from the valve area to the low shear stress region for the rest of the systole phase. Therefore, the platelets passing through the BHV experience the short exposure time to elevated shear stress in comparison to the MHV.

4.4 Comparison to previous work

The platelet activation thresholds proposed for the linear level of activation model based on the work by Hellums et al. [163] is $35\ dyne.s/cm^2$ and higher thresholds have been proposed based on the in vitro experiments ([158, 214]). The absolute value of activation using the linear level of activation during the systole phase for one cardiac cycle is shown in Fig. 1 in the paper. Other papers have reported almost the same maximum value for linear level of activation ($\approx 0.7(dyne.s/cm^2)$)

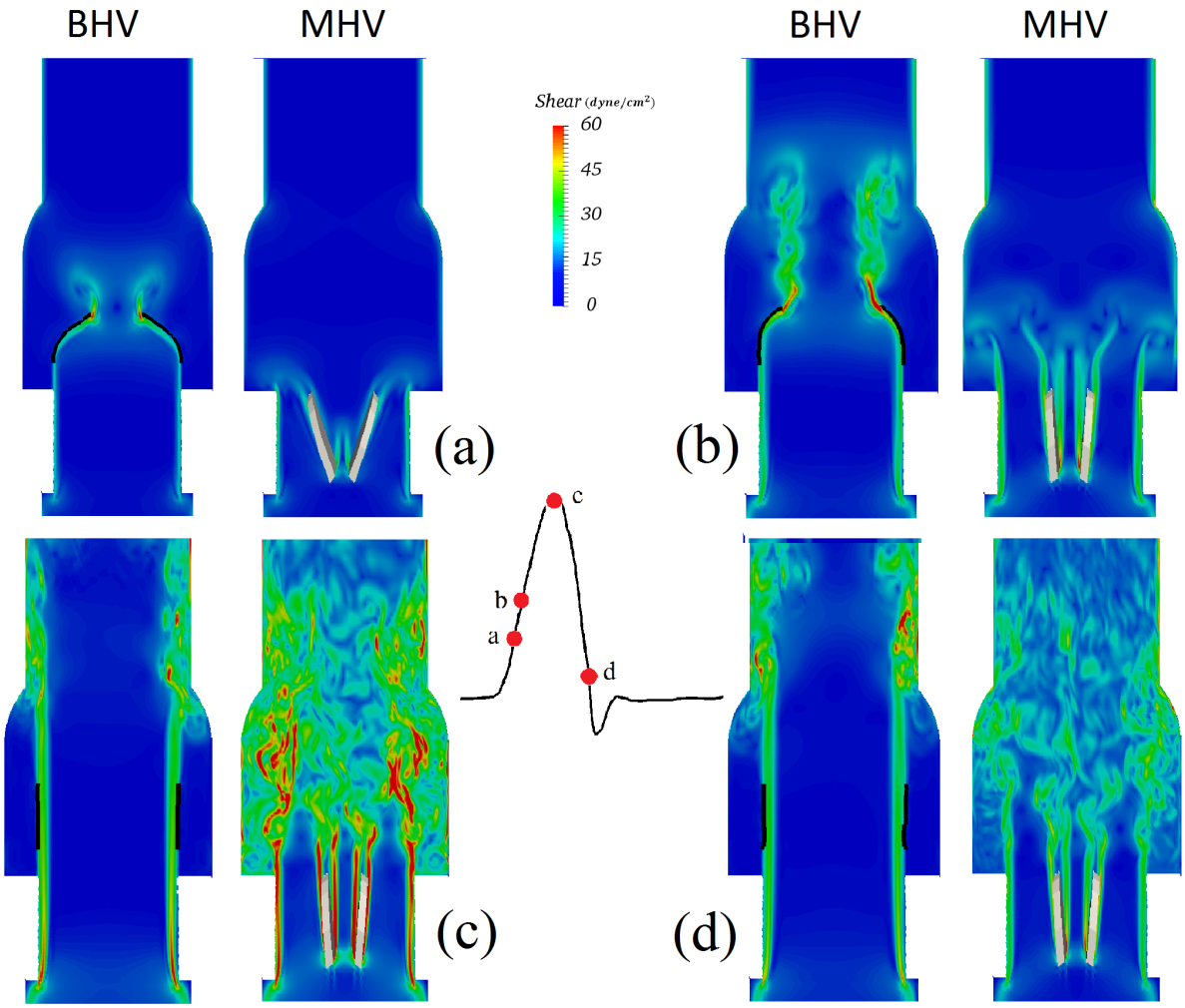

Figure 4.5: The scalar viscous shear stress for the MHV and BHV in a straight aorta during the systole phase at time t=(a) 52, (b) 93, (c) 200, and (d) 273 ms within a cardiac cycle. Reprinted from [5].

in MHV [215]).

Fig. 3 in the paper, shows the absolute value of newly platelet activation (ΔPAS) during the systole phase for one cardiac cycle which is in the range of the activation in previous work by morbiducci et al. [20]. Previous in vitro experiments by Yin et al. ([216, 217]) reported the platelet activation rate (the slope of the thrombin generation in the PAS assay) of $6 \times 10^{-4}/min$ and $8.114 \times 10^{-4}/min$ for a $27mm$ St. Jude Medical bileaflet and a $27mm$ Carbomedics bileaflet mechanical heart valve, respectively. Yin et al. [217] also measured platelet activation rate of $1.2 \times 10^{-3}/min$ for a $21mm$ St. Jude porcine bioprosthetic tissue valve. In our simulation, the platelet activation rate using Soares et al. model for the MHV and BHV was $1.33 \times 10^{-3}/min$ and $4.73 \times 10^{-4}/min$, respectively. The difference in the platelet activation rate in this study with the in vitro measurements might be due to the differences in the size of the valves (the orifice area) used in our study in comparison to the previous in vitro measurements. In addition, the in vivo measurements by Yin et al. [218] also showed that MHVs increase the risk of thromboembolism in comparison to native heart valves which is in accordance with our results.

4.5 Summary

The platelet activation in the MHVs can be due to non-physiological flow during the systole phase, the flow through the hinge, the leakage flow during diastole, or maybe a combination of all. Most of the previous studies have investigated the high shear stress through the hinge region during the diastole phase as the primary cause of the platelet activation in the MHVs ([200, 201, 202, 7, 44]). Although several studies have been conducted to investigate the platelet activation during the systole phase ([20, 210, 165, 219]), none of them compared the activation against a control case to show the significance of the systole phase in platelet activation. Our results indicate that the role of the systole phase in the activation of platelets is considerable. In fact, our results show that while at the beginning of the systole phase the activation for the BHV is slightly higher than the MHV, the activation in the MHV is several folds higher at the end of the systole phase. This is because the organized flow in the MHV breaks into small vortical structures right before peak systole, and stay within the sinus region until the next cycle. In contrast, the flow in the BHV becomes unstable

earlier than the MHV in the mid-acceleration phase, but the vortices do not stay in the sinus region after the peak systole because they are washed away by the strong jet flow through the BHV. As a consequence, platelets undergo higher shear stress and exposure time in a MHV relative to a BHV during the systole phase. Our results using different activation models are consistent and show the same trend.

5. COMPARISON OF PLATELET ACTIVATION THROUGH HINGE VS BULK FLOW IN BILEAFLET MECHANICAL HEART VALVES*

Bileaflet mechanical heart valves (BMHVs) are prone to thromboembolic complications which are believed to be initiated by platelet activation. Platelets are activated by non-physiologic shear stresses in the bulk flow or the leakage/hinge flow, whose contributions have yet to be quantified. Here, the contribution of bulk and hinge flow to the activation of platelets in BMHVs is quantified for the first time by performing simulations of the flow through a BMHV and resolving the hinge by overset grids (one grid for the bulk flow and two for the hinge regions coupled together using one-way and two-way interpolation). The section is organized as follows: in section 5.1 a background about the available hypothesis about the platelet activation in BMHVs and a literature review about the efforts have been made to address this issue is presented. Section 5.2 provides the detail of the computational setup, overset grids, and the numerical methods that have been used in this study. Section 5.3.1 investigates the effect of the interpolation method (one-way or two-way) on the numerical results. The effect of the hinge gap size on the flow velocity and the maximum shear stress through the hinge is discussed in section 5.3.2. The comparison of platelet activation which is generated through the bulk flow and hinge region is presented in section 5.3.3. Later, the validation and sensitivity studies are presented in section 5.4.2. Finally, the conclusion is discussed in section 5.6.

5.1 Background

It is believed that thrombus formation is initiated by platelet activation due to the non-physiological flow field and consequently elevated shear stress generated in BMHVs. This non-physiological flow is either generated by the hinge/leakage flow or the disorganized bulk flow by the leaflets/housing of BMHVs. Nevertheless, the contribution of hinge/leakage and bulk flows to platelet activation

*Reprinted with permission from "Comparison of platelet activation through hinge vs bulk flow in bileaflet mechanical heart valves" by M. Hedayat and I. Borazjani, 2019, Journal of biomechanics, 83, 280-290, Copyright 2019 by Elsevier Ltd.

has yet to be quantified.

The importance of hinge design in BMHVs was first noticed because of the high thrombus formation rate in the Medtronic Parallel BMHVs [201]. Since then several in vitro experiments have been conducted to characterize the flow and address the thromboembolic potentials in BMHVs ([202, 220, 221, 222, 223, 7, 25, 224, 225]). Travis et al. [226] and fallon et al. [227] showed considerable difference in change or markers of platelet damage for different gap sizes. Leo et al. [220] reported the gap size has a significant effect on the Reynolds shear stress (RSS) and strength of the leakage jet. In addition, they found that the regular gap size is less prone to thrombus formation in comparison to smaller or larger ones. Jun et al. [7] showed that the gap size has a significant influence on shear stress and washout potential of BMHVs. However, due to the small temporal and spatial scales and complex nature of the flow in the hinge region, these experiments provided limited information on the flow field in this region.

To compensate for the above shortcomings and obtain further understanding of the flow field and platelet activation in the hinge region, numerical simulations have been performed ([215, 228, 210, 229]). Simon et al. [200] investigated the importance of gap size on the flow field (washout ability and shear stress) in BMHVs. Later, Simon et al. [185] compared the thrombogenic performance (in terms of red blood cell damage) of three different hinge designs using one-way interpolation of velocities form a large scale simulation [46]. Yun et al. [56] extended the work by Simon et al. [185] to model the platelets more realistically using a particle-based method. Although these simulations provided a better understanding of the thromboembolic potential in the hinge region, they were focused on the hinge flow and did not compare the activation with the one from the bulk flow.

Several studies addressed the importance of the systole phase on blood damage and platelet activation ([230, 165, 20, 219, 210]). These papers showed that the wake and vortical structures generated near the BMHV leaflets and housing can expose blood elements to dynamic and elevated shear stress. However, the activation in systole was not compared against a control case to show its significance. Hedayat et al. [5] showed that the activation by the bulk flow in BMHVs during

systole is significant (several folds higher) relative to a bio-prosthetic heart valve as the control, but it was not compared against the activation by the hinge/leakage flow during diastole. Lamson et al. [231] compared red blood cell damage (hemolysis) in an MHV during different phases of a cardiac cycle by running forward flow through an open valve and backward flow through a closed valve. They found the contribution of backward flow to hemolysis to be comparable with that of the forward flow. However, hemolysis does not directly translate to platelet activation ([216, 157]). [44] and later Xenos et al. [208] evaluated platelet activation through two different BMHVs using the linear activation model during the systole and regurgitation flow phase by releasing particles separately in systole and diastole. None of them explicitly compared the total amount of platelet activation in each phase, but their results imply that the mean value of activation for platelet released during the forward phase is higher than the diastole. Nevertheless, the hinge area was not resolved in these simulations and the gap region was simulated by scaling down the valve geometry [44, 208].

In this chapter, we address the open question of whether the bulk of the hinge flow plays a more important role in the poor thrombogenic performance of BMHVs in terms of shear-induced platelet activation using a well-validated numerical framework (section 5.2). Shear-induced platelet activation is quantified using two well established activation models, i.e., the linear level of activation [186] and Soares models [4], to show the consistency of the results to different activation models (section 5.2). In order to address this multi-scale (aortic diameter $\approx$ $25.4\ mm$ vs. the hinge gap $\approx$ $150\ \mu m$) problem during the whole cardiac cycle, an overset grid (one grid for the bulk flow and two grids for the hinge regions) method is used. The significance of using two-way over one-way (which was the main strategy in previous works) coupling interpolation for the boundary condition for the hinge domain in an overset method is investigated (section 5.3.1). In addition, the effect of hinge gap width on the hemodynamic performance of hinge geometry and the platelet activation in MHVs is tested for two different gap sizes (250 and $150\ \mu m$) (section 5.3.2). Finally, the platelet activation in the bulk flow domain and the hinge region are quantified and compared in section 5.3.3. In the end, the conclusion and limitations are stated.

5.2 Methods and Materials

An overset method ([1]) is used to provide a high spatial resolution (with the grid size of $15\mu m$ in the hinge recess) near the hinge regions (Fig. 5.1). The boundary conditions on overset grid boundaries are obtained using both two-way and one-way coupling interpolation. In one-way interpolation, the boundary conditions of the hinge domains are interpolated form the velocities in the large-scale simulation ([46]) but the flow in the hinge domain does not affect the flow in the large-scale domain. In two-way interpolation, the boundary conditions in the hinge domains are interpolated from the large-scale domain while the region close to the hinge and leaflet gaps is blanked in the large-scale domain (Fig. 5.1) (this region is not solved in the large-scale domain but is solved in the hinge domain). The velocities for this blank region are interpolated from the hinge domains and given to the large-scale domain as boundary conditions.

The valves are placed as an immersed boundary in an idealized axisymmetric aorta geometry under a physiological flow condition ([46, 6, 7]). The hinge geometry is modeled approximately based on a $23\ mm$ St. Jude Medical BMHV. The model has two semicircular leaflet ears which pivot in butterfly-shaped hinge recesses (Fig. 5.1). Two gap sizes of $250\ \mu m$ (large gap) and $150\ \mu m$ (regular gap) are used in this study for the hinge region while the b-datum gap is kept constant ($200\mu m$) in all simulations. In addition, the gap between valve leaflets and housing is neglected in this study. The placement and the angle of leaflets and housing are exactly the same as previous bulk-flow simulations [46] and experiments [6, 7]. The simulations are carried out for one cycle and validated against experimental results.

5.2.1 Platelet activation

Because each model of platelet activation is tuned for a specific experiment, as explained by Grigioni et al. [207] and sheriff et al. [184], the model coefficients are not universal and change from experiment to experiment. To make sure that the conclusions are independent of the model, two activation models (the linear activation [186] and Soares model [4]) are used in this work. The linear activation model is simple and widely used but does not consider dynamic shear.

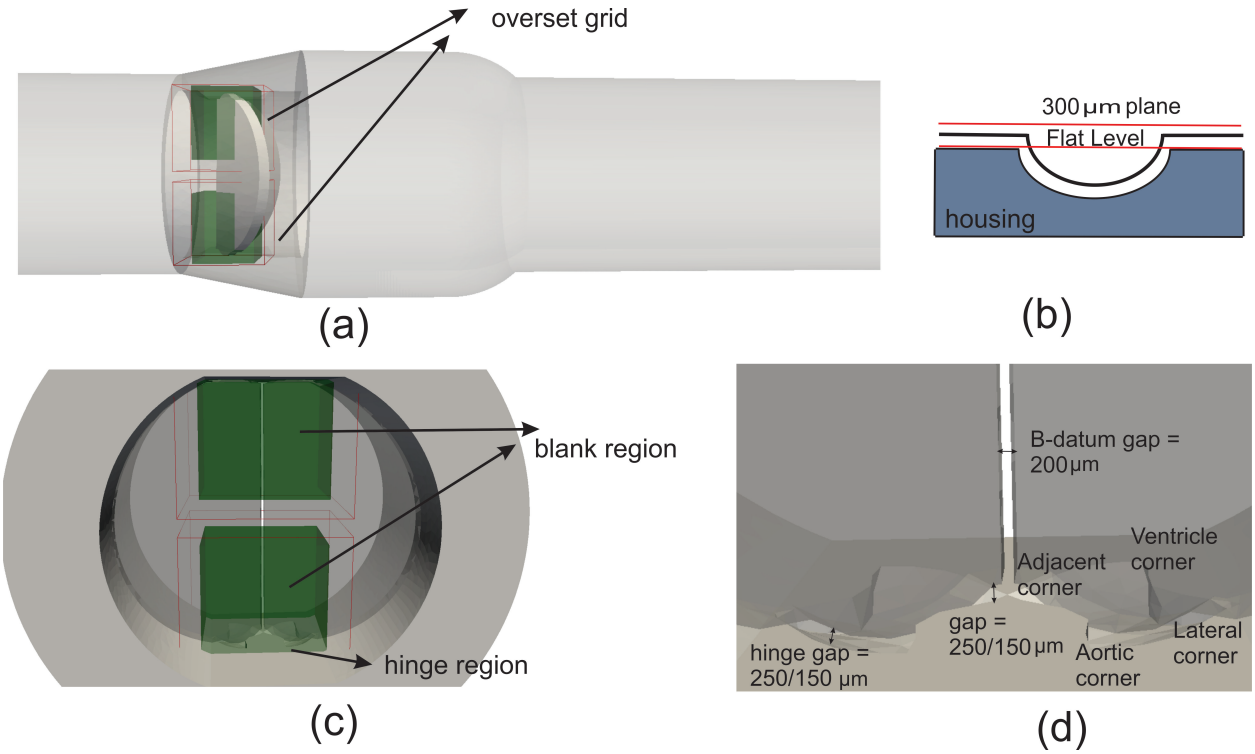

Figure 5.1: (a) large scale domain for over-set numerical simulation (b) flat level is chosen as the plane of reference (c) position of hinge domains and blank regions relative to hinge recess (d) hinge model with butterfly hinge recess. Reprinted from [3].

Soares model [4], which is based on the Platelet Activation State (PAS) [206] for dynamic shear stress ([183, 184, 4]), accounts for the transient nature of flow as well as loading rate and sensitization on platelet activation.

In this work a Eulerian framework [5] is utilized which considers activation as a continuum quantity. Since the Soares model requires a non-zero initial activation level, a background level of 1% is used for this model.

5.3 Results and Discussion

In section 5.3.1, the influence of the interpolation method (one-way and two-way coupling) is investigated on the numerical results compared to the experimental ones. In section 5.3.2, the effect of the hinge gap size is investigated on the flow characteristics and platelet activation in the hinge region. Finally, the platelet activation in the bulk flow is compared to the activation in the smaller hinge gap size ($150\ \mu m$) using Soares and linear level of activation models (section 5.3.3). The flat level (the plane where the semicircular hinge recess reaches the flat surface of housing) as well as the plane $300\ \mu m$ above it for the hinge domain (Fig. 5.1), and mid-plane normal to $x - axis$ for the bulk flow are selected to visualize the results similar to previous experiments ([222, 7]). Since both activation models show the same trend, only the results of the Soares model are shown here.

5.3.1 The interpolation method and comparison with experiments

Considering the small gap size of the hinge region and due to limitations in currently available computational resources, using an overset grid (larger grid size for bulk flow and smaller mesh size for near the hinge region) seems inevitable (to keep good spatial and temporal resolutions) to perform a simulation through BMHVs in order to simultaneously capture the large and small-scale flow features. In previous works ([56, 185, 200]), some simplifications were assumed for obtaining the boundary conditions of the domains near the hinge region. They extracted the velocity boundary conditions of small domains using one-way coupling interpolation from a large scale simulation [46] during the systole phase; while, for the diastole phase, they used a plug flow in a way to assure the pressure gradient of $80\ mmHg$ across the valves at mid-diastole. As will be

shown later, the one-way coupling interpolation for velocities can lead to acceptable results during the systole phase. However, due to the disorganized nature of the flow during the diastole phase assuming a plug backflow for the hinge domain is not that realistic.

Our results show that during the systole phase the scalar shear profile (Fig. 5.2 and Fig. 5.3) and the maximum magnitude of velocities on the flat plane (Fig. 5.4) are almost the same for both interpolations. However, the difference in velocity magnitude (through the hinge) due to interpolation is clearly visible during the diastole phase (Fig. 5.5-a and Fig. 5.5-c). Using one-way interpolation, at the mid-diastole the maximum velocity reaches $4.8\ m/s$ and $3.6\ m/s$ on the flat and $300\ \mu m$ planes, respectively, in $150\ \mu m$ hinge gap size. While using two-way interpolation, the maximum velocities of $2.4\ m/s$ and $2.8\ m/s$ are observed on the flat and $300\ \mu m$ planes, respectively. The shear stress also changes drastically with the choice of interpolation during diastole. Figure 5.2-a shows the maximum shear stress observed using one-way interpolation is approximately two times higher than two-way interpolation (Fig .5.3-a). Although the results of one-way interpolation (both maximum magnitude and glyph of velocity) are more close to the results of previous numerical simulations by Simon et al. [200], the maximum velocity ($4.8\ m/s$) is very different from the maximum velocity observed in experiments by Simon et al. [222] and Simon et al. [7] which is from $1.67\ m/s$ to $3.1\ m/s$ for different gap sizes. However, using two-way interpolation the maximum ($2.8\ m/s$) and the velocity vectors are more close to the results of the above experiments (see Fig.8 of [7] and also Table 5.1).

Similarly, one-way interpolation overestimates the maximum shear stress (Table 5.1) and obviously the flux through the hinge region which can drastically affect the prediction of platelet activation in BMHVs. Figure 5.6 compares the total activation, defined as the total amount of activation generated in the domain which is computed by the sum (integral) of platelet activation in the domain generated by the hinge region and b-datum gap during a cardiac cycle using Soares and linear models. The activation values in the figure are normalized by the total activation of the bulk flow at the end of the cardiac cycle in the bulk flow.

As was mentioned during the systole phase the one-way interpolation provides reasonable re-

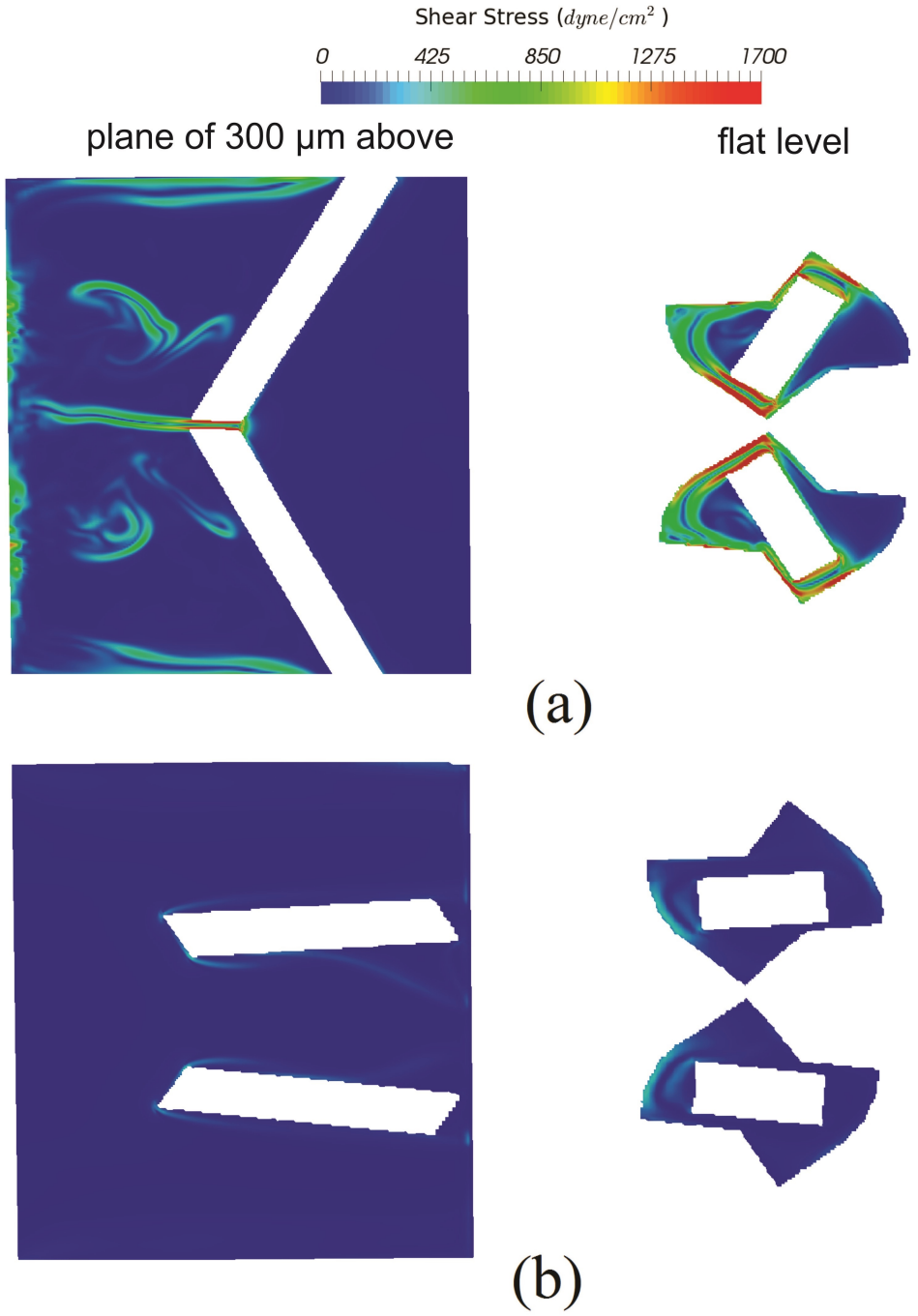

Figure 5.2: Scalar shear stress for hinge domain using one-way interpolation for gap size of $150\ \mu m$ for different plane of view (a) mid-diastole and (b) systole. Reprinted from [3].

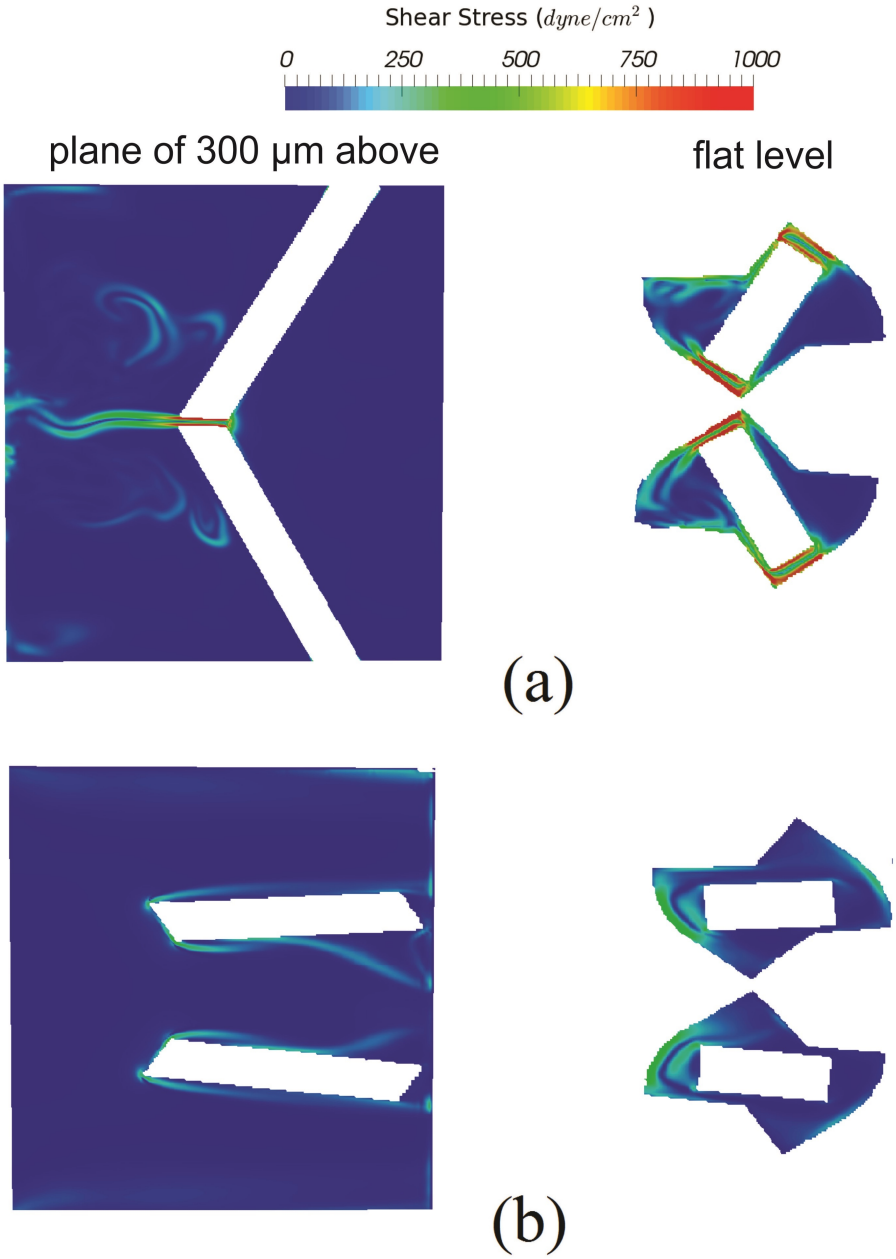

Figure 5.3: Scalar shear stress for hinge domain using two-way interpolation for gap size of $150\ \mu m$ for different plane of view (a) mid-diastole and (b) systole. Reprinted from [3].

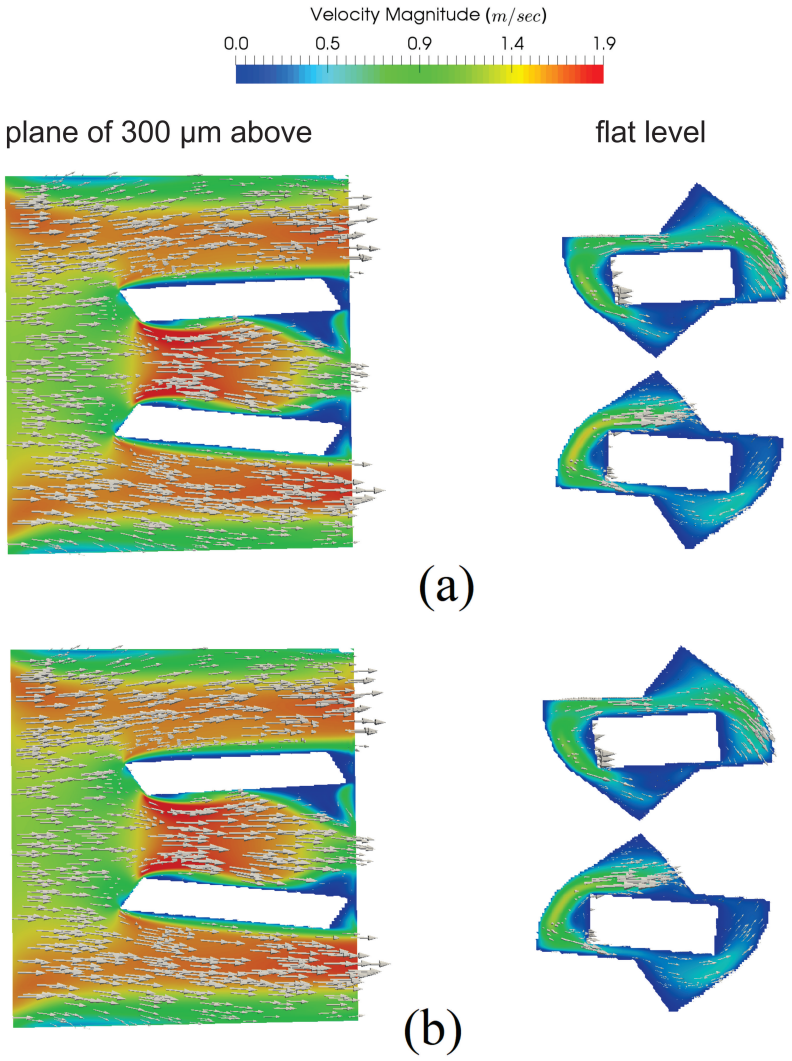

Figure 5.4: Velocity contours and vectors in the hinge domain with different interpolation methods at peak systole for the flat level and the plane of 300 μm using (a) one-way interpolation and (b) two-way interpolations. Reprinted from [3].

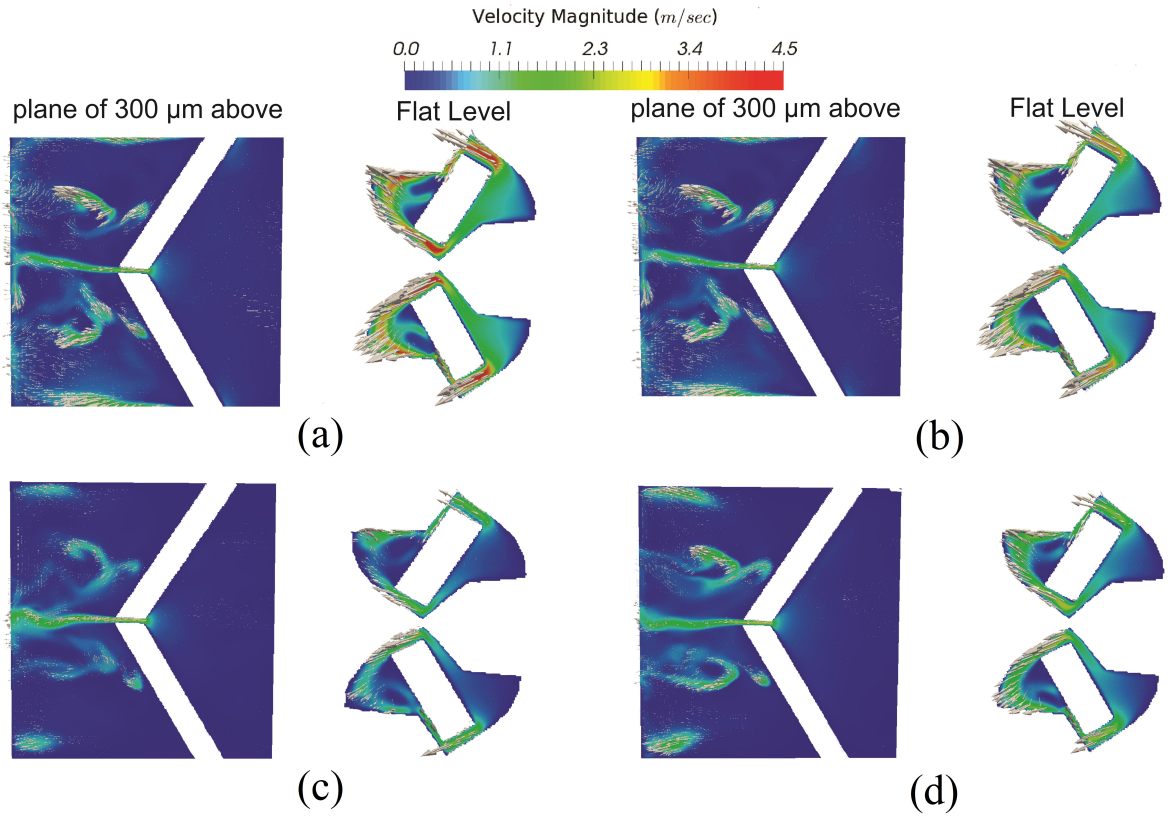

Figure 5.5: Velocity contour and vectors for hinge domain at mid-diastole for different plane of view (a) one-way interpolation gap size of 150 μm (b) one-way interpolation gap size of 250 μm (c) two-way interpolation gap size of 150 μm (d) two-way interpolation gap size of 250 μm. Reprinted from [3].

Table 5.1: Comparison of velocity and viscous shear stress at mid diastole using different interpolation methods for current study to the previous experiments for 23mm St. Jude Medical mechanical heart valve. Reprinted from [3].

Source	method	Gap (μm)	Plane (μm)	Max velocity (m/s)	Max shear stress ($dyne/cm^2$)
simon et al. [222]		100	flat	1.75	-
		100	390	2.27	-
jun et al. [7]		100	flat	2.57	> 300
		100	390	2.52	> 300
		200	flat	2.26	> 300
		200	390	2.91	> 300
jun et al. [25]		clinical	flat	2.62	≈ 600
		clinical	390	3.24	≈ 600
Current study	two-way	150	flat	2.38	1120
		150	300	2.85	1260
		250	flat	2.65	1170
		250	300	2.78	1230
	one-way	150	flat	4.83	1840
		150	300	2.63	1120
		250	flat	3.9	1560
		250	300	2.71	1130

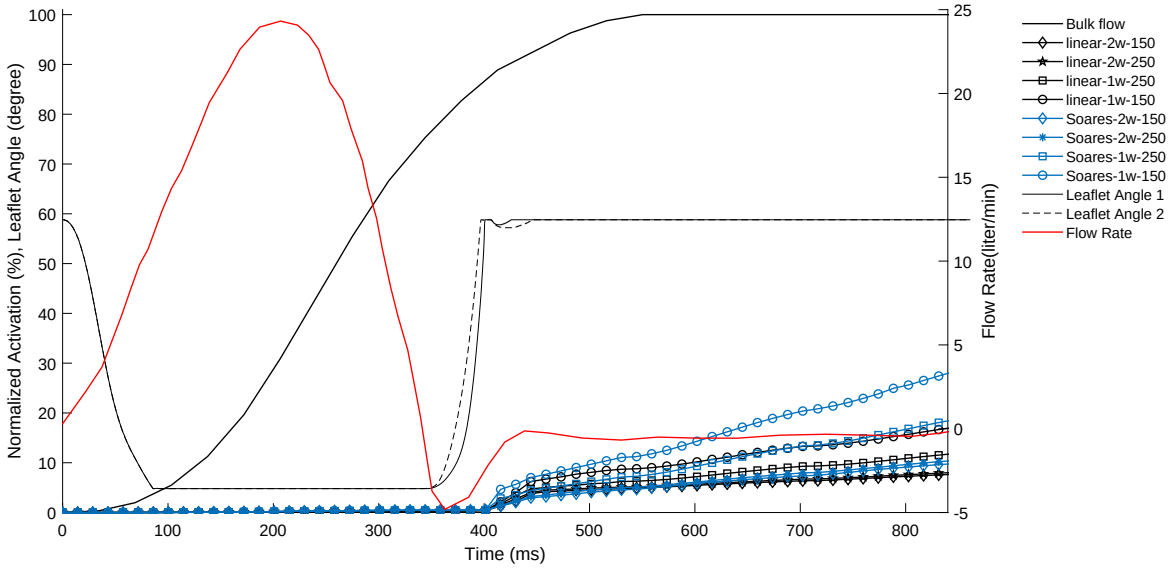

Figure 5.6: Comparison of total platelet activation for the bulk and the hinge (for difference gap sizes and interpolation models) flows using linear and Soares activation model within a cardiac cycle. The total activation is normalize by total total activation of the bulk flow at the end of cycle for each model. The leaflet angles and the flow rates are also plotted. 1w and 2w denote one-way and two interpolation, respectively. 150 and 250 denote the gap size of the hinge region. Linear and Soares denote the platelet activation model. Reprinted from [3].

sults in the hinge region. Thus, the total activation of one-way coupling is the same as the two-way one during systole in the hinge area. During diastole, however, the one-way interpolation generates much higher activation (more than two times) than the two-way interpolation for all gap sizes using both activation models. In addition, in one-way interpolation, the total platelet activation of the smaller ($150\ \mu m$) gap is higher than the larger one by approximately 50% and 35% (Fig. 5.6) using Soares and linear models, respectively, whereas two-way interpolation shows the opposite trend, i.e., the total activation the larger gap size is higher than the smaller one by 8% and 12% (Fig. 5.6) using Soares and linear activation models, respectively. The trend for the two-way interpolation is consistent with the experimental results of Travis et al. [226] and Leo et al. [223] showing lower activation is associated with regular gap size ($100\mu m$) compared to a larger one ($200\mu m$). Because of the overestimation of velocities, shear stress, and the total activation of the one-way coupling relative to the experiments, the one-way coupling is inadequate to obtain quantitative measures for activation in the hinge region. Therefore, we only discuss two-way coupling, whose results are close to previous experiments (Table 5.1 and Table 5.2).

5.3.2 Hinge flow and the gap size

The hinge gap width of BMHVs can vary due to manufacturing tolerance, or displacement of the leaflets, which can affect the flow in the hinge area. Our results show that the hinge gap size has a limited effect on the flow through the hinge during the systole phase, but it has a significant effect during the diastole in terms of velocity magnitudes which are directly related to washout ability in the hinge area (Fig. 5.5-c,d). The maximum magnitude of the velocity on the flat level in the smaller gap is less ($2.4\ m/s$) than the larger gap size ($2.8\ m/s$). However, the magnitude of the b-datum jet does not change considerably for different gap sizes ($\sim 2.8\ m/s$). The change of hinge gap size mainly influences the flow in the ventricle corner. The maximum velocity in the ventricle corner reduces from $2.1\ m/s$ in the larger gap size to $1.05\ m/s$ in the smaller one. This smaller velocity suggests that the $150\ \mu m$ gap size will have a weaker washout potential compared to the larger gap. The maximum shear stress observed in both gap sizes is in the same order of magnitude with slightly higher shear stress in the larger gap size ($1170\ dyne/cm^2$) in comparison

to the smaller gap ($1120\ dyne/cm^2$). The above trend for the shear stress and velocity magnitudes with change in gap size is similar to the recent experiments of Jun et al. [7].

The results of platelet activation calculated using the Soares model for larger and smaller gap sizes during the diastole phase are shown in Fig. 5.7. The maximum magnitude of platelet activation in both gaps is observed in ventricle corners. Furthermore, the activation contours show lower levels for the smaller gap than the larger one (Fig. 5.7). However, the activation due to the b-datum jet for different gap sizes shows no significant difference in the $300\ \mu m$ plane.

Comparing the total activation for different gap sizes by the two-way coupling in Fig. 5.6 shows that the total activation in the larger gap size is higher than the smaller one by 8% and 12% at the end of the cycle for linear and Soares models, respectively. This indicates that the larger gap size activates more platelets, which is consistent with the observation in the previous experiments ([226].

5.3.3 Platelet activation in bulk versus hinge flow

To compare the impact of the bulk and hinge flow on the performance of BMHVs in terms of platelet activation, the total activation generated in each phase of the cardiac cycle is calculated. Figure 5.6 compares the total platelet activation (activation production) caused by the hinge region and b-datum gap to the activation generated by the bulk flow during a cardiac cycle using Soares and linear activation models. As mentioned in the previous sections, the activation values in the figure are normalized by the total activation in the bulk flow at the end of the cycle. Figure 5.6 shows that the total activation at the end of the cycle generated by the bulk flow is several folds higher than the activation by the hinge region. In fact, the total activation of the hinge/leakage flow is only about 10% of the bulk flow for different gap sizes and the activation models. The reason for the higher total activation by the bulk flow will be closely examined below.

The trend of activation in Fig. 5.6 can be explained by the mechanics of activation. For the bulk flow, the total activation before mid-acceleration phase ($t = 100\ ms$) is almost negligible because the vortical structures are well organized and symmetric (Fig. 5.8 which results in low shear stress (Fig. 5.9a) and platelet activation in the bulk flow (Fig. 5.10a). The rate of activation (slope of the

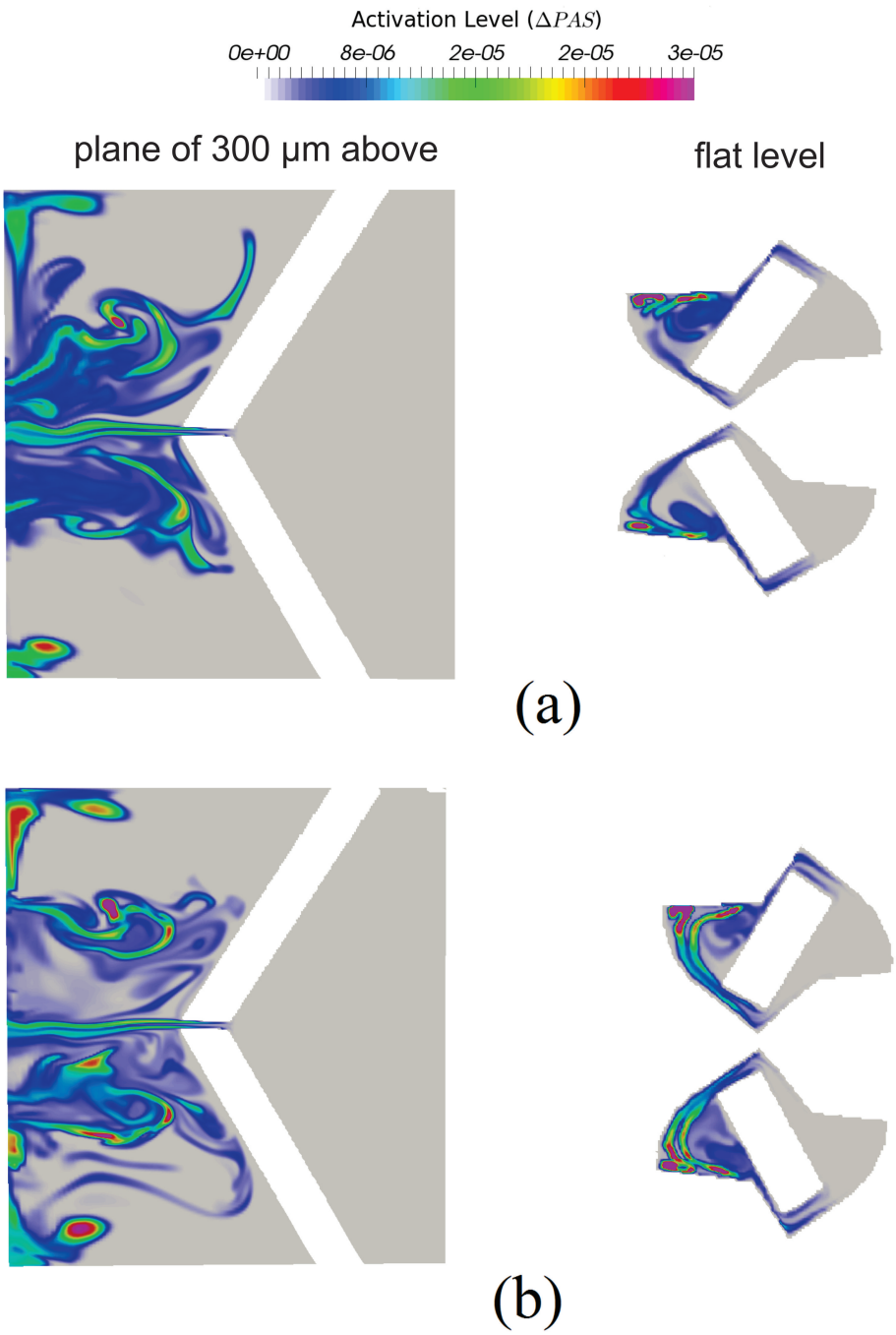

Figure 5.7: Platelet activation of hinge domain using Soares model and two-way interpolation for both gap sizes At mid-diastole for different plane of view (a) gap size $150\ \mu m$ and (b) gap size $250\ \mu m$. Reprinted from [3].

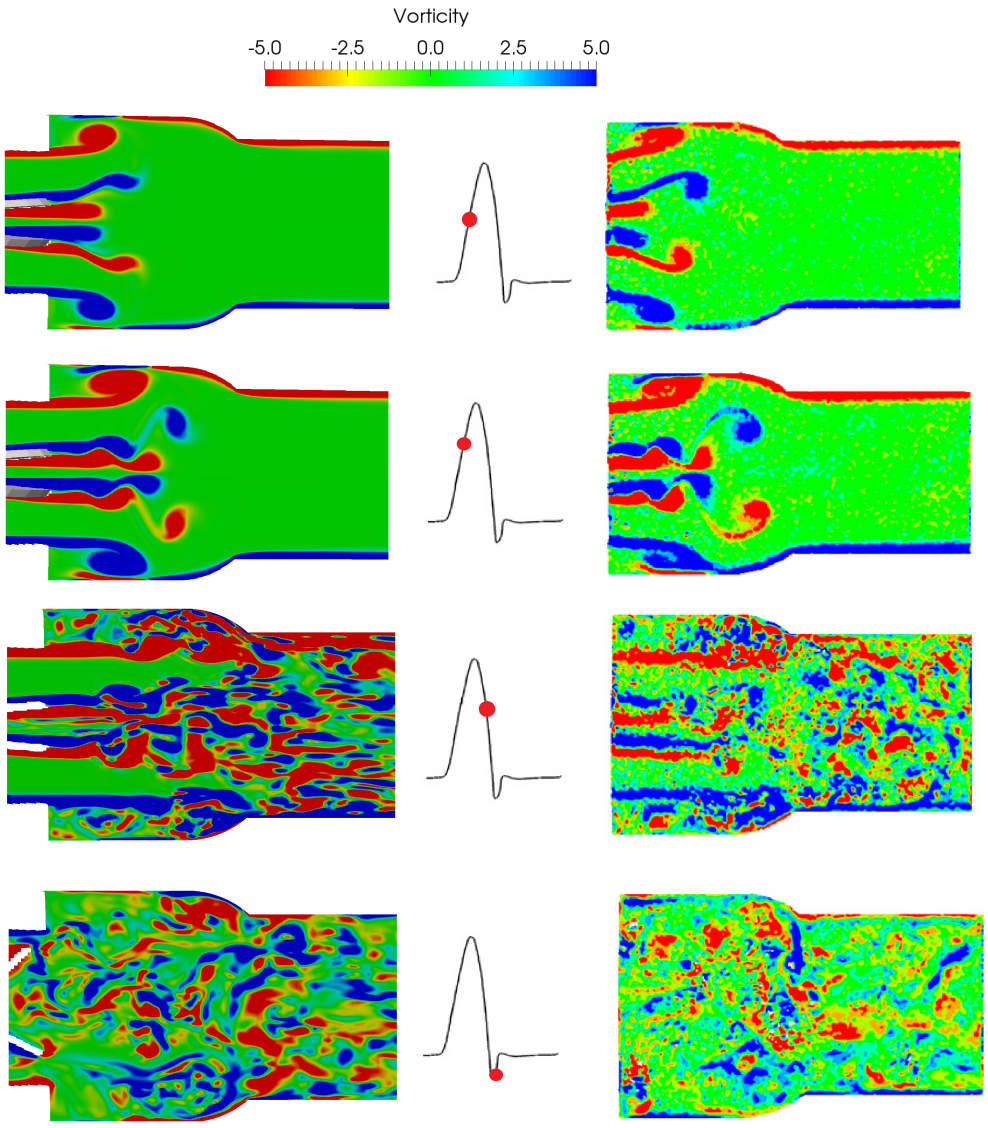

Figure 5.8: Comparison of out of plan vorticity using two-way coupling simulation with PIV measurements of Dasi et al [6] at four different time instants within a cardiac cycle. Reprinted from [3].

line in Fig. 5.6) reaches its maximum at the peak systole ($t = 200\ ms$) and this trend continues during the deceleration phase until the end of systole ($t = 360\ ms$). The rate of total activation during the deceleration phase is higher (1.5 times) than the acceleration phase because the vortical structures in the BMHV break down into small-scale disorganized vortices right before the peak systole (Fig. 5.8) similar to previous simulations and experiments [6, 46, 5], which consequently generates regions of high shear stress (Fig. 5.9 b-c) that activate platelets (Fig. 5.10 b-c) during the deceleration phase. The activation in the bulk flow mainly happens during the systole phase, but platelet activation still occurs with a slower rate until $t = 550\ ms$ (Fig. 5.6) because of the small vortical structures remain in the flow (Fig. 5.9 d, 5.10 d) that slowly dissipate. Due to the dissipation of vortical structures in the bulk flow, after $t = 550\ ms$ the shear stress and consequently the activation production is negligible, i.e., total activation remains constant (Fig. 5.6).

For the hinge and b-datum gap at the beginning ($t <$80 ms when the valves are opening) and the rest of systole the total activation is negligible (Fig. 5.6). This is interesting because the shear stress was not negligible during systole (Fig. 5.3) as discussed in the previous section. In fact, during the systole platelet activates due to the flow diving into the leaflet earings and the hinge recess as shown by streamlines in Fig. 5.11-b. The streamlines enter the hinge recess through the ventricular corner (from the gap between the leaflet flat surface and housing) and exit through the adjacent and aortic corner. Two regions of high shear stress near the ventricle corner (between the flat-level and leaflet surface) and near the adjacent corner can be observed in Fig. 5.3. However, the flow rate through this region during systole is small which can be seen by the magnitude of in-plane velocity (up to $\approx 0.5\ m/s$ during the peak systole) on the flat level (Fig. 5.11-c). Because of the small flow rate through the hinge recess, a lower number of platelets are exposed to high shear to get activated during systole, which renders the total activation of the hinge as negligible compared to the bulk flow.

The main activation in the hinge region and the b-datum gap happens during the diastole phase ($t = 400ms$ to $t = 860ms$ in Fig. 5.6) because of the leakage flow through 1) the gap between leaflet's earing and housing in the hinge recess; 2) the gap between the flat surface of leaflets and

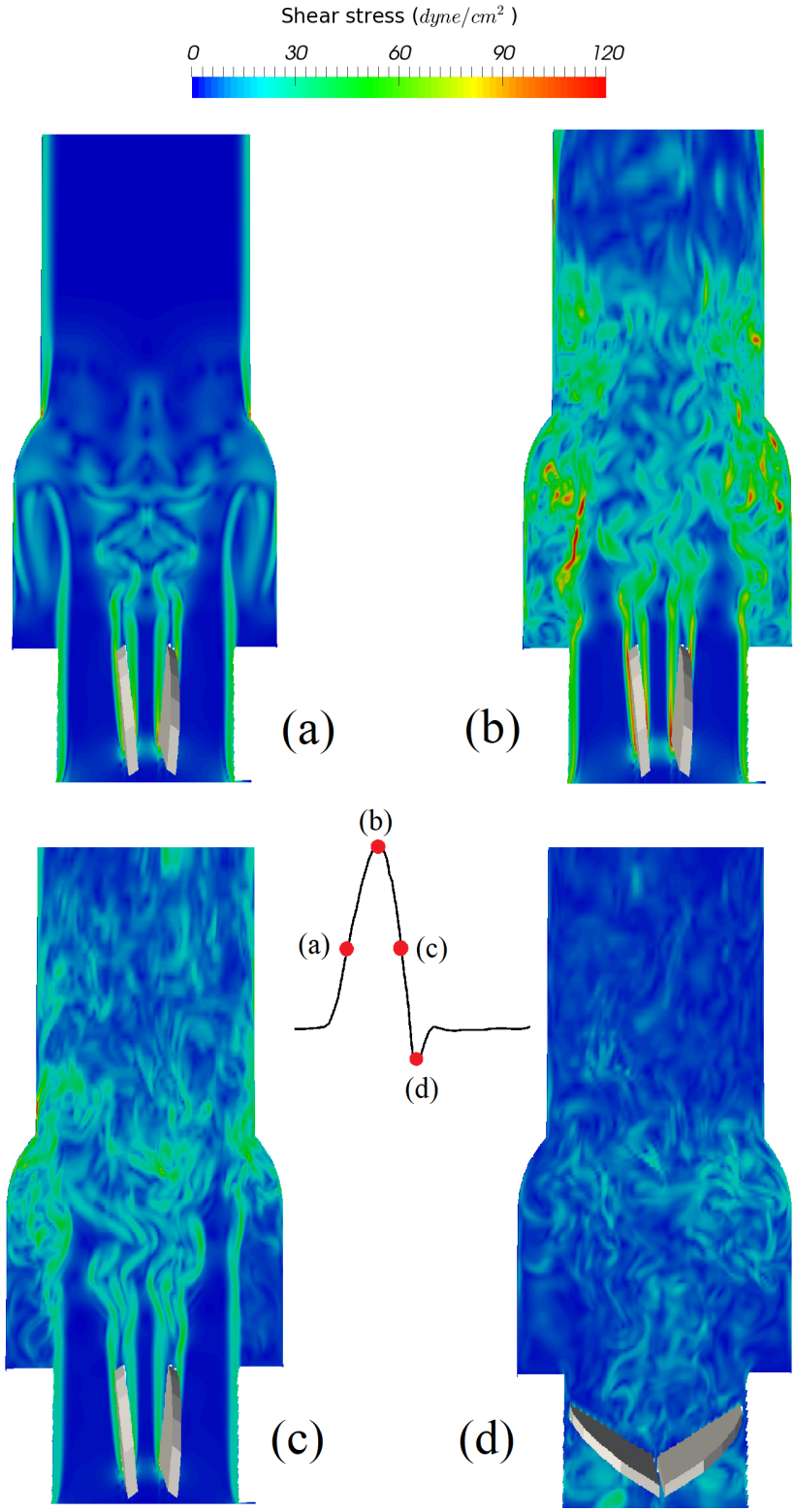

Figure 5.9: Scalar shear stress for the MHV in the large scale domain at time t=(a) 137, (b) 206, (c) 309, and (d) 412 ms within the cardiac cycle. Reprinted from [3].

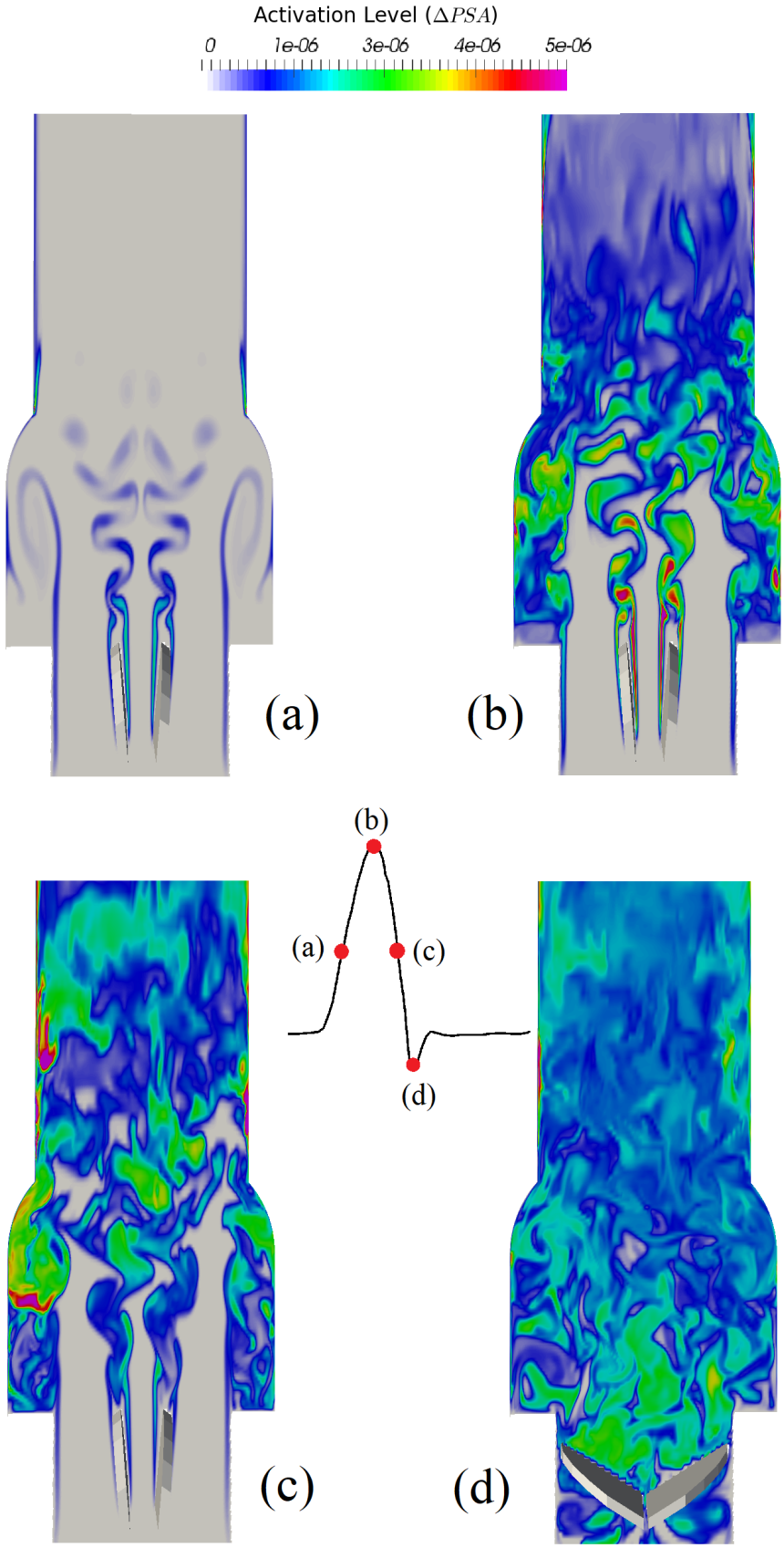

Figure 5.10: Platelet activation for the MHV in the large scale domain using the Soares activation model at time t=(a) 137, (b) 206, (c) 309, and (d) 412 ms within the cardiac cycle. Reprinted from [3].

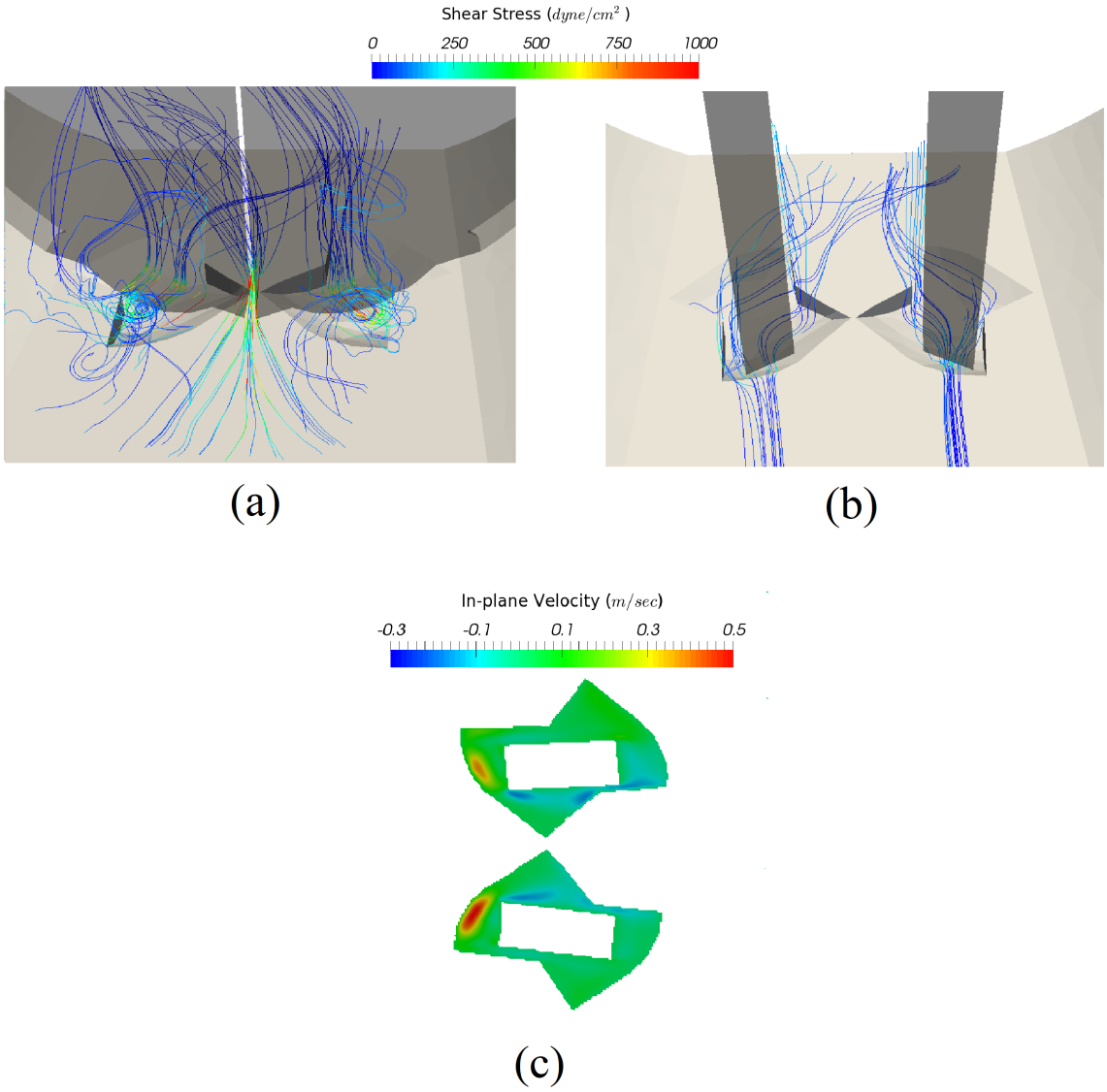

Figure 5.11: Three-dimensional streamtraces at peak systole (a) and mid-diastole (b) for small scale simulation near the hinge recess (c) In-plane velocity on flat level at peak systole. Reprinted from [3].

the housing, and 3) b-datum gap. These three gaps (Fig. 5.1 c) result in three leakage jets (Fig. 5.5-c and Fig. 5.11-a) which exit the hinge recess from lateral, adjacent and ventricle corners with the maximum velocity magnitude of $2.4\ m/s$ (at the adjacent corner). The leakage jets create regions of high shear stress near these three corners with the maximum magnitude of $1120\ dyne/cm^2$ at the adjacent corner (Fig. 5.3-a), which is much higher than the peak shear stress in the bulk flow ($\approx 200\ dyne/cm^2$). For the smaller gap size, the minimum of shear stress and velocity is observed in the ventricle corner. Fig. 5.7 shows the platelet activation at mid-diastole on the flat level using the Soares activation model. A high magnitude of the activation is observed downstream of the valves near the ventricle corner. This can be explained by the streamtraces (Fig. 5.11-a) in the hinge recess at mid-diastole (since the flow is almost steady in this phase the stream tracers and path-lines for platelets are almost the same). As can be seen, due to the reverse flow, the streamlines dive into the hinge recess mostly from the aortic corner then pass through the gap between leaflet's earing and hinge recess and exit the ventricle corner. The platelets moving through these streamlines will travel the longest distance and thus experience a longer exposure time under the elevated shear stress (in the hinge recess). The platelet activation on the plane of $300\mu m$ above the flat is also shown in Fig. 5.7 for the Soares model. The activation in this plane mainly happens due to the jet from the b-datum gap. The maximum velocity and shear of $2.8\ m/s$ and $1200\ dyne/cm^2$ can be seen on this plane (Fig. 5.5-c and Fig. 5.3-a).

The total activation depends on both the shear stress and the number of platelets exposed to shear stress, i.e., flow rate during diastole. In the diastole, during the rapid closure of the leaflets ($t = 430\ ms$), there is a sharp increase in the total platelet activation because of the high flow rate of the leakage flow (Fig. 5.6). After the valves close, the flow rate through the hinge and b-datum gap is almost constant (see the flow curve in Fig. 5.6). Consequently, the rate of activation in this phase is not changing much and the total activation is almost linear in this phase.

Based on the above discussion, even though the platelets in hinge region are exposed to much higher shear stress levels (compare Figs. 5.3 and 5.9) and locally show higher levels of activation (compare Figs. 5.7 and 5.10), the total amount of activation generated by hinge domain is less than

20% of the bulk domain mainly because of the low flow rate through the hinge domain compared to the bulk flow (Fig. 5.6). In fact, the mean flow rate of the leakage flow after the valve closure through the hinge region and the b-datum gap is only about 2% of the forward flow rate through the valve in the bulk flow (Fig. 5.6). Therefore, a considerably smaller number of platelets will be exposed to high shear during diastole compared to the bulk flow, which is the main reason for the lower total amount of activation generated in the hinge region (Fig. 5.6).

5.4 Validation and sensitivity studies

In this section, we validate our numerical simulations with the exact or closest available experiments for the hinge region, bulk flow, and platelet activation in the literature.

5.4.1 Validation of the bulk flow and leaflet kinematics

In this work, the exact setup of Dasi et al. [6], which was previously used to validate the MHV simulations of Borazjani et al. [46], is used to validate the bulk flow and valve kinematics obtained from both one-way and two-way simulations. The MHV's leaflet kinematics is compared with the experimental measurements of Dasi et al. [6]. As can be seen the leaflet kinematics is remarkably in agreement with the experimental results in terms of the overall duration and acceleration rates of the opening and closing phases (Fig. 5.12). The coupling method (one-way or two-way) between the hinge region and the bulk flow results in $20\ ms$ difference in the full closure of the leaflet. Nevertheless, both coupling methods are quite close to the measured kinematics.

In addition, the flow field is compared to the PIV visualization of Dasi et al. [6]. Fig. 5.8 compares the out of plan vorticity using a two-way coupling simulation with PIV measurements at four different time instants within a cardiac cycle. The flow field of numerical simulation matches well with the experiment. No significant difference observed between the one-way and two-way simulations at these four instants.

The pressure drop (backpressure between the aortic and ventricle sides of the valve) is shown in Fig. 5.13. The pressure is averaged over the planes $\pm 25.4\ mm$ upstream and downstream of the valve as in experiments by Jun et al. [7]. As can be seen the trend of pressure matches during

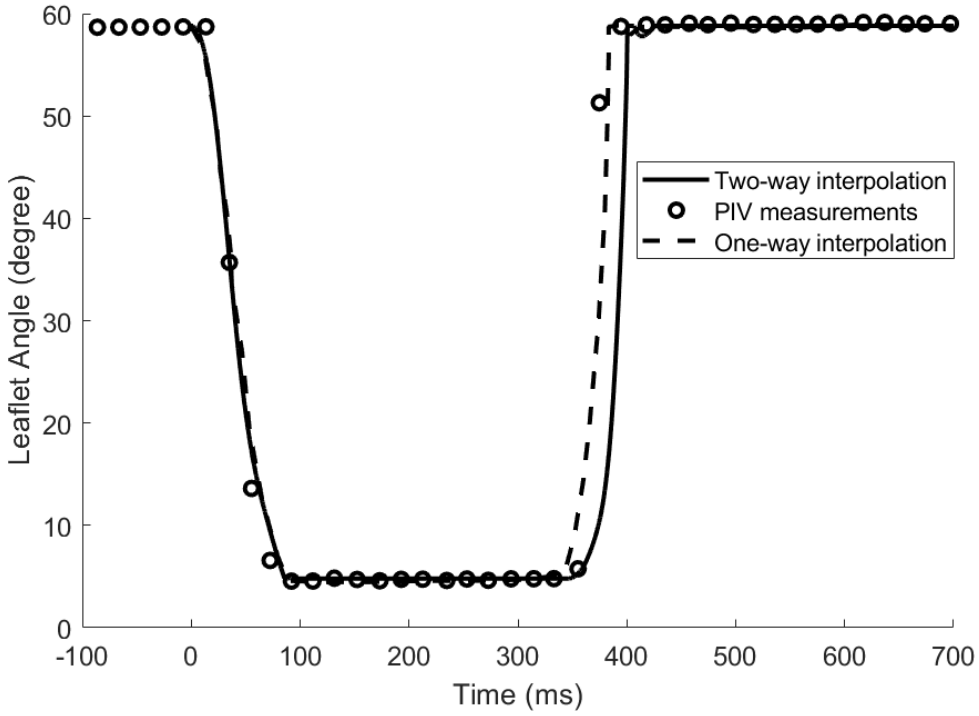

Figure 5.12: Comparison of the calculated leaflet kinematics with experimental observations [6]. Reprinted from [3].

the cardiac cycle with the experiment except for the rapid closure period. In addition, the diastolic pressure in our simulation is around $100\ mmHg$ while the pressure wave in the experiment is set to be $120\ mmHg$. The figure also plots the pressure difference on the boundary of the hinge domain ($\pm 6\ mm$) from the valves. As can be seen the interpolation method (one-way and two-way) considerably changes the pressure measurements in the hinge domain and as it is expected due to the higher velocity magnitudes in the hinge region for the one-way interpolation method a higher diastolic pressure difference is observed compared to two-way coupling.

Based on the above, the simulations provide all the flow features observed at the bulk level in the experiments similar to the previous publication Borazjani et al. [46]. In the next section, we validate the platelet activation framework.

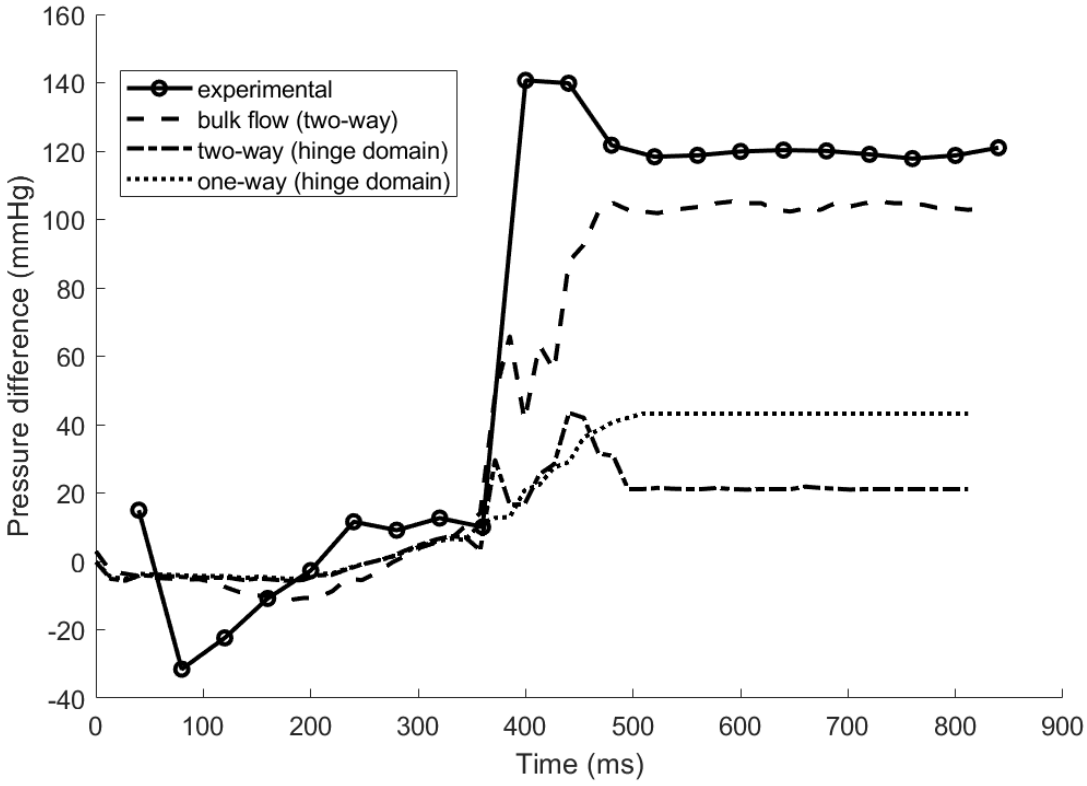

Figure 5.13: Pressure difference between the aortic and ventricle (for planes $\pm 25.4\ mm$ upstream and downstream of the valve) side during a cardiac cycle in the numerical simulations compared to the experiments by [7] for $23\ mm$ St. Jude BMHV. Reprinted from [3].

5.4.2 Sensitivity of the results to the initial activation distribution

The Soares model requires a non-zero initial activation [4]. The Soares model works best for an initial activation PAS_0 in the range of 0.0001 to 0.01. In order to compare the platelet activation in the bulk and hinge region using a random initialization of platelets (PAS_0), a truncated normal probability distribution function with the mean=0.005 and std=0.002 is with the maximum value of 0.01 and minimum value 0.0001 of used considering the above range of PAS_0 (0.0001 to 0.01) which is shown in the Fig. 5.14. The difference in the ratio of the platelet activation in the hinge region versus the bulk flow using random initialization compared to constant initialization of ($PAS_0 = 0.01$) was less than 2%. This indicates that the results are independent of the initial activation.

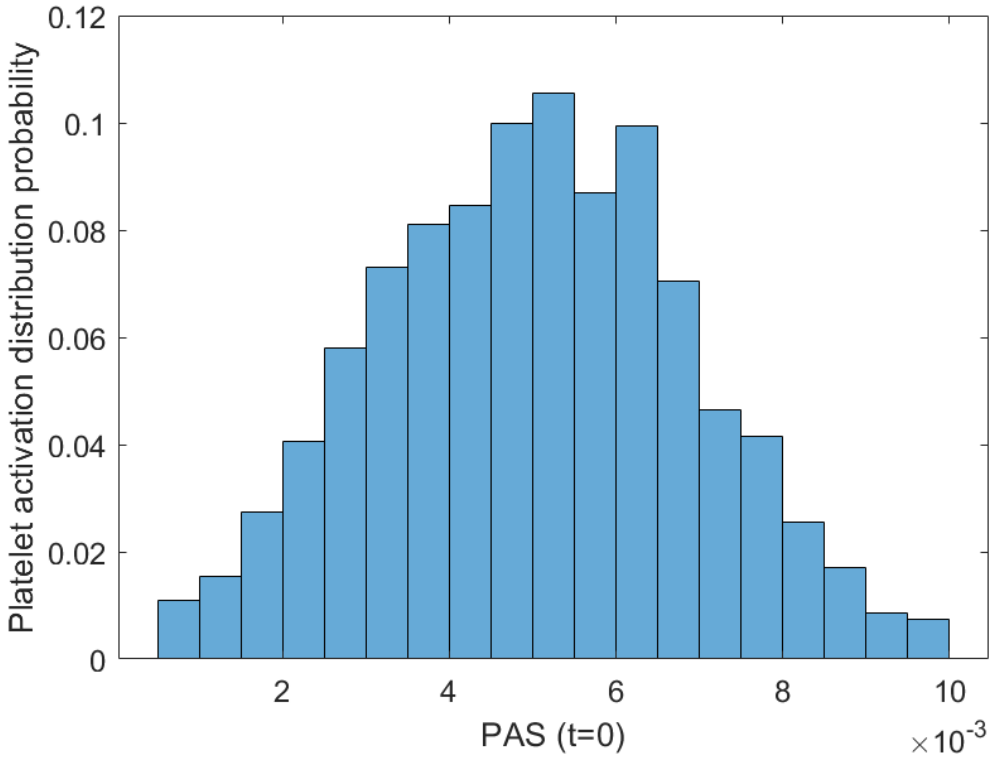

Figure 5.14: Truncated normal probability distribution used for $PAS0$ in Soares model. Reprinted from [3].

5.4.3 Validation/verification of the simulated hinge flow: Comparison with experiments and the role of the coupling method

Fig. 5.4 compares the effect of the one-way vs. two-way interpolation method between the bulk flow and the hinge domains on the velocity profile/magnitude near the hinge region at peak systole. Figure 5.4-a and 5.4-b shows the velocity magnitude and glyph on the flat level as well as the plane of $300\ \mu m$ for one-way and two-way interpolation, respectively. No significant difference is observed by using one-way or two-way interpolation on the velocity profile/magnitude at peak systole which is the case during the whole systole phase. As mentioned in the paper, the flow dives in the hinge recess from the aortic corner and exits the hinge recess from the ventricle corner.

The main difference in the results with different interpolation methods (between grids) is in the diastole phase, which is thoroughly discussed in the paper. This suggests the one-way interpolation can provide reasonable results during the systole phase. However, two-way interpolation is essential in the numerical simulation during the diastole.

Table 5.2 compares the average of the magnitude of the velocities and scalar shear stress in this study using two-way coupling interpolation with the corresponding range of ensemble average in the previous experiments on the flat level in different corners of the hinge recess at peak systole and mid-diastole. Viscous shear stress observed during the diastole is multiple times higher than the peak systole and the maximum value of the shear stress is observed in the lateral corner at mid-diastole which is in agreement with the experiment. The velocities in our simulations are in good agreement with the experiment while the shear stresses are somewhat higher. One reason can be that the shear stresses in the micro PIV are for in-plane shear stresses (not 3D shear stress tensor) which are calculated as below:

$$\sigma = \mu \, (\frac{\partial u_1}{\partial x_2} + \frac{\partial u_2}{\partial x_1}) \tag{5.1}$$

where u_1 and u_2 are the components of velocity in x_1 and x_2 directions on the plane, respectively. As discussed by [187], the shear stress from the 3D stress tensor is higher than the corresponding

2D ones.

Table 5.2: Comparison of velocity and viscous shear stress at the lateral, adjacent, and ventricular jets at the peak systolic and mid-diastolic phases for current study to the previous experiments on flat level. Reprinted from [3].

study	phase	corner	velocity range (m/s)	shear stress $(dyne/cm^2)$
jun et al. [7]	systole	lateral	0.15 -1.1	44 -450
		adjacent	0.25 -0.9	65 -410
	diastole	lateral	0.42 -0.86	3 -280
		adjacent	2.35 -2.57	100 -440
		ventricle	0.96 -1.8	82 -340
current study (average value)	systole	lateral	0.4	80
		adjacent	0.5	70
	diastole	lateral	2.3	700
		adjacent	2.65	1060
		ventricle	1.05	350

5.5 Limitations

The limitation of our study is that the simulations were performed for only one cardiac cycle and no region with activation higher than Hellums criterion ($35\ dyne.s/cm^2$) or $\Delta PAS = 1$ was identified during one-time passage. Nevertheless, such levels of activation can be reached after multiple passages through the valves. The implicit assumption of our comparison of total platelet activation in hinge vs. bulk flow, therefore, is that every passage generates similar activation in each region. This is a reasonable assumption as the cycle-to-cycle variations of the flow in mechanical valves are small [6], i.e., the similar flow field in each cycle, which creates similar shear exposure to platelets in consecutive cycles. In addition, due to the complexity of the platelet activation phenomenon, any mathematical model for predicting activation is limited to its range of verified validity and its assumptions (from simplifying assumptions in the experiments to neglecting chemical factors in platelet activation).

5.6 Conclusion

In this study, we developed a numerical framework that enables us to answer the open question about the role of systole phase (bulk flow) versus diastole phase (hinge/gap flow) in the poor thrombogenic performance of BMHVs in terms of shear-induced platelet activation. The results show that while the hinge area has higher shear stress and maximum local activation compared to the bulk flow, the total activation due to the bulk flow, contrary to the common belief [185, 201, 7], is several times higher than that of hinge/leakage flow using both activation models. This is mainly because of the higher flow rate during systole exposes more platelets to elevated shear in the bulk flow, whereas the low leakage flow rate during diastole ($\sim$2% of bulk flow at peak systole) exposes a lower number of platelets to much higher shear stress. The relative importance of the number of platelets exposed (flow rate) vs. the elevated shear and exposure time was ignored in the previous studies.

Comparing the results of one-way and two-way interpolation with the experiments ([222, 7]), shows that, although most of the previous numerical simulation ([200, 185, 56]) has used one-way interpolation due to computational simplicity, the results using this method will overestimate the velocities, shear stress, and the platelet activation during the diastole phase in the hinge region. In addition, our results show that hinge gap size can significantly affect the washout potential of BMHVs while the maximum shear stress and total activation do not change remarkably (less than 10%) for different hinge gap sizes. The larger gap size shows a better washout performance near the hinge region by having a higher maximum instantaneous velocity through the hinge ($2.8\ m/s$) in comparison to the smaller one ($2.4\ m/s$).

6. PATIENT-SPECIFIC VALVE DESIGN AND PLACEMENT: HYBRID ECHO-CFD

In the previous chapters, the hemodynamic performance of the mechanical heart valves in simplified geometries such as simplified aorta was investigated. To evaluate the hemodynamics performance of artificial heart valves and optimize their design and placement for specific patients employing medical images and combining them with CFD tools is essential. In this chapter, we show the results of an image-based CFD (without artificial valves) by combining the echocardiography images with our overset-CURVIB solver. Combining echo-CFD with artificial valve simulations is intended to be performed as a part of the future plan (section 7). This chapter is organized as follows: the computational setup for the simulations are discussed in section 6.2. Later, the comparison of reconstructed LV with their physiological range investigated in section 6.3.1. Then, the flow simulation using the reconstructed geometry is discussed in section 6.3.2. The effect of the mitral valve on the flow in the LV is investigated in section 6.3.2.1. The difference of flow pattern inside the healthy and AMI left-ventricles is investigated in section 6.3.2.2. The results of flow simulations using a hybrid echo-CFD framework are compared to Doppler ultrasound for both AMI and healthy LVs in section 6.4. Finally, the limitation of the work is discussed in section 6.5.

6.1 Background

Several noninvasive techniques have been used to characterize abnormal blood patterns that contribute to heart failure. Medical imaging techniques including cardiovascular magnetic resonance [232], and 3D echocardiography (echo) [233] have been widely used to visualize flow patterns in the cardiac system. However, they typically have lower spatial/temporal resolution compared to computational fluid dynamic (CFD) methods [232, 234]. CFD in combination with imaging techniques for geometric reconstruction can provide a powerful tool for investigating the flow pattern with more details in the cardiac system [235].

The geometric segmentation and reconstruction process from medical images along with the

assumptions for motions of valves and the endocardial wall can greatly influence the flow pattern inside the left-ventricle (LV) [236, 237, 132]. Currently, two types of techniques are available to model the motion of valves and the LV [234]: 1) fluid-structure interaction, and 2) prescribed models. In prescribed models, the motion of geometries are prescribed based on *in-vivo* measurements [238] or simplified equations to define the motion [132, 239, 240]. Of course, obtaining the motions from medical images is more realistic than prescribing the motion based on simplified equations. The fluid-structure interaction models have been widely used in numerical simulations [241, 242, 95, 243, 244] especially for capturing the motion of heart valves. However, due to the complexity of geometry, dynamic shape, and large deformation of LV and mitral valve these models are computationally expensive [85, 236], and the lack of data for tissue mechanical properties from *in-vivo* measurements makes using them quite challenging. Therefore, it is desirable to use image-based geometry/motion if available. However, the main concern about using the medical images in CFD simulations is their accuracy in terms of spatio-temporal resolution.

3D imaging techniques, e.g., computed tomography [245], cardiac magnetic resonance [246], 3D echo [247], and 2D ones, e.g., 2D echo [248], have been used for visualization of LV and its valves. Each of these imaging modalities has its own advantage and disadvantages which makes them suitable for specific applications. Among these, cardiac computed tomography and resonance can provide higher spatial resolution compared to echo, but are not as widely used as echo in daily practice due to their considerably higher image acquisition time, cost, the expertise required for the operation, and other drawbacks such as exposing patients to radiation and reacting to metal. 2D echo is the most widely used method for non-invasive assessment of the LV function because of its low cost and fast acquisition [249]. However, limited 2D cross-sections are available in this imaging technique thus a geometric reconstruction is needed to obtain 3D geometry of the LV and its valves, which is a challenging task. In addition, the 2D images inherently contain some extent of speckle noise. 3D echo provides the 3D geometry using a 3D full volume acquisition rather than a 2D acquisition. Therefore, 3D echo has better reproducibility and accuracy compared to 2D echo as it does not require geometric 3D reconstruction from 2D cross-sections. However, the complex

acquisition and lengthy data analysis made 3D echo less commonly used in clinical practice compared to 2D echo [250]. In addition, 2D echo can provide high temporal resolution (from 250 fps, down to 50 fps for resolving the whole heart) compared to other techniques [251] (e.g., computed tomography, and cardiac magnetic resonance), which is essential for capturing the flow features during a cardiac cycle due to the complex and fast three-dimensional motion of the LV. Therefore, our goal is to develop a method for patient-specific simulations of the flow within the LV, based on 2D echo.

The valvular geometry and leaflet motion can have a significant impact on the flow field inside the LV [252]. Due to the highly dynamic motion and geometry of the leaflets, the reconstruction of heart valves still remains a challenge. Typically, there is a trade-off between the spatial and the temporal accuracy of the 3D reconstruction of valves due to complex geometry. Hence, a wide range of simplifications, both for geometry and motion, have been used to model the ventricular valves during a cardiac cycle. However, the literature can be divided into three general categories: 1) simplifying both motion and geometry of valves to an on/off approach, where the switch between the on and off configuration occurs instantaneously without any intermediate positions [253, 254, 255]; 2) simplifying the geometries of valves due the lack of spatial resolution of the available imaging technique and calculate the motion of the valves with higher temporal resolution [252, 256]; 3) modeling the valves with higher spatial resolution and use simplifications or mathematical approaches to predict the motion of the valves [257, 258, 259, 260, 261]. Here, we reconstruct mitral and aortic valves using the segmented data from multiple-axis 2D echo images with the temporal resolution of more than 30 fps, while some geometric simplifications have been assumed for 3D reconstruction of valves due to a limited number of views from 2D echo in which the valves are visible.

Some studies considered the effect of ventricular valves in their LV simulations [262, 263, 132, 264, 256, 261, 252, 265, 266]. Due to the significant impact of the mitral valve on the performance of the heart, most LV simulations are just considering the effect of the mitral valve (neglecting the aortic valve) and the simulations are mainly limited to the diastolic phase [263, 256, 261, 252, 265,

266]. Charonko et al. [267] reported that the mitral vortex ring facilitates the filling and enhances flow transfer to the LV's apex. Dahl et al. [265] studied the effect of the mitral valve in a 2D simulation of LV. Their results show that asymmetric leaflets for the mitral valve as well as an adequate model for the left atrium are essential for resolving important flow features in the LV. Seo et al. [252] showed the mitral valve can significantly affect the vortex ring propagation and flow field inside LV. They also found that due to the asymmetry of the mitral valve a circulatory flow pattern can be generated in the LV which can enhance apical washout ability and reduce the risk of thrombus formation. Su et al. [256] investigated the effect of the mitral valve on vortex formation time. Their results showed that vortex formation time is a promising parameter to characterize the performance of the LV. Bavo et al. [268, 269] used 3D echo for real-time patient-specific flow simulation and investigated the effect of the mitral valve on the flow inside the LV for different clinical cases. However, only a few simulations studied the flow pattern inside the LV incorporated with both ventricular valves [264, 256, 262] and even fewer compared flow pattern in baseline LV with left ventricles with any kind of heart failure [256, 270, 271, 272].

In this study, the 3D reconstruction method developed in our group ([273, 251]) is coupled with our in-house CFD code [274], which is based on a sharp-interface immersed boundary method [80, 46, 1], to simulate the ventricular flows (section 6.3.2). The effect of the mitral valve on the hemodynamic of blood inside the LV is investigated in section 6.3.2.1. In addition, this framework is applied to a baseline LV and an LV with acute myocardial infarction (AMI) and the results are discussed in section 6.3.2.2. Later, the results of CFD simulations for both baseline and AMI left ventricles are compared to Doppler ultrasound velocity measurements obtained during the experiments (section 6.4). Finally, the limitations of our study as well as the feature works are explained in section 6.5.

6.2 Methods and materials

To handle the complex shape and motion of LV, a curvilinear immersed boundary method(CRVIB) [80, 169, 46] is used which is explained in detail in chapter 2. The CURVIB flow solver has been extensively validated for a variety of complex flow problems [1, 275] and implemented in var-

ious applications such as cardiovascular flows [276, 3, 5], aquatic motions and vortex dynamics [93, 277, 278, 94] and rheology of suspensions [279]. The 3D-reconstructed surfaces of LV from 2D-echo which are meshed using triangular elements are given to the flow solver as an input for each time step to classify the background domain's nodes into fluid, boundary, and solid using an efficient ray-tracing algorithm [46] which can handle thick, closed-surface bodies. To classify the nodes corresponding to heart valves, which are provided as thin structures, an immersed boundary node classification algorithm for thin bodies is used [95]. After immersed boundary nodes classification, the boundary conditions on the solid/fluid interface are reconstructed using the velocity of the 3D-reconstructed LV surface using no-slip condition. Finally, the blood flow is driven from/into LV using the volume flux equal to the volumetric change of the LV. The simulations are performed for two cardiac cycles to let the flow reach a quasi-steady state. To minimize the influences of the inlet/outlet boundary conditions on the flow inside the LV, simplified surfaces (not from any medical images) are generated to model left atrium and aorta. These geometries are generated in a way to make the dimensions of the surfaces have realistic values in comparison to the reconstructed LV based on data measurements in previous works [280, 281]. The complete reconstructed geometry used for flow simulations can be seen in Fig. 6.1. It is worth mentioning that only one of the aorta and atrium exist in the geometry at the same time (the aorta just exists during the systole phase and will be removed during diastole and an opposite pattern for left atrium).

The blood flows flux from the left atrium and aorta to/from the LV chamber is specified based on the volumetric change of the LV (the volumetric flux of LV is calculated based on the change of LV volume in two consecutive time-steps). In addition, the velocity boundary condition at the inlet of the atria is assumed to be uniform. The Navier-Stokes equation is non-dimensionalized with a diameter, $D = 16.38\ mm$, of the aortic orifice and the bulk velocity, $U = 0.598\ m/s$, with a time step $dt = 0.0109\ s$ over 2500 time instances during a cardiac cycle. Considering the blood viscosity to be $\nu = 3.3 \times 10^{-6} m^2/s$ leads to a Reynold's number of 2950 for the simulations. The LV geometry is discretized with approximately $50,000$ unstructured triangular mesh elements and is immersed in a background grid with a dimension of $5.19D \times 3.33D \times 6.32D$ (where D is the

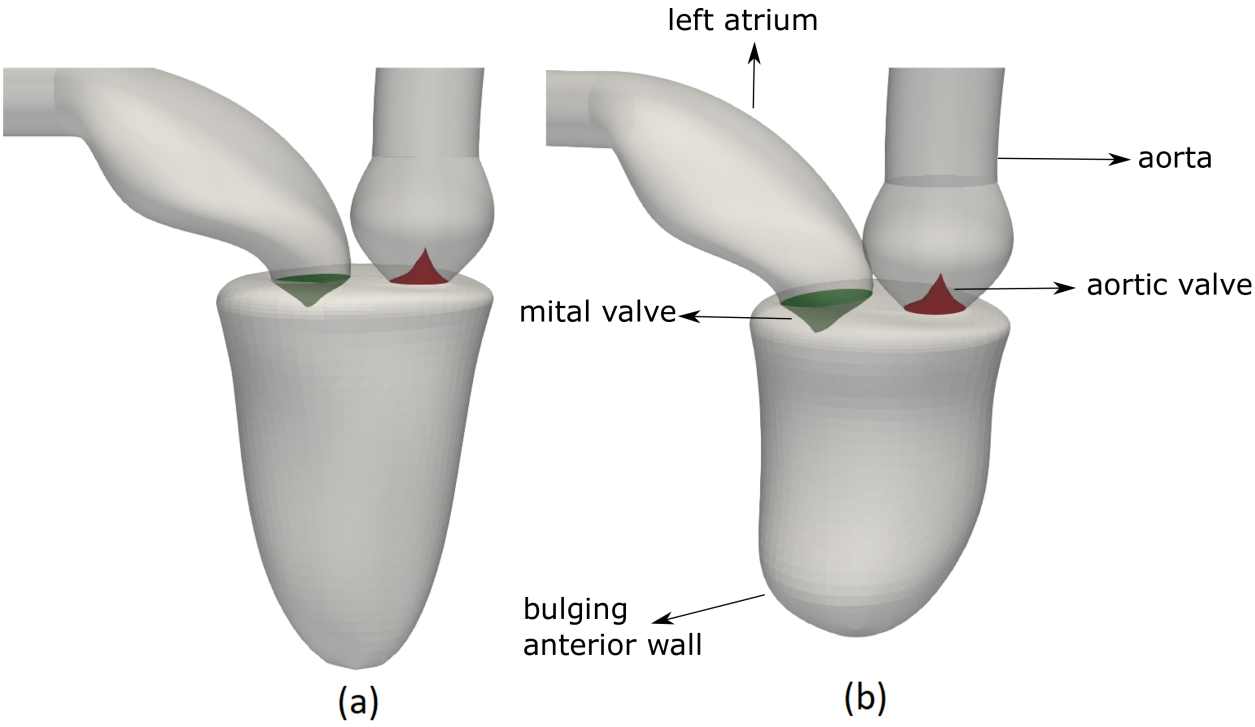

Figure 6.1: The final reconstructed LV based on 2D echo images attached to the approximated aorta and atrium surfaces for a) baseline and b) AMI case

aortic diameter) discretized with $161 \times 121 \times 201$ grid points in x, y and z directions, respectively.

6.3 Results and discussion

Here, the effect of fixed apex assumption on the final surface reconstruction and LV flux is studied. In addition, the sensitivity of the results (reconstruction and flow simulations) to the smoothing algorithm is investigated. Furthermore, the effect of ventricular valves especially the mitral valve on the flow field in the LV is studied. Finally, the flow hemodynamics of healthy and acute myocardial infarction LVs are compared with each other. The presented results are for healthy LV based on variable span weighted moving average smoothing algorithm unless it is mentioned otherwise.

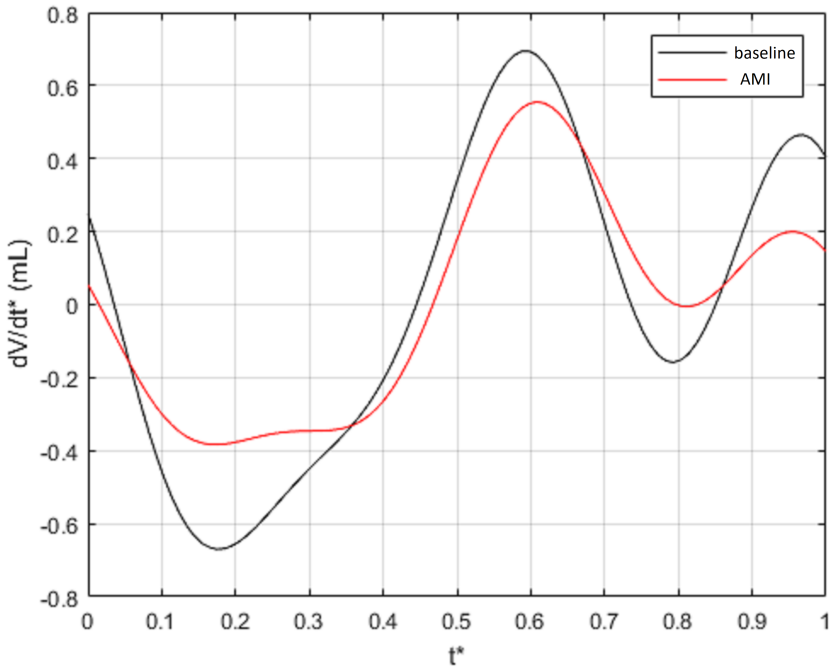

Figure 6.2: Comparison of a) volume (V), and b) flux (dV/dt) for baseline and AMI left ventricle during a cardiac cycle.

6.3.1 Comparison of LV parameters with their corresponding physiological range

Several parameters related to functionality of LV from reconstructed geometry are compared to their corresponding physiological ranges [282, 283] to show that the reconstruction from echo images is comparable to physiological data. The volume and volumetric flux versus time for both healthy and acute myocardial infarction LV are presented in Fig. 6.2. The time is non-dimensionalized in this figure to have the same time duration for both the healthy and acute myocardial infarction cases. Various parameters including EF, the ratio of maximum fluxes during the E-wave and A-wave (E/A Ratio), deceleration time and Stroke volume are calculated based on the curves in Fig. 6.2. Table 6.1 shows the comparison between the calculated parameters and their physiological ranges reported in previous *in-vivo* experiments [282, 284] for a porcine LV. As it can be seen in this table, the parameters calculated here for healthy LV lie within the physiological ranges of *in-vivo* experiments. However, the EF, and E/A ratio for the acute myocardial infarction afflicted LV lie outside the physiological ranges for healthy LV as can be expected.

Table 6.1: Comparison of the computed cardiac parameters of the reconstructed LV to their physiological range of Porcine LV (EF: ejection fraction, E/A ratio: ratio of maximum fluxes during the E-wave and A-wave)

	Physiological range	baseline	AMI
heart rate (bpm)	60 - 90 [283]	80	77
EF (%)	46.8 - 62.0 [282]	0.47	0.43
E/A ratio	0 - 1.4 [282]	1.38	2.5
deceleration-time (ms)	58 - 144 [282]	177	172
stroke-volume (mL)	13.1 -59 [282]	29	24
cardiac output (L/min)	-	2.3	1.85

6.3.2 Flow simulation for the reconstructed LV assembly

It is well known that the blood flow pattern in the LV has a direct impact on heart performance [239]. However, this flow pattern is directly related to the accuracy of LV reconstruction and valves' motion. Hence, in this section, the impact of ventricular valves and different smoothing algorithm for LV reconstruction as well as LV dysfunction on the performance of LV in terms of energy loss during the whole cardiac cycle is measured using the energy equation for a control volume as follows:

$$\frac{dE}{dt} = \dot{Q} - \dot{W} = \frac{\partial}{\partial t}\int_{CV} \rho e \, dV + \int_{CS} (\rho e + p)\vec{V}.d\vec{A} \tag{6.1}$$

where E is the total energy of the system (Fig. 6.3), $\dot{Q}$ is the rate of heat transfer to the system, $\dot{W}$ is the rate of work done on/by the system, CV is the control volume, CS is control surface, $\vec{V}$ velocity of flow, p is pressure, ρ is blood density, and e is the energy per unit mass

$$e = u + V^2/2 + \vec{g}z \tag{6.2}$$

where u is the internal energy of the fluid, $V^2/2$ is the kinetic energy. Integrating over a cardiac cycle assuming that $\frac{\partial}{\partial t}\int_{CV} \rho e \, dV$ is small and neglecting the heat transferred to the LV as well as

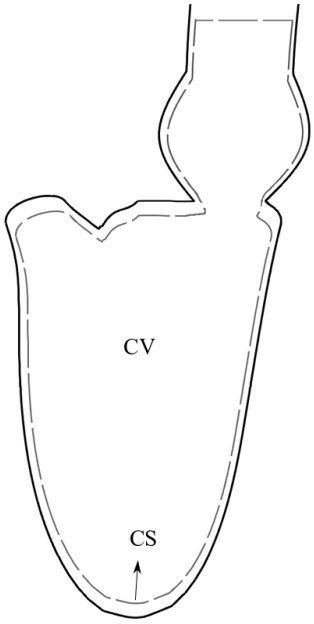

Figure 6.3: The schematic control volume (CV) and control surface (CS) used for calculating energy loss in the LV on the mid-plane passing through the aorta.

gravity and difference of internal energy of inlet and outlet, the above equation reduces to

$$loss = \int_0^T \int_{CS} \rho \left(p/\rho + V^2/2\right) \vec{V}.\vec{dA} \tag{6.3}$$

where T is time at the end of the cardiac cycle. Since acute myocardial infarction and healthy LVs have different stroke-volume and heart beat rate, to be able to compare the performance of the LV in different cases the rate of loss is calculated per lit of blood pumped in each simulation as follows:

$$\dot{loss}\ (J/lit) = \frac{loss}{SV} \tag{6.4}$$

where SV is the stroke-volume and heart rate is the heart rate. Table 6.2 compares the $\dot{loss}$ of the LV during a cardiac cycle for different smoothing algorithms, without heart valve, and acute myocardial infarction simulations.

Table 6.2: Comparison of LV $\dot{loss}$ for different test cases

case (smoothing)	$\dot{loss}\ (J/lit)$
baseline (variable span weighted moving average)	8.76
baseline without valve (variable span weighted moving average)	3.89
AMI (variable span weighted moving average)	10.3

6.3.2.1 Effect of mitral valve

The vortex ring generated during the rapid filling (E-wave) is one of the key characteristics of intraventricular flows [285]. Figure 6.4 shows the vortical structures inside healthy LV with incorporate ventricular valves during the diastole phase visualized by iso-surface of q-criteria [286]. For comparison, Fig. 6.5 shows the same visualization for the LV without valves at the same time instances. As can be observed in Fig. 6.4 at time $t/T = 0.448$ (t/T=instance time / cardiac cycle length), in the early diastolic phase where the mitral valve leaflets are just beginning to open, the vortex ring starts forming on the tip of the leaflet of the mitral valve. Since the mitral orifice is a circular this vortex ring has a circular shape. The vortex ring starts to pinch off and propagates inside the LV around the peak E-wave (Fig. 6.4-b). Due to the asymmetric geometry of mitral leaflets, the ring propagates towards the posterior wall of LV while starting to disintegrate as it approaches the wall. This ring finally hits the wall and begins to break down into small-scale vortical structures that fill the whole volume of LV. During the A-wave also another vortex ring is generated. However, this time the ring is weaker and dissipates faster without propagating much in the LV.

Comparing the q-criteria visualization of LV without the valve; it can be observed that the vortex ring starts forming at the mitral annulus (Fig. 6.5). Due to the absence of the mitral valves, the symmetric ring propagates towards the apex of LV. However, since the mitral annulus has a larger orifice area compared to the orifice of the mitral valve, the ring is weaker and the core of the vortex has smaller propagation speed. The peak velocity near the mitral annulus in LV with

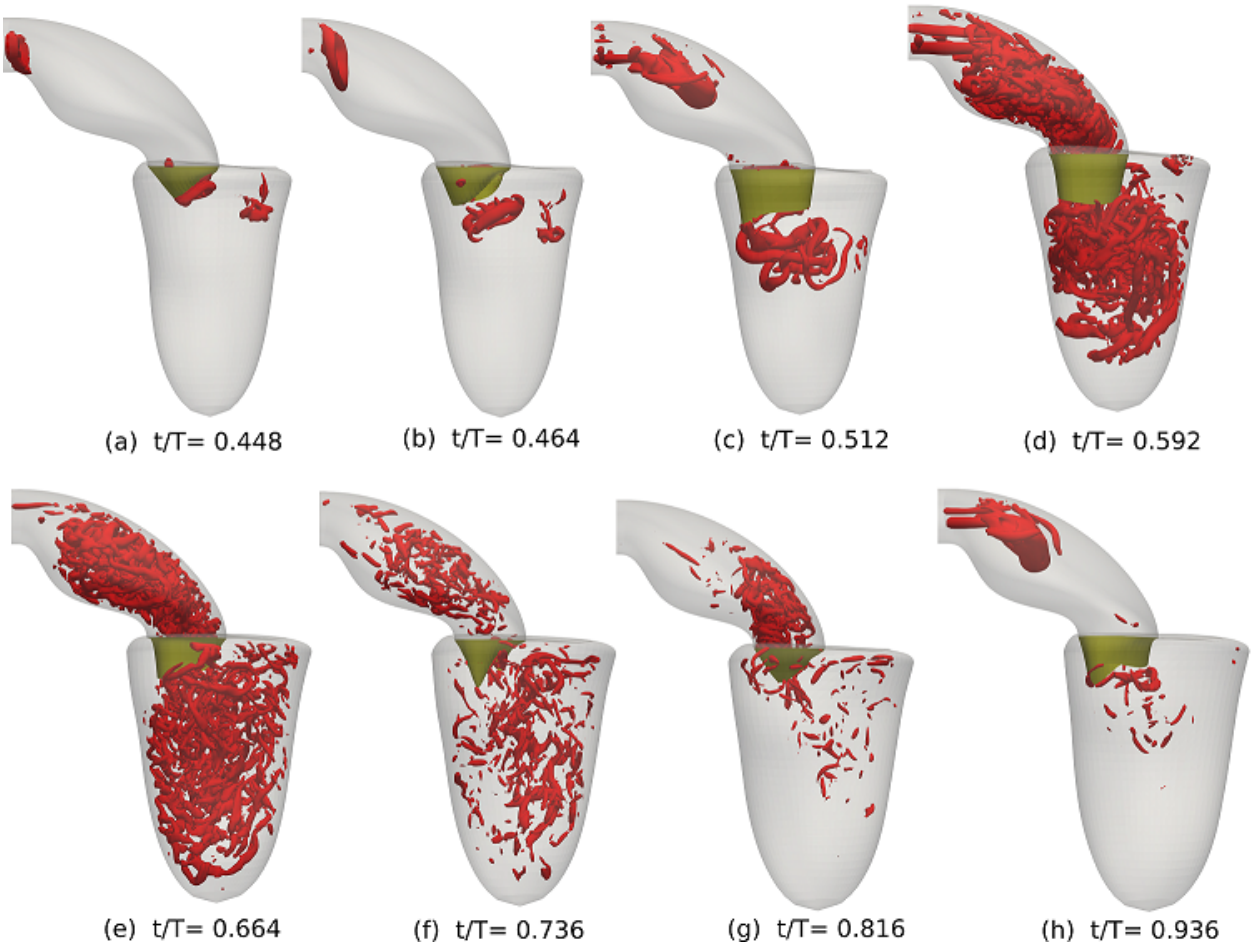

Figure 6.4: 3D vortical structures visualized at different time instances during the diastolic filling using the iso-surfaces of q-criteria for a baseline LV with reconstructed valves for different time instants during diastole (t/T=instance time / cardiac cycle length)

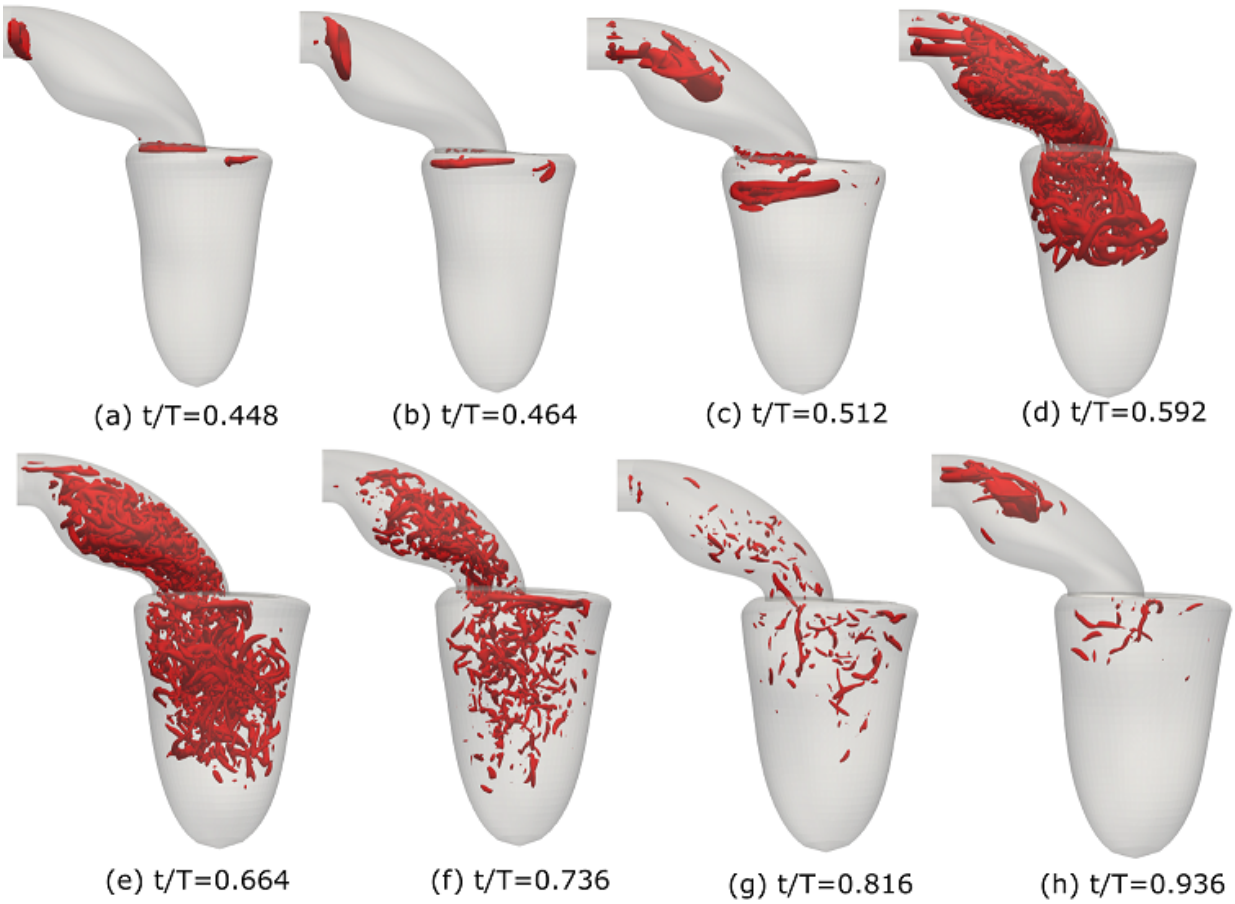

Figure 6.5: 3D vortical structures visualized at different time instances during the diastolic filling using the iso-surfaces of q-criteria for a baseline LV without valves, for different time instants during diastole (t/T=instance time / cardiac cycle length)

mitral valve is around $1.37\ m/s$ which is in agreement with the previously published physiological values for a healthy LV [53], whereas in the simulation without mitral valve this value is $0.76\ m/s$. Therefore, the vortex ring is not traveling far in the apical direction inside the LV and it starts breaking down after propagating about 30% of the LV length. This shallow vortex ring penetration depth that happens in the simulations without the mitral valve, can negatively affect the washout ability of LV in the apex region. In addition, as previously shown by Seo et al. [252] the presence of mitral valve results in a higher asymmetric diastolic flow pattern and consequently a counter-clockwise (CCW) circulation which increases the washout potential of LV. This is in agreement with our results which show the CCW circulation of about $63 \times 10^{-4}\ m^2/s$ and $41 \times 10^{-4}\ m^2/s$ for LV with and without the mitral valve, respectively, which is an increase of 35%. As it been shown in the previous study by Seo et al. [239], the asymmetric flow pattern during the diastole phase which is also reflected in the higher CCW circulation will increase the efficiency of blood ejects towards aorta during the systole phase. In addition, the effect of the aortic and mitral valve on the $\dot{loss}$ is investigated in Table 6.2. As can be seen the presence of ventricular valve's increases the $\dot{loss}$. This increase is mainly due to the presence of aortic valve during the systole. However, the presence of aortic valve is essential to prevent backflow during the diastolic phase.

6.3.2.2 Comparing healthy and acute myocardial infarction reconstructed LV

Acute myocardial infarction can significantly affect the performance of LV during the systole. Several studies [287, 288, 289] investigated the effect of the acute myocardial infarction on systolic functionalities in terms of EF and the amount of blood flux through the aorta. Figure 6.6 shows the maximum velocity of flow through the aortic orifice at peak systole. As can be seen, the magnitude of velocity in the healthy LV is higher than the acute myocardial infarction case which is due to the lower EF in the acute myocardial infarction LV.

Acute myocardial infarction can also affect the diastolic performance of the LV [290] in terms of the filling pattern. A bulge or dyskinetic region in the reconstructed endocardial of the acute myocardial infarction case can be seen in Fig. 6.7. The visualization of vortical structures using q-criteria in this figure shows the formation of a vortex ring from the tip of mitral leaflets the same

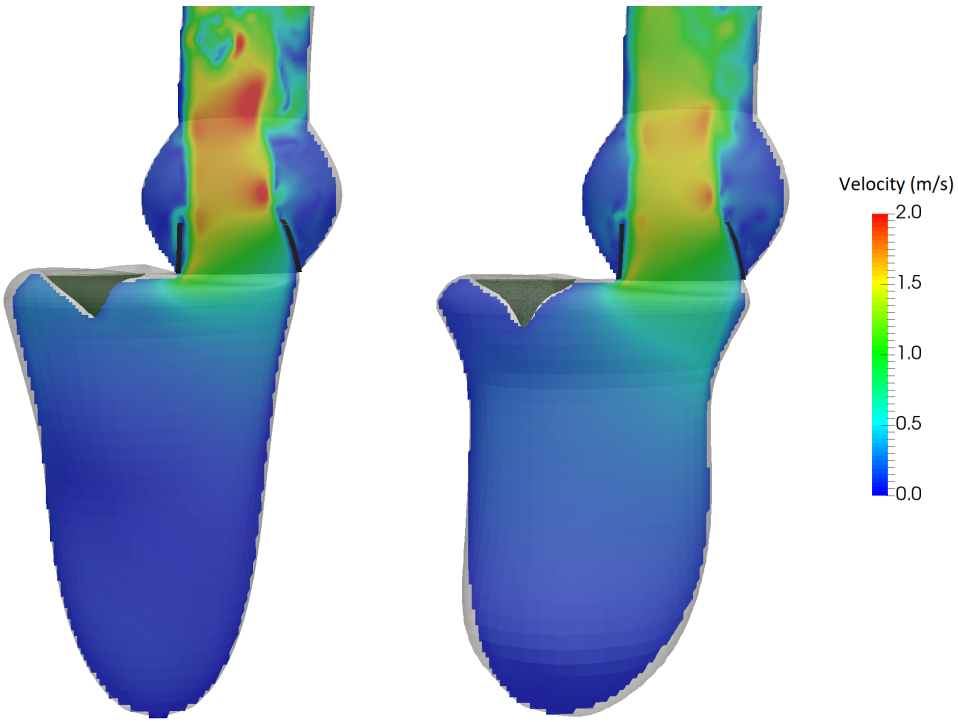

Figure 6.6: Comparison of the flow velocity in the aortic orifice at peak systole between (a) baseline (b) AMI left ventricle.

as the healthy subject. The vortex ring formed in the acute myocardial infarction subject is weaker and has a lower propagation velocity($1.12\ m/s$ compared to the healthy one $1.37\ m/s$) and thus it disintegrates and dissipates in the sooner. It can also be seen that in the acute myocardial infarction simulation the vortical structures are predominantly found in the region directly beneath the mitral annulus, as compared to a more uniform and looped sweeping of structures in a healthy subject. Comparison of the $\dot{loss}$ in Table 6.2 for acute myocardial infarction and healthy LV shows that the acute myocardial infarction LV has a higher $\dot{loss}$ by approximately 20% compared to the healthy one. The results suggest that $\dot{loss}$ can be used as a promising indicator to measure the performance of LV.

6.4 Validation and sensitivity study

To validate our hybrid echo-computational fluid dynamics framework for the hemodynamic analysis of left ventricle, the velocity calculated from the numerical simulations are compared to

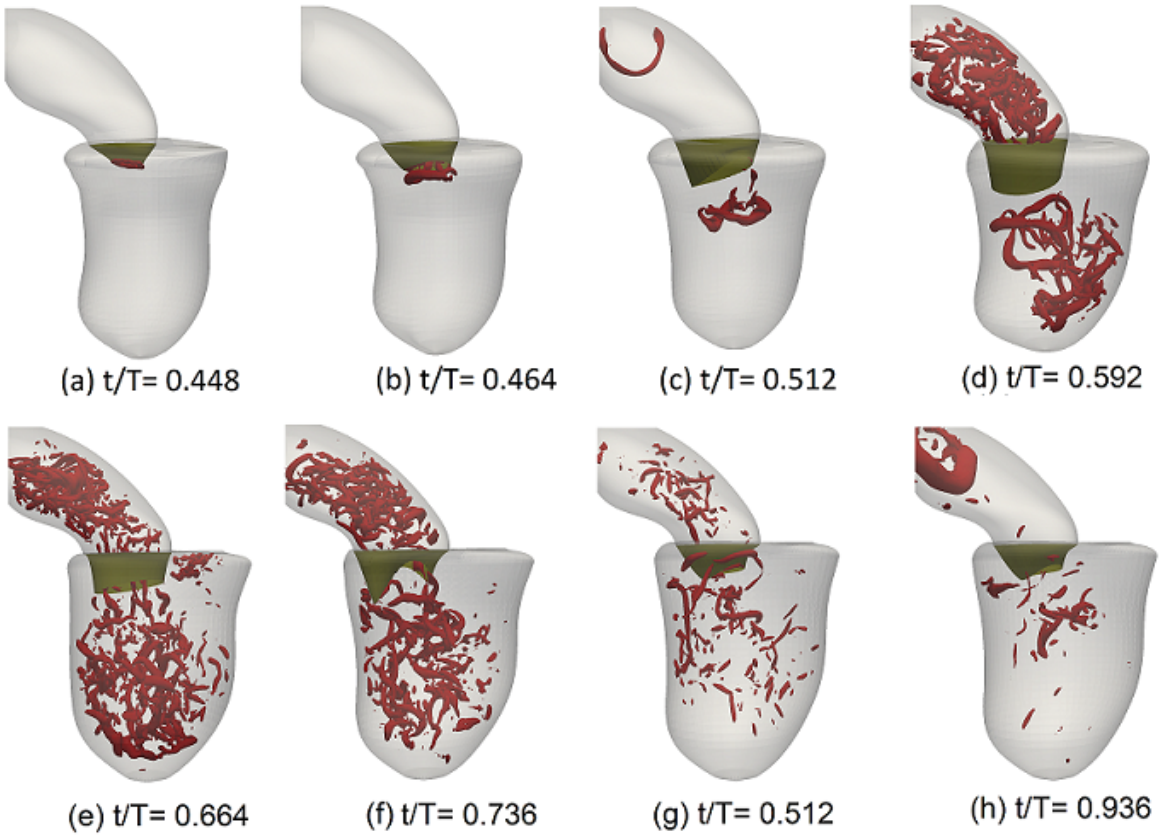

Figure 6.7: 3D vortical structures visualised at different time instances during the diastolic filling using the iso-surfaces of q-criteria for a acute myocardial infarction afflicted LV (t/T=instance time / cardiac cycle length)

Doppler ultrasound velocity measurements of the same experiments for both healthy and acute myocardial infarction cases on a section right under the mitral valve (Fig. 6.8). As can be seen in this figure the velocity calculated from the simulations are in good agreement with the experimental measurements during diastole for both healthy and acute myocardial infarction case. Since the section on which the velocity has been measured during the experiment will go through the atria during systole the results are not reported for this phase of the cardiac cycle. Although Doppler is a good measure for validation of flow inside LV, the comparison is limited to a component of the velocity normal to the section on which the measurements are performed during the experiments. To perform a more reliable validation other image modalities (e.g., 4D-MRI, PIV, etc.) should be performed along with the Doppler measurements for 3D flow visualization [291, 292]. In addition, the sensitivity of the final 3D-reconstruction of LV with respect to the number of long-axis sections used for the reconstruction in terms of the volumetric curve is shown in Fig. 6.9. The results show that the volume curve is not changing considerably by increasing the number of log-axis sections. These results are in agreement with previous research on 3D-reconstruction of LV from 2D-echo [293]. The effect of using a different number of sections as well as the temporal and spatial resolution on the 3D-reconstruction is investigated thoroughly by Rajan et al. [251]. Regarding the computational fluid dynamic simulations, the spatial and temporal resolution used in this study is similar to the previous study by Song and Borazjani [253] which was found to be fine enough to produce grid-independent results.

6.5 Limitations and future works

The segmentation task in 2D-echo is a challenging task due to the available speckle noises in these images. Therefore, most of the available segmentation methods (including the one used in this study) need some extent of manual segmentation. In addition, the valves are segmented manually by an expert which may expose the framework to an inter- and intra-observer variability. In the future, automatic segmentation using deep leaning method should be used to minimize the manual operations. The microanatomy of the valves (e.g., the mitral valve has two leaflets and a D-shape orifice versus the presented study in which the orifice is O-shape. In addition, the

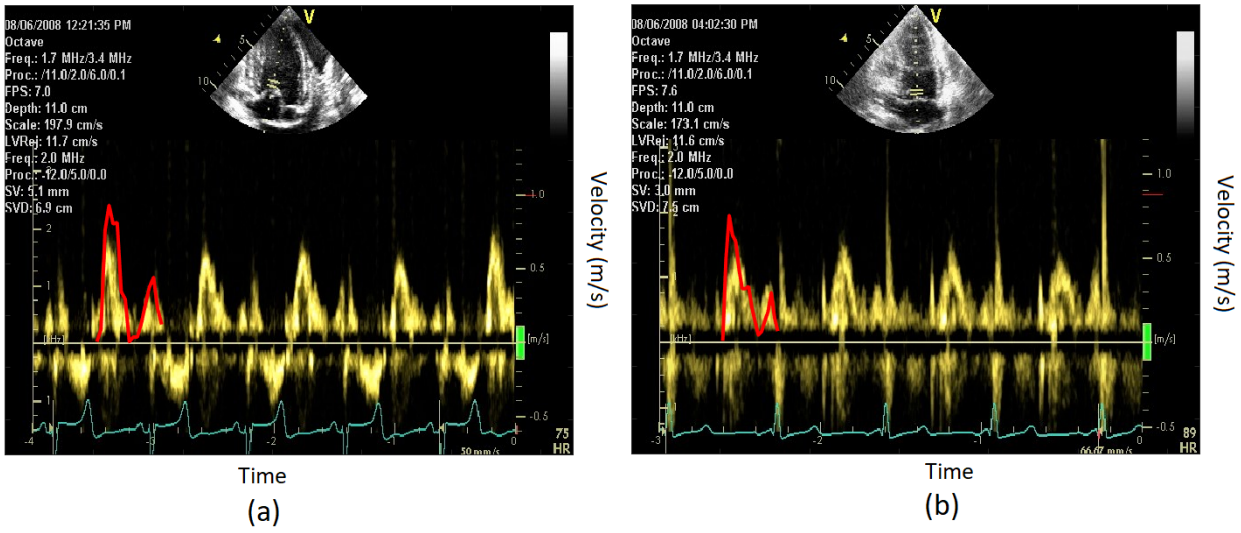

Figure 6.8: Comparison between the Doppler velocity measurements and the velocity from the numerical simulation during diastole on a section below the mitral valve.

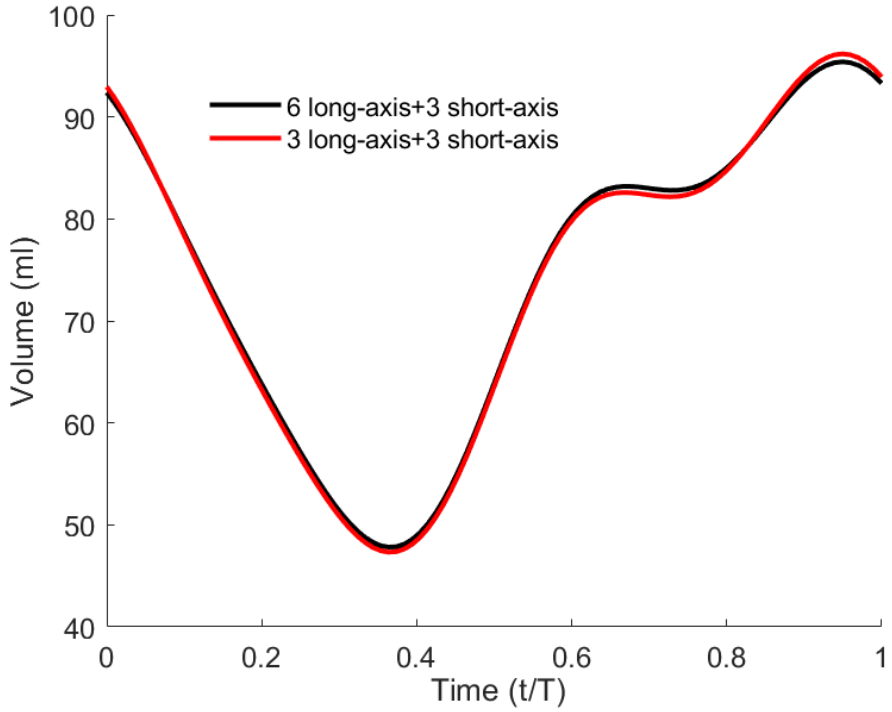

Figure 6.9: Comparison of the volume of 3D reconstructed baseline LV using different number of long-axis cross-sections.

mitral and aortic valves are not on the plane parallel to each other) is not accurate since the valves are reconstructed based on the limited number of views from 2D-echo images. In addition, the basal section of the LV is simplified (including the orientation of the mitral and aortic valves) due to a lack of available images and using the echo-pack segmentation software. Therefore, an improvement in the segmentation process is required to identify beyond the basal section. The effect of atria on the flow inside the LV is yet to be investigated. While some researchers found the influence of atria on the flow inside the LV insignificant [294], others reported the proper modeling of atria is essential especially for LVs with high ejection fraction [295]. In this work, the atria are generated based on simplifying assumptions and not from medical images. Therefore, the anatomy of the atria may not be physiological and need to be improved in future works. In addition, the final LV wall is smoothed out and the effect of the Left ventricular trabeculae is neglected (the effect of trabeculae is investigated in some literature e.g. by Sacco et al [240]). Furthermore, flow validation using 4D-flow MRI is needed to accurately validate the 3D flow structures inside the LV.

7. SUMMARY AND OUTLOOK*

Artificial heart valves are far from ideal. Thrombus formation is a major concern for recipients of mechanical heart valves (MHVs), which requires them to take anticoagulant drugs for the rest of their lives. Bioprosthetic heart valves (BHVs) do not require anticoagulant therapy but deteriorate after 10 to 15 years. Bileaflet mechanical heart valves (BMHVs) are prone to thromboembolic complications which are believed to be initiated by platelet activation. The main challenge inaccurate hemodynamic investigation of the prosthetic heart valves is different length scales involved in bulk and leakage flows during the cardiac cycle. For instance, the diameter of the mechanical heart valves typically varies from 21 to 25 mm where the leaflet can undergo large displacement of the same dimension. On the other hand, the hinge gap sizes in a BMHVs as an example of a mechanical heart valve has a dimension of around 100μ m. Therefore, performing a multi-scale simulation for simultaneously investigating the bulk flow and hinge region is a must.

Currently, two hypotheses are available regarding the main source of platelet activation in BMHVs. While researchers agree on the contribution of bulk flow during the systole phase in poor hemodynamic performance of BMHVs, it is mostly believed that the main source of platelet activation is the leakage flow through the hinge region because that the clot formation is typically observed near the hinge region. As the first step in testing this hypothesis, we quantified the role of bulk flow during the systole through BMHVs. Our results show that the activation in the bulk flow during the systole phase might play an essential role as well (section 4). This is based on our results obtained by comparing the thrombogenic performance of a MHV and a BHV (as control) in terms of shear-induced platelet activation under exactly the same conditions (section 4). Three different mathematical activation models including the linear level of activation, damage accumulation, and Soares model are tested to quantify the platelet activation during systole using the previous simulations of the flow through MHV and BHV in a straight aorta under the same physiologic flow

*Part of this chapter is reprinted with permission from "Platelet activation of mechanical versus bioprosthetic heart valves during systole" by M. Hedayat et al., 2017, Journal of biomechanics, 56, 111-116, Copyright 2017 by Elsevier Ltd.

conditions. Results indicate that the platelet activation in the MHV at the beginning of the systole phase is slightly less than the BHV. However, at the end of the systole phase, the platelet activation by the bulk flow for the MHV is several folds (1.41, 5.12 and 2.81 for the linear level of activation, damage accumulation, and Soares model, respectively) higher than the BHV for all tested platelet activation models (section 4).

Performing multi-scale flow simulation through heart valves is not trivial by using conventional numerical methods such as ALE methods or fixed grid immersed boundaries due to the enormous computational cost and different grid resolution needed for a different part of the simulation which can vary by 3 order of magnitude. Therefore, the use of overset grids for performing a multi-scale simulation is required. However, to reduce the computational cost associated with the overset grids due to the grid assembly and interpolation an efficient grid assembly algorithm is needed. To overcome this challenge a parallel dynamic overset framework has been developed for the curvilinear immersed boundary (overset-CURVIB) method to enable tackling a wide range of challenging flow problems (section 2). The dynamic overset grids are used to locally increase the grid resolution near complex immersed bodies, which are handled using a sharp interface immersed boundary method, undergoing large movements as well as arbitrary relative motions. The new framework extends the previous overset-CURVIB method with fixed overset grids and a sequential grid assembly to moving overset grids with an efficient parallel grid assembly. In addition, a new method for the interpolation of variables at the grid boundaries is developed which can drastically decrease the execution time and increase the parallel efficiency of our framework compared to the previous strategy. The moving/rotating overset grids are solved in a non-inertial frame of reference to avoid recalculating the curvilinear metrics of transformation while the background/stationary grids are solved in the inertial frame. The new framework is verified and validated against experimental data, and analytical/benchmark solutions (section 3). In addition, the results of the overset grid are compared with results over a similar single grid. The method is shown to be 2^{nd} order accurate, decrease the computational cost relative to a single grid, and good overall parallel speedup (section 3). The grid assembly takes less than 7% of the total CPU time even at the highest number of CPUs

tested in this work. The capabilities of our method are demonstrated by simulating the flow past a school of self-propelled aquatic swimmers arranged initially in a diamond pattern (section 3).

Using the overset-CURVIB flow solver a multi-scale simulation performed on a bileaflet mechanical heart valves to investigate the contribution of bulk and hinge flows to the activation of platelets in BMHVs (section 5) for the first time by performing simulations of the flow through a BMHV and resolving the hinge by overset grids (one grid for the bulk flow and two for the hinge regions coupled together using one-way and two-way interpolation). It was found that two-way coupling is essential to obtain correct hinge flow features. The platelet activation through the hinge for two gap sizes (250 and 150 μm) is compared to the activation in the bulk flow using two platelet activation models to ensure the consistency of the observed trends. The larger gap has a higher total activation, but a better washout ability due to higher velocities. The maximum shear stress observed in the bulk flow ($\sim$ 320 $dyne/cm^2$) is much smaller than the hinge ($\sim$ 1000 $dyne/cm^2$). However, the total activation by the bulk flow is found to be several folds higher than by the hinge/leakage flow. This is mainly due to the higher flow rate of the bulk flow which exposes many more platelets to shear stress than the leakage flow.

Simulation of heart valves in simplified geometries such as simplified aorta which was the subject of our research in section 4 and section 5 can provide essential information in investigating the hemodynamics and performance of the prosthetic heart valves. This simulation provides valuable information to improve the design of prosthetic heart valves. Several comparisons between the CFD simulations and in-vitro experiments have been performed which show the accuracy of CFD simulations in predicting the functionality of heart valves during a cardiac cycle. However, performing the simulation in idealized or simplified geometries and boundary conditions can provide limited (although important) information about the functionality of prosthetic devices in a specific patient where the simplified assumptions may not apply. In addition, the geometry, as well as the cardiac parameters including the heart rate, ejection fraction (EF), stoke-volume (SV), cardiac output and etc., can vary from one patient to another. Therefore, the implanted prosthetic valves can perform differently from patient to patient. patient-specific simulations can play an important

role in the development of medical devices such as heart valves. In addition, a reliable analysis of intraventricular flow under the realistic assumptions can provide a powerful indicator for the abnormal functionality of the cardiovascular system since the abnormal hemodynamics of the blood can result in the development of structural modifications in the cardiovascular system. Thus numerical simulation of the cardiovascular flows not only can lead to the diagnosis of existing abnormalities but also can help in the prediction of feature possible diseases. To evaluate the hemodynamics performance of artificial heart valves and optimize their design and placement for specific patients employing medical images and combining them with CFD tools is essential. in this section 6, echo is combined with CFD, i.e., an echo-CFD framework, to study ventricular flows. To achieve this, the previous 3D reconstruction from multiple 2D echo at standard cross-sections is extended by 1) reconstructing aortic and mitral valves from 2D echo and closing the LV geometry by approximating a superior wall; 2) incorporating the physiological assumption of the fixed apex as a reference (fixed) point in the 3D reconstruction; and 3) incorporating several smoothing algorithms to remove the nonphysical oscillations (ringing) near the basal section (section 6). The method is applied to echo images from a baseline left-ventricle (LV) and an LV after inducing acute myocardial infarction (AMI). The 3D reconstruction is validated by comparing it against a reference reconstruction from many echo sections while flow simulations are validated against the Doppler ultrasound velocity measurements. The sensitivity study shows that the choice of the smoothing algorithm does not change the flow pattern inside the LV. However, the presence of the mitral valve can significantly change the flow pattern during the diastole phase. In addition, the abnormal shape of an LV with AMI can drastically change the flow during diastole. Furthermore, the hemodynamic energy loss, as an indicator of the LV pumping performance, for different test cases is calculated, which shows a larger energy loss for an LV with AMI compared to the baseline one.

7.1 Future work

For future work, we plan to use the overset-CRVIB framework for investigating the thrombogenic performance analysis of trileaflet valves using a highly resolved flow simulation because these valves may have lower platelet activation compared to bileaflet ones as their flow during

systole is much closer to the bioprosthetic ones. In addition, to investigated the hemodynamics of heart valves for a specific patient under realistic conditions (e.g., realistic geometry, flow boundary condition, etc.), patient-specific fluid-structure interaction simulation by combining the echocardiography images and artificial hear valves is planned to be performed. These two ideas are further discussed below:

a) Thrombogenic performance analysis of trileaflet valves

The design of the current BMHVs is based on a design developed in the early 1970s. Since then there has been some progress in the design of mechanical heart valves. However, the current artificial heart valves are far from ideal. BMHVs generate a non-physiological flow pattern during the systole phase as well as high shear stress near the hinge region during the diastole. As discussed in section 4, the platelet activation due to non-physiological flow in the bulk flow is much higher compared to the BHVs (which generates flow similar to the native valve). In addition, As discussed in section 5, the activation during the systole is considerably higher compared to the hinge region. Concluding from these results, a valve with a central jet-like BHV might have lower activation compared to other types of valves. In order to compensate these issues, recently, trileaflet valves have been introduced. These valves combine the favorable hemodynamics of bioprosthetic heart valves with the durability of mechanical heart valves. During the systole, these valves generate the flow pattern similar to the bioprosthetic ones which can drastically reduce the area of high shear stress by providing a large central orifice area. In addition, this design provides a smooth closing during the deceleration phase and reduces the risk of exposing the platelets to a high level of shear stress in the hinge area. Investigating the thrombogenic performance of trileaflet valves through numerical simulations and comparing the hemodynamics as well as the platelet activation between trileaflet and BMHVs valves can provide a basis to move toward less thrombogenic mechanical prostheses and durable mechanical heart valves.

b) Combination of FSI simulation and platelet activation with echo-CFD

Patient-specific computational fluid dynamics can provide valuable information for clinical decision-making. Using the echo-CFD framework developed in this work provides the opportu-

nity to analyze the performance of the heart valves in more realistic conditions. By combining the FSI techniques with the echo-CFD framework as well as platelet activation a patient-specific analysis of mechanical heart valves will be possible which can provide the surgeons valuable information for surgery planning and eventually optimize the factors involved in the surgery such calculating the orientation and placement of the artificial valves in the surgeries to minimize the surgery compilation as well as choosing the right type of artificial valve for a specific patient.

REFERENCES

[1] I. Borazjani, L. Ge, T. Le, and F. Sotiropoulos, "A parallel overset-curvilinear-immersed boundary framework for simulating complex 3d incompressible flows," *Computers & fluids*, vol. 77, pp. 76–96, 2013.

[2] H. Dütsch, F. Durst, S. Becker, and H. Lienhart, "Low-reynolds-number flow around an oscillating circular cylinder at low keulegan–carpenter numbers," *Journal of Fluid Mechanics*, vol. 360, pp. 249–271, 1998.

[3] M. Hedayat and I. Borazjani, "Comparison of platelet activation through hinge vs bulk flow in bileaflet mechanical heart valves," *Journal of biomechanics*, vol. 83, pp. 280–290, 2019.

[4] J. S. Soares, J. Sheriff, and D. Bluestein, "A novel mathematical model of activation and sensitization of platelets subjected to dynamic stress histories," *Biomechanics and modeling in mechanobiology*, vol. 12, no. 6, pp. 1127–1141, 2013.

[5] M. Hedayat, H. Asgharzadeh, and I. Borazjani, "Platelet activation of mechanical versus bioprosthetic heart valves during systole," *Journal of Biomechanics*, vol. 56, pp. 111–116, 2017.

[6] L. Dasi, L. Ge, H. Simon, F. Sotiropoulos, and A. Yoganathan, "Vorticity dynamics of a bileaflet mechanical heart valve in an axisymmetric aorta," *Physics of Fluids*, vol. 19, no. 6, p. 067105, 2007.

[7] B. H. Jun, N. Saikrishnan, S. Arjunon, B. M. Yun, and A. P. Yoganathan, "Effect of hinge gap width of a st. jude medical bileaflet mechanical heart valve on blood damage potential—an in vitro micro particle image velocimetry study," *Journal of biomechanical engineering*, vol. 136, no. 9, p. 091008, 2014.

[8] B. Iung and A. Vahanian, "Epidemiology of valvular heart disease in the adult," *Nature Reviews Cardiology*, vol. 8, no. 3, pp. 162–172, 2011.

[9] M. A. Clark, F. G. Duhay, A. K. Thompson, M. J. Keyes, L. G. Svensson, R. O. Bonow, B. T. Stockwell, and D. J. Cohen, "Clinical and economic outcomes after surgical aortic valve replacement in medicare patients," *Risk management and healthcare policy*, vol. 5, p. 117, 2012.

[10] R. M. Suri and H. V. Schaff, "Is tissue valve the preferred option for patients aged 60 years and older?: Selection of aortic valve prostheses: contemporary reappraisal of mechanical versus biologic valve substitutes," *Circulation*, vol. 128, no. 12, pp. 1372–1380, 2013.

[11] P. Bloomfield, "Choice of heart valve prosthesis," *Heart*, vol. 87, no. 6, pp. 583–589, 2002.

[12] T. Carrel, W. P. Dembitsky, B. Mol, D. Obrist, G. Dreyfus, B. Meuris, B. Vennemannd, D. Lapeyre, and H. Schaffi, "Non-physiologic closing of bi-leaflet mechanical heart prostheses requires a new tri-leaflet valve design," *International Journal of Cardiology*, p. in press, 2020.

[13] P. Zilla, J. Brink, P. Human, and D. Bezuidenhout, "Prosthetic heart valves: catering for the few," *Biomaterials*, vol. 29, no. 4, pp. 385–406, 2008.

[14] P. Singhal, A. Luk, and J. Butany, "Bioprosthetic heart valves: impact of implantation on biomaterials," *ISRN Biomaterials*, vol. 2013, 2013.

[15] S. J. Head, M. Çelik, and A. P. Kappetein, "Mechanical versus bioprosthetic aortic valve replacement," *European heart journal*, vol. 38, no. 28, pp. 2183–2191, 2017.

[16] H. A. Simon, *Numerical simulations of the micro flow field in the hinge region of bileaflet mechanical heart valves*. PhD thesis, Georgia Institute of Technology, 2009.

[17] R. Figliola and T. Mueller, "On the hemolytic and thrombogenic potential of occluder prosthetic heart valves from in-vitro measurements," 1981.

[18] M. J. LEVER, "Cardiovascular assist systems," in *Biomaterials, artificial organs and tissue engineering*, pp. 179–190, Elsevier, 2005.

[19] R. Roudaut, K. Serri, and S. Lafitte, "Thrombosis of prosthetic heart valves: diagnosis and therapeutic considerations," *Heart*, vol. 93, no. 1, pp. 137–142, 2007.

[20] U. Morbiducci, R. Ponzini, M. Nobili, D. Massai, F. M. Montevecchi, D. Bluestein, and A. Redaelli, "Blood damage safety of prosthetic heart valves. shear-induced platelet activation and local flow dynamics: a fluid–structure interaction approach," *Journal of biomechanics*, vol. 42, no. 12, pp. 1952–1960, 2009.

[21] M. S. Zakaria, F. Ismail, M. Tamagawa, A. F. A. Aziz, S. Wiriadidjaja, A. A. Basri, and K. A. Ahmad, "Review of numerical methods for simulation of mechanical heart valves and the potential for blood clotting," *Medical & biological engineering & computing*, vol. 55, no. 9, pp. 1519–1548, 2017.

[22] B. Min Yun, C. K. Aidun, and A. P. Yoganathan, "Blood damage through a bileaflet mechanical heart valve: a quantitative computational study using a multiscale suspension flow solver," *Journal of biomechanical engineering*, vol. 136, no. 10, 2014.

[23] R. Carey, J. Porter, G. Richard, C. Luck, M. Shu, G. Guo, D. Elizondo, C. Kingsbury, S. Anderson, and B. Herman, "An interlaboratory comparison of the fda protocol for the evaluation of cavitation potential of mechanical heart valves.," *The Journal of heart valve disease*, vol. 4, no. 5, pp. 532–9, 1995.

[24] Z. He, B. Xi, K. Zhu, and N. Hwang, "Mechanisms of mechanical heart valve cavitation: investigation using a tilting disk valve model.," *The Journal of heart valve disease*, vol. 10, no. 5, pp. 666–674, 2001.

[25] B. H. Jun, N. Saikrishnan, and A. P. Yoganathan, "Micro particle image velocimetry measurements of steady diastolic leakage flow in the hinge of a st. jude medical® regent™ mechanical heart valve," *Annals of biomedical engineering*, vol. 42, no. 3, pp. 526–540, 2014.

[26] D. Hasler, A. Landolt, and D. Obrist, "Tomographic piv behind a prosthetic heart valve," *Experiments in Fluids*, vol. 57, no. 5, p. 80, 2016.

[27] V. Raghav, S. Sastry, and N. Saikrishnan, "Experimental assessment of flow fields associated with heart valve prostheses using particle image velocimetry (piv): recommendations for best practices," *Cardiovascular engineering and technology*, vol. 9, no. 3, pp. 273–287, 2018.

[28] H. Hatoum and L. P. Dasi, "Reduction of pressure gradient and turbulence using vortex generators in prosthetic heart valves," *Annals of biomedical engineering*, vol. 47, no. 1, pp. 85–96, 2019.

[29] V. Esfahanian, M. Hedayat, B. Baghapour, M. Torabzadeh, and S. Hosseini, "An implicit multigrid solver for high-order compressible flow simulations on gpus," 2013.

[30] V. Esfahanian, M. Allahyarri, and M. Hedayat, "High-order compact finite-difference on multi-block domains with parallelization implementation,"

[31] A. M. Akbarzadeh, A. Moosavi, and A. M. Kheirabadi, "Dewetting of evaporating thin films over nanometer-scale topographies," *Physical Review E*, vol. 90, no. 1, p. 012409, 2014.

[32] F. Rousta and B. Lessani, "Near-wall heat transfer of solid particles in particle-laden turbulent flows," *International Communications in Heat and Mass Transfer*, vol. 112, p. 104475, 2020.

[33] H. Asadi, M. Taeibi-Rahni, A. M. Akbarzadeh, K. Javadi, and G. Ahmadi, "Investigation of hydrodynamically dominated membrane rupture, using smoothed particle hydrodynamics–finite element method," *Fluids*, vol. 4, no. 3, p. 149, 2019.

[34] A. Mokhtare, A. Jafari, and E. P. Furlani, "Numerical simulation of flow and heat transfer of a ferrofluid in a partially filled porous channel in a gradient magnetic field,"

[35] H. Asadi, "Two-dimensional numerical investigation of oscillatory shear-driven flows in slip flow regime between two microscale concentric cylinders," in *Applied Mechanics and Materials*, vol. 704, pp. 299–304, Trans Tech Publ, 2015.

[36] M. Allahyari and K. Mohseni, "Numerical simulation of flows with shocks and turbulence using observable methodology," in *2018 AIAA Aerospace Sciences Meeting*, p. 0066, 2018.

[37] F. Sotiropoulos and I. Borazjani, "A review of state-of-the-art numerical methods for simulating flow through mechanical heart valves," *Medical & biological engineering & computing*, vol. 47, no. 3, pp. 245–256, 2009.

[38] R. van Loon, P. D. Anderson, and F. N. van de Vosse, "A fluid–structure interaction method with solid-rigid contact for heart valve dynamics," *Journal of computational physics*, vol. 217, no. 2, pp. 806–823, 2006.

[39] J. Stijnen, J. De Hart, P. Bovendeerd, and F. Van de Vosse, "Evaluation of a fictitious domain method for predicting dynamic response of mechanical heart valves," *Journal of Fluids and Structures*, vol. 19, no. 6, pp. 835–850, 2004.

[40] E. Shim and K. S. Chang, "Three-dimensional vortex flow past a tilting disc valve using a segregated finite element scheme," *Computational Fluid Dynamics Journal*, vol. 3, no. 1, pp. 205–222, 1994.

[41] E.-B. Shim and K.-S. Chang, "Numerical analysis of three-dimensional bjo¨ rk–shiley valvular flow in an aorta," 1997.

[42] L. Ge, H.-L. Leo, F. Sotiropoulos, and A. P. Yoganathan, "Flow in a mechanical bileaflet heart valve at laminar and near-peak systole flow rates: Cfd simulations and experiments," 2005.

[43] K. Liu, H. Radhakrishnan, and V. H. Barocas, "Simulation of flow around a thin, flexible obstruction by means of a deforming grid overlapping a fixed grid," *International journal for numerical methods in fluids*, vol. 56, no. 6, pp. 723–738, 2008.

[44] K. Dumont, J. Vierendeels, R. Kaminsky, G. Van Nooten, P. Verdonck, and D. Bluestein, "Comparison of the hemodynamic and thrombogenic performance of two bileaflet mechanical heart valves using a cfd/fsi model," *Journal of biomechanical engineering*, vol. 129, no. 4, pp. 558–565, 2007.

[45] R. Cheng, Y. Lai, and K. B. Chandran, "Two-dimensional fluid-structure interaction simulation of bileaflet mechanical heart valve flow dynamics.," *The Journal of heart valve disease*, vol. 12, no. 6, pp. 772–780, 2003.

[46] I. Borazjani, L. Ge, and F. Sotiropoulos, "Curvilinear immersed boundary method for simulating fluid structure interaction with complex 3d rigid bodies," *Journal of Computational physics*, vol. 227, no. 16, pp. 7587–7620, 2008.

[47] M. De Tullio, A. Cristallo, E. Balaras, and R. Verzicco, "Direct numerical simulation of the pulsatile flow through an aortic bileaflet mechanical heart valve," *Journal of Fluid Mechanics*, vol. 622, pp. 259–290, 2009.

[48] S. S. Abbas, M. S. Nasif, M. A. M. Said, and R. Al-Waked, "Numerical simulation of the non-newtonian blood flow through aortic bileaflet mechanical heart valve using fluid-structure interaction approach," in *AIP Conference Proceedings*, vol. 2035, p. 070003, AIP Publishing LLC, 2018.

[49] S. S. Abbas, M. S. Nasif, R. Al-Waked, and M. A. M. Said, "Numerical investigation on the relationship of cavitation initiation in bileaflet mechanical heart valves (bmhvs) with the aortic root geometry and valve's implantation rotation angle," *Journal of the Brazilian Society of Mechanical Sciences and Engineering*, vol. 42, no. 1, p. 23, 2020.

[50] M. Mokbel, D. Mokbel, A. Mietke, N. Traber, S. Girardo, O. Otto, J. Guck, and S. Aland, "Numerical simulation of real-time deformability cytometry to extract cell mechanical properties," *ACS Biomaterials Science & Engineering*, vol. 3, no. 11, pp. 2962–2973, 2017.

[51] F. De Vita, M. De Tullio, and R. Verzicco, "Numerical simulation of the non-newtonian blood flow through a mechanical aortic valve," *Theoretical and computational fluid dynamics*, vol. 30, no. 1-2, pp. 129–138, 2016.

[52] B. Khellaf and B. Boussad, "Computational hemodynamic investigation of a new bileaflet mechanical heart valve," *SIMULATION*, p. 0037549719886364, 2019.

[53] F. Sotiropoulos, T. B. Le, and A. Gilmanov, "Fluid mechanics of heart valves and their replacements," *Annual Review of Fluid Mechanics*, vol. 48, pp. 259–283, 2016.

[54] G. D'Avenio, G. Wang, Y. Li, D. Rafiroiu, G. De Angelis, and M. Grigioni, "Piv and cfd insight into the hinge and near-hinge flow fields of bileaflet mechanical heart valves," in *XIV Mediterranean Conference on Medical and Biological Engineering and Computing 2016*, pp. 694–699, Springer, 2016.

[55] H. A. Simon, L. Ge, F. Sotiropoulos, and A. P. Yoganathan, "Simulation of the three-dimensional hinge flow fields of a bileaflet mechanical heart valve under aortic conditions," *Annals of biomedical engineering*, vol. 38, no. 3, pp. 841–853, 2010.

[56] B. M. Yun, J. Wu, H. A. Simon, S. Arjunon, F. Sotiropoulos, C. K. Aidun, and A. P. Yoganathan, "A numerical investigation of blood damage in the hinge area of aortic bileaflet mechanical heart valves during the leakage phase," *Annals of biomedical engineering*, vol. 40, no. 7, pp. 1468–1485, 2012.

[57] J. Donea, S. Giuliani, and J.-P. Halleux, "An arbitrary lagrangian-eulerian finite element method for transient dynamic fluid-structure interactions," *Computer methods in applied mechanics and engineering*, vol. 33, no. 1-3, pp. 689–723, 1982.

[58] C. W. Hirt, A. A. Amsden, and J. Cook, "An arbitrary lagrangian-eulerian computing method for all flow speeds," *Journal of computational physics*, vol. 14, no. 3, pp. 227–253, 1974.

[59] J. Donea, A. Huerta, J.-P. Ponthot, and A. Rodríguez-Ferran, "Arbitrary l agrangian–e ulerian methods," *Encyclopedia of Computational Mechanics Second Edition*, pp. 1–23, 2017.

[60] S. Wang, B. Khoo, G. Liu, and G. Xu, "An arbitrary lagrangian–eulerian gradient smoothing method (gsm/ale) for interaction of fluid and a moving rigid body," *Computers & fluids*, vol. 71, pp. 327–347, 2013.

[61] A. Guardone, D. Isola, and G. Quaranta, "Arbitrary lagrangian eulerian formulation for two-dimensional flows using dynamic meshes with edge swapping," *Journal of Computational Physics*, vol. 230, no. 20, pp. 7706–7722, 2011.

[62] P. Wang, "Modeling material responses by arbitrary lagrangian eulerian formulation and adaptive mesh refinement method," *Journal of Computational Physics*, vol. 229, no. 5, pp. 1573–1599, 2010.

[63] R. Cheng, Y. G. Lai, and K. B. Chandran, "Three-dimensional fluid-structure interaction simulation of bileaflet mechanical heart valve flow dynamics," *Annals of biomedical engineering*, vol. 32, no. 11, pp. 1471–1483, 2004.

[64] J. Peraire, M. Vahdati, K. Morgan, and O. C. Zienkiewicz, "Adaptive remeshing for compressible flow computations," *Journal of computational physics*, vol. 72, no. 2, pp. 449–466, 1987.

[65] R. Löhner, "Adaptive remeshing for transient problems," *Computer Methods in Applied Mechanics and Engineering*, vol. 75, no. 1-3, pp. 195–214, 1989.

[66] M. J. Berger and P. Colella, "Local adaptive mesh refinement for shock hydrodynamics," *Journal of computational Physics*, vol. 82, no. 1, pp. 64–84, 1989.

[67] P. MacNeice, K. M. Olson, C. Mobarry, R. De Fainchtein, and C. Packer, "Paramesh: A parallel adaptive mesh refinement community toolkit," *Computer physics communications*, vol. 126, no. 3, pp. 330–354, 2000.

[68] B. S. Kirk, J. W. Peterson, R. H. Stogner, and G. F. Carey, "libmesh: a c++ library for parallel adaptive mesh refinement/coarsening simulations," *Engineering with Computers*, vol. 22, no. 3-4, pp. 237–254, 2006.

[69] C. Burstedde, L. C. Wilcox, and O. Ghattas, "p4est: Scalable algorithms for parallel adaptive mesh refinement on forests of octrees," *SIAM Journal on Scientific Computing*, vol. 33, no. 3, pp. 1103–1133, 2011.

[70] F. Alauzet, A. Loseille, and G. Olivier, "Time-accurate multi-scale anisotropic mesh adaptation for unsteady flows in cfd," *Journal of Computational Physics*, vol. 373, pp. 28–63, 2018.

[71] Y. Mori and C. S. Peskin, "Implicit second-order immersed boundary methods with boundary mass," *Computer methods in applied mechanics and engineering*, vol. 197, no. 25-28, pp. 2049–2067, 2008.

[72] W. Kim, I. Lee, and H. Choi, "A weak-coupling immersed boundary method for fluid–structure interaction with low density ratio of solid to fluid," *Journal of Computational Physics*, vol. 359, pp. 296–311, 2018.

[73] Y. Ma, J. Cui, N. R. Vadlamani, and P. Tucker, "Hierarchical geometry modelling using the immersed boundary method," *Computer Methods in Applied Mechanics and Engineering*, vol. 355, pp. 323–348, 2019.

[74] M. Wang, Y. Feng, D. Owen, and T. Qu, "A novel algorithm of immersed moving boundary scheme for fluid–particle interactions in dem–lbm," *Computer Methods in Applied Mechanics and Engineering*, vol. 346, pp. 109–125, 2019.

[75] F. P. Baaijens, "A fictitious domain/mortar element method for fluid–structure interaction," *International Journal for Numerical Methods in Fluids*, vol. 35, no. 7, pp. 743–761, 2001.

[76] N. A. Patankar, P. Singh, D. D. Joseph, R. Glowinski, and T.-W. Pan, "A new formulation of the distributed lagrange multiplier/fictitious domain method for particulate flows," *International Journal of Multiphase Flow*, vol. 26, no. 9, pp. 1509–1524, 2000.

[77] D. M. Ingram, D. M. Causon, and C. G. Mingham, "Developments in cartesian cut cell methods," *Mathematics and Computers in Simulation*, vol. 61, no. 3-6, pp. 561–572, 2003.

[78] R. Glowinski, T.-W. Pan, T. I. Hesla, D. D. Joseph, and J. Periaux, "A fictitious domain approach to the direct numerical simulation of incompressible viscous flow past moving rigid bodies: application to particulate flow," *Journal of Computational Physics*, vol. 169, no. 2, pp. 363–426, 2001.

[79] M.-C. Lai and C. S. Peskin, "An immersed boundary method with formal second-order accuracy and reduced numerical viscosity," *Journal of computational Physics*, vol. 160, no. 2, pp. 705–719, 2000.

[80] A. Gilmanov and F. Sotiropoulos, "A hybrid cartesian/immersed boundary method for simulating flows with 3d, geometrically complex, moving bodies," *Journal of computational physics*, vol. 207, no. 2, pp. 457–492, 2005.

[81] W. Bennett, N. Nikiforakis, and R. Klein, "A moving boundary flux stabilization method for cartesian cut-cell grids using directional operator splitting," *Journal of Computational Physics*, vol. 368, pp. 333–358, 2018.

[82] C. S. Peskin, "The immersed boundary method," *Acta numerica*, vol. 11, pp. 479–517, 2002.

[83] R. Mittal and G. Iaccarino, "Immersed boundary methods," *Annu. Rev. Fluid Mech.*, vol. 37, pp. 239–261, 2005.

[84] F. Sotiropoulos and X. Yang, "Immersed boundary methods for simulating fluid–structure interaction," *Progress in Aerospace Sciences*, vol. 65, pp. 1–21, 2014.

[85] I. Borazjani, "A review of fluid-structure interaction simulations of prosthetic heart valves," *Journal of long-term effects of medical implants*, vol. 25, no. 1-2, 2015.

[86] C. S. Peskin, "Flow patterns around heart valves: a numerical method," *Journal of computational physics*, vol. 10, no. 2, pp. 252–271, 1972.

[87] A. M. Bavo, G. Rocatello, F. Iannaccone, J. Degroote, J. Vierendeels, and P. Segers, "Fluid-structure interaction simulation of prosthetic aortic valves: comparison between immersed boundary and arbitrary lagrangian-eulerian techniques for the mesh representation," *PloS one*, vol. 11, no. 4, p. e0154517, 2016.

[88] A. Gilmanov, H. Stolarski, and F. Sotiropoulos, "Flow–structure interaction simulations of the aortic heart valve at physiologic conditions: The role of tissue constitutive model," *Journal of biomechanical engineering*, vol. 140, no. 4, p. 041003, 2018.

[89] H. Asgharzadeh, H. Asadi, H. Meng, and I. Borazjani, "A non-dimensional parameter for classification of the flow in intracranial aneurysms. ii. patient-specific geometries," *Physics of Fluids*, vol. 31, no. 3, p. 031905, 2019.

[90] N. K. Patel, A. P. S. Bhalla, and N. A. Patankar, "A new constraint-based formulation for hydrodynamically resolved computational neuromechanics of swimming animals," *Journal of Computational Physics*, vol. 375, pp. 684–716, 2018.

[91] M. Daghooghi and I. Borazjani, "Self-propelled swimming simulations of bio-inspired smart structures," *Bioinspiration & biomimetics*, vol. 11, no. 5, p. 056001, 2016.

[92] H. Garg, A. K. Soti, and R. Bhardwaj, "A sharp interface immersed boundary method for vortex-induced vibration in the presence of thermal buoyancy," *Physics of Fluids*, vol. 30, no. 2, p. 023603, 2018.

[93] H. Asadi, H. Asgharzadeh, and I. Borazjani, "On the scaling of propagation of periodically generated vortex rings," *Journal of Fluid Mechanics*, vol. 853, pp. 150–170, 2018.

[94] A. Akbarzadeh and I. Borazjani, "A numerical study on controlling flow separation via surface morphing in the form of backward traveling waves," in *AIAA Aviation 2019 Forum*, p. 3589, 2019.

[95] I. Borazjani, "Fluid–structure interaction, immersed boundary-finite element method simulations of bio-prosthetic heart valves," *Computer Methods in Applied Mechanics and Engineering*, vol. 257, pp. 103–116, 2013.

[96] I. Borazjani, L. Ge, and F. Sotiropoulos, "High-resolution fluid–structure interaction simulations of flow through a bi-leaflet mechanical heart valve in an anatomic aorta," *Annals of biomedical engineering*, vol. 38, no. 2, pp. 326–344, 2010.

[97] A. Kheradvar, E. M. Groves, A. Falahatpisheh, M. K. Mofrad, S. H. Alavi, R. Tranquillo, L. P. Dasi, C. A. Simmons, K. J. Grande-Allen, C. J. Goergen, *et al.*, "Emerging trends in heart valve engineering: Part iv. computational modeling and experimental studies," *Annals of biomedical engineering*, vol. 43, no. 10, pp. 2314–2333, 2015.

[98] B. E. Griffith, "Immersed boundary model of aortic heart valve dynamics with physiological driving and loading conditions," *International Journal for Numerical Methods in Biomedical Engineering*, vol. 28, no. 3, pp. 317–345, 2012.

[99] M. Daghooghi and I. Borazjani, "The hydrodynamic advantages of synchronized swimming in a rectangular pattern," *Bioinspiration & biomimetics*, vol. 10, no. 5, p. 056018, 2015.

[100] Y. Li, K.-J. Paik, T. Xing, and P. M. Carrica, "Dynamic overset cfd simulations of wind turbine aerodynamics," *Renewable Energy*, vol. 37, no. 1, pp. 285–298, 2012.

[101] S. Deng, T. Xiao, B. van Oudheusden, and H. Bijl, "A dynamic mesh strategy applied to the simulation of flapping wings," *International Journal for Numerical Methods in Engineering*, vol. 106, no. 8, pp. 664–680, 2016.

[102] M. J. Berger and J. Oliger, "Adaptive mesh refinement for hyperbolic partial differential equations," *Journal of computational Physics*, vol. 53, no. 3, pp. 484–512, 1984.

[103] W.-L. Chen, F. Lien, and M. Leschziner, "Local mesh refinement within a multi-block structured-grid scheme for general flows," *Computer Methods in Applied Mechanics and Engineering*, vol. 144, no. 3-4, pp. 327–369, 1997.

[104] W. D. Henshaw and D. W. Schwendeman, "Parallel computation of three-dimensional flows using overlapping grids with adaptive mesh refinement," *Journal of Computational Physics*, vol. 227, no. 16, pp. 7469–7502, 2008.

[105] T. Holst and T. Pulliam, "Overset solution adaptive grid approach applied to hovering rotorcraft flows," in *27th AIAA Applied Aerodynamics Conference*, p. 3519, 2009.

[106] D. Angelidis, S. Chawdhary, and F. Sotiropoulos, "Unstructured cartesian refinement with sharp interface immersed boundary method for 3d unsteady incompressible flows," *Journal of Computational Physics*, vol. 325, pp. 272–300, 2016.

[107] V. Govindarajan, H. S. Udaykumar, L. H. Herbertson, S. Deutsch, K. B. Manning, and K. B. Chandran, "Impact of design parameters on bi-leaflet mechanical heart valve flow dynamics," *The Journal of heart valve disease*, vol. 18, no. 5, p. 535, 2009.

[108] S. Krishnan, "An adaptively refined cartesian grid method for moving boundary problems applied to biomedical systems," 2006.

[109] J. H. Spühler, J. Jansson, N. Jansson, and J. Hoffman, "3d fluid-structure interaction simulation of aortic valves using a unified continuum ale fem model," *Frontiers in physiology*, vol. 9, p. 363, 2018.

[110] F. Alauzet and A. Loseille, "High-order sonic boom modeling based on adaptive methods," *Journal of Computational Physics*, vol. 229, no. 3, pp. 561–593, 2010.

[111] W. Jones, E. Nielsen, and M. Park, "Validation of 3d adjoint based error estimation and mesh adaptation for sonic boom prediction," in *44th AIAA Aerospace Sciences Meeting and Exhibit*, p. 1150, 2006.

[112] T. Michal and J. Krakos, "Anisotropic mesh adaptation through edge primitive operations," in *50th AIAA Aerospace Sciences Meeting including the New Horizons Forum and Aerospace Exposition*, p. 159, 2012.

[113] R. D. Hornung, A. M. Wissink, and S. R. Kohn, "Managing complex data and geometry in parallel structured amr applications," *Engineering with Computers*, vol. 22, no. 3-4, pp. 181–195, 2006.

[114] B. Peng and C. Zhou, "An approach of dynamic mesh adaptation for simulating 3-dimensional unsteady moving-immersed-boundary flows," *International Journal for Numerical Methods in Fluids*, vol. 87, no. 4, pp. 180–201, 2018.

[115] P. De Sampaio, P. R. M. Lyra, K. Morgan, and N. P. Weatherill, "Petrov-galerkin solutions of the incompressible navier-stokes equations in primitive variables with adaptive remeshing," *Computer Methods in Applied Mechanics and Engineering*, vol. 106, no. 1-2, pp. 143–178, 1993.

[116] C. Gruau and T. Coupez, "3d tetrahedral, unstructured and anisotropic mesh generation with adaptation to natural and multidomain metric," *Computer Methods in Applied Mechanics and Engineering*, vol. 194, no. 48-49, pp. 4951–4976, 2005.

[117] G. Compere, E. Marchandise, and J.-F. Remacle, "Transient adaptivity applied to two-phase incompressible flows," *Journal of Computational Physics*, vol. 227, no. 3, pp. 1923–1942, 2008.

[118] J. L. Steger and J. A. Benek, "Method of composite meshes for finite and infinite domain with a piecewise-smooth boundary," *Proc. Steklov Inst. Math.*, vol. 96, p. 145–185, 1968.

[119] G. Starius, "Composite mesh difference methods for elliptic boundary value problems," *Numerische Mathematik*, vol. 28, no. 2, pp. 243–258, 1977.

[120] G. Starius, "On composite mesh difference methods for hyperbolic differential equations," *Numerische Mathematik*, vol. 35, no. 3, pp. 241–255, 1980.

[121] J. L. Steger and J. A. Benek, "On the use of composite grid schemes in computational aerodynamics," *Computer Methods in Applied Mechanics and Engineering*, vol. 64, no. 1-3, pp. 301–320, 1987.

[122] R. Meakin and N. Suhs, "Unsteady aerodynamic simulation of multiple bodies in relative motion," in *9th Computational Fluid Dynamics Conference*, p. 1996, 1989.

[123] G. Chesshire and W. D. Henshaw, "Composite overlapping meshes for the solution of partial differential equations," *Journal of Computational Physics*, vol. 90, no. 1, pp. 1–64, 1990.

[124] W. D. Henshaw, "A fourth-order accurate method for the incompressible navier-stokes equations on overlapping grids," *Journal of computational physics*, vol. 113, no. 1, pp. 13–25, 1994.

[125] H. Tang, S. C. Jones, and F. Sotiropoulos, "An overset-grid method for 3d unsteady incompressible flows," *Journal of Computational Physics*, vol. 191, no. 2, pp. 567–600, 2003.

[126] A. Vreman, "A staggered overset grid method for resolved simulation of incompressible flow around moving spheres," *Journal of Computational Physics*, vol. 333, pp. 269–296, 2017.

[127] T. M. Burton and J. K. Eaton, "Analysis of a fractional-step method on overset grids," *Journal of Computational Physics*, vol. 177, no. 2, pp. 336–364, 2002.

[128] T. M. Burton and J. K. Eaton, "Fully resolved simulations of particle-turbulence interaction," *Journal of Fluid Mechanics*, vol. 545, pp. 67–111, 2005.

[129] M. G. Al-Azawy, A. Turan, and A. Revell, "An overset mesh approach for valve closure: An lvad application.," in *BIODEVICES*, pp. 145–151, 2016.

[130] L. Ge, S. C. Jones, F. Sotiropoulos, T. M. Healy, and A. P. Yoganathan, "Numerical simulation of flow in mechanical heart valves: grid resolution and the assumption of flow symmetry," *J. Biomech. Eng.*, vol. 125, no. 5, pp. 709–718, 2003.

[131] F. Khalili, "Fluid dynamics modeling and sound analysis of a bileaflet mechanical heart valve," 2018.

[132] T. B. Le and F. Sotiropoulos, "Fluid–structure interaction of an aortic heart valve prosthesis driven by an animated anatomic left ventricle," *Journal of computational physics*, vol. 244, pp. 41–62, 2013.

[133] G. Zagaris, M. T. Campbell, D. J. Bodony, E. Shaffer, and M. D. Brandyberry, "A toolkit for parallel overset grid assembly targeting large-scale moving body aerodynamic simulations," in *Proceedings of the 19th international meshing roundtable*, pp. 385–401, Springer, 2010.

[134] J. Crabill, F. D. Witherden, and A. Jameson, "A parallel direct cut algorithm for high-order overset methods with application to a spinning golf ball," *Journal of Computational Physics*, vol. 374, pp. 692–723, 2018.

[135] G. K. Kenway, A. Mishra, N. R. Secco, K. Duraisamy, and J. Martins, "An efficient parallel overset method for aerodynamic shape optimization," in *58th AIAA/ASCE/AHS/ASC Structures, Structural Dynamics, and Materials Conference*, p. 0357, 2017.

[136] N. Suhs, S. Rogers, and W. Dietz, "Pegasus 5: An automated pre-processor for overset-grid cfd," in *32nd AIAA Fluid Dynamics Conference and Exhibit*, p. 3186, 2002.

[137] R. Noack, D. Boger, R. e. Kunz, and P. Carrica, "Suggar++: An improved general overset grid assembly capability," in *19th AIAA Computational Fluid Dynamics*, p. 3992, 2009.

[138] J. Alonso, S. Hahn, F. Ham, M. Herrmann, G. Iaccarino, G. Kalitzin, P. LeGresley, K. Mattsson, G. Medic, P. Moin, *et al.*, "Chimps: A high-performance scalable module for multi-physics simulations," in *42nd AIAA/ASME/SAE/ASEE Joint Propulsion Conference & Exhibit*, p. 5274, 2006.

[139] J. Sitaraman, M. Floros, A. Wissink, and M. Potsdam, "Parallel domain connectivity algorithm for unsteady flow computations using overlapping and adaptive grids," *Journal of Computational Physics*, vol. 229, no. 12, pp. 4703–4723, 2010.

[140] R. Meakin, "Object x-rays for cutting holes in composite overset structured grids," in *15th AIAA computational fluid dynamics conference*, p. 2537, 2001.

[141] D. Belk and R. Maple, "Automated assembly of structured grids for moving body problems," in *12th Computational Fluid Dynamics Conference*, p. 1680, 1995.

[142] Z. Wang and V. Parthasarathy, "A fully automated chimera methodology for multiple moving body problems," *International Journal for Numerical Methods in Fluids*, vol. 33, no. 7, pp. 919–938, 2000.

[143] W. Henshaw, "Overture: An object-oriented framework for overlapping grid applications," in *32nd AIAA Fluid Dynamics Conference and Exhibit*, p. 3189, 2002.

[144] P. Buning and T. Pulliam, "Cartesian off-body grid adaption for viscous time-accurate flow simulations," in *20th AIAA computational fluid dynamics conference*, p. 3693, 2011.

[145] W. Sickles, A. Denny, and R. Nichols, "Time-accurate cfd predictions for the jdam separation from an f-18c aircraft," in *38th Aerospace Sciences Meeting and Exhibit*, p. 796, 2000.

[146] Z. Shen, D. Wan, *et al.*, "Rans computations of added resistance and motions of a ship in head waves," *International Journal of Offshore and Polar Engineering*, vol. 23, no. 04, pp. 264–271, 2013.

[147] S. T. Miller, R. Campbell, C. Elsworth, J. Pitt, and D. Boger, "An overset grid method for fluid-structure interaction," *World Journal of Mechanics*, vol. 4, no. 07, p. 217, 2014.

[148] Z. Shen, D. Wan, and P. M. Carrica, "Dynamic overset grids in openfoam with application to kcs self-propulsion and maneuvering," *Ocean Engineering*, vol. 108, pp. 287–306, 2015.

[149] B. Roget and J. Sitaraman, "Robust and efficient overset grid assembly for partitioned unstructured meshes," *Journal of Computational Physics*, vol. 260, pp. 1–24, 2014.

[150] J. E. Martin, R. W. Noack, and P. M. Carrica, "Overset grid assembly approach for scalable computational fluid dynamics with body motions," *Journal of Computational Physics*, vol. 390, pp. 297–305, 2019.

[151] W. Wang, C. Yan, S. Wang, Y. Huang, and W. Yuan, "An efficient, robust and automatic overlapping grid assembly approach for partitioned multi-block structured grids," *Proceedings of the Institution of Mechanical Engineers, Part G: Journal of Aerospace Engineering*, vol. 233, no. 4, pp. 1217–1236, 2019.

[152] W. J. Horne and K. Mahesh, "A massively-parallel, unstructured overset method for mesh connectivity," *Journal of Computational Physics*, vol. 376, pp. 585–596, 2019.

[153] G. D. Dangas, J. I. Weitz, G. Giustino, R. Makkar, and R. Mehran, "Prosthetic heart valve thrombosis," *Journal of the American College of Cardiology*, vol. 68, no. 24, pp. 2670–2689, 2016.

[154] J. Sheriff, *Shear-induced platelet sensitization and the development of an activation model*. PhD thesis, The Graduate School, Stony Brook University: Stony Brook, NY., 2010.

[155] C. Brown III, R. Lemuth, J. Hellums, L. Leverett, and C. Alfrey, "Response of human platelets to shear stress.," *ASAIO Journal*, vol. 21, no. 1, pp. 35–39, 1975.

[156] C. H. Brown, L. B. Leverett, C. W. Lewis, C. P. Alfrey, and J. D. Hellums, "Morphological, biochemical, and functional changes in human platelets subjected to shear stress," *The Journal of laboratory and clinical medicine*, vol. 86, no. 3, pp. 462–471, 1975.

[157] H. Hosseinzadegan and D. K. Tafti, "Modeling thrombus formation and growth," *Biotechnology and Bioengineering*, 2017.

[158] J. Ramstack, L. Zuckerman, and L. Mockros, "Shear-induced activation of platelets," *Journal of biomechanics*, vol. 12, no. 2, pp. 113–125, 1979.

[159] J. Hellums, D. Peterson, N. Stathopoulos, J. Moake, and T. Giorgio, "Studies on the mechanisms of shear-induced platelet activation," in *Cerebral ischemia and hemorheology*, pp. 80–89, Springer, 1987.

[160] P. L. Blackshear Jr, F. D. Dorman, and J. H. Steinbach, "Some mechanical effects that influence hemolysis," 1965.

[161] L. Wurzinger, R. Opitz, P. Blasberg, and H. Schmid-Schönbein, "Platelet and coagulation parameters following millisecond exposure to laminar shear stress.," *Thrombosis and haemostasis*, vol. 54, no. 2, pp. 381–386, 1985.

[162] M. Giersiepen, L. Wurzinger, R. Opitz, and H. Reul, "Estimation of shear stress-related blood damage in heart valve prostheses–in vitro comparison of 25 aortic valves.," *The International journal of artificial organs*, vol. 13, no. 5, pp. 300–306, 1990.

[163] J. D. Hellums, "1993 whitaker lecture: biorheology in thrombosis research," *Annals of biomedical engineering*, vol. 22, no. 5, pp. 445–455, 1994.

[164] M. Grigioni, U. Morbiducci, G. D'Avenio, G. Di Benedetto, and C. Del Gaudio, "A novel formulation for blood trauma prediction by a modified power-law mathematical model," *Biomechanics and Modeling in Mechanobiology*, vol. 4, no. 4, pp. 249–260, 2005.

[165] Y. Alemu and D. Bluestein, "Flow-induced platelet activation and damage accumulation in a mechanical heart valve: numerical studies," *Artificial organs*, vol. 31, no. 9, pp. 677–688, 2007.

[166] K. K. Yeleswarapu, J. F. Antaki, M. V. Kameneva, and K. R. Rajagopal, "A mathematical model for shear-induced hemolysis," *Artificial Organs*, vol. 19, no. 7, pp. 576–582, 1995.

[167] D. W. Ross, L. H. Ayscue, J. Watson, and S. A. Bentley, "Stability of hematologic parameters in healthy subjects: Intraindividual versus interindividual variation," *American journal of clinical pathology*, vol. 90, no. 3, pp. 262–267, 1988.

[168] M. Hedayat and I. Borazjani, "A parallel dynamic overset grid framework for immersed boundary methods," *arXiv preprint arXiv:1910.09315*, 2019.

[169] L. Ge and F. Sotiropoulos, "A numerical method for solving the 3d unsteady incompressible navier–stokes equations in curvilinear domains with complex immersed boundaries," *Journal of computational physics*, vol. 225, no. 2, pp. 1782–1809, 2007.

[170] I. Borazjani and A. Akbarzadeh, "Large eddy simulations of flows with moving boundaries," in *Modeling and Simulation of Turbulent Mixing and Reaction*, pp. 201–225, Springer, 2020.

[171] H. Asgharzadeh and I. Borazjani, "A newton–krylov method with an approximate analytical jacobian for implicit solution of navier–stokes equations on staggered overset-curvilinear grids with immersed boundaries," *Journal of computational physics*, vol. 331, pp. 227–256, 2017.

[172] M. Vinokur, "An analysis of finite-difference and finite-volume formulations of conservation laws," *Journal of computational physics*, vol. 81, no. 1, pp. 1–52, 1989.

[173] M. Beddhu, L. K. Taylor, and D. L. Whitfield, "Strong conservative form of the incompressible navier–stokes equations in a rotating frame with a solution procedure," *Journal of Computational Physics*, vol. 128, no. 2, pp. 427–437, 1996.

[174] S. Balay, S. Abhyankar, M. F. Adams, J. Brown, P. Brune, K. Buschelman, L. Dalcin, A. Dener, V. Eijkhout, W. D. Gropp, D. Karpeyev, D. Kaushik, M. G. Knepley, D. A. May, L. C. McInnes, R. T. Mills, T. Munson, K. Rupp, P. Sanan, B. F. Smith, S. Zampini, H. Zhang, and H. Zhang, "PETSc users manual," Tech. Rep. ANL-95/11 - Revision 3.11, Argonne National Laboratory, 2019.

[175] T. P. W. C. J. S. S. K. K. R. P.G. Buning, D.C. Jesperson, "Overflow users manual," *Research report*, 1998.

[176] N. A. Petersson, "An algorithm for assembling overlapping grid systems," *SIAM Journal on Scientific Computing*, vol. 20, no. 6, pp. 1995–2022, 1999.

[177] Y. Lee and J. Baeder, "High-order overset method for blade vortex interaction," in *40th AIAA Aerospace Sciences Meeting & Exhibit*, p. 559, 2002.

[178] Y. Lee and J. Baeder, "Implicit hole cutting-a new approach to overset grid connectivity," in *16th AIAA Computational Fluid Dynamics Conference*, p. 4128, 2003.

[179] W. Liao, J. Cai, and H. M. Tsai, "A multigrid overset grid flow solver with implicit hole cutting method," *Computer methods in applied mechanics and engineering*, vol. 196, no. 9-12, pp. 1701–1715, 2007.

[180] X. Hu, Z. Lu, J. Zhang, X. Liu, W. Yuan, S. Liang, and H. Zhang, "A parallel algorithm for chimera grid with implicit hole cutting method," *The International Journal of High Performance Computing Applications*, p. 1094342019845042, 2019.

[181] P. Schneider and D. H. Eberly, *Geometric tools for computer graphics*. Elsevier, 2003.

[182] M. H. Kroll, J. D. Hellums, L. McIntire, A. Schafer, and J. Moake, "Platelets and shear stress," *Blood*, vol. 88, no. 5, pp. 1525–1541, 1996.

[183] M. Nobili, J. Sheriff, U. Morbiducci, A. Redaelli, and D. Bluestein, "Platelet activation due to hemodynamic shear stresses: damage accumulation model and comparison to in vitro measurements," *ASAIO journal (American Society for Artificial Internal Organs: 1992)*, vol. 54, no. 1, p. 64, 2008.

[184] J. Sheriff, J. S. Soares, M. Xenos, J. Jesty, and D. Bluestein, "Evaluation of shear-induced platelet activation models under constant and dynamic shear stress loading conditions relevant to devices," *Annals of biomedical engineering*, vol. 41, no. 6, pp. 1279–1296, 2013.

[185] H. A. Simon, L. Ge, F. Sotiropoulos, and A. P. Yoganathan, "Numerical investigation of the performance of three hinge designs of bileaflet mechanical heart valves," *Annals of biomedical engineering*, vol. 38, no. 11, pp. 3295–3310, 2010.

[186] D. Bluestein, L. Niu, R. T. Schoephoerster, and M. K. Dewanjee, "Fluid mechanics of arterial stenosis: relationship to the development of mural thrombus," *Annals of biomedical engineering*, vol. 25, no. 2, pp. 344–356, 1997.

[187] L. Ge, L. P. Dasi, F. Sotiropoulos, and A. P. Yoganathan, "Characterization of hemodynamic forces induced by mechanical heart valves: Reynolds vs. viscous stresses," *Annals of Biomedical Engineering*, vol. 36, no. 2, pp. 276–297, 2008.

[188] J. Apel, R. Paul, S. Klaus, T. Siess, and H. Reul, "Assessment of hemolysis related quantities in a microaxial blood pump by computational fluid dynamics," *Artificial Organs*, vol. 25, no. 5, pp. 341–347, 2001.

[189] R. L. Panton, *Incompressible flow*. John Wiley & Sons, 2006.

[190] G. Strang, "On the construction and comparison of difference schemes," *SIAM Journal on Numerical Analysis*, vol. 5, no. 3, pp. 506–517, 1968.

[191] R. J. LeVeque, *Finite volume methods for hyperbolic problems*, vol. 31. Cambridge university press, 2002.

[192] S. Gottlieb and C.-W. Shu, "Total variation diminishing runge-kutta schemes," *Mathematics of computation of the American Mathematical Society*, vol. 67, no. 221, pp. 73–85, 1998.

[193] D. Kim and H. Choi, "Immersed boundary method for flow around an arbitrarily moving body," *Journal of Computational Physics*, vol. 212, no. 2, pp. 662–680, 2006.

[194] I. Borazjani and F. Sotiropoulos, "On the role of form and kinematics on the hydrodynamics of self-propelled body/caudal fin swimming," *Journal of Experimental Biology*, vol. 213, no. 1, pp. 89–107, 2010.

[195] I. Borazjani and F. Sotiropoulos, "Numerical investigation of the hydrodynamics of carangiform swimming in the transitional and inertial flow regimes," *Journal of experimental biology*, vol. 211, no. 10, pp. 1541–1558, 2008.

[196] J. Videler and F. Hess, "Fast continuous swimming of two pelagic predators, saithe (pollachius virens) and mackerel (scomber scombrus): a kinematic analysis," *Journal of experimental biology*, vol. 109, no. 1, pp. 209–228, 1984.

[197] W. S. Nesbitt, E. Westein, F. J. Tovar-Lopez, E. Tolouei, A. Mitchell, J. Fu, J. Carberry, A. Fouras, and S. P. Jackson, "A shear gradient–dependent platelet aggregation mechanism drives thrombus formation," *Nature medicine*, vol. 15, no. 6, p. 665, 2009.

[198] M. Friedman and G. Van den Bovenkamp, "The pathogenesis of a coronary thrombus.," *The American journal of pathology*, vol. 48, no. 1, p. 19, 1966.

[199] M. Friedman, "The coronary thrombus: its origin and fate," *Human pathology*, vol. 2, no. 1, pp. 81–128, 1971.

[200] H. A. Simon, L. Ge, I. Borazjani, F. Sotiropoulos, and A. P. Yoganathan, "Simulation of the three-dimensional hinge flow fields of a bileaflet mechanical heart valves under physiologic conditions," *Annals of biomedical engineering*, vol. 38, no. 3, p. 1257, 2010.

[201] J. Ellis, T. Healy, A. Fontaine, R. Saxena, and A. Yoganathan, "Velocity measurements and flow patterns within the hinge region of a medtronic parallel bileaflet mechanical valve with clear housing.," *The Journal of heart valve disease*, vol. 5, no. 6, pp. 591–599, 1996.

[202] J. T. Ellis, B. R. Travis, and A. P. Yoganathan, "An in vitro study of the hinge and near-field forward flow dynamics of the st. jude medical® regent™ bileaflet mechanical heart valve," *Annals of biomedical engineering*, vol. 28, no. 5, pp. 524–532, 2000.

[203] A. J. Martin and J. R. Christy, "An in-vitro technique for assessment of thrombogenicity in mechanical prosthetic cardiac valves: evaluation with a range of valve types," *JOURNAL OF HEART VALVE DISEASE*, vol. 13, no. 3, pp. 509–520, 2004.

[204] R. Boreda, R. Fatemi, and S. Rittgers, "Potential for platelet stimulation in critically stenosed carotid and coronary arteries," *J Vasc Invest*, vol. 1, no. 1, pp. 26–37, 1995.

[205] L. Goubergrits, "Numerical modeling of blood damage: current status, challenges and future prospects," *Expert review of medical devices*, vol. 3, no. 5, pp. 527–531, 2006.

[206] J. Jesty and D. Bluestein, "Acetylated prothrombin as a substrate in the measurement of the procoagulant activity of platelets: elimination of the feedback activation of platelets by thrombin," *Analytical biochemistry*, vol. 272, no. 1, pp. 64–70, 1999.

[207] M. Grigioni, C. Daniele, U. Morbiducci, G. D'Avenio, G. Di Benedetto, and V. Barbaro, "The power-law mathematical model for blood damage prediction: Analytical developments and physical inconsistencies," *Artificial organs*, vol. 28, no. 5, pp. 467–475, 2004.

[208] M. Xenos, G. Girdhar, Y. Alemu, J. Jesty, M. Slepian, S. Einav, and D. Bluestein, "Device thrombogenicity emulator (dte)- design optimization methodology for cardiovascular devices: A study in two bileaflet mhv designs," *Journal of biomechanics*, vol. 43, no. 12, pp. 2400–2409, 2010.

[209] D. Bluestein, E. Rambod, and M. Gharib, "Vortex shedding as a mechanism for free emboli formation in mechanical heart valves," *TRANSACTIONS-AMERICAN SOCIETY OF MECHANICAL ENGINEERS JOURNAL OF BIOMECHANICAL ENGINEERING*, vol. 122, no. 2, pp. 125–134, 2000.

[210] B. M. Yun, C. K. Aidun, and A. P. Yoganathan, "Blood damage through a bileaflet mechanical heart valve: a quantitative computational study using a multiscale suspension flow solver," *Journal of biomechanical engineering*, vol. 136, no. 10, p. 101009, 2014.

[211] W. Vongpatanasin, L. D. Hillis, and R. A. Lange, "Prosthetic heart valves," *New England Journal of Medicine*, vol. 335, no. 6, pp. 407–416, 1996.

[212] N. Purvis Jr and T. Giorgio, "The effects of elongational stress exposure on the activation and aggregation of blood platelets.," *Biorheology*, vol. 28, no. 5, pp. 355–367, 1990.

[213] D. Bluestein, Y. Li, and I. Krukenkamp, "Free emboli formation in the wake of bi-leaflet mechanical heart valves and the effects of implantation techniques," *Journal of biomechanics*, vol. 35, no. 12, pp. 1533–1540, 2002.

[214] J. Sheriff, D. Bluestein, G. Girdhar, and J. Jesty, "High-shear stress sensitizes platelets to subsequent low-shear conditions," *Annals of biomedical engineering*, vol. 38, no. 4, pp. 1442–1450, 2010.

[215] B. M. Yun, D. B. McElhinney, S. Arjunon, L. Mirabella, C. K. Aidun, and A. P. Yoganathan, "Computational simulations of flow dynamics and blood damage through a bileaflet mechanical heart valve scaled to pediatric size and flow," *Journal of biomechanics*, vol. 47, no. 12, pp. 3169–3177, 2014.

[216] W. Yin, Y. Alemu, K. Affeld, J. Jesty, and D. Bluestein, "Flow-induced platelet activation in bileaflet and monoleaflet mechanical heart valves," *Annals of biomedical engineering*, vol. 32, no. 8, pp. 1058–1066, 2004.

[217] W. Yin, S. Gallocher, L. Pinchuk, R. T. Schoephoerster, J. Jesty, and D. Bluestein, "Flow-induced platelet activation in a st. jude mechanical heart valve, a trileaflet polymeric heart valve, and a st. jude tissue valve," *Artificial Organs*, vol. 29, no. 10, pp. 826–831, 2005.

[218] W. Yin, I. B. Krukenkamp, A. E. Saltman, G. Gaudette, K. Suresh, O. Bernal, J. Jesty, and D. Bluestein, "Thrombogenic performance of a st. jude bileaflet mechanical heart valve in a sheep model," *ASAIO journal*, vol. 52, no. 1, pp. 28–33, 2006.

[219] Y. Alemu, G. Girdhar, M. Xenos, J. Sheriff, J. Jesty, S. Einav, and D. Bluestein, "Design optimization of a mechanical heart valve for reducing valve thrombogenicity—a case study with ats valve," *ASAIO journal*, vol. 56, no. 5, pp. 389–396, 2010.

[220] H.-L. Leo, Z. He, J. T. Ellis, and A. P. Yoganathan, "Microflow fields in the hinge region of the carbomedics bileaflet mechanical heart valve design," *The journal of thoracic and cardiovascular surgery*, vol. 124, no. 3, pp. 561–574, 2002.

[221] K. B. Manning, V. Kini, A. A. Fontaine, S. Deutsch, and J. M. Tarbell, "Regurgitant flow field characteristics of the st. jude bileaflet mechanical heart valve under physiologic pulsatile flow using particle image velocimetry," *Artificial organs*, vol. 27, no. 9, pp. 840–846, 2003.

[222] H. A. Simon, H.-L. Leo, J. Carberry, and A. P. Yoganathan, "Comparison of the hinge flow fields of two bileaflet mechanical heart valves under aortic and mitral conditions," *Annals of biomedical engineering*, vol. 32, no. 12, pp. 1607–1617, 2004.

[223] H. Leo, H. A. Simon, L. P. Dasi, and A. P. Yoganathan, "Effect of hinge gap width on the microflow structures in 27-mm bileaflet mechanical heart valves," *Journal of Heart Valve Disease*, vol. 15, no. 6, p. 800, 2006.

[224] E. Klusak, A. Bellofiore, S. Loughnane, and N. J. Quinlan, "High-resolution measurements of velocity and shear stress in leakage jets from bileaflet mechanical heart valve hinge models," *Journal of biomechanical engineering*, vol. 137, no. 11, p. 111008, 2015.

[225] P. S. H. Zhang, A. R. Dalal, J. Y. Kresh, and G. W. Laub, "A novel technique for experimental flow visualization of mechanical valves," *ASAIO Journal*, vol. 62, no. 2, pp. 133–138, 2016.

[226] B. R. Travis, U. M. Marzec, H. L. Leo, T. Momin, C. Sanders, S. R. Hanson, and A. P. Yoganathan, "Bileaflet aortic valve prosthesis pivot geometry influences platelet secretion and anionic phospholipid exposure," *Annals of biomedical engineering*, vol. 29, no. 8, pp. 657–664, 2001.

[227] A. M. Fallon, N. Shah, U. M. Marzec, J. N. Warnock, A. P. Yoganathan, and S. R. Hanson, "Flow and thrombosis at orifices simulating mechanical heart valve leakage regions," *Journal of biomechanical engineering*, vol. 128, no. 1, pp. 30–39, 2006.

[228] P. Hanafizadeh, N. Mirkhani, M. R. Davoudi, M. Masouminia, and K. Sadeghy, "Non-newtonian blood flow simulation of diastolic phase in bileaflet mechanical heart valve implanted in a realistic aortic root containing coronary arteries," *Artificial organs*, vol. 40, no. 10, 2016.

[229] Y. H. Kuan, F. Kabinejadian, V.-T. Nguyen, B. Su, A. P. Yoganathan, and H. L. Leo, "Comparison of hinge microflow fields of bileaflet mechanical heart valves implanted in different

sinus shape and downstream geometry," *Computer methods in biomechanics and biomedical engineering*, vol. 18, no. 16, pp. 1785–1796, 2015.

[230] D. Bluestein, W. Yin, K. Affeld, and J. Jesty, "Flow-induced platelet activation in a mechanical heart valve," *Journal of Heart Valve Disease*, vol. 13, no. 3, pp. 501–508, 2004.

[231] T. C. Lamson, G. Rosenberg, D. B. Geselowitz, S. Deutsch, D. R. Stinebring, J. A. Frangos, and J. M. Tarbell, "Relative blood damage in the three phases of a prosthetic heart valve flow cycle.," *Asaio Journal*, vol. 39, no. 3, pp. M626–M633, 1993.

[232] M. S. Elbaz, E. E. Calkoen, J. J. Westenberg, B. P. Lelieveldt, A. A. Roest, and R. J. van der Geest, "Vortex flow during early and late left ventricular filling in normal subjects: quantitative characterization using retrospectively-gated 4d flow cardiovascular magnetic resonance and three-dimensional vortex core analysis," *Journal of Cardiovascular Magnetic Resonance*, vol. 16, no. 1, p. 78, 2014.

[233] D. Rodriguez Muñoz, M. Markl, J. L. Moya Mur, A. Barker, C. Fernández-Golfín, P. Lancellotti, and J. L. Zamorano Gómez, "Intracardiac flow visualization: current status and future directions," *European Heart Journal–Cardiovascular Imaging*, vol. 14, no. 11, pp. 1029–1038, 2013.

[234] S. N. Doost, D. Ghista, B. Su, L. Zhong, and Y. S. Morsi, "Heart blood flow simulation: a perspective review," *Biomedical engineering online*, vol. 15, no. 1, p. 101, 2016.

[235] I. Borazjani, J. Westerdale, E. M. McMahon, P. K. Rajaraman, J. J. Heys, and M. Belohlavek, "Left ventricular flow analysis: recent advances in numerical methods and applications in cardiac ultrasound," *Computational and mathematical methods in medicine*, vol. 2013, 2013.

[236] R. Mittal, J. H. Seo, V. Vedula, Y. J. Choi, H. Liu, H. H. Huang, S. Jain, L. Younes, T. Abraham, and R. T. George, "Computational modeling of cardiac hemodynamics: Current status and future outlook," *Journal of Computational Physics*, vol. 305, pp. 1065–1082, 2016.

[237] E. Votta, T. B. Le, M. Stevanella, L. Fusini, E. G. Caiani, A. Redaelli, and F. Sotiropoulos, "Toward patient-specific simulations of cardiac valves: state-of-the-art and future directions," *Journal of biomechanics*, vol. 46, no. 2, pp. 217–228, 2013.

[238] T. Schenkel, M. Malve, M. Reik, M. Markl, B. Jung, and H. Oertel, "Mri-based cfd analysis of flow in a human left ventricle: methodology and application to a healthy heart," *Annals of biomedical engineering*, vol. 37, no. 3, pp. 503–515, 2009.

[239] J. H. Seo and R. Mittal, "Effect of diastolic flow patterns on the function of the left ventricle," *Physics of Fluids*, vol. 25, no. 11, p. 110801, 2013.

[240] F. Sacco, B. Paun, O. Lehmkuhl, T. L. Iles, P. A. Iaizzo, G. Houzeaux, M. Vázquez, C. Butakoff, and J. Aguado-Sierra, "Left ventricular trabeculations decrease the wall shear stress and increase the intra-ventricular pressure drop in cfd simulations," *Frontiers in Physiology*, vol. 9, p. 458, 2018.

[241] A. Santiago, J. Aguado-Sierra, M. Zavala-Aké, R. Doste-Beltran, S. Gómez, R. Arís, J. C. Cajas, E. Casoni, and M. Vázquez, "Fully coupled fluid-electro-mechanical model of the human heart for supercomputers," *International journal for numerical methods in biomedical engineering*, vol. 34, no. 12, p. e3140, 2018.

[242] H. Watanabe, S. Sugiura, H. Kafuku, and T. Hisada, "Multiphysics simulation of left ventricular filling dynamics using fluid-structure interaction finite element method," *Biophysical journal*, vol. 87, no. 3, pp. 2074–2085, 2004.

[243] M. Sharzehee, S. S. Khalafvand, and H.-C. Han, "Fluid-structure interaction modeling of aneurysmal arteries under steady-state and pulsatile blood flow: a stability analysis," *Computer methods in biomechanics and biomedical engineering*, vol. 21, no. 3, pp. 219–231, 2018.

[244] A. Shahidian and A. G. Hassankiadeh, "Stress analysis of internal carotid artery with low stenosis level: the effect of material model and plaque geometry," *Journal of Mechanics in Medicine and Biology*, vol. 17, no. 06, p. 1750098, 2017.

[245] H. Watabe, A. Sato, H. Nishina, T. Hoshi, A. Sugano, Y. Kakefuda, Y. Takaiwa, H. Aihara, Y. Fumikura, Y. Noguchi, *et al.*, "Enhancement patterns detected by multidetector computed tomography are associated with microvascular obstruction and left ventricular remodelling in patients with acute myocardial infarction," *European heart journal*, vol. 37, no. 8, pp. 684–692, 2015.

[246] S. A. Morris and T. C. Slesnick, "Magnetic resonance imaging," *Visual Guide to Neonatal Cardiology*, pp. 104–108, 2018.

[247] M. J. Monaghan, "Role of real time 3d echocardiography in evaluating the left ventricle," *Heart*, vol. 92, no. 1, pp. 131–136, 2006.

[248] M. Tee, J. A. Noble, and D. A. Bluemke, "Imaging techniques for cardiac strain and deformation: comparison of echocardiography, cardiac magnetic resonance and cardiac computed tomography," *Expert review of cardiovascular therapy*, vol. 11, no. 2, pp. 221–231, 2013.

[249] M. A. Chamsi-Pasha, P. P. Sengupta, and W. A. Zoghbi, "Handheld echocardiography: current state and future perspectives," *Circulation*, vol. 136, no. 22, pp. 2178–2188, 2017.

[250] R. M. Lang, V. Mor-Avi, L. Sugeng, P. S. Nieman, and D. J. Sahn, "Three-dimensional echocardiography: the benefits of the additional dimension," *Journal of the American College of Cardiology*, vol. 48, no. 10, pp. 2053–2069, 2006.

[251] N. K. Rajan, Z. Song, K. R. Hoffmann, M. Belohlavek, E. M. McMahon, and I. Borazjani, "Automated three-dimensional reconstruction of the left ventricle from multiple-axis echocardiography," *Journal of Biomechanical Engineering*, vol. 138, no. 1, p. 011003, 2016.

[252] J. H. Seo, V. Vedula, T. Abraham, A. C. Lardo, F. Dawoud, H. Luo, and R. Mittal, "Effect of the mitral valve on diastolic flow patterns," *Physics of fluids*, vol. 26, no. 12, p. 121901, 2014.

[253] Z. Song and I. Borazjani, "The role of shape and heart rate on the performance of the left ventricle," *Journal of biomechanical engineering*, vol. 137, no. 11, p. 114501, 2015.

[254] H. Watanabe, S. Sugiura, and T. Hisada, "The looped heart does not save energy by maintaining the momentum of blood flowing in the ventricle," *American Journal of Physiology-Heart and Circulatory Physiology*, vol. 294, no. 5, pp. H2191–H2196, 2008.

[255] X. Zheng, J. Seo, V. Vedula, T. Abraham, and R. Mittal, "Computational modeling and analysis of intracardiac flows in simple models of the left ventricle," *European Journal of Mechanics-B/Fluids*, vol. 35, pp. 31–39, 2012.

[256] B. Su, R. San Tan, J. Le Tan, K. W. Q. Guo, J. M. Zhang, S. Leng, X. Zhao, J. C. Allen, and L. Zhong, "Cardiac mri based numerical modeling of left ventricular fluid dynamics with mitral valve incorporated," *Journal of biomechanics*, vol. 49, no. 7, pp. 1199–1205, 2016.

[257] S. S. Khalafvand, F. Xu, J. Westenberg, F. Gijsen, and S. Kenjeres, "Intraventricular blood flow with a fully dynamic mitral valve model," *Computers in biology and medicine*, vol. 104, pp. 197–204, 2019.

[258] C. Chnafa, S. Mendez, R. Moreno, and F. Nicoud, "Using image-based cfd to investigate the intracardiac turbulence," in *Modeling the Heart and the Circulatory System*, pp. 97–117, Springer, 2015.

[259] K. Vellguth, J. Brüning, L. Tautz, F. Degener, I. Wamala, S. Sündermann, U. Kertzscher, T. Kuehne, A. Hennemuth, V. Falk, *et al.*, "User-dependent variability in mitral valve segmentation and its impact on cfd-computed hemodynamic parameters," *International Journal of Computer Assisted Radiology and Surgery*, pp. 1–10, 2019.

[260] K. Vellguth, J. Brüning, L. Goubergrits, L. Tautz, A. Hennemuth, U. Kertzscher, F. Degener, M. Kelm, S. Sündermann, and T. Kuehne, "Development of a modeling pipeline for the prediction of hemodynamic outcome after virtual mitral valve repair using image-based cfd," *International journal of computer assisted radiology and surgery*, vol. 13, no. 11, pp. 1795–1805, 2018.

[261] C. Chnafa, S. Mendez, and F. Nicoud, "Image-based large-eddy simulation in a realistic left heart," *Computers & Fluids*, vol. 94, pp. 173–187, 2014.

[262] W. Mao, A. Caballero, R. McKay, C. Primiano, and W. Sun, "Fully-coupled fluid-structure interaction simulation of the aortic and mitral valves in a realistic 3d left ventricle model," *PloS one*, vol. 12, no. 9, p. e0184729, 2017.

[263] B. Su, F. Kabinejadian, H. Q. Phang, G. P. Kumar, F. Cui, S. Kim, R. San Tan, J. K. F. Hon, J. C. Allen, H. L. Leo, *et al.*, "Numerical modeling of intraventricular flow during diastole after implantation of bmhv," *PloS one*, vol. 10, no. 5, p. e0126315, 2015.

[264] B. Su, L. Zhong, X.-K. Wang, J.-M. Zhang, R. San Tan, J. C. Allen, S. K. Tan, S. Kim, and H. L. Leo, "Numerical simulation of patient-specific left ventricular model with both mitral and aortic valves by fsi approach," *Computer methods and programs in biomedicine*, vol. 113, no. 2, pp. 474–482, 2014.

[265] S. K. Dahl, J. Vierendeels, J. Degroote, S. Annerel, L. R. Hellevik, and B. Skallerud, "Fsi simulation of asymmetric mitral valve dynamics during diastolic filling," *Computer methods in biomechanics and biomedical engineering*, vol. 15, no. 2, pp. 121–130, 2012.

[266] C. Carmody, G. Burriesci, I. Howard, and E. Patterson, "An approach to the simulation of fluid–structure interaction in the aortic valve," *Journal of biomechanics*, vol. 39, no. 1, pp. 158–169, 2006.

[267] J. J. Charonko, R. Kumar, K. Stewart, W. C. Little, and P. P. Vlachos, "Vortices formed on the mitral valve tips aid normal left ventricular filling," *Annals of biomedical engineering*, vol. 41, no. 5, pp. 1049–1061, 2013.

[268] A. M. Bavo, A. M. Pouch, J. Degroote, J. Vierendeels, J. H. Gorman, R. C. Gorman, and P. Segers, "Patient-specific cfd simulation of intraventricular haemodynamics based on 3d ultrasound imaging," *Biomedical engineering online*, vol. 15, no. 1, p. 107, 2016.

[269] A. Bavo, A. M. Pouch, J. Degroote, J. Vierendeels, J. H. Gorman, R. C. Gorman, and P. Segers, "Patient-specific cfd models for intraventricular flow analysis from 3d ultrasound imaging: Comparison of three clinical cases," *Journal of biomechanics*, vol. 50, pp. 144–150, 2017.

[270] S. S. Khalafvand, E. Y.-K. Ng, L. Zhong, and T.-K. Hung, "Fluid-dynamics modelling of the human left ventricle with dynamic mesh for normal and myocardial infarction: preliminary study," *Computers in biology and medicine*, vol. 42, no. 8, pp. 863–870, 2012.

[271] V. Vasudevan, A. J. J. Low, S. P. Annamalai, S. Sampath, K. K. Poh, T. Totman, M. Mazlan, G. Croft, A. M. Richards, D. P. de Kleijn, *et al.*, "Flow dynamics and energy efficiency of flow in the left ventricle during myocardial infarction," *Biomechanics and modeling in mechanobiology*, vol. 16, no. 5, pp. 1503–1517, 2017.

[272] A. Imanparast, N. Fatouraee, and F. Sharif, "Comprehensive computational assessment of blood flow characteristics of left ventricle based on in-vivo mri in presence of artificial myocardial infarction," *Mathematical biosciences*, vol. 294, pp. 143–159, 2017.

[273] T. R. Patel, *3D Reconstruction of Left Ventricle with Mitral and Aortic Valves from Multiple Axis 2D Echocardiography at Standard Cross Sections and Flow Simulations*. PhD thesis, State University of New York at Buffalo, 2018.

[274] M. Hedayat, T. R. Patel, M. Belohlavek, K. R. Hoffmann, and I. Borazjani, "A hybrid echocardiography-computational fluid dynamics framework for ventricular flow simulations," *arXiv preprint arXiv:1909.09307*, 2019.

[275] A. M. Akbarzadeh and I. Borazjani, "Large eddy simulations of a turbulent channel flow with a deforming wall undergoing high steepness traveling waves," *Physics of Fluids*, vol. 31, no. 12, p. 125107, 2019.

[276] H. Asgharzadeh, H. Asadi, H. Meng, and I. Borazjani, "A non-dimensional parameter for classification of the flow in intracranial aneurysms. II. patient-specific geometries," *Physics of Fluids*, vol. 31, p. 031905, mar 2019.

[277] A. Akbarzadeh and I. Borazjani, "Reducing flow separation of an inclined plate via travelling waves," *Journal of Fluid Mechanics*, vol. 880, pp. 831–863, 2019.

[278] U. E. Ogunka, M. Daghooghi, A. M. Akbarzadeh, and I. Borazjani, "The ground effect in anguilliform swimming," *Biomimetics*, vol. 5, no. 1, p. 9, 2020.

[279] M. Daghooghi and I. Borazjani, "The effects of irregular shape on the particle stress of dilute suspensions," *Journal of Fluid Mechanics*, vol. 839, pp. 663–692, 2018.

[280] O. Vriz, V. Aboyans, A. D'Andrea, F. Ferrara, E. Acri, G. Limongelli, A. Della Corte, C. Driussi, M. Bettio, F. R. Pluchinotta, *et al.*, "Normal values of aortic root dimensions in healthy adults," *American Journal of Cardiology*, vol. 114, no. 6, pp. 921–927, 2014.

[281] K. Otani, A. Nakazono, I. S. Salgo, R. M. Lang, and M. Takeuchi, "Three-dimensional echocardiographic assessment of left heart chamber size and function with fully automated quantification software in patients with atrial fibrillation," *Journal of the American Society of Echocardiography*, vol. 29, no. 10, pp. 955–965, 2016.

[282] A. Rösner, B. Bijnens, M. Hansen, O. J. How, E. Aarsæther, S. Müller, G. R. Sutherland, and T. Myrmel, "Left ventricular size determines tissue doppler-derived longitudinal strain and strain rate," *European Journal of Echocardiography*, vol. 10, no. 2, pp. 271–277, 2008.

[283] T. Abdisa, "Review on practical guidance of veterinary clinical diagnostic approach," *Int J Vet Sci Res*, vol. 3, no. 1, pp. 006–025, 2017.

[284] U. Reiter, G. Reiter, M. Manninger, G. Adelsmayr, J. Schipke, A. Alogna, A. Rajces, A. F. Stalder, A. Greiser, C. Mühlfeld, *et al.*, "Early-stage heart failure with preserved ejection fraction in the pig: a cardiovascular magnetic resonance study," *Journal of Cardiovascular Magnetic Resonance*, vol. 18, no. 1, p. 63, 2016.

[285] M. Gharib, E. Rambod, A. Kheradvar, D. J. Sahn, and J. O. Dabiri, "Optimal vortex formation as an index of cardiac health," *Proceedings of the National Academy of Sciences*, vol. 103, no. 16, pp. 6305–6308, 2006.

[286] G. Haller, "An objective definition of a vortex," *Journal of fluid mechanics*, vol. 525, pp. 1–26, 2005.

[287] H. D. White, R. M. Norris, M. A. Brown, P. Brandt, R. Whitlock, C. J. Wild, *et al.*, "Left ventricular end-systolic volume as the major determinant of survival after recovery from myocardial infarction," *Circulation*, vol. 76, no. 1, pp. 44–51, 1987.

[288] M. J. S. St, M. A. Pfeffer, T. Plappert, J. L. Rouleau, L. A. Moyé, G. R. Dagenais, G. A. Lamas, M. Klein, B. Sussex, and S. Goldman, "Quantitative two-dimensional echocardiographic measurements are major predictors of adverse cardiovascular events after acute myocardial infarction. the protective effects of captopril.," *Circulation*, vol. 89, no. 1, pp. 68–75, 1994.

[289] J. E. Møller, K. Egstrup, L. Køber, S. H. Poulsen, O. Nyvad, and C. Torp-Pedersen, "Prognostic importance of systolic and diastolic function after acute myocardial infarction," *American heart journal*, vol. 145, no. 1, pp. 147–153, 2003.

[290] J. E. Møller, P. A. Pellikka, G. S. Hillis, and J. K. Oh, "Prognostic importance of diastolic function and filling pressure in patients with acute myocardial infarction," *Circulation*, vol. 114, no. 5, pp. 438–444, 2006.

[291] T. B. Le, M. S. Elbaz, R. J. Van Der Geest, and F. Sotiropoulos, "High resolution simulation of diastolic left ventricular hemodynamics guided by four-dimensional flow magnetic resonance imaging data," *Flow, Turbulence and Combustion*, vol. 102, no. 1, pp. 3–26, 2019.

[292] S. Khalafvand, J. Voorneveld, A. Muralidharan, F. Gijsen, J. Bosch, T. van Walsum, A. Haak, N. de Jong, and S. Kenjeres, "Assessment of human left ventricle flow using statistical shape modelling and computational fluid dynamics," *Journal of biomechanics*, vol. 74, pp. 116–125, 2018.

[293] K. Tanabe, M. Belohlavek, D. Jakrapanichakul, R. Y. Bae, J. F. Greenleaf, and J. B. Seward, "Three-dimensional echocardiography: Precision and accuracy of left ventricular volume measurement using rotational geometry with variable numbers of slice resolution," *Echocardiography*, vol. 15, no. 6, pp. 575–580, 1998.

[294] V. Vedula, R. George, L. Younes, and R. Mittal, "Hemodynamics in the left atrium and its effect on ventricular flow patterns," *Journal of biomechanical engineering*, vol. 137, no. 11, p. 111003, 2015.

[295] B. Su, X. Wang, F. Kabinejadian, C. Chin, T. T. Le, and J.-M. Zhang, "Effects of left atrium on intraventricular flow in numerical simulations," *Computers in biology and medicine*, vol. 106, pp. 46–53, 2019.